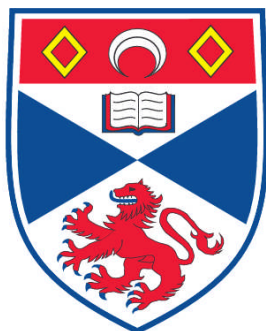


MESOPOROUS CRYSTALLINE METAL OXIDES

Wenbo Yue

A Thesis Submitted for the Degree of PhD
at the
University of St. Andrews



2009

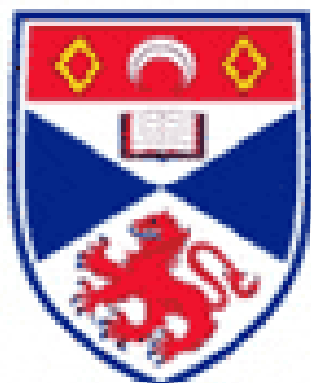
Full metadata for this item is available in
Research@StAndrews:FullText
at:
<http://research-repository.st-andrews.ac.uk/>

Please use this identifier to cite or link to this item:
<http://hdl.handle.net/10023/830>

This item is protected by original copyright

This item is licensed under a
Creative Commons License

Mesoporous Crystalline Metal Oxides



University
of
St Andrews

Wenbo Yue

PhD Dissertation

School of Chemistry, University of St. Andrews

Supervisor: Dr. Wuzong Zhou

March 2009



Declaration

I,, hereby certify that this thesis, which is approximately words in length, has been written by me, that it is the record of work carried out by me and that it has not been submitted in any previous application for a higher degree.

date signature of candidate

I was admitted as a research student in [month, year] and as a candidate for the degree of in [month, year]; the higher study for which this is a record was carried out in the University of St Andrews between[year] and[year].

date signature of candidate

I hereby certify that the candidate has fulfilled the conditions of the Resolution and Regulations appropriate for the degree of in the University of St Andrews and that the candidate is qualified to submit this thesis in application for that degree.

date signature of supervisor

In submitting this thesis to the University of St Andrews we understand that we are giving permission for it to be made available for use in accordance with the regulations of the University Library for the time being in force, subject to any copyright vested in the work not being affected thereby. We also understand that the title and the abstract will be published, and that a copy of the work may be made and supplied to any bona fide library or research worker, that my thesis will be electronically accessible for personal or research use unless exempt by award of an embargo as requested below, and that the library has the right to migrate my thesis into new electronic forms as required to ensure continued access to the thesis. We

have obtained any third-party copyright permissions that may be required in order to allow such access and migration, or have requested the appropriate embargo below.

date signature of candidate

Embargo on both all of printed copy and electronic copy for the same fixed period of years (maximum five) on the following ground:

publication would be commercially damaging to the researcher, or to the supervisor, or the University;

publication would preclude future publication;

publication would be in breach of law or ethics

date signature of supervisor

Acknowledgements

Firstly I am cordially grateful to my supervisor Dr Wuzong Zhou for his help of imparting the knowledge of electron microscopy, crystallography, and directing me to design the experiments, solving problems in experiments and writing scientific papers and dissertation. Moreover he took care of my life in St Andrews and taught me to become a true chemist. He is one of the persons I respect and appreciate very much in the world.

And I would also like to thank Mr. Ross Blackley, who trained me on high resolution transmission electron microscopy and X-ray diffraction; Mrs Sylvia Williamson for her help of BET experiments; Mr. Adrian H. Hill and Prof. Andrew Harrison for the work of SQUID magnetometry, which was used to examine the magnetic character of mesoporous Co_3O_4 ; Mr. Xiaoxiang Xu, Mr. Pierrot S. Attidekou, Mr. Chamnan Randorn and Prof. John T. S. Irvine for examination of the proton conductivity, Li insertion and photoactivity properties of mesoporous TiO_2 ; Mr. Chong Liu, Prof. Dongyuan Zhao and Prof. Heyong He for their support to my visit to Fudan University in China.

Subsequently, I need to say “thank you” to Mr. Calum Dickinson who gave me many helps in discussions of my experiments and operations of HRTEM and XRD; to Mr Zixue Su with who I worked and played (e.g. football, basketball and badminton) together; and to many other Chinese guys in the University of St Andrews who were so nice to me.

Finally, I should thank my parents who brought me up and always supported me. They are invaluable to me in the world. Miss Yue Hou, a special lady for me in this world, brings happiness to me and will be with me forever in my life. I am grateful for her to take care of me.

I also thank St Andrews University for the EaStCHEM scholarship.



Abstract

Mesoporous monocrystalline metal oxides (e.g. Co_3O_4 , Cr_2O_3 , NiO , CeO_2 , In_2O_3 and WO_3) templated by SBA-15 or KIT-6 were synthesised successfully by using a simple solvent-free approach, the so-called solid-liquid method, which was the principal development of methodology in this project. A metal-containing precursor, whose melting point is lower than its decomposition temperature, was directly ground with a mesoporous silica and impregnated into the pores of the silica template after melting when the temperature was increased above its melting point. The liquid precursor then decomposed to form metal oxide inside the silica pores when the temperature was further increased to its decomposition temperature and crystallization temperature of the oxide. The structural characterisations of these porous metal oxides were performed by using TEM, XRD and N_2 adsorption/desorption techniques. The solid-liquid method is convenient and solvent-free. On the other hand, its limitation is that the precursor must have a melting point lower than its decomposition temperature.

A novel porous single crystal of rutile TiO_2 as well as anatase nanocrystal-silica composite was also synthesised successfully for the first time using SBA-15 and KIT-6 as templates. These materials have interesting properties of proton conductivity, Li insertion and photoactivity. Likewise, the characterisation of porous TiO_2 was achieved by using XRD, TEM, SAED and N_2 adsorption/desorption. The residual SiO_2 component in porous TiO_2 was detected by using the EDX technique.

Porous cubic metal oxides of Co_3O_4 , NiO , CeO_2 and In_2O_3 were prepared using novel mesoporous silicas FDU-12 and SBA-16, which contain spherical nanocavities linked together by smaller windows. These porous materials have larger surface areas than those templated by SBA-15 and KIT-6. Unlike the cubic metal oxides, syntheses of porous crystals of non-cubic metal oxides such as rhombohedral Cr_2O_3 , Fe_2O_3 and hexagonal TiO_2 , WO_3 were not successful when using cage-containing mesoporous silicas as templates. The three-dimensional arrangements of nanospheres in porous

crystals of cubic oxides mentioned above were observed by TEM and the corresponding larger surface areas were confirmed by N₂ adsorption/desorption technique.

Additionally, fabrication of porous crystals of other metal oxides such as MgO, ZnO and ZrO₂ were unsuccessful by using either mesoporous silicas or mesoporous carbons as templates. Possible drawbacks of using mesoporous silica and carbon as templates were discussed.

Contents

Declaration	I
Acknowledgements	III
Abstract	V
Contents	VII
1 Introduction	1
1.1 Disordered mesoporous material	2
1.2 Ordered mesoporous silica	4
1.2.1 SBA-15	7
1.2.2 KIT-6	7
1.2.3 FDU-12 and SBA-16	8
1.3 Functionalised mesoporous silica	9
1.4 Metal/metal oxides incorporated mesoporous silica	11
1.5 Ordered mesoporous carbon	14
1.5.1 CMK-n	14
1.5.2 FDU-n	16
1.6 Ordered mesoporous metals and metal oxides	19
1.6.1 Soft templating route	20
1.6.2 Hard templating route	22
1.6.2.1 Mesoporous silica as a template	22
1.6.2.2 Mesoporous carbon as a template.....	28
1.7 Impregnation methodology	31
1.7.1 Evaporation method	32
1.7.2 Other methods	32
1.8 Anodic mesoporous metal oxide films	32
1.9 Aims and objectives	34

2 Experimental	36
2.1 Synthesis of mesoporous hard templates	36
2.1.1 Mesoporous silica	36
2.1.1.1 SBA-15	37
2.1.1.2 KIT-6	37
2.1.1.3 FDU-12	37
2.1.1.4 SBA-16	38
2.1.2 Mesoporous Carbon	38
2.1.2.1 C-FDU-12 and C-SBA-16	38
2.1.2.2 FDU-15	39
2.2 Impregnation of precursors and crystallisation	39
2.2.1 Evaporation method	39
2.2.2 Solid-liquid method	41
2.3 Removal of hard template	42
2.3.1 Silica template	42
2.3.2 Carbon template	43
2.4 Characterisation methods	43
2.4.1 High resolution transmission electron microscopy	44
2.4.1.1 HRTEM instrument	44
2.4.1.2 TEM imaging theory	45
2.4.1.3 Select area electron diffraction	51
2.4.1.4 Energy dispersive X-ray analysis	52
2.4.2 X-ray diffraction	54
2.4.3 Nitrogen adsorption and desorption	57
2.4.4 Thermogravimetric/differential thermal analysis	61
2.5 Physico-chemical properties	61
2.5.1 Proton conductivity	61
2.5.2 Li ion storage	62
2.5.3 Photocatalysis	63

3 Solid liquid method	64
3.1 Mesoporous silica template	65
3.1.1 SBA-15	65
3.1.2 KIT-6	66
3.2 Porous metal oxides synthesised using the solid-liquid method	66
3.2.1 Co_3O_4	67
3.2.2 Cr_2O_3	69
3.2.3 NiO	71
3.2.4 CeO_2	73
3.2.5 In_2O_3	75
3.2.6 WO_3	77
3.3 Comparison between the evaporation and solid-liquid methods	79
3.3.1 Porous Cr_2O_3 synthesised using the two methods	80
3.3.2 $\text{Pb}(\text{NO}_3)_2$ and $(\text{NH}_4)_2\text{Cr}_2\text{O}_7$ used as precursors	83
4 Novel porous metal oxides templated by SBA-15 and KIT-6	86
4.1 TiO_2	87
4.1.1 TiO_2 templated by KIT-6	87
4.1.1.1 Proton conductivity	94
4.1.1.2 Li ion insertion capability	95
4.1.2 TiO_2 templated by SBA-15	97
4.1.2.1 Li ion insertion capability	108
4.1.2.2 Photoactivity	109
4.2 MgO and CuO	111
4.3 Ga_2O_3 and ZnO	116
4.4 La_2O_3 and ZrO_2	117
5 Porous metal oxides templated by FDU-12 and SBA-16	122
5.1 Mesoporous silicas of FDU-12 and SBA-16	123

5.2 Cubic metal oxides	124
5.2.1 Co_3O_4	124
5.2.2 NiO	128
5.2.3 CeO_2	130
5.2.4 In_2O_3	132
5.3 Non-cubic metal oxides	133
5.3.1 Cr_2O_3 and Fe_2O_3	134
5.3.2 TiO_2 and WO_3	136
5.4 Tetragonal MnO_2 and cubic Mn_2O_3	137
6 Metal oxides templated by mesoporous carbons	142
6.1 Mesoporous carbon	143
6.1.1 C-FDU-12 and C-SBA-16	143
6.1.2 FDU-15	145
6.2 MgO and CuO templated by C-FDU-12 and C-SBA-16	145
6.3 MgO and ZnO templated by FDU-15	148
7 Conclusions and future work	151
7.1 Conclusion	151
7.2 Future work	154
References	155
Publications	168

1. Introduction

Porous materials are also called cellular solids that are solids containing pores such as cavities, channels or interstices.¹ The porosity, density, specific surface area and pore size are usually used to describe a porous solid. In particular, the pore size of porous material is most important for its application in catalysis, electrode and gas sensors. According to the size of pores (IUPAC notation),² porous materials are classified into macroporous materials, which have pore diameters of more than 50 nm; mesoporous materials, which have pore diameters between 2 nm and 50 nm; and microporous materials, which have pore diameters of less than 2 nm (Figure 1-1).

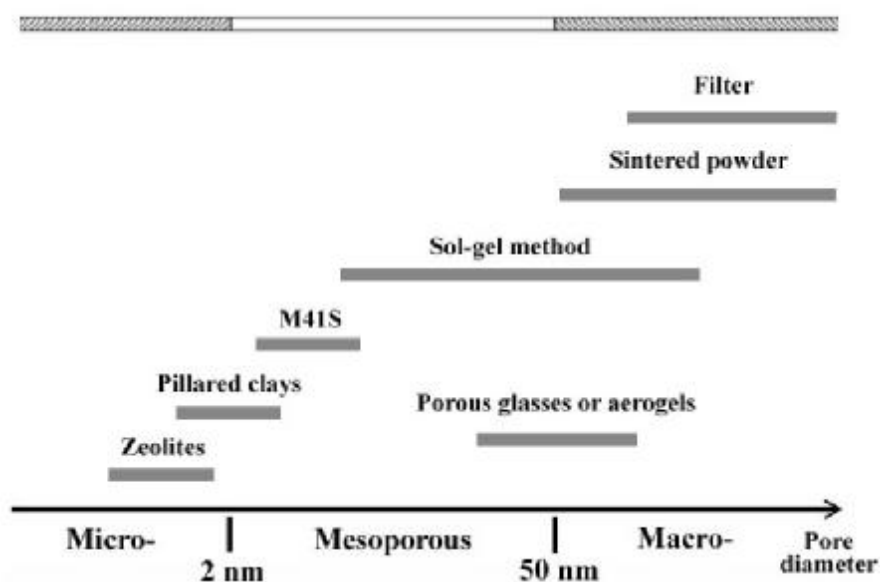


Figure 1-1. Pore size of typical porous ceramics¹

Microporous and mesoporous inorganic solids are widely used as catalysts and sorption media due to their large surface area and porosity structure. The most well-known microporous materials, with an ordered porosity, synthesised by a template are zeolites.³ Zeolites (Greek, zein, "to boil"; lithos, "a stone") are aluminosilicate minerals and have a microporous structure. The first zeolite was discovered by Swedish mineralogist A. F. Cronstedt in 1756 and it was a usual microporous material whose pore size was ca. 0.5 nm. In 1987, the Davis group synthesised the aluminophosphate VPI-5, an 18-ring microporous material with the largest pore diameter of 1.3 nm.⁴ This was the first of a series of zeolite-like materials with extra large pores. Then UTD-1 and CIT-5, both containing extra-large pore

14-ring zeolite with a pore diameter of over 1 nm, were synthesised by Davis group in 1996 and 1997, respectively.^{5,6}

Shape-selective catalysis is one of the important functions of zeolite catalysts which can be tuned by controlling the pore size and structure of zeolites.⁷⁻⁹ However, the small pore size of zeolites may affect the transfer of reagents and products and limit the catalytic range of large molecules such as organic materials and biomolecules. Therefore zeolites with large pore sizes (more than ten angstroms in diameter) would be attractive. The pore size of zeolites can be increased via an increase of the ring members, for example, in VPI-5, 18-membered rings exist. However, based on the aluminophosphate crystalline framework, the increase of pore size is limited because too large rings may lead to instability in the framework and the porous structure of the zeolites would collapse during the synthetic process.

Mesoporous materials containing pores diameters of 2-50 nm can solve the aforementioned problems of applications for reactions of large molecules inherent to microporous materials and have wide applications in nanoreactors, electronic devices, gas sensors and catalysts.¹⁰⁻¹³

1.1 Disordered mesoporous material

Typical mesoporous materials include some kinds of silica and alumina as well as metals and metal oxides with various kinds of similarly-sized mesopores. According to the IUPAC notation, a mesoporous material can be divided into disordered and ordered materials in the mesostructure. The typical disordered mesoporous silica, KIT-1, which is similar to MCM-41 with high surface area, was reported by Ryoo et al. in 1996.^{14,15} However, its pore structure is a three-dimensional disordered arrangement of interconnected channels instead of a hexagonal packing of straight channels in MCM-41. The mesoporous KIT-1 was synthesised by an electrostatic templating route using hexadecyltrimethylammonium chloride (HTACl) as the surfactant, sodium silicate as a silica source and ethylenediaminetetraacetic acid tetrasodium (EDTANa₄) as a salt. The silicate was hydrothermally polymerised surrounding HTA micelles in aqueous solution at 373 K and the pH of the reaction mixture was adjusted to 10 with acetic acid to form the porous silica after the temperature was cooled down to room temperature.

In 1995, a worm-like disordered mesoporous silica, which was denoted as MSU-X, had been prepared by the hydrolysis of tetraethyl orthosilicate (TEOS) in a structure-directing agents (SDA) of nontoxic and biodegradable polyethylene oxide (PEO) surfactants by Pinnavaia and co-workers.^{16,17} The disordered worm-like channels of MSU-X had a pore size range of 2.0-5.8 nm and can be adjusted by controlling the size and structure of the surfactant molecules. Additionally mixed metal oxides, based on silica but also including titanium and zirconium, Ti-MSU-1 and Zr-MSU-1, had also been prepared by the hydrolysis of the corresponding alkoxides in the presence of PEO surfactants. McGrath et al. (1997) used the lyotropic L₃ phase as a template to form mesoporous monolithic silicates with large, uniform, but disordered pore networks.¹⁸ Unlike other mesoporous silicates templated by the surfactant micelles, the bicontinuous pores of this silicate L₃ phase were ~ 6 nm in diameter and were filled with water, which reduced the effect of blockage of the surfactant in the pores.

The disordered mesoporous silica KIT-1, as a catalyst, lacks strong acid sites. Therefore a new family of disordered mesoporous aluminosilicates (DMAS), hydrothermally stable and with strong surface acidity, was developed from MSU-X by Zhao et al. in 2001.¹⁹ The solids were synthesised by using polymeric aluminosilicate as the precursor, and the cationic surfactant cetyltrimethylammonium bromide (CTAB) as the structure-directing agent. These DMAS are very similar to mesoporous MCM-41, with a uniform mesopore size of 3.0 nm, but with stronger surface acid strength and higher cracking activities than highly ordered Al-containing MCM-41.

Except the templating method using surfactant as soft template in solution, a new method using small non-surfactant templates had been developed to synthesise disordered mesoporous silica (denoted as TUD-1, Jansen et al., 2001) with high surface areas, foam-like pore networks and hydrothermal stability.²⁰ The control of the intermolecular interaction among organic templates and inorganic species is crucial to form mesopores networks. In the first step, a mixture of tetraethylorthosilicate (TEOS), triethanolamine (TEA) and water formed a homogeneous gel after aging and drying in air. The TEOS in mixture hydrolyzed to create the silica following the partial condensation of the silanol species with each other and with some of the TEA. A white mesoporous TUD-1 can be obtained finally by the removal of the template via either Soxhlet extraction or calcination. This new

disordered mesoporous material, TUD-1, has a three dimensional foam-type structure with pore diameter of 2.5-25 nm, high surface areas of $\sim 1000 \text{ m}^2/\text{g}$, and high thermal and hydrothermal stability. Recently, the new disordered mesoporous silica containing zeolite composites, TUD-C and TUD-M²¹⁻²³ were reported by Wang et al. in 2008 and the disordered mesoporous silica support of the composites was developed from TUD-1, using tetrapropyl ammonium hydroxide (TPAOH) as the framework.

Mesoporous silica films can be also prepared by using chemical vapor deposition (CVD) technique to introduce silica source. The first ordered mesoporous silica films prepared by a vapour infiltration technique using tetraethoxysilane (TEOS) or trimethylethoxysilane (TMES) as the precursors under acidic conditions were reported in Ueyama group a few years ago.^{24,25} A new disordered mesoporous silica film has been prepared by this vapor phase method recently.²⁶ The triblock copolymer/silica composite with a wormhole-like disordered structure was formed via the TEOS molecules penetrated into a triblock copolymer film. The final product of disordered silica film has the uniform tortuous pore channels with a diameter of 6-7 nm.

In addition, disordered mesoporous metal oxides were also reported and had wide potential applications. For example, a disordered mesoporous rutile TiO_2 was synthesised recently by Wang et al. within an anionic surfactant matrix, and its Li insertion property was examined.²⁷ This highly crystalline disordered mesoporous TiO_2 has high surface area of $245\text{-}300 \text{ m}^2/\text{g}$ and tunable mesopores in diameter of 2.2-3.8 nm. It can accommodate 0.7 Li ($\text{Li}_{0.7}\text{TiO}_2$, 235 mA h g^{-1}) at the first discharge and has a reversible capacity of 0.55 Li ($\text{Li}_{0.55}\text{TiO}_2$, 185 mA h g^{-1}) after the second discharge.

1.2 Ordered mesoporous silica

Figure 1-2 shows the classification of ordered mesoporous materials including ordered mesoporous pure and modified silicas, ordered mesoporous metals, metal oxides and mixed oxides, and mesoporous carbons.²⁸ Mesoporous silica is a kind of very important ordered mesoporous materials and has been explored extensively.

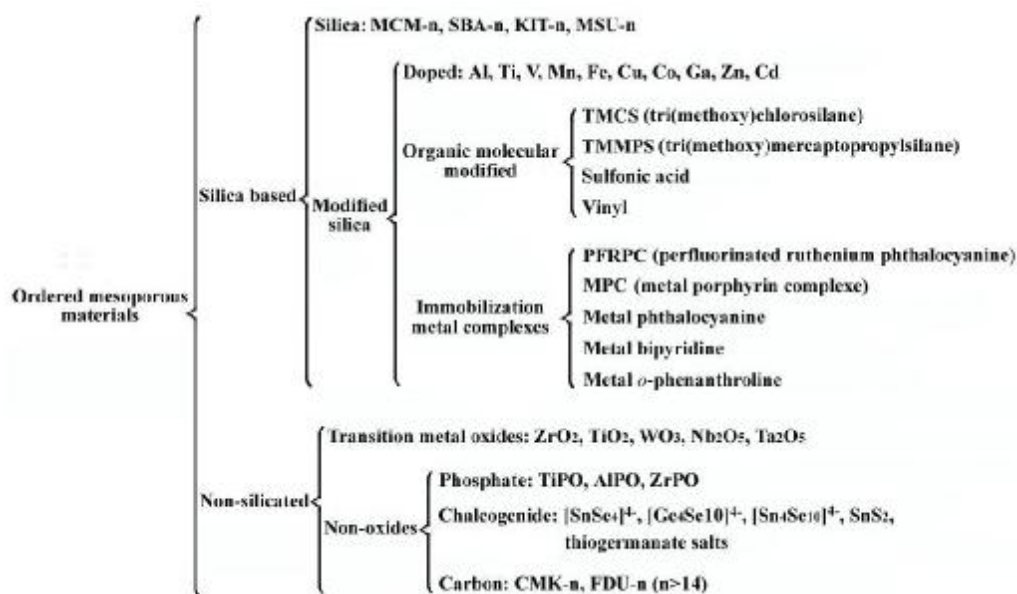


Figure 1-2. The classification of ordered mesoporous materials.²⁸

The first general accepted mesoporous materials, the M41S class (particularly MCM-41) with pores ordered on the long range, were synthesised by a research group of the former Mobil Oil Company in 1992.^{29,30} The mesoporous MCM-41 synthesised by using cetyltrimethylammonium bromide (CTAB) as a structure-directing agent (SDA) in a basic solution has a hexagonal structure (space group $p6mm$) and contains cylindrical channels. The synthetic process, shown in Figure 1-3, is as follows. Organic template firstly self-assemble to micelles and the micelles congregate to hexagonal arrays in basic conditions. Silica source, tetraethyl orthosilicate (TEOS), is introduced into the hexagonal framework and forms mesoporous silica after maturing for 48 h at 100 °C. The organic template can be removed by a thermal treatment.

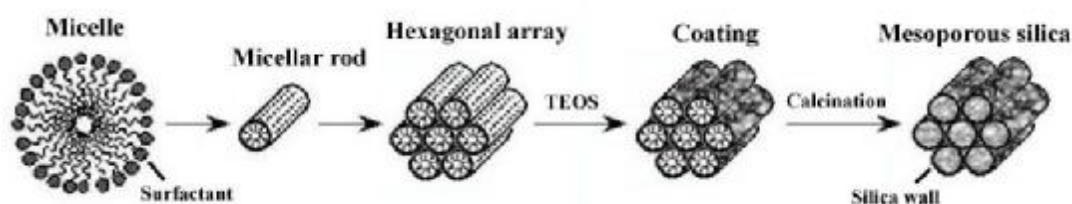


Figure 1-3. Schematic diagram of the formation of MCM-41.³⁰

MCM-41 (Mobil Composition of Matter No.41) molecular sieve exhibits a hexagonal mesopore system with uniform pore size that may be tuned from ~1.6 nm to 10 nm and large surface areas of above 1000 m²/g. Another family member, MCM-48, consists of two independent and intricately interwoven networks of

mesoporous channels.^{29,31} Both MCM-41 and MCM-48 had been applied as catalysts for various chemical reactions, a support for drug delivery system and an adsorbent in waste water treatment.³²⁻³⁶ Figure 1-4 shows the schematic diagram of the mesoporous structures of MCM-41 and MCM-48, respectively.

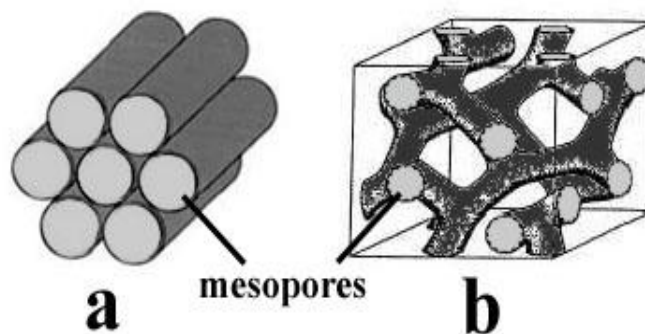


Figure 1-4. Schematic diagram of mesoporous structures of (a) MCM-41 and (b) MCM-48, respectively.^{29,30}

In 1990, another mesoporous material KSW-1, synthesised by reaction of single layered polysilicates, namely kanemite, with alkyltrimethylammonium chloride under a basic condition by stirring at 65 °C for one week, was reported by Yanagisawa et al.³⁷ Mesoporous KSW-1 has a pore diameter in a range of 2-4 nm depending on the alkyl group used and a surface area of 900 m²/g. Similar to the structure of mesoporous MCM-41, KSW-1 has also a hexagonally ordered pore structure. However, the formation mechanisms of MCM-41 and KSW-1 are not same. For the KSW-1 synthesis, the sodium ion between the layered structures of kanemite was replaced by alkyltrimethylammonium and the sheets folded to form a hexagonal structure.³⁸

However, this kind of mesoporous silica synthesised using a templating mechanism (liquid crystal templating-LCT) has a low hydrothermal stability and no connection between neighbouring pore channels. Subsequently some new ordered mesoporous silicas, SBA-15 and KIT-6, with similar structures to MCM-41 and MCM-48, have been prepared by Zhao et al.^{39,40} and Ryoo et al.,⁴¹ respectively. Compared with MCM-41 and MCM-48, SBA-15 and KIT-6 have similar large surface areas and uniform pore size distributions, but high hydrothermal stability. Additionally SBA-15 and KIT-6 have small nanochannels connecting neighbouring main channels (Figure 1-5).

1.2.1 SBA-15

Unlike MCM-41, which is templated by a cationic quaternary ammonium surfactant (ionic surfactant), SBA-15 is synthesised by using a non-ionic triblock copolymer, which is made up from poly (ethylene oxide)-poly (propylene oxide)-poly (ethylene oxide) chains (PEO-PPO-PEO), as a template.^{39,40} Firstly, Pluronic P123 (EO₂₀PO₇₀EO₂₀) surfactant is dissolved in acidic aqueous media and self-assembled. Silica source, normally tetraethylorthosilicate (TEOS) or tetramethoxysilane (TMOS), is added to the solution and forms a silica coating on the surface of micelles. The silica/copolymer solution is aged at 100 °C for 24-72 h to increase the hydrothermal stability. The surfactant template is removed by a thermal treatment at 550 °C for 5 h. This type of mesoporous silica has not only a large pore size (5-30 nm) and wall thickness (3-6 nm), which can be tailored by addition of a swelling agent 1,3,5 trimethylbenzene (TMB), but also a large surface area (850-910 m²/g). Moreover its hydrothermal stability is high. SBA-15 has a hexagonal unit cell, similarly to MCM-41, containing hexagonally ordered cylindrical pores connected by small nanochannels. Figure 1-5(a) shows the mathematical representations of the SBA-15 structure (space group $p6mm$) with connecting micropores.⁴²

1.2.2 KIT-6

KIT-6 is another type of mesoporous silica synthesised by using a combination of triblock copolymer (Pluronic P123) and butanol for controlling the structure in an aqueous solution.⁴¹ The thermal and hydrothermal stability of KIT-6 can be enhanced by aging at 100 °C for 24-72 h, and the surfactant can be removed after thermal treatment at 550 °C for 5 h. The structure of the mesopores in KIT-6, similar to MCM-48, is body-centered cubic (space group $Ia\bar{3}d$). It consists of a pair of interpenetrating bicontinuous pores, whose size can be controlled from 4 to 12 nm in diameter under a simple hydrothermal treatment (25-35 °C). Surface area of KIT-6 can be reached to 800-960 m²/g. Figure 1-5(b) shows the mathematical representations of cubic KIT-6 structure with the pair of interpenetrating bicontinuous pores.⁴²

1.2.3 FDU-12 and SBA-16

Unlike SBA-15 and KIT-6, in which the basic building unit of pores is cylindrical, both FDU-12 and SBA-16 consist of spherical nano-cavities linked together by very short nano-channels or windows. FDU-12 has a face-centred cubic structure (space group $Fm\bar{3}m$)^{43,44} and SBA-16 has a body-centred cubic structure (space group $Im\bar{3}m$).^{40,45} Accordingly, each spherical nanocage is 12 coordinated in FDU-12, but 8 coordinated by the neighbouring nanocages in SBA-16. The large cavities in both phases are produced in the presence of triblock copolymer templates, Pluronic F127 (EO₁₀₆PO₇₀EO₁₀₆). The pore sizes of SBA-16 and FDU-12 are normally about 5.4 nm and 10-12.3 nm in diameter, respectively. It is even possible to increase the pore size up to 27 nm in FDU-12 with a hydrothermal treatment at 15 °C,⁴⁴ and the size of the entrances joining two adjacent cavities can be tuned in the range of 4-9 nm in diameter using different maturation temperatures in a range from 100 to 140 °C. The surface areas of both FDU-12 and SBA-16 are over 700 m²/g. Figure 1-5(c) and (d) show the mathematical representations of cubic SBA-16⁴⁶ and FDU-12⁴⁷ structure with small connecting micropores, respectively.

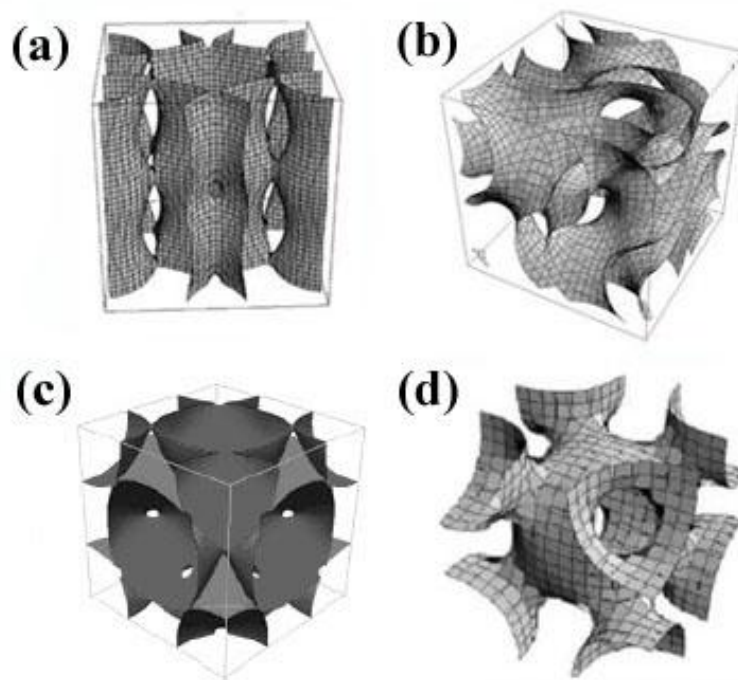


Figure 1-5. Mathematical diagrams of mesoporous structures for (a) SBA-15, (b) KIT-6, (c) FDU-12 and (d) SBA-16.^{42,46,47}

1.3 Functionalised mesoporous silica

Although the new mesoporous M41S class, especially MCM-41 and MCM-48, have large surface areas ($>1000 \text{ m}^2/\text{g}$), tunable pore sizes (2-10 nm) and large pore volumes ($>0.7 \text{ cm}^3/\text{g}$), they have weak hydrothermal stability, low ion exchange capacity, and very small number of Lewis acid sites on the surface. These properties confine their application as catalysts. Therefore, functionalisation of the silica walls has been investigated by introducing heteroatom, organics, or metal oxides to increase their catalytic properties. This functionalisation can occur at either the synthesis step (*in situ*) or in a post synthesis step.

In situ functionalisation is typically carried out by introducing organics during the mesoporous silica formation, such as the organically functionalized mesoporous silicas prepared by the co-condensation of tetraethoxysilane and organosiloxanes in the presence of surfactant templates.⁴⁸ This functionalised mesoporous material with covalently linked, ordered and hybrid inorganic-organic networks has a higher thermal stability for the organics. On the other side, a very stable organically modified MCM, aminopropyl-modified MCM, is prepared by mixing silica source (TEOS) and organics source (AMPS) with a mixture of ethanol, distilled water and n-dodecylamine before thermal treatment.⁴⁹ The aminopropyl-MCM has not only a high thermal stability ($> 500 \text{ }^\circ\text{C}$) but also a high solvent stability that the aminopropyl groups can not be extracted by ethanol under reflux. However, the desired organic group addition can change the phase of the material. For example, the addition of different percentages of 3-mercaptopropyltriethoxysilane (MPTES) in the preparation of mesoporous silicas results in the structure variety of silica from $p6mm$ to $Ia\bar{3}d$ using P123 as the template and from $Fm\bar{3}m$ to $P6_3/mmc$ using F127 as the template.⁵⁰ This phenomenon that mesoporous silica functionalised *in situ* by addition of desired organics can vary in structure can not be found in post-synthesis functionalisation.

Grafting functional groups to the walls instead of forming functional groups *in situ* as a part of the walls is called post-synthesis functionalisation. Unlike the *in situ* functionalisation which may change the mesoporous silica structure, the post synthesis functionalisation will normally not lead to a structural change because the mesoporous silica phase forms already before the functionalisation. Typically, the same functional groups used in the *in situ* method, such as thiol, chloride, amine and

carboxylic acid functional groups, can be also attached by siloxypropane tethers to the siliceous surface of SBA-15,⁵¹ Figure 1-6 shows some examples of post-synthesis functionalisations of mesoporous silica. Furthermore, the end of the functional chains grafted to the silica walls can be altered further to another functional group such as the C-CN converting to C-COOH in H⁺/H₂O condition (Figure 1-6). The grafting process can not affect the formed structure of mesoporous silica, whereas it would reduce the pore size, such as the pore size of SBA-15 reducing from ~10 nm to 5.1-5.6 nm after the post-synthesis functionalisation.⁵¹

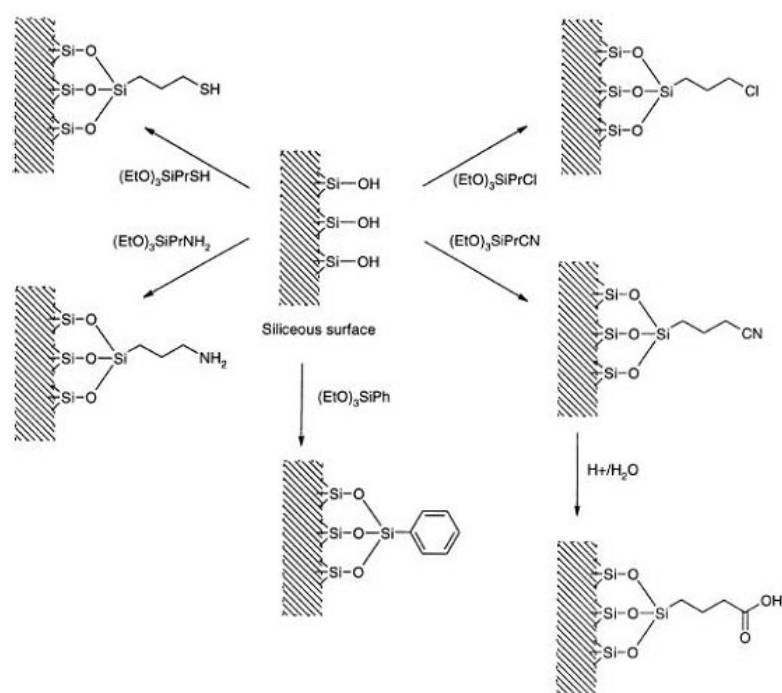


Figure 1-6. Some examples of post-synthesis functionalisation of mesoporous silica.

51

The uniform mesopores of the silica, functionalized by the catalytically active groups using either *in situ* method or post-synthesis method, can selectively catalyze the organics by determining which molecules can enter. Taking *in situ* functionalisation as an example, a mesoporous MCM-41/Nafion composite prepared from tetraethoxysilane and Nafion gel solution by using cetyltrimethylammonium surfactant as a template is a highly selective catalyst for α -methylstyrene dimerisation to form the corresponding acyclic dimer.⁵² For an example of post-synthesis functionalisation, the sulfonic mesoporous materials (MCM-41-SO₃H) prepared by immobilization of 3-mercaptopropyl groups and oxidation with H₂O₂ on the MCM-41

walls, can selectively catalyze the biphasic glycerol to the high monoglyceride yield.⁵³ Mesoporous TEMPO-MCM-41 systems prepared either by grafting using trialkoxyorganosilane bearing 2,2,6,6-tetramethyl-1-piperidinyloxy (TEMPO) or by coupling onto previously anchored 3-aminopropylsilyl chains can selectively oxidize the primary alcohols towards either carboxylates or aldehydes.⁵⁴

1.4 Metal/metal oxides incorporated mesoporous silica

Besides organic-functionalised mesoporous silicas, metal-incorporated mesoporous silicas have also high activity and selectivity as catalysts. The first metal-incorporated mesoporous, Al-MCM-41,²⁹ was prepared to increase the Lewis acid sites on the mesopore surface, and has a high activity in the vapor-phase Beckmann rearrangement of cyclohexanone oxime to ϵ -caprolactam and conversion of acetone.^{55,56} However, such incorporation often results in a reduction of ordering of the pores.⁵⁷ Subsequently, following the mesoporous silica development, many metals and metal oxides were incorporated into mesoporous silicas and used as catalysts. The metals can be incorporated to the silica walls by using embedding and grafting techniques.

The metals can be embedded into the framework in the growth stage of the mesoporous silicas, normally by mixing a metal organic salt with the silica source in a solution containing the surfactant template.^{58,59} Another method to embed metals is the use of a metal-surfactant composite instead of standard surfactant, which retained the metals after removal of the surfactant by calcination.⁶⁰ Because the metal-containing surfactants are not commercially available and need to be synthesised,⁶¹ the grafting technique is more convenient and economical in comparison with the embedding technique. The grafting technique for introducing metals, similarly to the grafting in the post-synthesis functionalisation, is that the metal complexes are anchored with the silanol groups on the surface of silica pores after the mesoporous silica formation.⁶² Figure 1-7 shows a computer-generated illustration of the accommodation of Cp_2TiCl_2 molecules inside a siliceous MCM-41 pore (3 nm in diameter). To avoid aggregation of the metal particles to reduce the catalytic activity, some organometallic compounds are often used in the synthesis.

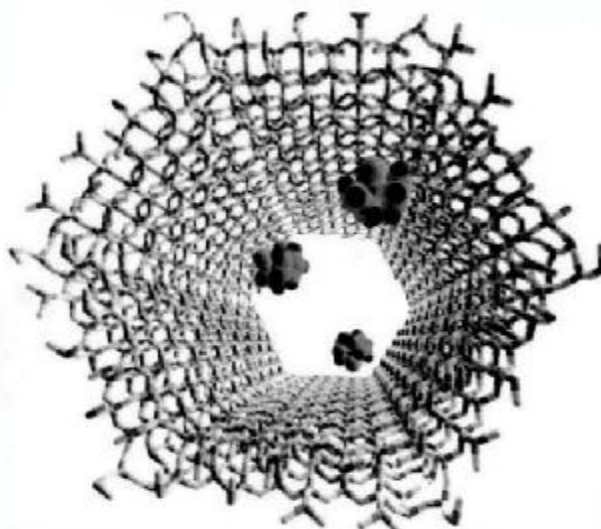


Figure 1-7. The computer-generated illustration of the accommodation (diffusion/adsorption) of molecules of titanocene dichloride inside a pore (3 nm diameter) of siliceous MCM-41.⁶²

Many metal-containing ordered mesoporous silicas have been widely used as catalysts, such as metal-MCM-41 and metal-MCM-48. Ti-MCM-41⁵⁸ can oxidize 2,6-ditert-butyl phenol to the corresponding quinone and olefins, cycloolefins to epoxides, and convert benzene to phenol. Oldroyd et al. (1996) compared Ti-MCM-41 prepared by the embedding technique and grafting technique,⁶³ and found that the grafted Ti-MCM-41 catalysts have a higher activity than embedded Ti-MCM-41 for epoxidation. W-MCM-41 showed an activity for highly selective oxidation of cyclopentene to glutaraldehyde by aqueous H_2O_2 ⁶⁴ and Au-MCM-41 showed an activity for highly selective oxidation of cyclohexane using oxygen.⁶⁵ Cr-MCM-41/MCM-48 as heterogeneous catalysts for liquid phase oxidation reactions,⁶⁶ V-MCM-41/MCM-48 as catalysts for the selective oxidation of propane in gas phase⁶⁷ and Pd-MCM-41/MCM-48 as heterogeneous catalysts for hydrocarboxylation of aryl olefins and alcohols⁶⁸ were also reported. Additionally mesoporous MCM-41 and MCM-48 containing metal oxides such as Fe_2O_3 , ZnO and PbO were synthesised by using the incipient wetness method, and the quantum confinement of the incorporated nanoparticles in MCM-41 and MCM-48 was confirmed via diffuse reflectance ultraviolet-visible spectroscopic study.⁶⁹

Meanwhile metal-containing disordered mesoporous silica can also be prepared and used as catalysts, such as Rb-AIKIT-1 for the reaction of the benzaldehydes with ethyl cyanoacetate in toluene⁷⁰ and Ag-KIT-1 for partial oxidation of ethylene.⁷¹ Additionally the mesoporous KIT-1 supported the metal oxides of MoO₃ or NiO catalysts exhibited higher catalytic activities for thiophene hydrodesulfurization than MCM-41 and NaY zeolite supported catalysts.⁷²

SBA-15, a novel ordered mesoporous silica with larger surface areas, uniform pore size and high hydrothermal stability, is a good catalyst support. According to the previous reports, for example, Cu-SBA-15 had a high catalytic activity in hydroxylation of phenol by H₂O₂, with 62.4 % conversion and 97 % selectivity to the diphenol (the mixture of catechol (CAT) and hydroquinone (HQ)).⁷³ Ni-SBA-15 catalyst prepared by using an incipient wetness impregnation method led to a higher conversion of CH₄ and CO₂ under the reaction conditions.⁷⁴ Zr-SBA-15 synthesised directly using zirconium nitrate and tetraethyl orthosilicate as precursor, exhibited high activity in the isomerisation of n-pentane at 35 °C after sulphated, and the conversion of n-pentane reached to 93.9 %.⁷⁵ V-SBA-15 directly synthesised in an acidic and peroxidic medium exhibited superior catalytic performance for oxidative dehydrogenation of propane.⁷⁶

Recently, Zhu group focused on the research of SBA-15 containing metal oxide nanoparticles, and a series of metal oxides such as CuO, MgO, Cr₂O₃, Fe₂O₃ and ZnO were highly dispersed in SBA-15 respectively, by manually grinding the corresponding precursor salts with SBA-15 before calcination of these mixtures. The samples prepared by this solvent-free method showed higher catalytic activities in trapping volatile nitrosamines (NPYR) than those prepared by impregnation method. Additionally the ZnO-SBA-15 composites exhibited photoluminescence (PL) properties.⁷⁷⁻⁷⁹ Figure 1-8 shows the synthetic process of metal oxides loaded mesoporous silicas. *In situ* coating of MgO or CuO in SBA-15 mesopores was also reported by Zhu group⁸⁰ by directly adding simple precursor salts into the synthetic process of mesoporous silica.

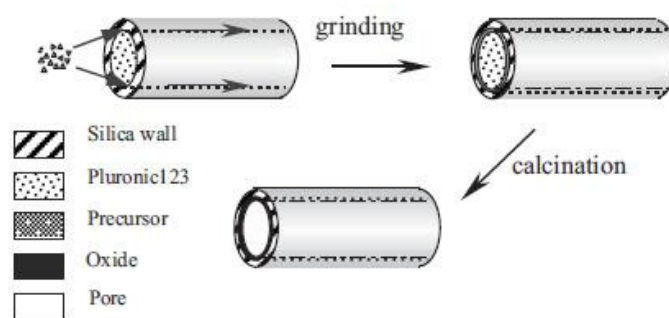


Figure 1-8. Schematic diagram of the solid-state procedure for loading oxides using as-made mesoporous silica as a support.⁷⁸

1.5 Ordered mesoporous carbon

Due to the properties of electron-conducting frameworks, high surface areas, and large pores, mesoporous carbon became an important family member of the mesoporous materials, which had potential applications in catalysis, adsorption and separation, electrochemistry, solar cells, lithium ion batteries, and hydrogen-storage systems.⁸¹⁻⁸⁵ Ordered mesoporous carbon can be synthesised by two methods, the hard-templating method such as CMK- n ($n \geq 1$) prepared in Ryoo group and the soft-templating method such as FDU- n ($n \geq 14$) prepared in Zhao group.

1.5.1 CMK- n

Mesoporous silica, used besides as catalyst, adsorbent and in separation, can also be used as a hard template for casting mesoporous materials, such as the mesoporous carbon labelled CMK- n ($n \geq 1$). In 1999, Ryoo et al. synthesised the first mesoporous carbon framework, CMK-1, using MCM-48 silica as a template.⁸⁶ The simple synthesis procedure is that the carbon sources, sucrose, and sulphuric acid were impregnated into the mesopores of MCM-48 before a thermal treatment at 800-1100 °C under vacuum, and the mesoporous carbon framework was formed by the sulphuric acid catalysed carbonisation. The silica template can be removed in a 10 wt.% hydrofluoric acid solution. Mesoporous carbon, CMK-1, has a three-dimensional structure with uniform mesopores (3 nm in diameter) and a large surface area (1380 m²/g).

Subsequently mesoporous carbon CMK-2,⁸⁷ CMK-3⁸⁸ and CMK-5⁸⁹ were synthesised using SBA-1 and SBA-15 as the templates, respectively. CMK-3 has a perfect inverse replica structure of SBA-15, a hexagonal arrangement of nanorods connected by small windows (Figure 1-9(b)). CMK-3 had a larger pore size of 4.5 nm and a larger surface area of 1520 m²/g than CMK-1. In addition, the difference of MCM-41 and SBA-15 in structure can be obviously distinguished by comparison of their inverse carbon replicas (Figure 1-9). The carbon replica of MCM-41 gave some individual nanorods without any connecting whereas the carbon replica of SBA-15, CMK-3, maintained a three dimensional hexagonal arrangement of nanorods, connecting by some small bridges.

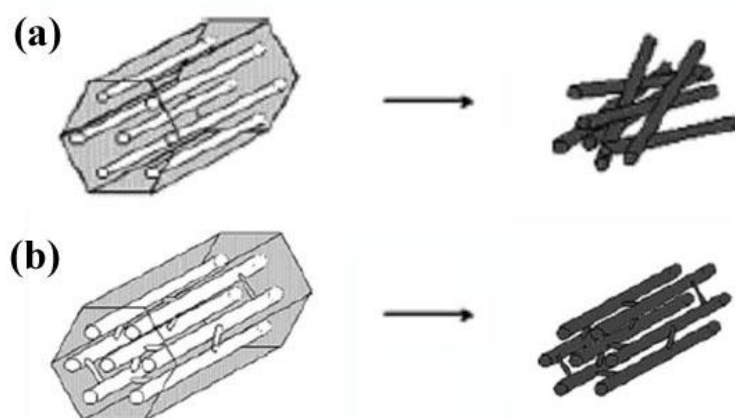


Figure 1-9. Schematic diagram of mesopore systems (left) and the carbon replicas (right) of (a) MCM-41 and (b) SBA-15.⁸⁸

While many mesoporous silicas with various three-dimensional morphologies, such as hexagonal SBA-15, cubic KIT-6, cubic FDU-12 and SBA-16, were developed, the corresponding mesoporous carbons, such as CMK-3,5 (space group $p6mm$),^{88,89} CMK-8,9 (space group $Ia\bar{3}d$),⁴¹ C-FDU-12 (space group $Fm\bar{3}m$) and C-SBA-16 (space group $Im\bar{3}m$)⁴³ with perfectly inverse structure, can also be prepared by using these silicas as templates. The small nanobridges connect the neighbouring nanorods or nanospheres to form 3D mesoporous network, which differed from the individual nanorods templated by MCM-41. Figure 1-10 shows the expected mesoporous carbon structures templated by of (a) SBA-15, (b) KIT-6, (c) FDU-12 and (d) SBA-16, respectively.

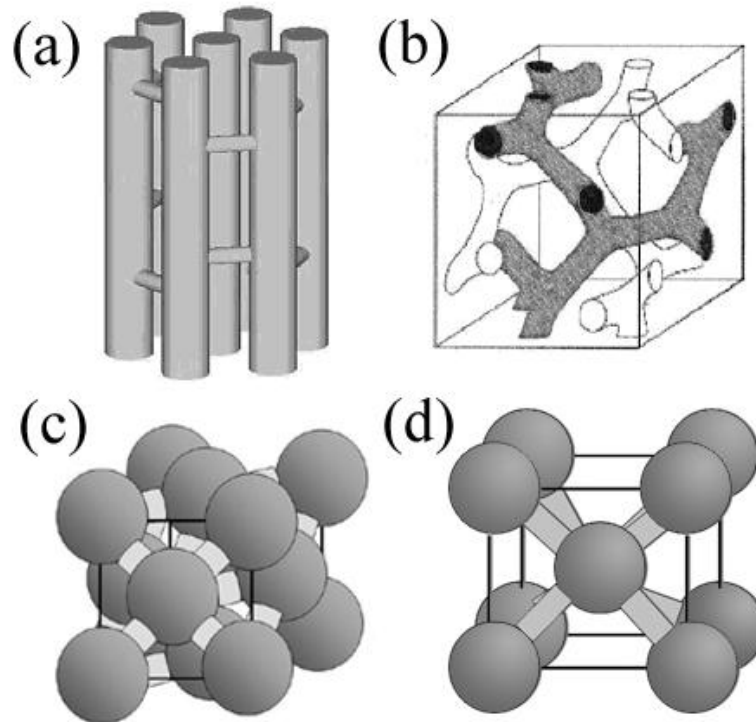


Figure 1-10. The morphologies of negative replicas of (a) SBA-15, (b) KIT-6, (c) FDU-12 and (d) SBA-16, respectively.

1.5.2 FDU-n

The nanocasting method for producing porous carbon using mesoporous silicas as hard templates has been explored, as for CMK-3 mentioned above. However, the drawbacks of this synthetic method are that extra steps are needed to prepare either the template or the final product, which reduces the yield of the product. Additionally, the silica and surfactant templates were waste in this synthetic process. Therefore a new approach to prepare mesoporous carbons directly using surfactant templates was explored gradually instead of the nanocasting method. Alkylphenols can generate a hierarchical structure via selectively hydrogen-bonding to the polystyrene-block-poly(4-vinylpyridine) (PS-P4VP), and a self-assembly process occurs when mixing phenolic resins and block copolymers (BCPs).⁹⁰⁻⁹² A typical mesoporous carbon film was synthesised in the Dai group^{93,94} through carbonization of a nanostructured phenolic resin and PS-P4VP. This mesoporous carbon film is a hexagonally packed carbon-channel array and has very large, highly ordered and well-oriented uniform mesopores of 33.7 ± 2.5 nm in diameter. The block copolymers

not only direct the formation of the phenolic resin nanostructure but also serve as templates for nanopores. Subsequently a mixture of phloroglucinol, formaldehyde, and F127 triblock copolymer were selected as the carbon precursor and the template to synthesise the mesoporous carbons with monolith, fiber and film morphologies, which had the surface areas of 377.9, 593.0 and 569.1 m²/g and the corresponding average pore sizes of 9.5, 6.1 and 5.4 nm, respectively.

A mesoporous carbon with ordered channel structure (COU-1) had also been successfully fabricated by avoiding the use of hard templates. COU-1⁹⁵ was prepared via a direct carbonization of an organic-organic nanocomposite of that resorcinol/formaldehyde (RF) and triethyl orthoacetate (EOA) were the carbon source and triblock copolymer Pluronic F127 was the soft template. The products have a hexagonally arranged pore system with a uniform pore size of 7.4, 6.2 and 5.9 nm, and a large surface area of 624, 1274 and 1354 m²/g after carbonization at 400, 600 and 800 °C, respectively. Figure 1-11 shows the two routes to synthesise ordered mesoporous carbons using hard templates and soft-templates. In hard-templating route, the ordered mesoporous silicas (OMSs) were synthesised firstly by coating the self-assembled surfactants (Figure 1-11(a)), and the final OMS was achieved after removal of surfactant by a thermal treatment (Figure 1-11(b)). The carbon source was impregnated into the mesopores of OMS (Figure 1-11(c)) and carbonized inside the mesopores (Figure 1-11(d)). The formed ordered mesoporous carbon (OMC) can be obtained after the silica template was removed by dissolving in HF solution.

On the other hand, the OMCs such as COU-1 can be prepared in soft-templating route. A carbon precursor is directly deposited on the surface of self-assembled surfactants (Figure 1-11(c)') and transfers to OMC after a thermal treatment in an inert gas. Then the soft templates are removed by calcination in air (Figure 1-11(d)'). Therefore the latter route has fewer steps than the former, which can increase the product yield as well as save resource. It is worth nothing that the OMCs (Figure 1-11(d)') prepared with the soft-templating route have the same structures as the OMSs (Figure 1-11(b)), i.e. a hexagonal arrangement of cylindrical nanopores. On the contrary, the OMCs (Figure 1-11(d)) synthesised with the hard-templating route have a negative structure of OMSs.

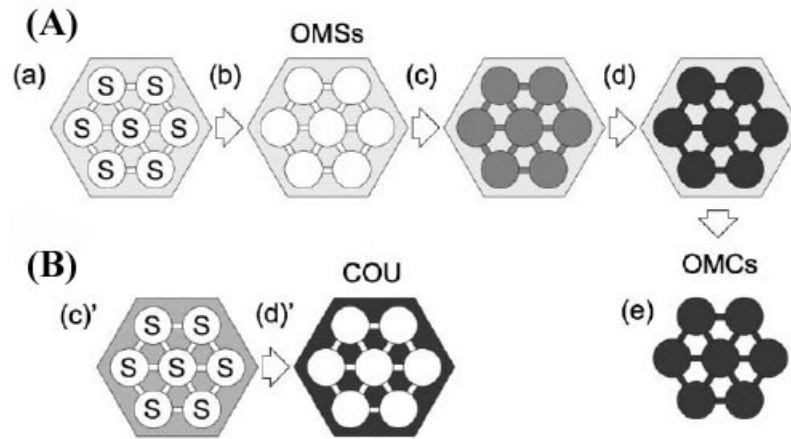


Figure 1-11. Schematic diagram of the synthesis routes for ordered mesoporous carbons; (A) Hard-templating route and (B) Soft-templating route.⁹⁵ S in (a) and (c)' stands for surfactant.

Recently a series of mesoporous carbons with various morphologies, designated FDU- n ($n \geq 14$) have been prepared by Zhao group. A highly ordered mesoporous polymer as well as carbon can be synthesised by a developed method using resol (phenol/formaldehyde) as a precursor and a solvent evaporation induced self-assembly (EISA) of triblock copolymer as a template. The structure of mesoporous polymer and carbon, such as hexagonal or cubic structure can be tuned by selection of triblock copolymer (e. g. P123 and F127) or adjusting proportion of the precursor and template. A typical synthesis is as follows: firstly a carbon precursor Solution-P (phenol/formaldehyde) was prepared by dissolving phenol and formaldehyde solution in basic solution until a clear precursor solution was obtained. Then the as-made solution-P was added to a solution containing well dispersive triblock copolymer. For FDU-15, hydrocarbon (hexadecane or decane) was used as a swelling agent. After a hydrothermal treatment, mesoporous polymer specimens with various morphologies were obtained. The corresponding mesoporous carbon samples were achieved after a thermal treatment under nitrogen flow. Highly ordered mesoporous carbon FDU-16 with a body-centered cubic structure (space group $Im\bar{3}m$) and FDU-15 with a 2-D hexagonal structure (space group $p6m$) can be formed by using Pluronic F127 and P123 as templates, respectively. Mesoporous carbon FDU-14 with a body-centered cubic structure containing bicontinuous pores (space group $Ia\bar{3}d$) can be generated when the molar ratio of P123/phenol is higher than

0.04.⁹⁶⁻⁹⁸ FDU-14, FDU-15 and FDU-16 have large surface areas of 550-1000, 460-1040 and 670-1030 m²/g, and tunable uniform pore sizes of 2.8-3.8, 3.8-6.8 and 3.2-3.5 nm when forming at different temperatures (350-800 °C). Especially for FDU-15, the pore size can also be tailored by simply varying the additions of hydrocarbon molecules. Mesoporous carbon FDU-17 can be synthesised using a phenolic resol precursor and a reverse amphiphilic triblock copolymer PO₅₃EO₁₃₆PO₅₃ (PO: propylene oxide; EO: ethylene oxide) template by the evaporation-induced self-assembly (EISA) method.⁹⁹ This novel mesoporous carbon has a 3D face-centered cubic structure (space group $Fd\bar{3}m$) with a large surface area of around 870 m²/g and tunable bimodal mesopores of 3.2-4.0 nm and 5.4-6.9 nm, respectively. Mesoporous carbon FDU-18 with thick walls of 11.5-12.4 nm was also synthesised via EISA approach by using a novel amphiphilic diblock copolymer, poly(ethylene oxide)-b-poly(methyl methacrylate) (PEO-b-PMMA), as a template, soluble resol as a carbon source and THF as a solvent.^{100,101} FUD-18 has a face-centered cubic close-packed mesostructure (space group $Fm\bar{3}m$) with a high surface area up to 1050 m²/g and a uniform large pore of ~10.5 nm.

1.6 Ordered mesoporous metals and metal oxides

Although mesoporous silica and mesoporous carbon have large surface areas, uniform pore sizes and large pore volumes, they lack ion exchange capacity and Lewis acid sites on the surface, which limit their application in catalysis. Accordingly mesoporous silicas were usually functionalised by introducing heteroatom, organics or metal oxides to increase their catalytic activities. Many mesoporous silicas with loading of metal oxides, e.g. Fe₂O₃-, ZnO-, PbO-containing MCM-41 or MCM-48,⁶⁹ and CuO-, MgO-, Cr₂O₃-, Fe₂O₃-, ZnO-containing SBA-15,⁷⁷⁻⁸⁰ were prepared and used as catalysts. However, the oxide particles could block the mesopores or be embedded in the silica walls, which might reduce the catalytic sites of the catalysts. Furthermore, some transition metal oxides can react with SiO₂. For example, Ti in TiO₂ can be partially substituted by Si from amorphous SiO₂ of the mesopore wall, inhibiting its photocatalytic activity.¹⁰² Therefore the new self-support mesoporous transition metal oxides with large surface areas, high ordered uniform mesopores and large pore volumes would exhibit higher catalytic activity and has become an attractive research project in recent years. At present, the ordered mesoporous metal

oxides can be synthesised by using two methods, soft-templating route and hard-templating route.

1.6.1 Soft templating route

Since mesoporous silicas can be formed by deposition of silica precursor on the surface of self-assembled surfactants through electrostatic force, hydrogen bonding, covalent or van der Waals interaction, other mesoporous materials, such as mesoporous metal or metal oxides, can be synthesised in the same way using metal-precursors instead of silica precursors. The first ordered mesoporous metal was synthesised by Attard et al. in 1997 after they used a similar method to prepare mesoporous silica in 1995.^{103,104} Ordered mesoporous platinum (Pt) can be synthesised by using hexachloroplatinic acid (HCPA) and ammonium tetrachloroplatinate (ATCP) as a platinum source and C₁₆(EO)₈ (octaethyleneglycol monohexadecyl ether) to form a lyotropic liquid-crystalline phase. The mesoporous Pt is achieved by reduction of platinum salts, generating a hexagonal mesostructure within the liquid-crystalline phase. The final mesoporous platinum was collected from the reagents (e.g. platinum salts, surfactant and reducing agent) by treatment with acetone, water, hydrochloric acid, water and acetone. A solvent removal of surfactant by extraction was used instead of calcination to keep the mesoporous structure of the product intact. Attard et al. also synthesised platinum thin film in an aqueous environment by the electrodeposition of the metal with the lyotropic liquid crystalline phases of surfactant templates.¹⁰⁵ The products can be potentially used as the mesoporous electrodes for batteries, fuel cells, electrochemical capacitors and sensors. However the mesoporous metals prepared using soft templates are all amorphous materials.

In 1994, a series of mesostructured transition-metal oxides, with amorphous walls, were synthesised by using surfactants as templates in Stucky group.^{106,107} However, some materials stayed within the lamellar phase, and the surfactant can not be removed by calcination or solvent extraction, that would lead to a collapse of the porous structure. A year later, the first thermally stable transition metal oxide molecular sieve (Ti-TMSI) was synthesised by a modified sol-gel process using titanium isopropoxide bis-acetylacetonate as the precursor and alkylphosphate surfactants as the template.¹⁰⁸ This mesoporous TiO₂ was hexagonally packed with a surface area of 200 m²/g. In 1996, a new mesoporous zirconia compound (45 wt%

ZrO₂, 54 wt% Zr₃(PO₄)₄ and 0.5-1 wt% Zr(SO₄)₂) with high surface areas (230-390 m²/g) and regular pore systems were prepared using zirconium sulfate or zirconium propoxide as the Zr source.¹⁰⁹ Its stability can be amended by addition of phosphates. Both mesoporous titanium and zirconium were formed using ionic surfactants as the structure-directing agents until non ionic triblock copolymers were found to be good soft templates.

In 1998, at the same time of the preparation of mesoporous silica SBA-15 by Zhao et al. in the Stucky group, several mesoporous metal oxides including TiO₂, ZrO₂, Al₂O₃, Nb₂O₅, Ta₂O₅, WO₃, HfO₂, SnO₂,¹¹⁰ and mixed oxides including SiAlO_{3.5}, SiTiO₄, ZrTiO₄, Al₂TiO₅ and ZrW₂O₈¹¹¹ were synthesised successfully by using the non-ionic triblock copolymers (e.g. P123 or F127) as structure-directing agents in non-aqueous solutions, and inorganic salts as soluble and hydrolysable precursors to form the polymerised metal oxide framework. These porous metal oxides have not only high thermal stability, large surface areas (105-300 m²/g depending on different densities), uniform pore sizes (3.5-7.0 nm), but also thick channel walls (3.5-6.0 nm). Unlike the ionic surfactants directed porous metal oxides, these materials have nanocrystals in the amorphous wall ranging from less than 1 nm to about 3 nm. Subsequently, Tian et al. in Zhao group developed this non-ionic soft-templating approach, by using synergic inorganic acid-base pairs instead of inorganic salts as the precursors. A wide variety of porous composites including metal phosphates, metal borates, metal oxides and mixed metal oxides (e.g. TiO₂, ZrO₂, TiPO, ZrPO and AlPO) with highly ordered, homogeneous, stable and multicomponent mesostructures, can be prepared via inorganic acid-base interplay in the self-assembled surfactants.^{112,113} Figure 1-12 shows the general ‘acid-base pair’ principles for the rational combinations of inorganic precursors. The metallic sources, alkoxides (alkalinity) and salts (acidity), were selected as a self-generated reaction medium with the correct acidity to make the self-adjusted sol-gel synthesis. No extra reagents (such as HCl or NH₃) were needed to adjust the pH of the desired sol-gel reactions. Some amphoteric solvents such as C₂H₅OH or CH₃OH, to the contrary, are recommended to join the synthesis. Routes A, B and E in Figure 1-12 are new routes for the preparation of mesoporous materials in comparison with the common routes C (syntheses of mesoporous silicas)^{39,110} and D (syntheses of mesostructured metal chalcogenide),¹¹⁴ and routes F, G can not work well for mesoporous material formation.

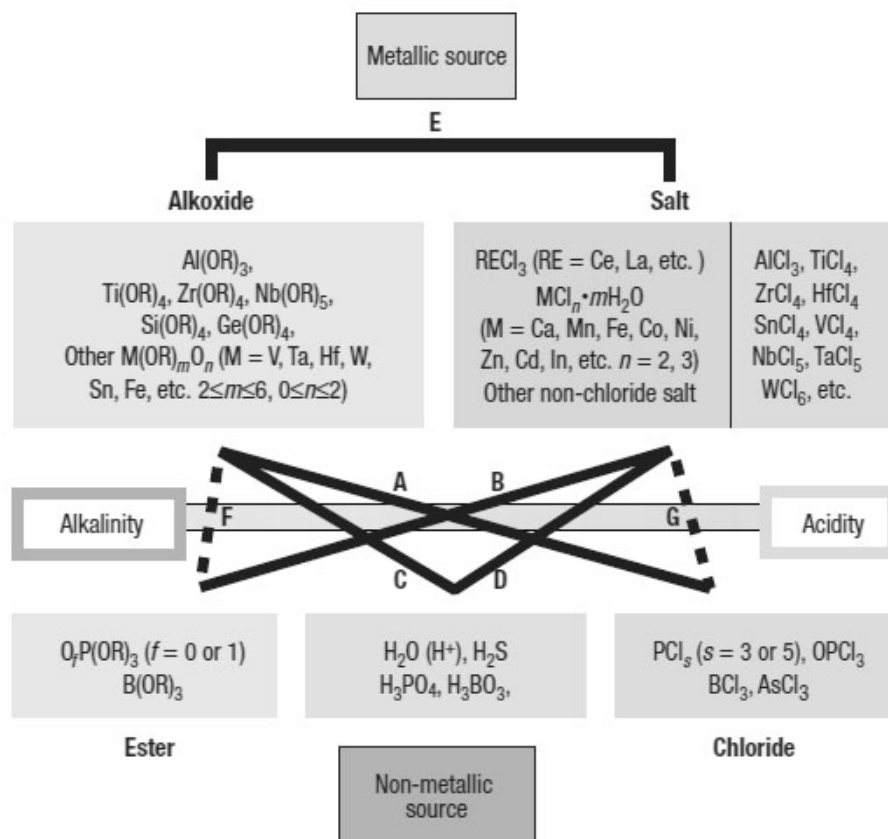


Figure 1-12. Schematic diagram of the 'acid-base pair' concept and guided synthetic routes for mesoporous minerals.¹¹²

1.6.2 Hard templating route

Although mesoporous metal and metal oxides can be synthesised successfully in soft templating route, they are all amorphous or nanocrystal-amorphous materials, which have low thermal stability and less application in catalyst, conductivity, Li ion batteries. However, due to the low decomposition temperature of soft template, these mesoporous metal oxides prepared by using soft templates can not be crystallised by simple thermal treatment. On the other hand, hard templates with high thermal stability, such as mesoporous silicas (e.g. SBA-15)³⁹ or carbons (e.g. CMK-3),⁸⁸ can be used to synthesise crystalline mesoporous metal and metal oxides at high temperature.

1.6.2.1 Mesoporous silica as a template

Up to date, several mesoporous silicas had been selected to serve as hard templates for casting mesoporous crystals. The most attractive porous silicas for this purpose

are SBA-15, KIT-6, FDU-12 and SBA-16 though other mesoporous silicas can also be used (e.g. MCM-48). On the other hand, many crystalline mesoporous metals and transition metal oxides had been synthesised using those silica templates, including Pt, Cr₂O₃, Co₃O₄, In₂O₃, NiO, CeO₂, WO₃, Fe₂O₃, MnO₂ and V₂O₅, and the expected porous morphologies are shown in Figure 1-10.

Pt and other metals

The first porous metal synthesised using silica template, Pt/SBA-15 as well as Ag/SBA-15, Au/SBA-15, were prepared in Stucky group in 2000.¹¹⁵ The loading of metals was only about 5 %, possibly resulting in a large proportion of nanowires with minor phase of 3D porous metal products. H₂AuCl₄·3H₂O, Pt(NH₃)₄(NO₃)₂ and AgNO₃ were selected as the metal-precursors. The metal nanowires had a much large range from 50 nm to 1 μm in length, controlled by the loading percentage and annealing temperature and time, and 7 nm in diameter, controlled by the mesopore size of SBA-15.

In 2001, monocrystalline Pt was synthesised in the Ryoo group by using MCM-48 as a hard template and tetraamineplatinum (II) nitrate (Pt(NH₃)₄(NO₃)₂) as the metal precursor.¹¹⁶ The Pt-containing compound in MCM-48 mesopores was reduced to Pt(0) under H₂ flow and the Pt(0) content in the silica template could reach to 30-60 wt%. With such a high loading, mesoporous Pt with 3D cubic structure (space group *Ia3d*) was generated other than nanowires. Its intertwined pore channels were in a rather large range of 50-400 nm in diameter. An interesting phenomenon can be found that the platinum only replicates one of the bicontinuous pore framework. Similar behaviour can also be found in the mesoporous platinum templated by KIT-6.⁴¹ Porous single crystals of Pt templated by SBA-15 were also synthesised by the same group in 2001.¹¹⁷ The 3D hexagonal arrangement of Pt nanorods (3.5 nm in diameter) can be observed by TEM.

Cr₂O₃

Cr₂O₃ has a rhombohedral structure with the unit cell parameters $a = 0.4959$ nm and $c = 1.359$ nm, space group $R\bar{3}c$, and plays an important role in magnetism and catalysis such as hydrogenation of aliphatic carboxylic acids and oxidative dehydrogenation of ethane with carbon dioxide.^{118,119}

The first monocrystalline porous metal oxide templated by mesoporous silica is porous Cr_2O_3 synthesised by Zhu et al. in He group in 2003 using SBA-15 as a hard template and $\text{H}_2\text{Cr}_2\text{O}_7$ as a metal-containing precursor.¹²⁰ This porous Cr_2O_3 prepared by using the surface modification method has large particle size and even the original morphologies of the template particles could be maintained, probably because the density of Cr in $\text{H}_2\text{Cr}_2\text{O}_7$ is higher than hydrated chromium nitrate (used later as another precursor for Cr_2O_3) and the ionic interaction between the functional group inside the pores and the anions of $\text{Cr}_2\text{O}_7^{2-}$ is stronger than the capillary force in the other methods, leading to a high loading level of the precursor. The purity of the sample was high as well. Subsequently the KIT-6 templated Cr_2O_3 was produced using the dual-solvent method later in the same group in 2005.¹²¹ A peculiar phenomenon found in this porous specimen was that the crystal orientations seem to have a close relation with the symmetry of the mesopore structure. The nature of this property has not been understood and the phenomenon was not observed from other porous crystals.

Porous Cr_2O_3 templated by SBA-15 and KIT-6 was also produced using the evaporation method by Tian et al. in Zhao group^{122,123} and Dickinson et al. in our group.¹²⁴ Comparing the image contrast patterns of the KIT-6 templated Co_3O_4 and Cr_2O_3 , it was found that both the bicontinuous pores in KIT-6 can be replicated by Co_3O_4 , but only one of them was replicated by Cr_2O_3 ,¹²⁴ which is very similar to porous Pt templated by KIT-6 and MCM-48.^{86,114} This difference can also be detected by the surface area measurements. However, the reason for this difference is still unknown though Dickinson et al. suggested that the high temperature for crystal growth of Cr_2O_3 destroyed the inter-pore channels in KIT-6.¹²⁴ The specific surface area of porous Cr_2O_3 templated by KIT-6 is $74 \text{ m}^2/\text{g}$, which is equivalent to $114.2 \text{ m}^2/\text{cm}^3$, and about half of the surface area per unit volume of KIT-6-templated Co_3O_4 . Both products have high yields as concluded from the TEM observations. The different surface areas agree with the single-pore replication in Cr_2O_3 and double-pore replication in Co_3O_4 . In addition, the confinement effect of the nanoscale pores to the crystal growth of Cr_2O_3 had been investigated. It was found that the crystal growth temperature of this oxide inside the pores, $350 \text{ }^\circ\text{C}$, is lower than that without the presence of porous template.¹²⁴

Some physical and chemical properties of the porous single crystals of Cr_2O_3 were investigated by Dickinson et al. as well.¹²⁵ With cooling outside of a magnet field (zfc)

before increasing the heat and then cooling with a magnetic field (f_c), the magnetic behaviour is similar above 100 K, but changes between with/without applied external field under 100 K. The electrochemical reaction of lithium with porous Cr_2O_3 has been investigated by Dupont et al. in 2008 in comparison with non-porous material.¹²⁶

Co_3O_4

Co_3O_4 has a cubic structure with the unit cell parameter, $a = 0.8085$ nm, space group $Fd\bar{3}m$. It is an efficient catalyst to oxidize H_2 , CO, NO and methane.¹²⁷⁻¹²⁹

Porous single-crystals of Co_3O_4 templated by SBA-15 and KIT-6 were prepared using the evaporation method by Tian et al.¹²² and Wang et al.,¹³⁰ respectively. $\text{Co}(\text{NO}_3)_2 \cdot 6\text{H}_2\text{O}$ was used as the precursor in all syntheses. The loading level of the nitrate could be high, leading to a high yield of the final product, which can be confirmed by the surface areas of Co_3O_4 . For example, porous Co_3O_4 templated by KIT-6 has a surface area of $92 \text{ m}^2/\text{g}$.¹²⁴ According to Dickinson's investigation of the decomposition process of the nitrate and crystal growth of Co_3O_4 , both the decomposition temperature and the crystal formation temperature inside the pores were reduced in comparison with the processes outside the pores.¹²⁴ The decomposition routes inside and outside the pores were also different. In the pores, the starting precursor, cobalt nitrate hexahydrate, lost four water molecules to crystallize into the cobalt nitrate dihydrate, $\text{Co}(\text{NO}_3)_2 \cdot 2\text{H}_2\text{O}$. This crystalline phase then transformed into cobalt hydroxide nitrate monohydrate, $\text{Co}(\text{OH})\text{NO}_3 \cdot \text{H}_2\text{O}$ by losing one NO_3^- anion and a proton. Co_3O_4 was formed at the final stage, when the temperature reached to over 150°C , by losing the second NO_3^- anion and the remaining water molecule.

On the other hand, based on mesoporous Co_3O_4 framework, crystalline porous LiCoO_2 templated by SBA-15 and KIT-6 can be synthesised by treating a lithium source with as-made Co_3O_4 ,¹³¹ and have superior capacity retention on cycling compared with normal LiCoO_2 because of its large surface areas.

NiO

NiO has also a face-centered cubic structure with $a = 0.4176$ nm, space group $Fm\bar{3}m$. This material has a good electrochemical capacitance and has a potential application in electrochemical devices.¹³²⁻¹³⁴

Porous NiO templated by SBA-15 was synthesised using the evaporation method by Tian et al.,¹²² and its electrochemical capacitance was studied by Wang et al..¹³² It was found that the capacitance of porous NiO was about 120 F/g, four times larger than that of NiO directly obtained from decomposing nickel nitrate without presence of porous template, due to the much larger surface areas. Additionally, comparing these mesoporous materials with microporous materials (<2 nm), the mesoporous NiO showed a good rate capability, which implied that the ion motion was not limited by the ordered mesoporous structure.

CeO₂

CeO₂ which has a cubic structure with the unit cell dimension, $a = 0.54124$ nm, space group $Fm\bar{3}m$, is a good catalyst for oxidation of acrylic acid and CO, and methanol decomposition.¹³⁵⁻¹³⁸

Porous CeO₂ templated by SBA-15 was also one of the porous metal oxides synthesised by Tian et al. using the evaporation method.¹²² KIT-6 templated CeO₂ was prepared using the same method by Shen et al.¹³⁵ and Rossinyol et al..¹³⁹ The CO catalytic oxidation using porous CeO₂ as a catalyst was also examined by Shen et al. in 2005. In comparison with the normal CeO₂ powder, the mesoporous CeO₂ showed a higher catalytic activity for the oxidation of CO to CO₂ at relatively low temperature. This improvement of the catalytic performance can be attributed to the mesoporous structure with a large effective surface area.

In₂O₃

In₂O₃ has a cubic structure with $a = 1.0118$ nm, space group $Ia\bar{3}$. It is an important transparent conductive oxide, and has potential applications in solar cells, ultraviolet-visible (UV) lasers, detectors and gas sensors.¹⁴⁰⁻¹⁴³

Zhao's group first produced porous In₂O₃ using the one-step nanocasting method¹⁴⁴ and the evaporation method.¹²² In the former, In(NO₃)₃ as the precursor was directly added to the synthetic system for mesoporous silica and the In₂O₃ crystal grew in the pores when the mesostructured surfactant-silica monolith was calcined at 550 °C for removing the surfactant molecules. It was believed that indium formed metal nanoparticles and aggregated in the pores due to its low melting point, and was finally oxidized into In₂O₃ crystals. Both SBA-15 like (space group $p6mm$) and KIT-6

like (space group $Ia\bar{3}d$) phases of porous In_2O_3 were obtained. In the evaporation method, Tian et al. used hydrated $\text{In}(\text{NO}_3)_3$ as precursor and microwave-digested SBA-15, SBA-16, FDU-1 as templates to synthesise porous crystals of In_2O_3 .

Fe_2O_3

Rhombohedral Fe_2O_3 , similarly to Cr_2O_3 , with $a = 0.5032$ nm, $c = 1.3733$ nm, space group $R\bar{3}c$, is an important catalyst for hydroxylation of phenol, selective hydrogenation of acetic acid and methanol decomposition, and probably a good material used in rechargeable lithium batteries.¹⁴⁵⁻¹⁴⁸ It is expected that porous Fe_2O_3 would present some interesting properties.

The first attempt of preparing SBA-15 templated porous Fe_2O_3 using the surface modification method led to nanowires without three dimensional connection.¹⁴⁵ The possible problem is low density and low quality of the small inter-pore channels in the SBA-15 template. Porous Fe_2O_3 with negative replication structure of SBA-15 was produced using the evaporation method by Tian et al.,¹²² although the crystallinity was very low. Recently, Jiao et al. observed the single-crystal of porous Fe_2O_3 templated by KIT-6 from a sample prepared using the evaporation method, as well as some porous Fe_2O_3 with disordered walls.¹⁴⁹ The same group also reported synthesis of crystalline porous iron oxides with different oxidation states, Fe_3O_4 , $\alpha\text{-Fe}_2\text{O}_3$ and $\gamma\text{-Fe}_2\text{O}_3$.¹⁵⁰ The magnetic properties of mesoporous Fe_3O_4 and $\gamma\text{-Fe}_2\text{O}_3$ had been examined as well, and the materials exhibit magnetic freezing above 340 K.

MnO_2

MnO_2 is of interest in Li/ MnO_2 batteries and has been widely used as magnetic materials, electrode materials and catalysts.¹⁵¹⁻¹⁵⁵

After the SBA-15 templated porous Mn_xO_y composites were synthesised using the evaporation method by Tian et al.,¹²² KIT-6 templated porous MnO_2 was produced later using the evaporation method by Zhou et al.,¹⁵⁶ Luo et al.,¹⁵⁷ and Feng et al..¹⁵⁸ Although the mesoporous manganese oxides mentioned above are all polycrystalline, the electrochemical measurements of lithium-ion batteries using ordered mesoporous $\beta\text{-MnO}_2$ electrode exhibited high initial capacity, excellent high rate discharge performance and supreme cycling reversibility.^{157,158} Recently Feng et al. synthesised ordered mesoporous Mn_2O_3 and Mn_3O_4 with crystalline walls successfully and the

mesoporous Mn_2O_3 can be converted to Mn_3O_4 without destroying the ordered mesostructure under the H_2 flow.¹⁵⁹

WO_3

Tungsten oxide has a wide range of interesting catalytic, electrochromic and gas sensing properties.¹⁶⁰⁻¹⁶³ The most popular structure of WO_3 is orthorhombic with $a = 0.7383$ nm, $b = 0.7512$ nm and $c = 0.3846$ nm (space group P), although the unit cell parameters are variable with different oxygen contents.

When SBA-15 was used as a template for producing porous crystals of WO_3 using the surface modification method by Zhu *et al.* in 2003,¹⁶⁴ only WO_3 nanowires were observed from the product. The synthesis conditions were improved later and perfect three dimensional porous single-crystal WO_3 was fabricated in 2005.¹⁶⁵ KIT-6 templated WO_3 was also produced using the evaporation method by Rossinyol *et al.*¹³⁹ In these syntheses, phosphotungstic acid ($\text{H}_3\text{PW}_{12}\text{O}_{40}$) was used as the precursor and in the surface modification method the SBA-15 silica inner surface was aminosilylated by γ -aminopropyltriethoxysilane (APTS) and tungstophosphoric acid then underwent immobilization inside the channels.

Others

V_2O_5 nanowires can be synthesised by using a functional silica template γ -aminopropyltriethoxysilane(APTS)-SBA-15 in He group in 2004¹⁶⁶ and the aqueous solution of DVA precursor prepared by acidification of $(\text{NH}_4)_6\text{V}_{10}\text{O}_{28}$. Additionally mesoporous OsO_4 templated by MCM-48 was synthesised by Lee *et al.* in 2003¹⁶⁷ using $\text{Os}_3(\text{CO})_{12}$ as the Os-precursors. This porous OsO_4 has superior heterogeneous catalytic activity in oxidative cleavage and dihydroxylation. However, further investigations of these porous metal oxides, including improvement of the crystallinity, structural determination, and morphology control, etc. are yet to be carried out.

1.6.2.2 Mesoporous carbon as a template

Some porous metal oxides, such as CuO , MgO and ZnO , which can not be synthesised by using mesoporous silica as a template, might be prepared by using mesoporous carbon, such as CMK-3, as a template. Because the mesoporous carbon CMK-3 is templated by SBA-15 and consists of a hexagonal arrangement of nanorods

connected by small nanobridges, the products templated by CMK-3 should have a similar structure to SBA-15, namely a hexagonal arrangement of cylindrical pores connected by small channels. The syntheses process using two hard templates, mesoporous silica (SBA-15) and mesoporous carbon (CMK-3), was usually named as the double replication process.

SiO₂

In 2002, the first mesoporous oxides templated by mesoporous carbon, SiO₂, were synthesised successfully by Lu et al.¹⁶⁸ and Kang et al.¹⁶⁹ In Lu's work, the mesoporous silica named as 'SNU-1' was prepared by using TEOS as the precursor and CMK-3 as the hard template, and had a hexagonal ordered channels, which is the same structure with SBA-15 and can be observed by TEM. However the pore size and surface area of SNU-1 were 4.9 nm and 557 m²/g, which are lower than the pore size (5.8 nm) and surface area (680 m²/g) of the original Al-SBA-15 template. A similar phenomenon was found by Kang et al., the silica replica was synthesised by using Na₂SiO₃ as the precursor and CMK-3 as the template. The pore size and surface area of the mesoporous silica replica were 6.47 and 685 m²/g, which are lower than the pore size (8.11 nm) and surface area (776 m²/g) of the SBA-15 template.

Al₂O₃

While the mesoporous silica can be templated by CMK-3, other porous oxides such as Al₂O₃ can be also synthesised and demonstrated later by Liu et al. (2006).¹⁷⁰ The crystalline ordered alumina molecular sieves (OCAMS-1) were synthesised through repeatedly filling aluminum nitrate into the pores of CMK-3 and allowing decomposition of the nitrate and growing of oxide inside pores. The mesoporous γ -Al₂O₃ can be obtained after the carbon template was removed by calcination. Similarly to the silica replicas, the OCAMS-1 has a hexagonal structure and lower pore size of 4.6-6.1 nm in comparison with the pore size (6.6 nm) of SBA-15.

MgO

Mesoporous MgO, which can not be obtained by decomposition of Mg(NO₃)₂ within the SBA-15 pores, can be synthesised in a double replication procedure by using SBA-15 templated CMK-3 as the hard template. Roggenbuck et al. in Tiemann group^{171,172} made a crystalline porous MgO through infiltrating the carbon pore with

$\text{Mg}(\text{NO}_3)_2$ and converting it to MgO at 573 K. The carbon matrix was finally removed by thermal combustion. The synthesised mesoporous MgO has a hexagonal arrangement of cylindrical mesopores and crystalline pore walls. Figure 1-13 shows the consecutive structure replication procedure using mesoporous SBA-15 silica (Figure 1-13(a)) and CMK-3 carbon (Figure 1-13(b)) to synthesise crystalline mesoporous MgO (Figure 1-13(c)).

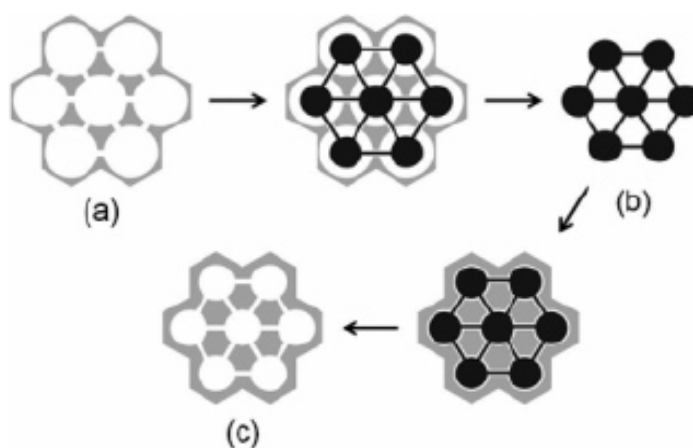


Figure 1-13. Schematic diagram of the double replication process from (a) SBA-15 silica, (b) CMK-3 carbon to (c) mesoporous MgO.¹⁷²

CuO

Meanwhile, crystalline mesoporous CuO templated by CMK-3 was synthesised successfully by Lai et al. in 2007 using $\text{Cu}(\text{NO}_3)_2$ as the precursor.¹⁷³ The mesoporous CuO has a hexagonal structure with a large surface area of $149 \text{ m}^2/\text{g}$ and uniform pore size of 5.46 nm.

ZnO

Among the mesoporous metal oxides, ZnO is a very attractive material due to its behavior in heterogeneous catalysis such as methanol synthesis from CO_2 over Cu/ZnO catalysts.¹⁷⁴ Therefore, after synthesis of the mesoporous silica SNU-1, crystalline mesoporous ZnO had been synthesised later in Lu group in 2007 by using a special organometallic single-source $\text{CH}_3\text{ZnO}(\text{CH}_2)_2\text{OCH}_3$ as the precursor and CMK-3 as the hard template.¹⁷⁵ Compared to the crystalline ZnO prepared through the true liquid-crystal templating, which has a surface area of $85 \text{ m}^2/\text{g}$, the ordered mesoporous ZnO templated by CMK-3 has a much larger surface area of $192 \text{ m}^2/\text{g}$.

Subsequently, the mesoporous ZnO, with a periodically ordered, uniform pore systems and crystalline pore walls, had been synthesised using $\text{Zn}(\text{NO}_3)_2$ as the precursor and CMK-3 as the template in Tiemann group.^{176,177} Although it has only a normal surface area of $51 \text{ m}^2/\text{g}$, the porous oxides still exhibited superior gas-sensing properties for CO and NO_2 as compared to non-porous ZnO sensors.

Others

Additionally, crystalline mesoporous CeO_2 was also generated by Roggenbuck et al. in Tiemann group using $\text{Ce}(\text{NO}_3)_3$ as the precursor and CMK-3 carbon as a structure matrix.¹⁷⁸ The porous CeO_2 had a large surface area of $148 \text{ m}^2/\text{g}$ and uniform pores with a diameter of 5 nm, and exhibited substantially higher catalytic activity in methanol decomposition than the non-porous sample. However, the porous CeO_2 synthesised in the double replication procedure is polycrystalline, it can be also prepared directly using silica template, and has monocrystalline property^{135,139} and a larger surface area of $198 \text{ m}^2/\text{g}$.¹⁷⁹ Thus the polycrystalline mesoporous CeO_2 templated by CMK-3 seems to be not significant.

Roggenbuck et al. also investigated various strategies to obtain high loading rates by impregnating CMK-3 carbon with metal nitrates.¹⁸⁰ 1) the modification of the pore walls of CMK-3 carbon could increase the impregnation efficiency from 30 % to 50%; 2) Utilisation of tetrahydrofuran (THF) instead of water as the solvent for metal nitrate also increased the impregnation efficiency from 40% to 80%; 3) The ‘incipient wetness’ technique was more efficient (80% impregnation efficiency) than the ‘wet impregnation’ method (30%) for CMK-3 carbon.

1.7 Impregnation methodology

The general route for producing the porous single crystals of metal oxides templated by mesoporous silicas includes the following steps: impregnating a metal-containing precursor into the silica pores, allowing the precursor to decompose inside the pores during a thermal treatment, controlling the crystal growth of the metal oxide at a higher temperature, and finally removing the silica template by using either a 10% HF aqueous solution at room temperature or a 2M NaOH solution at 70-90 °C. Obviously, the most important step is the impregnation. Four methods of impregnation have been developed in the last five years: the so-called surface

modification method, dual-solvent method, one-step nanocasting method and evaporation method, respectively.

1.7.1 Evaporation method

The evaporation method is very convenient and used by several groups.^{122,124} The mesoporous silica template is mixed with a selected metal nitrate in ethanol. The nitrate precursor is expected to migrate into the pores by a capillary action during the evaporation process of ethanol. This method was applied for the first time by Tian et al.¹²² in 2003 to synthesise porous metal oxides of Cr_2O_3 , Mn_xO_y , Fe_2O_3 , Co_3O_4 , NiO , In_2O_3 and CeO_2 templated by SBA-15, and was adopted by other groups thereafter.

1.7.2 Other methods

The surface modification method is an original method applied for the first synthesis of crystalline mesoporous metal oxides, SBA-15 templated Cr_2O_3 in 2003.¹²⁰ In the surface modification method, the inner wall of a silica template is aminosilylated using γ -aminopropyltriethoxysilane (APTS) to form a functionalized template. A metal-containing precursor, usually a selected heteropolyacidic precursor (e.g. $\text{H}_2\text{Cr}_2\text{O}_7$ and $\text{H}_3\text{PW}_{12}\text{O}_{40}$), is anchored.^{120,165} The driving force of the migration of the precursor molecules is mainly ionic attraction.

In the one-step nanocasting method,¹⁴⁴ the nitrate precursor is directly added to the synthetic system of mesoporous silica, forming highly ordered single crystals during a thermal treatment, and the organic surfactant was removed simultaneously.

In the dual-solvent method,¹²¹ a suspension of mesoporous silica in dry hexane is mixed with an aqueous solution of metal nitrate. The nitrate precursor is expected to move into the pores of silica during an overnight stirring.

1.8 Anodic mesoporous metal oxide films

As reviewed above, ordered mesoporous materials, such as the mesoporous metals, metal oxides and mixed oxides, can usually be synthesised using a template, either soft template (e.g. P123) or hard template (e.g. SBA-15 or CMK-3). Whereas mesoporous metal oxide films can also be prepared by using a novel method without templating, namely the anodic oxidation method. In the anodic oxidation method, a metal foil, which is usually polished and washed by several solvents to flatten and

clean the surface, is used as a precursor. The treated metal foil is pressed against an o-ring in the electrochemical cell, usually made of three electrodes. One side of the metal foil explores to a suitable electrolyte. The metal can be oxidized to metal oxide and a hexagonal mesopore array (or a hexagonally ordered array of nanotubes) can be created after an electrochemical reaction.

Al₂O₃

Although anodic oxide coatings can be formed in various electrolytes, porous structure of anodic oxide coating, e.g. anodic aluminum oxide (AAO), was observed firstly and investigated with electron microscopy in 1953.¹⁸¹ Subsequently the structure of AAO was amended and the formation mechanism was investigated by several groups.¹⁸²⁻¹⁸⁴ An ordered hexagonal pore arrays of the AAO can be obtained in both oxalic and sulfuric acid electrolyte and the size of each single pore was determined by the anodizing voltage.

TiO₂

Anodic titanium oxide (ATO) has high potential applications in gas-sensing, self-cleaning materials and photoanode in dye-sensitized solar cells.¹⁸⁵⁻¹⁸⁷ Therefore, the ATO made of smooth ordered nanotubes was synthesised using 0.5 wt% NH₄F in glycerol (1,2,3-propanetriol) or 1M (NH₄)₂SO₄ as the electrolytes and its formation mechanism was investigated by Macak et al. in 2005.¹⁸⁸ Its electrical resistance can be changed by exposure to hydrogen.¹⁸⁵ Recently, a new mechanism was brought forward by Su et al. in these laboratories in 2008 to explain both the formation of AAO and ATO,¹⁸⁹ and further syntheses of other anodic metal oxides are in progress.

Other porous anodic metal oxides

Additionally other self-organized porous metal oxide layers, such as SnO₂ formed in an oxalic acid electrolyte,¹⁹⁰ V₂O₅ formed in an electrolyte of benzoic acid (C₆H₅COOH) mixing with a saturated aqueous solution of borax and acetone (1:1),¹⁹¹ Nb₂O₅ formed in mixed H₂SO₄/HF electrolytes,¹⁹² Ta₂O₅ formed in H₂SO₄ electrolytes containing low concentrations of HF (0.1- 5 wt %),¹⁹³ HfO₂¹⁹⁴ and ZrO₂¹⁹⁵ formed in H₂SO₄ electrolytes containing NaF, were all synthesised successfully. Their ordered pores can be tuned by altering the concentration of electrolytes, the anodization voltage and the time for anodic oxidation.

1.9 Aims and objectives

From the aforementioned introduction, mesoporous materials have some good properties in comparison with the zeolite due to their large surface areas, pore sizes and pore volumes. Compared to the disordered mesoporous materials, the ordered mesoporous materials can be used as selective catalysts or nanoreactors because of their ordered uniform pores. Therefore many ordered mesoporous materials such as mesoporous silica (e.g. MCM-41 and SBA-15) and mesoporous metal oxides (e.g. TiO_2) were synthesised by using ionic or non-ionic surfactants. However, these porous materials are almost amorphous because the soft template can not be kept during the crystallisation at high temperature. Additionally the mesoporous silica lacks the ion exchange capacity and Lewis acid sites on the surface, and has to be functionalized by organics, metals or metal oxides to increase its catalytic activity. Whereas the metal oxides particles may block the silica pores or embed in the silica walls, which reduces the catalytic activity of the metal oxides. Therefore, some self-support mesoporous metal or metal oxides were synthesised by using hard templates (e.g. SBA-15 and CMK-3). These new porous materials have high stability, high crystallinity, large surface area, uniform pore size and large pore volume.

The aims of this project concentrate on the syntheses and characterisations of mesoporous metal oxides, investigation of the synthetic mechanism and refinement of the synthetic conditions as well as their potential applications. Although several metal oxides have been previously synthesised successfully and investigated for their properties, some new developments have been achieved in this project: 1) a new synthesis method (Solid liquid method), which is more convenient and economical for industry, has been established instead of the evaporation method and the corresponding mechanism has been studied; 2) novel monocrystalline porous rutile TiO_2 templated by SBA-15 and KIT-6, and porous anatase nanocrystal-silica composites have been synthesised and their properties such as proton conductivity, Li ion insertion and photocatalytic activity have been investigated; 3) mesoporous metal oxides, such as Co_3O_4 templated by mesoporous silicas FDU-12 and SBA-16, have been synthesised and it was found that they have larger surface areas than those templated by SBA-15 and KIT-6; 4) the difficulties of making some porous metal oxides, e.g. MgO , ZnO and ZrO_2 , using mesoporous silicas or carbons as hard templates, have been investigated.

Characterisations of these porous metal oxides were performed by using HRTEM, EDX, SAED, XRD, N₂ adsorption and desorption, and TG/DTA.

2. Experimental

A common method to synthesise crystalline mesoporous metal oxides is as follows: the metal precursor is impregnated into mesoporous template and decomposes inside the pores of template, the crystals of the metal oxide are formed and grow inside the pores, and the porous product is finally obtained by removal of the template. Therefore some factors including the selection of metal precursors and mesoporous templates, impregnation method and removal of template are important to the synthesis of porous crystalline metal oxides. In this study, the single crystals of porous Co_3O_4 , In_2O_3 , NiO , CeO_2 , Mn_2O_3 , Cr_2O_3 , WO_3 , Fe_2O_3 and TiO_2 were synthesised using the solid-liquid or evaporation methods, with mesoporous silica as the template.¹⁹⁶⁻²⁰⁰ Characterisations of these porous metal oxides were made using high resolution transmission electron microscopy (HRTEM), energy dispersive X-ray analysis (EDX), select area electron diffraction (SAED), and nitrogen adsorption and desorption. Their physicochemical properties, such as proton conductivity, Li ion insertion and photoactivity, were also investigated.

2.1 Synthesis of mesoporous hard templates

Ordered mesoporous silicas were synthesised using self-assembled surfactants as soft templates in an acidic solution.^{39,41} Ordered mesoporous carbons were prepared by using either mesoporous silica as a hard template (e.g. CMK-3)⁸⁸ or self-assembled surfactant as a soft template (e.g. FDU-15).⁹⁸ Herein both mesoporous silicas such as FDU-12 and mesoporous carbons such as FDU-15 were used as hard templates to synthesise porous crystalline metal oxides.

2.1.1 Mesoporous silica

Ordered mesoporous silica was synthesised by using an amphiphilic molecule (e.g. Pluronic P123 ($\text{EO}_{20}\text{PO}_{70}\text{EO}_{20}$)) as a soft template. As a result of their amphiphilic nature, the surfactant molecules form micelles before arranging into supramolecular arrays in acidic media. The silica source (e.g. tetraethyl orthosilicate) forms around these supramolecular arrays resulting in ordered mesoporous silica. The stable silica can then be obtained by a maturation process and the surfactant template removed by calcination.

2.1.1.1 SBA-15

For synthesis of SBA-15, in detail, 4.0 g of Pluronic P123 (EO₂₀PO₇₀EO₂₀) was dissolved in a beaker containing 130 mL of distilled water and 20 mL of 37% HCl (hydrochloric acid). This solution was stirred in a temperature probe controlled oil bath at 40 °C until the surfactant was dissolved completely. 8.5 g of TEOS (tetraethylorthosilicate) was added to the solution, stirring for 24 h. The solution containing white precipitate was transferred into a Teflon bottle and matured in an oven at 100 °C for 48-72 h. This maturation process allows the silica to be stable and hydrostable. The white precipitate was filtered, washed with distilled water three times and dried at 40 °C. The as-prepared SBA-15/surfactant was put in a crucible and placed in a muffle furnace for calcination. The temperature rose at 1 °C/min from room temperature to 550 °C, and kept at 550 °C for 5 h before cooling down to room temperature. The organic template was burned off in air at that temperature, whilst the mesostructure of silica was remained.³⁹

2.1.1.2 KIT-6

In a typical synthesis procedure for KIT-6, 3.0 g of Pluronic P123 was dissolved in 115 mL of distilled water in a beaker, and 5 mL of HCl (37%) was added to the beaker, and the solution was stirred at 40 °C until clear (> 5h). 3.0 g of butanol was added to this clear solution dropwise with stirring for 1 h before adding 6.45 g of TEOS. After 24 h, the solution containing white precipitate was transferred into a Teflon bottle and matured in an oven at 100 °C for 48~72 h. The white precipitate was filtered, washed with distilled water three times and dried at 40 °C. The as-prepared KIT-6/surfactant was calcined at 550 °C for 5 h to remove the surfactant.⁴¹

2.1.1.3 FDU-12

In synthesis of FDU-12, 2.0 g of Pluronic F127 (EO₁₀₆PO₇₀EO₁₀₆) and 5.0 g of KCl (potassium chloride) were dissolved in 100 mL of distilled water and 20 mL of HCl (37%) in a beaker, and the solution was stirred at 40 °C until clear (> 1h). 2.0 g of TMB (trimethylbenzene) was added to this clear solution dropwise, stirring for 24 h. 8.3 g of TEOS was then added to the solution and stirred for a further 24 h. The solution was matured in an oven at 100 °C for 48-72 h. The white precipitate was filtered, washed with distilled water three times and dried at 40 °C. The as-prepared FDU-12/surfactant was calcined at 550 °C for 5 h to remove the surfactant.⁴³

2.1.1.4 SBA-16

For synthesising SBA-16, 2.0 g of Pluronic F127 and 4.0 g of KCl were dissolved in 100 mL of distilled water and 20 mL of HCl (37%) in a beaker with stirring at 40 °C. 8.6 g of TEOS was added to the solution, stirring for 24 h until clear. The solution was transferred into a Teflon bottle and matured in an oven at 100 °C for 48-72 h. The white precipitate was filtered, washed with distilled water three times and dried at 40 °C. The as-prepared SBA-16/surfactant was calcined at 550 °C for 5 h to remove the surfactant.⁴⁰

2.1.2 Mesoporous carbon

Some ordered mesoporous carbons, such as CMK-3, were synthesised by using mesoporous silicas as templates. Sucrose was used as carbon source and was impregnated into the pores of mesoporous silica with H₂SO₄. After mesoporous carbon was formed in nitrogen, the silica template was removed using an aqueous HF (hydrofluoric acid) solution.

Mesoporous carbons of FDU-14, FDU-15 and FDU-16 were synthesised in a basic solution by using P123 or F127 as a soft template. Solution-P (phenol/formaldehyde)⁹⁸ was used as carbon source and decomposed to generate carbon inside the pores of this supramolecular template. Additionally, in the synthesis of FDU-15, hydrocarbon (hexadecane or decane) was used as a swelling agent.

2.1.2.1 C-FDU-12 and C-SBA-16

In a typical synthesis procedure for mesoporous carbon, C-FDU-12 and C-SBA-16, 1.0 g of FDU-12 or SBA-16 was added to a solution containing 1.25 g of sucrose, 0.14 g of H₂SO₄ and 5.0 g of distilled water. After stirring for 1 h, the mixture was placed in a muffle furnace and was heated from room temperature to 100 °C. The temperature was kept at 100 °C for 6 h. Then the temperature was increased to 160 °C and maintained at 160 °C for 6 h before cooling down to room temperature. The heating rate was 1 °C/min. This procedure was repeated by mixing 0.8 g of sucrose, 0.09 g of H₂SO₄ and 5.0 g of distilled water with the dark product. The mixture was then heated in a tube furnace at 850 °C for 4 h under N₂ protection. The heating rate was 2 °C/min. The carbon filled mesoporous silica was washed in 5 wt% HF aqueous solution with rapid stirring for 3 h to remove silica template. The mesoporous carbon was collected by centrifugation, washed in distilled water and dried at 40 °C.⁴³

2.1.2.2 FDU-15

Mesoporous carbon FDU-15 was synthesised by using triblock copolymer P123 as a template and phenol/formaldehyde (Solution-P) as a carbon precursor. The carbon precursor Solution-P can be synthesised by dissolving 2.0 g of phenol and 7.0 mL of formaldehyde solution (40 wt %) in 50 mL of 0.1 M NaOH (sodium hydroxide) solution, stirring at 70 °C for 30 min. A clear precursor solution was obtained.

1.6 g of hexadecane or decane was added to the solution of 3.2 g P123 in 50 mL of water with stirring at 40 °C for 5 h. A white mixture was obtained when 60 mL of Solution-P was added to this solution and changed to dark red when it was stirred at 65 °C for about 3 h. A dark red precipitation appeared after the mixture was stirred at 65 °C for 24 h. The mixture was stirred at 65 °C for 72 h and then at 70 °C for 24 h. The final product was collected by centrifugation and filtration, washed with water, and dried in air. The obtained sample was calcined at 800 °C for 3 h in a nitrogen flow to obtain mesoporous carbons FDU-15. The heating rate was fixed at 1 °C/min.⁹⁸

2.2 Impregnation of precursors and crystallisation

The general route for producing the porous single crystals of metal oxides templated by mesoporous silicas includes the following steps: impregnating a metal-containing precursor into the silica pores, allowing the precursor to decompose inside the pores during a thermal treatment, controlling the crystal growth of the metal oxide at a higher temperature, and finally removing the silica template by using either a 10% HF aqueous solution at room temperature or a 2M NaOH solution at 80 °C. Obviously, the most important step is the impregnation. Until now, there are five methods which have been used for successful impregnation of metal-containing precursors into the pores of silica. The most popular methods include the evaporation method and the solid-liquid method.

2.2.1 Evaporation method

The evaporation method is simple and has been used by several groups.¹²² The mesoporous silica template is mixed with a selected metal nitrate in ethanol. The nitrate precursor is generally accepted to migrate into the pores by a capillary action during the evaporation of ethanol.

For example, 0.8 g of manganese nitrite aqueous solution (50%) was mixed with 0.15 g of FDU-12 or SBA-16 in 6.5 mL ethanol under stirring for 2 h. The mixture was collected after ethanol and water were evaporated, and then heated from room temperature to 500 °C (forming MnO₂) and 600 °C (forming Mn₂O₃) with a temperature heating rate of 1 °C/min, and maintained at the final temperature for 5 h. The black MnO₂/silica or Mn₂O₃/silica was obtained when cooled down to room temperature.

As another example, the titanium precursor, Ti(NO₃)₄ solution, could be obtained via dissolving titanium hydroxide in excess HNO₃ solution.^{201,202} The titanium source, such as titanium isopropoxide (Ti[OCH(CH₃)₂]₄) or tetrabutyl titanate (Ti[OC₄H₉]₄), was dissolved in ethanol by stirring and distilled water was added dropwise into the solution until no more white precipitate of titanium hydroxide was formed. The white precipitate was recovered by filtering and washing with distilled water. After drying, 0.2 g of the titanium hydroxide was dissolved in excess HNO₃ (68%) solution to form a Ti(NO₃)₄ solution. Subsequently, 0.15 g of SBA-15 or KIT-6 was mixed with the Ti(NO₃)₄ solution under stirring for 2 h, and the mixture was transferred into a 50 mL crucible and dried at 40 °C. The dried white powder was placed in a muffle furnace for calcination. The temperature was increased from room temperature up to 50, 100, 200, 300, 400 and 600 °C with a rate of 1 °C/min, and the specimens were kept at the terminal temperatures for 5 h before being cooled down to room temperature. The white TiO₂/silica was obtained when temperature cooled down to room temperature.

In addition, for syntheses of other porous metal oxides, 1 mmol of precursor M(NO₃)_n·xH₂O (M = Mg, Cd, Ga, Zn, La or Zr) was mixed with 0.15 g of SBA-15 in 6.5 mL ethanol with stirring for 2 h. The mixture was collected after ethanol was evaporated out, and then was heated from room temperature to 500 °C with a temperature heating rate of 1 °C/min, and maintained at the final temperature for 5 h. The product containing the silica template was collected when cooled down to room temperature.

A similar synthetic method was applied when porous carbon was used as a template. 1 mmol of precursor M(NO₃)_n·xH₂O (M = Mg, Cu or Zn) was mixed with 0.2 g of mesoporous carbon (e.g. C-FUD-12 and FDU-15) in 6.5 mL ethanol or THF under stirring for 2 h. The mixture was collected after the solvent was evaporated, and then heated from room temperature to 400 °C with a temperature heating rate of 1 °C/min. The temperature maintained at 400 °C for 5 h to form porous metal

oxides/carbon.

In the present project, it was found that the impregnation process of a precursor might not take place during the evaporation, but mainly occurred during calcinations after the evaporation when the precursor melted. Therefore, the solution precursors mentioned above could be replaced by solid nitrates.

2.2.2 Solid-liquid method

The solid-liquid method¹⁹⁸ was developed from the evaporation method. A metal-containing precursor was ground with a mesoporous silica template, and was expected to move into the pores of the template after melting when the mixed solid was heated to a temperature above the melting point of the precursor. The advantage of this method is solvent-free and simplicity. Its limitation, on the other hand, is that the precursor must have a melting point lower than its decomposition temperature.

A general route of synthesis is as follows, using synthesis of porous WO_3 from tungstophosphoric acid as an example: 1 mmol of precursor $\text{M}(\text{NO}_3)_n \cdot x\text{H}_2\text{O}$ ($\text{M} = \text{Co}, \text{Ni}, \text{Ce}, \text{Cr}, \text{In}$ or Fe) or 0.1 mmol of tungstophosphoric acid ($\text{H}_3\text{PW}_{12}\text{O}_{40}$) was mixed with 0.15 g of mesoporous silica (e.g. SBA-15 and FDU-12), and was ground finely for a few minutes in an agate mortar and pestle. The mixed solid was put into a crucible, and heated in a muffle furnace from room temperature to 500 °C (600 °C for mixture $\text{H}_3\text{PW}_{12}\text{O}_{40}$ /silica) with a temperature heating rate of 1 °C/min. The temperature was maintained at 500 °C (or 600 °C for WO_3 /silica) for 5 h. The corresponding metal oxides/silica was collected after the temperature cooled down to room temperature.

To investigate the mechanisms of the precursor impregnation, and the crystal growth in the silica pores, a series of Cr-containing specimens templated by SBA-15 were synthesised by using both evaporation method and solid liquid method, and collected after different stages of the thermal treatment, e.g. at 70 °C, a little higher than the melting point (66 °C) of $\text{Cr}(\text{NO}_3)_3 \cdot 9\text{H}_2\text{O}$, 110 °C, just above the decomposition temperature (100 °C) of $\text{Cr}(\text{NO}_3)_3 \cdot 9\text{H}_2\text{O}$, and 350 °C (the crystallization temperature of Cr_2O_3 in SBA-15), respectively. To reveal the difference between the evaporation method and solid-liquid method, the crystal growth of PbO from $\text{Pb}(\text{NO}_3)_2$, which decomposes at a lower temperature (>205 °C) without melting, was tested using both methods. $(\text{NH}_4)_2\text{Cr}_2\text{O}_7$, which decomposes at

180 °C without melting, was also selected as a precursor for further confirmation of the difference between two methods.

2.3 Removal of hard template

Mesoporous silica template can be removed by HF solution or hot NaOH solution (80 °C), and mesoporous carbon can be removed by a calcination at 700 °C for 2 h or 500 °C for 18 h.

2.3.1 Silica template

There are two methods to remove silica template: using HF and hot NaOH solution. Therefore, the method selected for removal of the silica depends on the properties of the metal oxides in acidic or alkaline media.

HF

The metal oxide containing mesoporous silicas were mixed with 10% HF in a polyethylene bottle, and stirred for 6 h. The solution was transferred to the centrifuge tube in a centrifuge at 3000 revolutions/min for 5 minutes to separate the product from the liquid. This procedure was repeated and the specimen was washed with water twice. The sample was then collected after drying at 40 °C.

For a typical synthesis, Co_3O_4 -, Cr_2O_3 - or WO_3 -containing mesoporous silica was immersed in an aqueous 10 wt % HF solution to remove the silica templates, and recovered by centrifugation and washed with distilled water twice before drying at 40 °C.

NaOH

The mesoporous silica can also be removed in a 2M NaOH solution at about 80 °C. The solution was transferred to the centrifuge tube before stirring for 6 h, and centrifuged at 3000 revolutions/min for 5 minutes to separate the product. The sample was washed with water twice and then dried at 40 °C. The reason for using NaOH solution instead of HF solution to remove silica is because these oxides are soluble in HF solution.

The mesoporous silica containing metal oxides (NiO , CeO_2 , Fe_2O_3 , In_2O_3 , MnO_2 ,

Mn₂O₃, MgO, CdO, Ga₂O₃, ZnO, La₂O₃ and ZrO₂) were immersed in hot NaOH solution at 80 °C to remove the silica template, and recovered by centrifugation and washed with distilled water twice before drying at 40 °C.

TiO₂ is a weak amphoteric oxide, so 0.2 M NaOH solution was used instead of 2M NaOH to remove silica template, to avoid the erosion of the mesoporous TiO₂ crystals. In detail, the white powder of as-made TiO₂/SBA-15 was mixed with 0.2 M NaOH solution by stirring for 2~3 mins at 80 °C, and the suspending solution was centrifuged to separate TiO₂. This process was repeated once and then the TiO₂ precipitate was washed by distilled water twice. The porous TiO₂ powder was collected after drying at 40 °C.

2.3.2 Carbon template

Mesoporous carbon was usually removed by simple calcination at a high temperature (> 500 °C). For a typical synthesis, mesoporous carbon containing MgO, CuO or ZnO were heated continuously in a muffle furnace from 400 °C to 700 °C, and kept at 700 °C for 2 h or to 500 °C, and kept at 500 °C for 18 h, with a temperature heating rate of 2 °C/min, after the metal oxides formation at 400 °C. The porous products were obtained after the temperature cooled down to room temperature.

2.4 Characterisation Methods

The porous single crystals (PSCs) of metal oxides were analysed using high resolution transmission electron microscopy (HRTEM), selected area electron diffraction (SAED), energy dispersive X-ray analysis (EDS or EDX), powder X-ray diffraction (XRD), nitrogen adsorption and desorption (the BET method) and thermo-gravimetric /differential thermal analysis (TG/DTA). The crystallographic structure of samples can be analysed by HRTEM and SAED. EDX is an analytical technique used for the elemental analysis or chemical characterisation of a sample. XRD is a technique used to characterise the crystallographic structure and crystallite size (grain size). Mesoporous materials can be characterised using N₂ absorption/desorption technique, which can reveal the surface area, pore size distribution and pore volume of materials. Thermogravimetric Analysis (TGA) is a

type of testing that examines the change in weight of samples in relation to the change in temperature, which can examine characteristics of materials, degradation temperatures and the level of inorganic and organic components in materials.

2.4.1 High resolution transmission electron microscopy

HRTEM is an important technique used to analyse crystal structures and lattice imperfections in various kinds of materials on an atomic scale.²⁰³⁻²⁰⁵ At present, the highest resolution realised is 0.07 nm.²⁰³ SAED and EDX equipments are normally attached to TEM instrument.

2.4.1.1 HRTEM instrument

HRTEM instrument is composed of electron-optical system, vacuum system and electrical system. Figure 2-1 shows a diagrammatic representation of the transmission electron microscopy instrument and operation. The electron-optical system includes electric illumination system, imaging system, image observation and recording system, and sample chamber. Electric illumination system can be divided into the electron gun, condenser lens and adjustment device. The electron gun can use three kinds of electron sources, a plain tungsten (W) filament, a W filament with a LaB₆ crystal tip or a field emission gun. The acceleration voltage is usually 50-200 kV (Figure 2-1). The Condenser lens is used to converge the electron beam emitted from electron gun to penetrate samples. The imaging system of TEM is usually composed of objective lens, intermediate lens and projector lens. The high and low magnification imaging can be adjusted by using these lens or part of them. The electron will lose energy by collision with gas in air, which causes the decrease of the average free path of electron motion. Thus the vacuum, at least 1.33×10^{-2} Pa, is necessary for the electron to pass completely down the column (1.33×10^{-4} Pa \sim 1.33×10^{-5} Pa is for 200 kV acceleration voltage). Additionally, the high vacuum can prolong the filament life, keep good insulation surroundings and reduce the sample contamination. The electrical system includes high voltage power supply of electron gun, current power supply of magnetic lens, power supply of various electrical equipments, power supply of vacuum system, safety protection electrical equipment and computer control system.

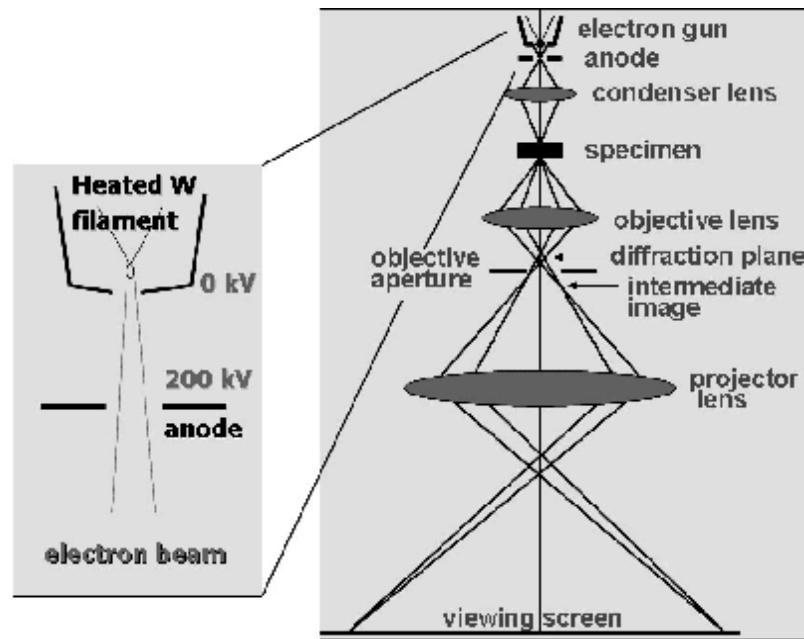


Figure 2-1. Diagrammatic representation of the transmission electron microscopy instrument.

2.4.1.2 TEM imaging theory

Transmission electron microscopy uses an electron beam as a light source to make images. In 1924, de Broglie postulated wave-particle duality, so that the wavelength associated with a particle is given by equation (2.1),

$$\lambda = \frac{h}{mv} \quad (2.1)$$

where h is Planck's constant (6.62×10^{-34} J·s). The wavelength (λ) is equal to Planck's constant (h) divided by the product of the mass (m) and the velocity (v) of the particle. In TEM, the velocity of an electron is relative to acceleration voltage (equation 2.2).

$$eV = \frac{1}{2}mv^2 \quad (2.2)$$

The kinetic energy of an electron (eV) is equal to the product of half the mass (m) and velocity (v) squared. Therefore, as the acceleration voltage is low, the velocity of

electron (equation 2.3) is much smaller than that of light.

$$v = \sqrt{\frac{2eV}{m}} \quad (2.3)$$

Its mass is nearly equal to the electron rest mass ($m = m_0$). So according to equation (2.1) and (2.3), the λ obtained by an equation (2.4)

$$I = \frac{h}{\sqrt{2em_0V}} \quad (2.4)$$

can be expressed as $I = \frac{12.25}{\sqrt{V}}$ ($h = 6.62 \times 10^{-34}$ J·s, $e = 1.60 \times 10^{-19}$ C, $m_0 = 9.11 \times 10^{-31}$ kg). As the acceleration voltage is very high, the velocity of the electron will be comparable to the speed of light. The equation needs relativistic corrections according to equation 2.5.

$$I = \frac{h}{\sqrt{2em_0V(1 + \frac{eV}{2m_0c^2})}} \quad (2.5)$$

λ obtained by this equation (2.5) can be expressed as $I = \frac{12.25}{\sqrt{V(1 + 0.9788 \times 10^{-6}V)}}$.

The value of the wavelength is 0.00251 nm when the voltage is 200 kV, which is much smaller than that of visible light (390 ~ 760 nm) and X-rays (e.g. λ of Cu $K_\alpha = 0.154$ nm).

As an ideal point light source is imaged by a lens, there is a bright region in the centre (Airy disk) with a series of concentric rings in the image plane, which is called Airy pattern (Figure 2-2(a)). One Airy disk will be overlapped by another when the distance between two objective points decrease, which causes low resolution and limits the magnification of microscopy. The lowest resolution distance was determined as the distance between two objective points (Δr_0) when the distance between two corresponding Airy disk centres is equal to one Airy disk's radius

(Figure 2-2(c)). According to equation (2.6),

$$\Delta r_0 \approx 0.61 \frac{\lambda}{n \sin b} \quad (2.6)$$

the value of Δr_0 is relative to the wavelength (λ) of light source. Thus a high resolution can be obtained by using an electron beam with a small wavelength.

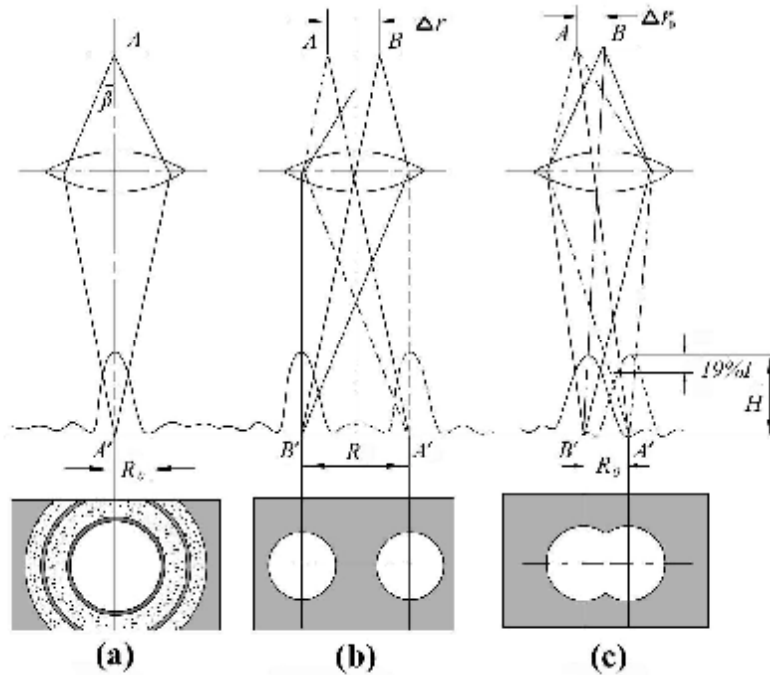


Figure 2-2. Light diffraction and the resolution of optical lens, (a) one Airy pattern, (b) long distance between two Airy disks, (c) short distance between two Airy disks.²⁰³

The electron beam moving in the axisymmetrical magnetic field is similar to light passing through a lens. This is the principle behind TEM, that samples can be imaged by receiving the electron beam which passed through the samples and was congregated by magnetic lens.

In detail, the electron beam is generated in an electron gun by heating a tungsten or LaB₆ filament in vacuum. The electrons are accelerated from the gun (cathode) towards the anode by applying a high voltage (200 KV). The electrons will have no potential energy and high kinetic energy as they arrive at the anode. The accelerated beam is focused by a set of condenser lenses, and on the specimen. After the beam

passes through the specimen, the objective lens produces the primary magnified image of the specimen. The specimen image was further enlarged many times by a series of projector lenses. Finally, the electron beam is transferred to the resulting image displayed on the viewing screen or recorded photographically/digitally (Figure 2-1).

The important factors to influence the quality of TEM image resolution are various types of aberration. It is impossible to get a 100% perfect magnetic lens, so the defect of magnetic lens lead to spherical aberration, astigmatism, image distortion and chromatic aberration. The spherical aberration results from the different refraction ability of electron beam between magnetic fields in adaxial area and abaxial area, and leads to a least defocus spot (r_s). The radius of the least defocus spot can be calculated by equation (2.7) with the spherical-aberration coefficients (C_s) and the half-aperture angle (α) of electromagnetic lens.

$$r_s = \frac{1}{4} C_s a^3 \quad (2.7)$$

According to the equation (2.7), when the spherical-aberration coefficients (C_s) or the half-aperture angle (α) of electromagnetic lens are reduced, the least defocus spot (r_s) decreases, which accordingly reduces the influence of spherical aberration and increase the quality of the image resolution. Therefore, the increase of the magnetic field intensity and the decrease of the grating aperture are selected to reduce the spherical-aberration coefficients (C_s) and can reduce the half-aperture angle (α), respectively.

The change of the wavelength or energy leads to the focus change of electromagnetic lens and chromatic aberration. The least defocus spot (r_c) caused by chromatic aberration can be obtained by equation (2.8) ($\Delta E/E$ is the energy rate of the change of electron beam).

$$r_c = C_c a \left| \frac{\Delta E}{E} \right| \quad (2.8)$$

The method to reduce the chromatic aberration is via improving the stability of acceleration voltage, increasing the magnetic field intensity and reducing the

chromatic aberration coefficients (C_c).

Astigmatism is a kind of aberration caused by non-rotational symmetry of the magnetic field of the electromagnetic lens. The least defocus spot (r_a) can be calculated by equation (2.9) (Δf_a is the focus difference caused by non-rotational symmetry of magnetic field).

$$r_a = \frac{\Delta f_a a}{2} \tag{2.9}$$

Astigmatism can be reduced by using an astigmatic instrument.

Figure 2-3 shows the fundamental principle of these three types of aberration formation in TEM. Additionally, a kind of diffraction aberration results from the diffraction effect in TEM and can be reduced by increasing the half-aperture angle (α) of the electromagnetic lens, which also leads to increase spherical aberration. Therefore a proper half-aperture angle (α) is selected by taking the two aberrations into consideration.

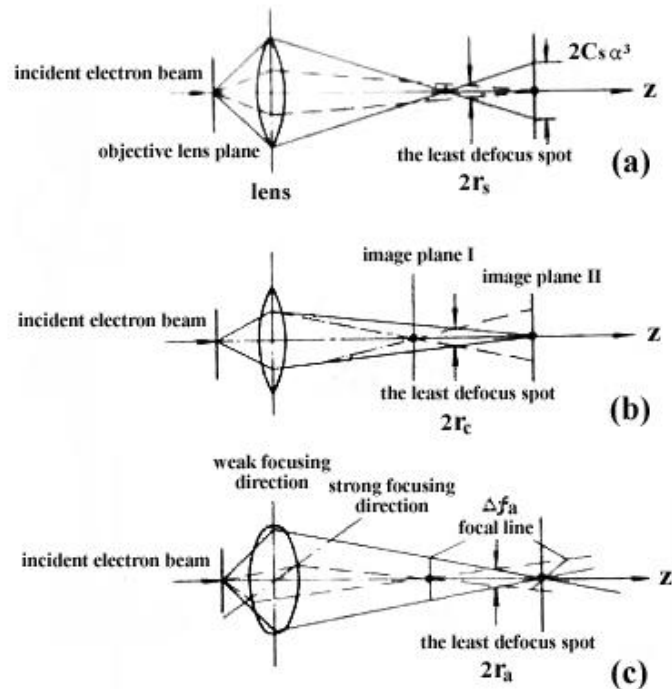


Figure 2-3 the schematic drawing of the aberration formation in TEM. (a) spherical aberration, (b) chromatic aberration and (c) astigmatism.²⁰³

The image contrast of TEM, including scattering (mass-thickness) contrast, diffraction contrast and phase contrast, is the foundation of TEM images. Differences in mass and thickness in the parts of samples have different scattering ability, which generates scattering (mass-thickness) contrast. The intensity of electron beam (I) can be calculated by using the thickness (t), atomic weight (A) and density (ρ) of the sample and scattering cross section (σ_a) (equation 2.10).

$$I = I_0 e^{-\frac{kS_a}{A} \cdot r t} \quad (2.10)$$

Thus the intensity difference of electron beam (G) between neighbouring points can be obtained in equation (2.11) and abbreviated in equation (2.12).

$$G = \frac{I_1 - I_2}{I_1} = 1 - e^{-K(\frac{S_{a1}}{A_1} \cdot r_1 t_1 - \frac{S_{a2}}{A_2} \cdot r_2 t_2)} \quad (2.11)$$

$$G = k(\frac{S_{a1}}{A_1} \cdot r_1 t_1 - \frac{S_{a2}}{A_2} \cdot r_2 t_2) \quad (2.12)$$

According to equation (2.12), the larger the atomic weight (A), the higher the scattering angle, and therefore the less electrons available for imaging leading to darker areas in the corresponding place in the sample. Moreover, the intensity difference (G) is also relative to the thickness (t) and density (ρ) of the sample due to the equation (2.12). The different intensity of electron beam generates the scattering contrast image of samples.

On the other hand, the size of sample must be very small for HRTEM imaging. Therefore the image contrast caused by the scattering contrast is weak and the phase contrast plays more of a leading role on imaging. The scattering wave and direct transmitted wave generates a phase difference and leads to the interference on the image plane via convergence by objective lens. The various phase differences lead to a differential interference on the image plane, which makes a phase contrast image. Some samples have uniform thickness and near-neighbour atomic number and the scattering contrast in this sample image is not obvious. The TEM image contrast of this thin sample is relative to the crystal structure of this sample. Diffraction contrast

is caused by addition of the diffracted beam intensity, which is relative to the crystal structure of the sample, to transmitted beam intensity. Accordingly, the diffraction contrast image reflects the crystal characterisation of samples.

2.4.1.3 Select area electron diffraction

Selected area electron diffraction (SAED) is a technique used in TEM to examine the crystallography of a sample.²⁰³ In a TEM, the ordered atoms in a specimen act as a diffraction grating to the electrons because the wavelength of high-energy electrons is slightly smaller than the spacings between neighbouring atoms in a specimen. Thus the electron beam passes through a thin crystalline specimen and is scattered to particular angles determined by the crystal structure of the sample. There are three basic SAED patterns according to different crystal types. A regular 2D pattern indicates that the specimen is a single crystal (Figure 2-4, a), a set of dotted rings indicate polycrystalline material (Figure 2-4, b) and a set of diffuse rings indicate amorphous material (Figure 2-4, c). The specimen often needs to be tilted to a particular angle in both x and y directions to obtain the best diffraction pattern.

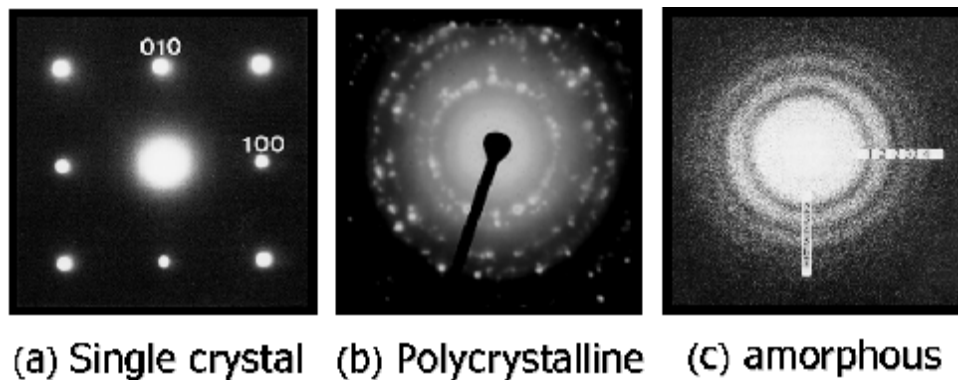


Figure 2-4. Diffraction patterns of (a) single crystal, (b) polycrystalline material and (c) amorphous material.

Figure 2-5 shows the diagram of the relationship between the reciprocal d-spacing (d^*) and the distance between the diffraction rings or spots (D^*). The d-spacing (d) of crystalline specimen can be calculated by equation (2.13) where d^* is the reciprocal d-spacing, D^* is the distance between spots on the negative and L is the camera length.

$$d = \frac{1}{d^*} = \frac{l}{2 \sin \theta} = \frac{Ll}{D^*} \quad (2.13)$$

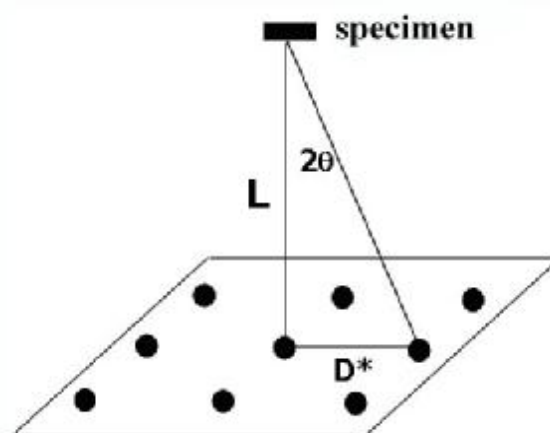


Figure 2-5. Diagram of relationship between d^* and D^* , D^* is the distance between the certain two diffraction spots and L is the camera length.

Unlike XRD, a SAED pattern is a magnified image of the reciprocal lattice cross-section and can reflect directly to the crystal structure of specimens. All spots of a pattern can be indexed by indexing two independent spots. The SAED patterns of the specimen can be indexed by the determination of the unit cell of the sample crystal. If the unit cell is unknown, two or more diffraction patterns from different directions, usually obtained by tilting the specimen, are required to calculate the unit cell.

2.4.1.4 Energy dispersive X-ray analysis

Energy dispersive X-ray spectroscopy (EDX) is an analytical technique used for the elemental analysis and determination of chemical composition of a material.²⁰³ Each element has a unique atomic structure and emits characteristic X-ray when the matter is hit by charged particles such as electrons, protons or a beam of X-rays. In EDX, the high energy electron beam excites an electron in an inner shell of an atom and ejects it from the shell. An electron from an outer, higher energy shell fills the electron hole where the emitted electron was and the difference in energy between the higher energy shell and lower energy shell is released in the form of an X-ray (Figure

2-6). The wavelength or energy of this kind of X-ray is relative to the type of elements. Therefore the elements present in a specimen can be determined by using EDX. The wavelength (λ) and the energy (E) have a relationship in equation (2.14).

$$I = \frac{12396}{E} \quad (2.14)$$

Moreover, the intensity of the characteristic X-ray is relative to the elementary concentration of the specimen so that the proportion of all kinds of elements in the samples can be calculated using EDX. The local defects in the sample can be detected by using elemental mapping, which gives the distribution of the target element.

Figure 2-6 shows the diagram of the basic principle of EDX. The electron in the K shell of an atom was excited by electron beam and the electron hole is filled by the electron in L shell. The difference in energy between the K shell and L shell can be emitted in the form of X-ray (K_{α}). The characteristic X-ray K_{α} is received and measured by an energy dispersive spectrometer fixed in TEM. By analogy, the K_{β} is released when the electron in the M shell fills the electron hole in the K shell and the L_{α} is released when the electron in the M shell fills the electron hole in the L shell (Figure 2-6).

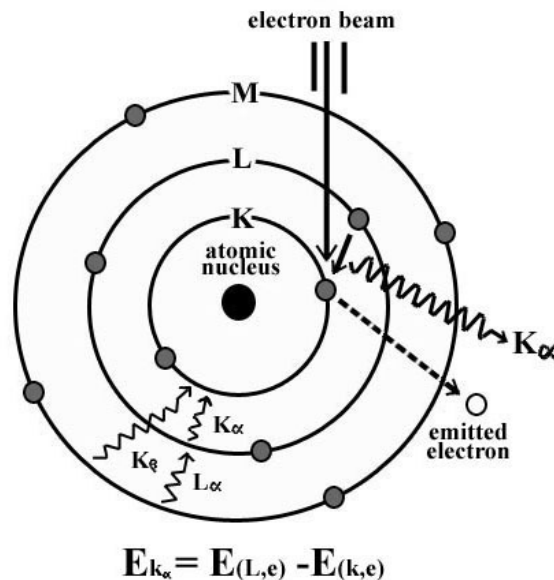


Figure 2-6. Diagram of the electron in the K shell excited by electron beam, the electron hole filled by the electron in the L shell and the X-ray of K_{α} released.

Sample preparation for TEM

The common method to prepare a powder sample for TEM is by solvent suspension. Acetone or ethanol is usually chosen as solvent because they easily evaporate at room temperature. The sample was ground well using a pestle and mortar, then acetone was added to the sample and the suspension was ground again. A few drops of the solution were dropped onto a holey carbon film on a copper grid, or the copper grid was immersed into the suspension for a few seconds. The target sample is deposited onto the carbon film after the solvent evaporated. If the sample is inclined to stick together and can not be separated by grinding, it can be separated in solvent by sonication.

If the sample reacts with the common solvent such as acetone, ethanol and water, a dry preparation method can be used. The sample is ground well and the copper grid was put into the powder for a few seconds in order for the powder to stick onto the carbon film. Excess powder is removed by tapping the copper grid.

The PSC samples for TEM examination were prepared using the solvent suspension method.

2.4.2 X-ray diffraction

X-ray diffraction is a technique based on the elastic scattering of x-rays from crystal structures. The crystalline sample can scatter the x-rays when the x-rays hits the sample and the scattered x-rays interfere with each other constructively or destructively to produce a diffraction pattern on a detector.^{203,206} Figure 2-7(a) and (b) is the schematic diagram of crystalline sample scattering the x-rays. The Bragg equation (2.15) indicates a relationship of the path difference ($n\lambda$) and the spacing (d) between the planes in the atomic lattice, the angle (θ) between the incident ray and the scattering planes, where n is an integer determined by the order given and λ is the wavelength of x-rays, when the two scattered x-rays interfere constructively (Figure 2-7a).

$$n\lambda = 2d \sin \theta \quad (2.15)$$

Figure 2-7(b) shows a destructive interference of two scattered x-rays and the scattered intensity is zero.

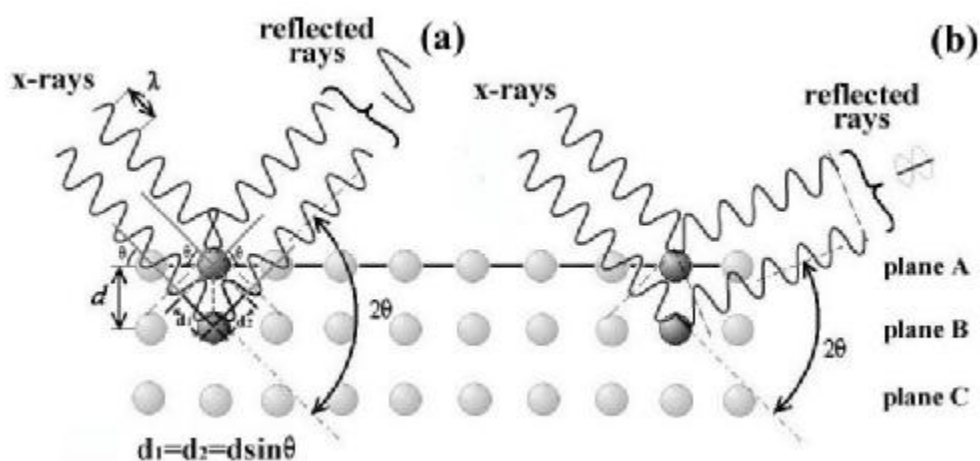


Figure 2-7. Schematic diagram of (a) constructive interference and (b) destructive interference of two scattered x-rays reflected by two planes in the atomic lattice.

Theory and operation of XRD

Powder X-ray diffraction (XRD) is an analytical technique used to characterise the crystallographic structure, crystallite size (grain size) and preferred orientation of samples. The generation of X-rays is similar to the X-ray in EDX that usually a tungsten filament is heated up and emits electrons towards a copper (or molybdenum) anode (Figure 2-8a). The copper atom loses an electron in the K shell and the vacancy is filled with a higher energy level electron such as from the L shell or the M shell. This process releases energy in the form of an X-ray named as Cu K_{α} (the electron in the L shell filling the electron hole in the K shell) or Cu K_{β} (the electron in the M shell filling the electron hole in the K shell). The wavelength of Cu K_{α} is 0.154 nm calculated by using equation (2.14) with the energy of Cu K_{α} (8040 eV). Figure 2-8 is a schematic diagram of transmission XRD (Figure 2-8b) and reflective XRD (Figure 2-8c).

Figure 2-8 (b) shows the schematic diagram of the transmission XRD. The emitted Cu X-rays will pass through a monochromator made of a crystal with a specific orientation before the X-rays are scattered by the sample. Only the Cu K_{α} X-ray can be allowed to pass the monochromator and the unwanted X-rays such as Cu K_{β} are forbidden. Therefore a unique x-ray source can increase the resolution of XRD patterns, especially for two diffraction peaks which are close to each other. However, for some crystals, the intensity of diffraction peaks is too weak to be identified.

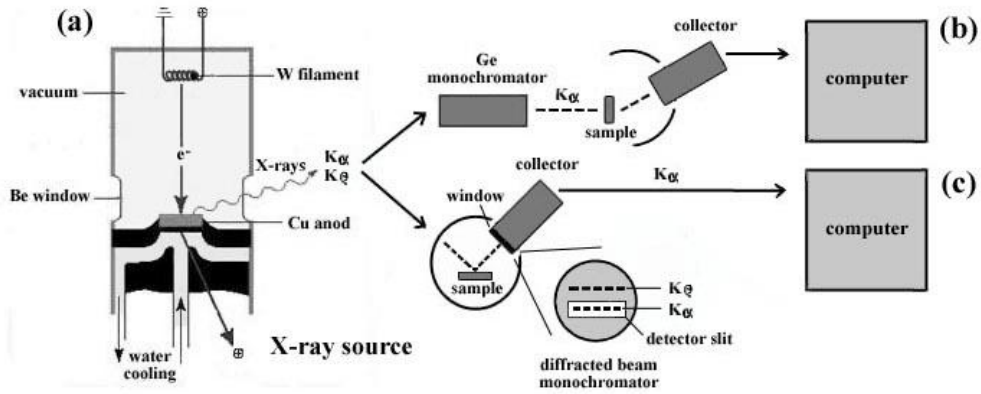


Figure 2-8. Schematic diagram of (b) transmission XRD and (c) reflection XRD with the same X-ray generation apparatus (a).

Figure 2-8(c) shows the schematic diagram of the reflection XRD. The Cu X-rays are not filtered and are directly scattered by the sample at an angle towards the detector. A diffracted beam monochromator with a narrow slit covers the detector window and allows Cu K_{α} X-rays through. The XRD pattern can be obtained by rotating the detector to different angles. Some crystals which can not be characterised using transmission XRD can be detected by reflective XRD.

Additionally, the crystallite size (grain size) can also be calculated via the characteristic peak width of the XRD pattern by using the Debye-Scherrer formula (2.16), where β is the width of the peak at half maximum intensity of a specific plane (hkl), k is a constant that varies with the method of taking the breadth ($0.89 < k < 1$), λ is the wavelength of incident x-rays and θ is the centre angle of the peak.²⁰⁷ It is the quantitative equivalent of saying that the XRD peaks are wider when the sample's crystallites are smaller.

$$D_{hkl} = \frac{k\lambda}{b \cos \theta} \quad (2.16)$$

Sample preparation and measurement for XRD

The sample powder is ground well using a pestle and mortar and fills in the shallow pit of a metal plate with smoothing the surface of the sample. The metal plate containing the sample is placed in the chamber of the reflective diffractometer. The

diffractometer uses a W filament and a Cu anode operating at 40 kV. The Cu K_{α} including both $K_{\alpha 1}$ (0.15406 nm) and $K_{\alpha 2}$ (0.154439 nm) X-rays, with the average wavelength being 0.15418 nm, is collected by a diffracted beam monochromator in detector. The XRD pattern is collected between $2\theta = 10^{\circ}$ and 90° , with 1°min^{-1} scan rates and 0.2° step sizes.

The sample powder can also be characterised by a transmission diffractometer. A small amount of the sample powder is ground well and placed between the centres of two plastic discs. The two plastic discs with the sample in the centre is fixed by a metal disc and then placed in a holder of the transmission diffractometer. The diffractometer uses a W filament and a Cu anode operating at 40 kV. Only Cu $K_{\alpha 1}$ X-rays of wavelength 0.154056 nm can pass the Ge monochromator and be collected by the detector. The XRD pattern is collected between $2\theta = 10^{\circ}$ and 90° , with 1°min^{-1} scan rates and 0.2° step sizes.

The PSC samples were prepared and characterised by using a reflection diffractometer.

Comparison between XRD and SAED

XRD data is collected from a large amount of sample and the XRD pattern is average data, which transfer 3D information to a 1D display. It is difficult to index the peaks or work out the structure if the sample is unknown. But if the sample is limited in a range of known samples, which have been determined by standard samples, XRD is a fast way to determine this sample and detect all peaks of it. Compared with XRD, SAED detects a local area of the sample, and transfers 2D information to 2D display, with each spot corresponding to one peak. It is easier to index the peaks of the sample using the data from SAED pattern such as d-spacings and inter-plane angles. But the whole information of the sample can not be collected completely by SAED. In many cases, determination of a structure by using both XRD and SAED is a powerful method.

2.4.3 Nitrogen adsorption and desorption

When gas molecules come in contact with some solids, they will accumulate on the surface of the solid and form adsorption layers. This process is called gas adsorption. Because adsorption is an action occurring on the solid surface, when the solid has a

porosity and large inner surface area, they can also adsorb gas or liquid. According to the different interaction force between adsorbent and adsorbate, the adsorption process is generally classified as physisorption and chemisorption. In physisorption, the interaction between adsorbent and adsorbate is weak van der Waals forces, accordingly, this adsorption process is reversible, fast and there is no chemical reaction. On the contrary, the chemisorption is based on the interaction of covalent bonding, which is irreversible process and is a slow reaction.

The N₂ adsorption and desorption process on the surface of porous metal oxides is physical adsorption and can be used to examine the surface area, pore volume and pore size distribution.

BET theory

According to the ideal adsorption on the solid surface, the Langmuir adsorption equation (2.17)²⁰⁸ was brought forward by Irving Langmuir in 1916 and expresses the relationship of molecules adsorption on a solid surface and gas pressure concentration of adsorbate above the solid surface at a fixed temperature, where θ is the percentage coverage of the surface, P is the gas pressure or concentration, a is a constant.

$$q = \frac{a \cdot P}{1 + a \cdot P} \quad (2.17)$$

In 1938, Brunauer, Emmett and Teller brought forward a multimolecular adsorption theory²⁰⁹ on the assumption that: 1. the solid surface is even; 2. the multimolecular adsorption may be possible and the first adsorption layer is physical adsorption; 3. there is no reaction between each adsorption layer. The resulting BET adsorption equation is expressed by (2.18), where P and P_0 are the equilibrium and the saturation pressure of adsorbates at the temperature of adsorption, V is the adsorbed gas quantity, and V_m is the monolayer adsorbed gas quantity. c is the BET constant.

$$V = \frac{V_m c P}{(P_0 - P) \left[1 + (c - 1) \frac{P}{P_0} \right]} \quad (2.18)$$

Adsorption is usually described through adsorption isotherms plotted by using adsorption equations (2.17, 2.18). The amount of adsorbate on the adsorbent is a function of its pressure at constant temperature in the equation. The adsorbent with different structure can be determined by its typical adsorption isotherm.

Adsorption isotherms of different materials

The adsorption isotherm depends on the structure of adsorbent, adsorption heat and other physicochemical properties. The adsorption isotherm of various adsorbents can be obtained at a constant temperature and a wide range of relative pressures. Figure 2-9 shows six types of N_2 adsorption and desorption isotherms from different kinds of materials. The type I adsorption isotherm (Figure 2-9a) is a typical isotherm of microporous materials. At low relative pressure, the adsorbate fills in the micropores of adsorbent, leading to a sharp slope of the isotherm. At high relative pressure, the micropores of adsorbent has been filled fully with the adsorbate and the adsorption on the surface of macropores or the outer surface of adsorbent leads to slope of the isotherm to be horizontal or near to horizontal. When the relative pressure P/P_0 is near to 1, a 'tail' curve can be observed in the adsorption isotherm. The type II adsorption isotherm (Figure 2-9b) is formed by adsorption on the surface of macroporous or nonporous materials. The inflexion in the adsorption isotherm expresses the completion of the monolayer adsorption and the start of multilayer adsorption. The type III adsorption isotherm (Figure 2-9c) is related to the weak interaction of Adsorbent-Adsorbate and the strong interaction of Adsorbate-Adsorbate. Therefore the multilayer adsorption is generated before the completion of the monolayer adsorption, which expresses a rapid increase of quantity adsorbed during the adsorption process. The type IV adsorption isotherm with a hysteresis loop (Figure 2-9d) is a typical isotherm of mesoporous materials. When the relative pressure P/P_0 increases, the mesopores of adsorbent is filled with the adsorbate and its radius reduces. The gas adsorbate is condensed to liquid on the surface of mesopores. The capillary condensation in the mesopores leads to a rapid increase of quantity adsorbed and a second inflexion appears in the adsorption isotherm. In Figure 2-9(d), at a certain range of relative pressure P/P_0 , lower relative pressure is needed in desorption process when the quantity adsorbed is the same as that in adsorption process. This is attributed to the different processes occurring as N_2 is condensed from gas to multilayer adsorbed phase compared to the process of evaporation from the adsorbed

phase to gas upon desorption.. Few mesoporous or microporous adsorbent can form the type V adsorption and desorption isotherm (Figure 2-9e) due to the weak interaction of the Adsorbent-Adsorbate and the strong interaction of the Adsorbate-Adsorbate. The adsorbent forming type VI adsorption isotherm (Figure 2-9e) is rare, and the isotherm expresses the multilayer adsorption formed gradually on the even nonporous surface of adsorbent. Each step in the isotherm corresponds to the quantity adsorbed in different adsorption layer.

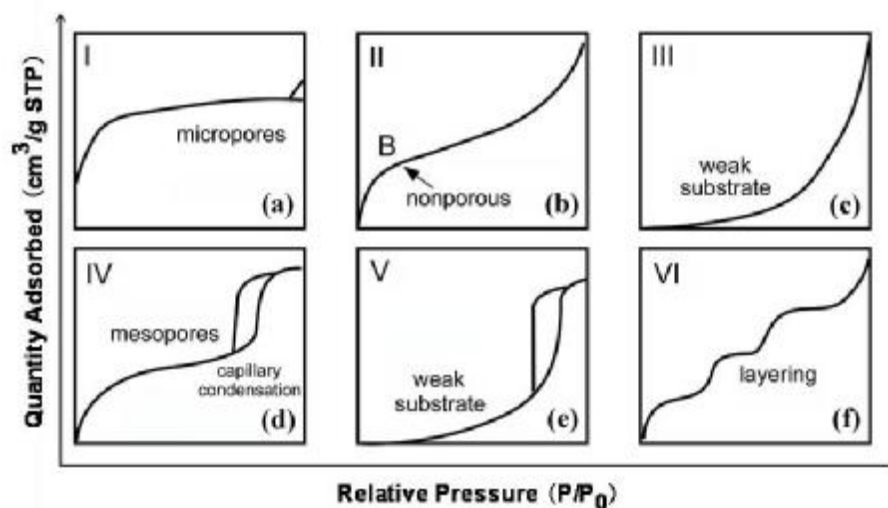


Figure 2-9. Six types of adsorption and desorption isotherm from different kinds of materials.

Sample preparation for N₂ adsorption/desorption analysis

The porous metal oxides were weighed (>20 mg) before placed at the bottom of a glass tube with a spherical bottom and pre-dried using a hairdryer. The glass tube containing the specimen was heated at 150 °C for 1 h by a machine under vacuum to remove water in samples and then recovered at room temperature. The specimen/glass tube was immersed in liquid nitrogen in the chamber of the micromeritics instrument ASAP 2020. The N₂ adsorption/desorption process for the specimen at 77 K was measured using micromeritics instrument ASAP 2020 and plotted as a graph by the computer. After completing the measurement, the specimen was weighed accurately to calibrate the BET data.

The experimental data of N₂ adsorption/desorption of the porous metal oxides were collected by Mrs. Sylvia Williamson using a Micromeritics instrument ASAP 2020.

2.4.4 Thermogravimetric/differential thermal analysis

The thermogravimetric/differential thermal analysis (TG/DTA) is a simultaneous measurement instrument including TG, which is a type of measurement of weight changes in a material in relation to the change of temperature (or time) under a controlled atmosphere, and DTA system, which is a thermoanalytic technique.²¹⁰ Thermogravimetric Analysis (TGA) was used mainly in reaction speed and acceleration degradation tests, measurement of the thermal stability and composition of a material, analysis of the water and ash content, and evaluation of decomposition, oxidation and heat resistance of specimens. In differential thermal analysis (DTA), the material with an inert reference is heated under identical conditions and the temperature difference between sample and reference was detected and recorded. This differential temperature between sample and reference, either exothermic or endothermic, provides temperature data on the transformations such as crystallisation, melting, sublimation and phase change.

KIT-6 containing $\text{Ti}(\text{NO}_3)_4$ complexes sample was examined by a Rheometric Scientific TG 1000M + TA instruments SDT 2960. The sample was placed in the holder and heated from room temperature to 800 °C (5 °C/min), and then cooled down to 30 °C (5 °C/min) under flowing air at a rate of 20 ml/min.

The $\text{Ti}(\text{NO}_3)_4$ complexes/silica was examined by technical staff Mrs. Sylvia Williamson using a Perkin Elmer TGA/DTA.

2.5 Physico-chemical properties

Porous metal oxides have a wide range of potential applications such as catalysis, nanoreactors, electronic devices and gas sensors due to their large surface area, large pore volume and ordered pore network. The porous rutile TiO_2 and anatase nanocrystal-silica composites were synthesised and examined for its properties on proton conductivity, Li storage and photocatalysis, respectively.

2.5.1 Proton conductivity

The proton conductivity of the porous rutile TiO_2 was measured by a.c. impedance spectroscopy. The pellets for measuring were 13 mm in diameter and 3-4 mm in thickness and were obtained by pressing powders under $5 \times 10^3 \text{ kg cm}^{-2}$. PTFE bonded

carbon black (Carbot Vulcan 72R) and carbon paper (Torory TGPH-090) were used as the electrode and the current collector, respectively. The whole assembly was then pressed between two pieces of carbon paper for current collection. The detailed construction is schematically shown in Figure 2-10. The impedance data were collected from room temperature to 100 °C after holding for 1 hour at each temperature to reach equilibrium. A Schlumberger Solartron 1255 frequency response analyser coupled with a 1287 electrochemical interface controlled by Z-plot electrochemical impedance software was used. The frequency range was from 1 MHz to 100 mHz at 100 mV r.m.s. The humidity effect on the proton conductivity of porous rutile TiO₂ was carried out via controlling vapour flow obtained at different temperature.¹⁹⁹

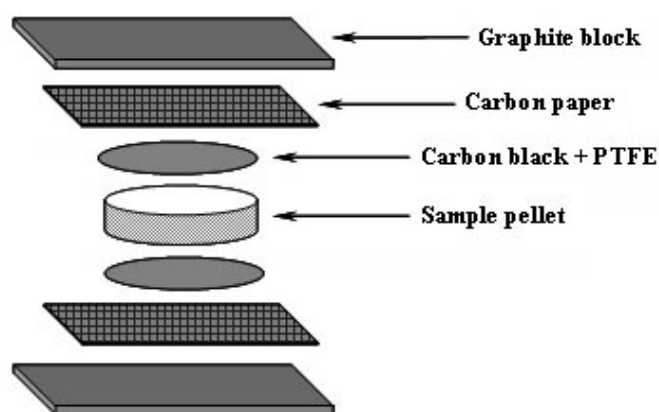


Figure 2-10. Schematic diagram of the specimen preparation for measuring the proton conductivity of porous rutile TiO₂.

2.5.2 Li ion storage

For electrochemical characterisation, electrode materials were prepared as 'Bellcore' type electrodes, and assembled into coin cells, as previously described.²¹¹ A slurry was made by grinding 11.6 % by weight of the dry active material and 1.4 % by weight Super S carbon together, and then adding 5.5 % by weight polyvinylidene fluoride (PVDF), 9.5 % by weight propylene carbonate (PC) and 72 % by weight acetone. The slurry was stirred for 4 h in a 50 °C water bath and then doctor bladed onto a glass plate, to form a self-supporting sheet, typically 100 – 200 µm thick after the evaporation of the acetone. The electrode sheet was cut into discs, and the trapped PC was leached out using ether, until the individual electrodes reached constant weight. The resulting porous electrodes were dried under vacuum and transferred to

an argon-filled glove box. A MacPile (Bio-logic) battery testing system was used to collect the electrochemical data. Galvanostatic cycling was recorded between set potential limits, typically 0.8 and 3.5 V, after the first reduction sweep. There was 1 h relaxation time at the endpoints. Potentiostatic data were recorded with 1 h relaxation time at the endpoints (typically 0.8 and 3.5 V with a step rate of 20 mV/h).¹⁹⁹

2.5.3 Photocatalysis

Photoactivity of the porous anatase nanocrystal-silica composite was evaluated on the basis of the decomposition of methylene blue (MB) in an aqueous solution. 0.1 g of sample powder was suspended in 200 mL of a 5×10^{-5} M MB solution (0.5g/L) in the 250 mL round bottom flask by air bubbling. This mixture was first suspended in the dark for 30 minutes to reach the adsorption equilibrium before irradiation with a high intensity discharge 250 W iron doped metal halide UV bulb (UV Light Technology Ltd., Birmingham, UK) equipped with UV cutoff filter (an equipment which can filter out ultraviolet rays), The mixture temperature was controlled at about 25 °C using a water bath for infrared radiation and lamp heating removal. After irradiation, 2 mL of the mixture was collected and centrifuged at the irradiation time intervals (hourly). The photoactivity was examined by monitoring the reduction of the absorbance at 665 nm. The spectrophotometric measurements were carried out using Perkin Elmer Lambda35 UV/Vis spectrometer.²⁰⁰

3. Solid-liquid method

The most important process of the synthesis of porous metal oxides templated by mesoporous silicas is the impregnation of metal-containing precursor inside the pores of silica. Four methods of impregnation have been developed in the last five years: the so-called surface modification method,^{120,165} dual-solvent method,¹²¹ one-step nanocasting method¹⁴⁴ and evaporation method,^{122,124} respectively. The evaporation method was used usually due to its simple process. In detail, the mesoporous silica template was mixed with a selected metal nitrate in ethanol, and the nitrate precursor was generally accepted to migrate into the pores by a capillary action during the evaporation process.

Table 1. Melting point (MP) and decomposition temperature (DT) of the nitrate precursors for porous transition metal oxides.

Precursor	MP(°C)	DT(°C)	Oxide
Co(NO ₃) ₂ ·6H ₂ O	55	>74	Co ₃ O ₄ (>150°C)
Cr(NO ₃) ₃ ·9H ₂ O	66	>100	Cr ₂ O ₃ (>350°C)
Ni(NO ₃) ₂ ·6H ₂ O	56.7	>110	NiO
Ce(NO ₃) ₃ ·6H ₂ O	96	200	CeO ₂
In(NO ₃) ₃ ·xH ₂ O	100	>100	In ₂ O ₃
H ₃ PO ₄ W ₁₂ ·xH ₂ O	107	>385	WO ₃
Pb(NO ₃) ₂		205~223	PbO
(NH ₄) ₂ Cr ₂ O ₇		180	Cr ₂ O ₃ (>180°C)

Generally, a metal nitrate has a low melting point and its decomposition temperature is usually higher than its melting point. Therefore the solid-liquid method¹⁹⁸ was developed based on these characteristics of metal nitrate. In detail, a metal-containing precursor was ground with the mesoporous silica template, and was expected to migrate into the pores of silica after melting when it was heated up to a temperature above its melting point. The liquid precursor would then decompose to generate the metal oxide inside the silica pores when the temperature was increased above its decomposition temperature. The advantage of this synthetic method is that it is convenient and solvent-free. Its limitation is that the precursor must have a melting point lower than its decomposition temperature. Table 1 shows the melting point and decomposition temperature of some metal nitrates used as the precursors (H₃PO₄W₁₂·xH₂O was used as the W-precursor). Mesoporous silicas of SBA-15 and KIT-6 were selected as hard templates.

3.1 Mesoporous silica template

The popular mesoporous silicas used as hard templates, such as SBA-15 and KIT-6, can be synthesised via addition of silica source (e.g. TEOS), various surfactants (e.g. P123) and additives (e.g. TMB) in an acidic solution. The morphology and pore size of self-assembled molecules in solution depended on the acidity of the solution, the reaction temperature and the selection of surfactants and additives. Recently these mesoporous silicas with various morphologies and pore sizes were used as hard templates for preparation of crystalline mesoporous metal oxides such as Co_3O_4 and Cr_2O_3 particles.^{122,124,198}

3.1.1 SBA-15

SBA-15 has a similar structure to MCM-41, consisting of hexagonally ordered cylindrical pores, except all cylindrical pores in SBA-15 are connected together by small nanochannels. SBA-15 was firstly synthesised by Zhao et al. in 1998,³⁹ using amphiphilic triblock copolymers, $\text{EO}_{20}\text{PO}_{70}\text{EO}_{20}$ (Pluronic P123), as a template. This synthetic process needed an acidic condition and a relatively low synthesis temperature (35 °C to 80 °C). The uniform pore size (5-30 nm) and pore wall thickness (3-6 nm) can be tuned by addition of various co-solvent organic molecules such as 1,3,5-trimethylbenzene (TMB). Figure 3-1 shows TEM images of the hexagonal structure of SBA-15 (space group $p6mm$) from different orientations, with the section view of the hexagonal structure in the [001] zone axis (Figure 3-1a) and the side view of the cylindrical pores in the [110] zone axis (Figure 3-1b).

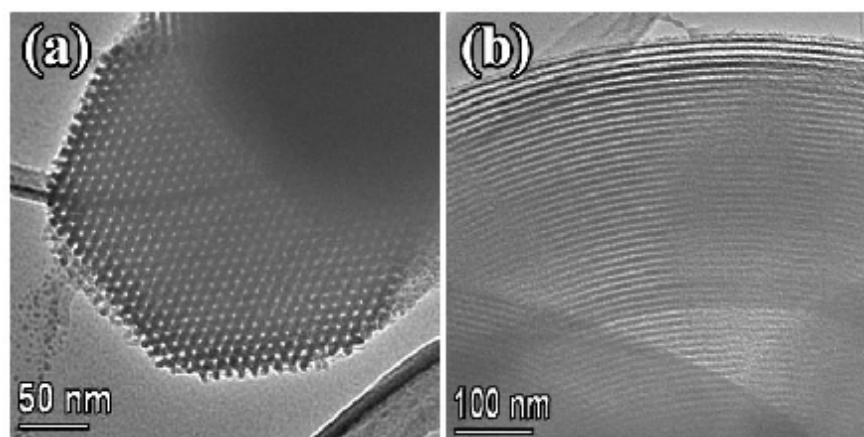


Figure 3-1. TEM images of SBA-15 viewed down (a) [001] zone axis and (b) [110] zone axis.

3.1.2 KIT-6

KIT-6 is another type of mesoporous silica and was first synthesised by the Ryoo group in 2003 using the triblock copolymer (Pluronic P123) and butanol, to control the structure of the surfactant in an aqueous solution.⁴¹ The mesostructure of KIT-6, analogous to MCM-48,³¹ is body-centered cubic (space group $Ia\bar{3}d$). It consists of a pair of interpenetrating bicontinuous pores, and the pore size is tunable from 4 to 12 nm in diameter via a simple hydrothermal treatment (25-35 °C). The characteristic structure of KIT-6 could not be observed in the 2D TEM image. Figure 3-2 shows TEM image of the mesostructure of KIT-6, looking down the [111] zone axis in the cubic structure.

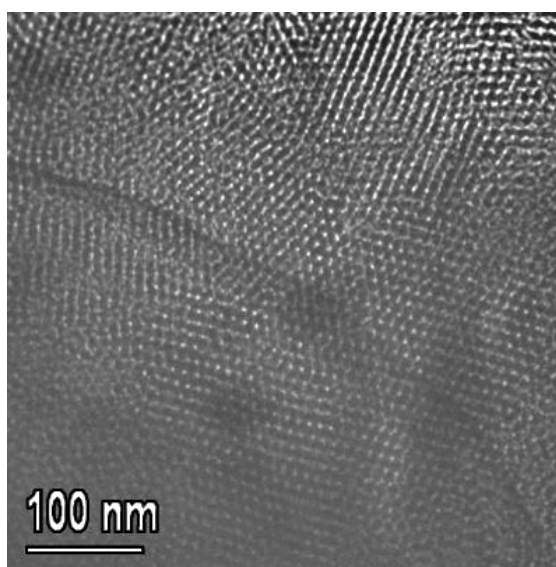


Figure 3-2. TEM image of KIT-6 viewed down the [111] zone axis.

3.2 Porous metal oxides synthesised using the solid-liquid method

According to the solid-liquid method and the properties of metal nitrates shown in Table 1, metal nitrates of $\text{Co}(\text{NO}_3)_2 \cdot 6\text{H}_2\text{O}$, $\text{Cr}(\text{NO}_3)_3 \cdot 9\text{H}_2\text{O}$, $\text{Ni}(\text{NO}_3)_2 \cdot 6\text{H}_2\text{O}$, $\text{Ce}(\text{NO}_3)_3 \cdot 6\text{H}_2\text{O}$, $\text{In}(\text{NO}_3)_3 \cdot x\text{H}_2\text{O}$ and $\text{H}_3\text{PO}_4\text{W}_{12} \cdot x\text{H}_2\text{O}$ were selected as the precursors to synthesise crystalline porous metal oxides using the solid-liquid method and mesoporous silicas of SBA-15 and KIT-6 were used as the templates. The products of porous metal oxides were characterised by using HRTEM, XRD, EDX, and SAED.

3.2.1 Co₃O₄

Co₃O₄ is an efficient catalyst for oxidation of H₂, CO, NO and methane.^{13,127-129} Porous single-crystals of Co₃O₄ templated by SBA-15 and KIT-6 have been synthesised by using the evaporation method,^{122,123,130} and the formation and growth mechanism of Co₃O₄ with and without mesoporous silica were investigated by Dickinson et al..¹²⁴

From Table 1, Co(NO₃)₂·6H₂O used as the precursor has a low melting point (55 °C) and a higher decomposition temperature (>74 °C). Therefore the solid-liquid method can be applied to synthesise crystalline porous Co₃O₄. Figure 3-3(a,c) show TEM images of porous Co₃O₄ templated by SBA-15 and KIT-6 respectively, indicating that porous Co₃O₄, in both templates, were synthesised successfully by using the solid-liquid method. The porous Co₃O₄ particle in Figure 3-3(a) has the inverse structure of SBA-15, viewed down the [110] zone axis of the SBA-15 like mesostructure, and has the inverse structure of KIT-6 in Figure 3-3(c), viewed down the [111] zone axis of the KIT-6 like mesostructure.

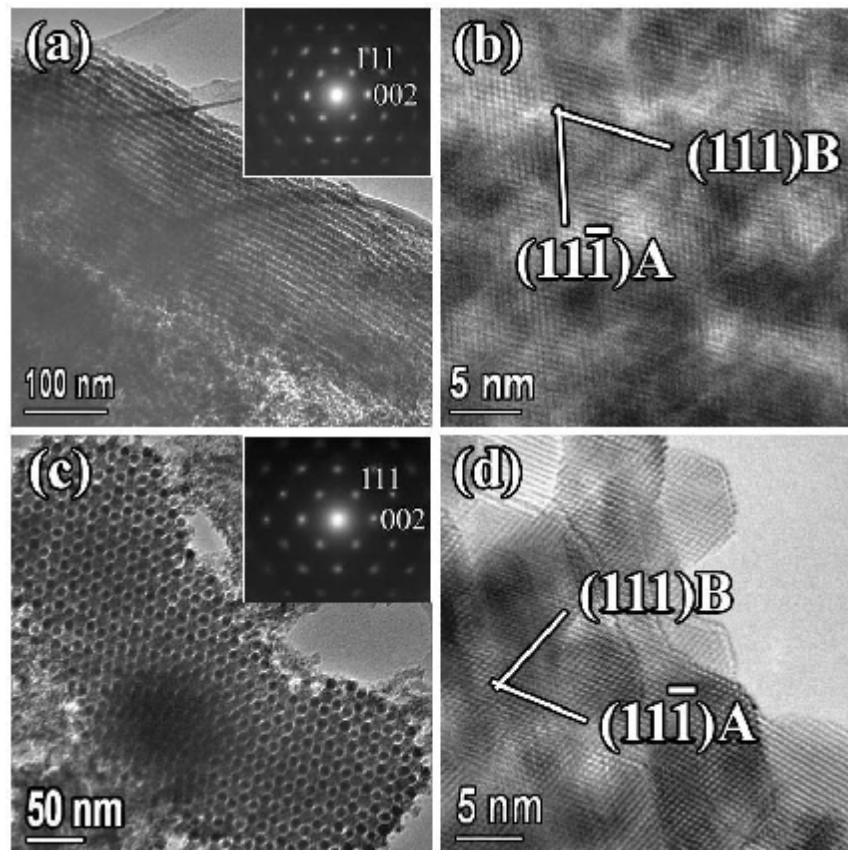


Figure 3-3. TEM and HRTEM images of porous Co₃O₄ crystals templated by (a,b) SBA-15 and (c,d) KIT-6, respectively. The SAED patterns and HRTEM images are indexed to the cubic Co₃O₄ structure.

The corresponding SAED patterns (insets of Figure 3-3a,c) indicate that these metal oxide particles are both single crystals, and are indexed to the Co_3O_4 structure, space group $Fd\bar{3}m$ with $a = 0.8085$ nm. HRTEM images of the porous Co_3O_4 particles templated by SBA-15 in Figure 3-3(b) and KIT-6 in Figure 3-3(d) further confirmed that these porous particles are single crystals, and both monocrystalline particles shown in HRTEM images are viewed down the $[\bar{1}10]$ zone axis of the Co_3O_4 structure.

The EDX spectrum (Figure 3-4) shows only Co and O elements, which is coming from Co_3O_4 . No silicon was detected, indicating that the silica template was removed completely.

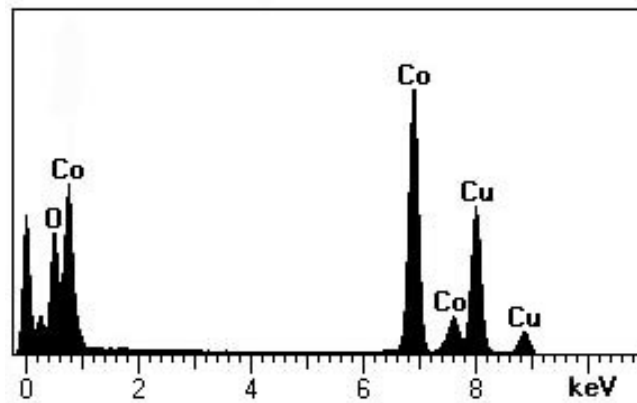


Figure 3-4. EDX graph of porous Co_3O_4 templated by SBA-15.

The XRD pattern, in Figure 3-5, is indexed to the Co_3O_4 structure (space group $Fd\bar{3}m$), confirming that the specimen is pure Co_3O_4 crystals.

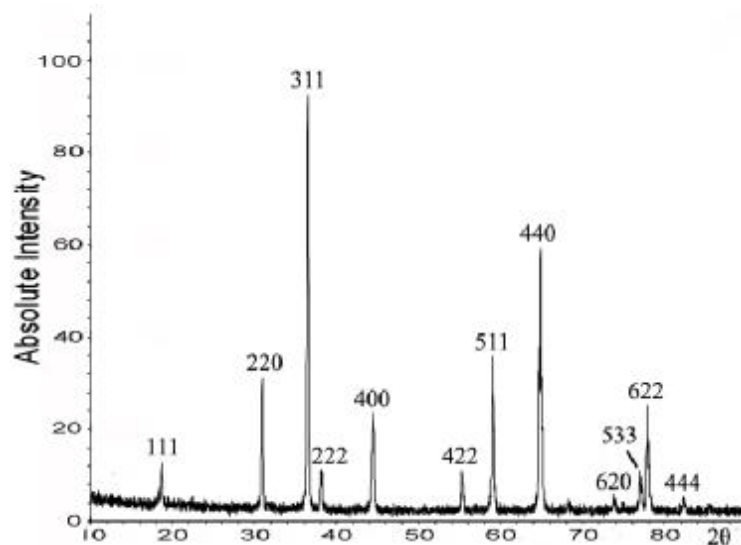


Figure 3-5. XRD pattern of porous Co_3O_4 templated by SBA-15.

3.2.2 Cr₂O₃

Cr₂O₃ plays an important role in magnetics and catalysis such as polymerisation of caprolactam and dodecalactam, hydrogenation of aliphatic carboxylic acids and oxidative dehydrogenation of ethane with carbon dioxide.^{118,119} The first three dimensional porous single crystal, Cr₂O₃ templated by SBA-15, was synthesised by using the surface modification method in 2003.¹²⁰ This was followed by KIT-6 templated Cr₂O₃ being produced by using the dual-solvent method.¹²¹ Recently, porous Cr₂O₃ templated by SBA-15 and KIT-6 were also prepared using the evaporation method by Tian et al.¹²² and Dickinson et al.,¹²⁴ respectively.

The melting point (66 °C) of Cr(NO₃)₃·9H₂O is lower than its decomposition temperature (>100 °C). So it was selected as the Cr-precursor and the solid-liquid method was used to produce crystalline porous Cr₂O₃. Figure 3-6(a) and (c) are TEM images of porous Cr₂O₃ templated by SBA-15 and KIT-6, viewed down the [110] and [111] zone axes of the mesostructures, respectively. The SAED patterns (insets of Figure 3-6a,c) are both a regular array of spots, indicating that these porous crystals are all single crystals, and are indexed to the Cr₂O₃ structure (space group $R\bar{3}c$, $a = 0.4958$ nm and $c = 1.3594$ nm). HRTEM images (Figure 3-6b,d) further confirm the monocrystalline properties. As demonstrated in the KIT-6 templated Cr₂O₃ produced using the dual-solvent method,¹²¹ some observed principal crystal orientations of Cr₂O₃ are parallel to the principal orientations of the mesopore network. However, this phenomenon was not observed in either the KIT-6 templated Cr₂O₃ crystals in the present project or other porous metal oxides. Therefore the crystal orientation of porous metal oxides synthesised using the solid-liquid method¹⁹⁸ has no relation with the orientation of the mesopore network.

Comparing the image contrast patterns of the KIT-6 templated Co₃O₄ and Cr₂O₃ (Figure 3-3c and 3-6c), it is found that both the bicontinuous pores in KIT-6 can be replicated by Co₃O₄, but only one of them is replicated by Cr₂O₃.¹²⁴ This difference can also be detected by the surface area measurements. However, the reason for this difference is still unknown, although Dickinson et al.,¹²⁴ speculated that the high temperature for crystal growth of Cr₂O₃ destroyed the inter-pore channels in KIT-6.

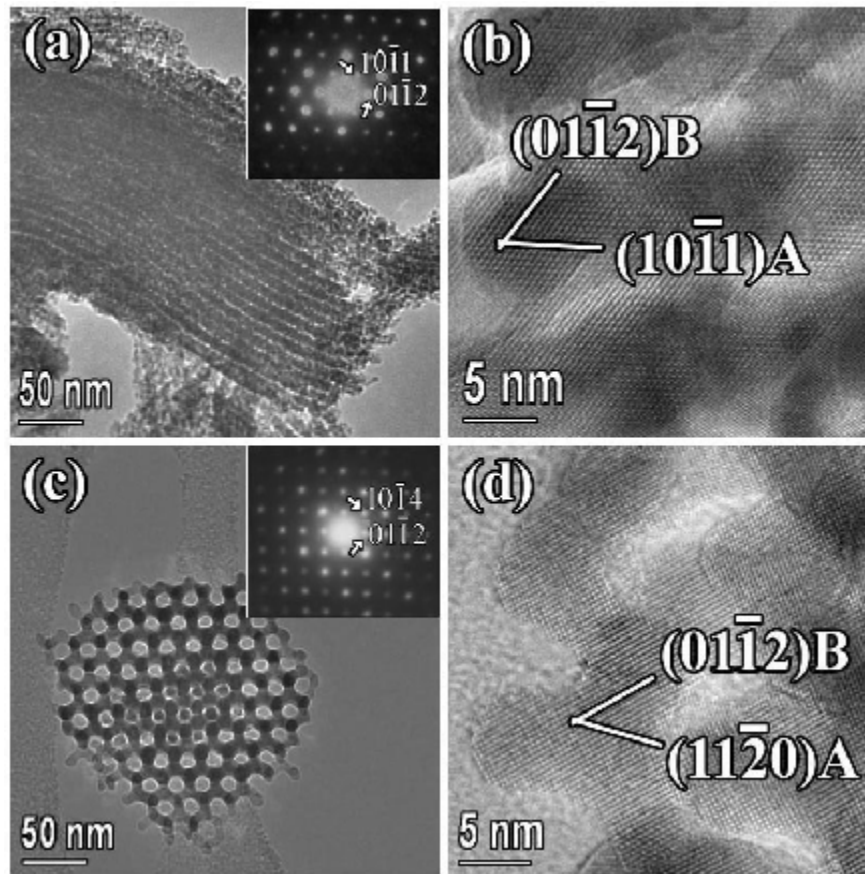


Figure 3-6. TEM and HRTEM images of porous Cr_2O_3 crystals templated by (a,b) SBA-15 and (c,d) KIT-6, respectively. The SAED patterns and HRTEM images are indexed to the Cr_2O_3 structure.

Only Cr and O elements were detected in the EDX spectrum (Figure 3-7) of the Cr_2O_3 products, indicating the complete removal of the silica template.

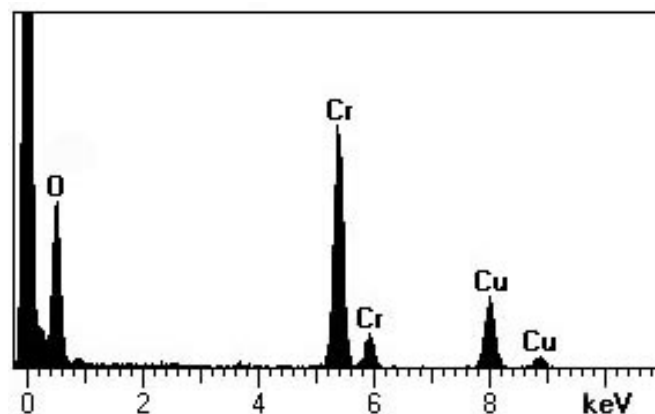


Figure 3-7. EDX spectrum of porous Cr_2O_3 templated by SBA-15.

The XRD pattern (Figure 3-8) only shows the characteristic diffraction peaks of Cr_2O_3 crystals (space group $R\bar{3}c$), indicating that no impurity was formed, and the observed XRD reflections are quite broad, indicating the characteristic nanoscale units in the specimens.

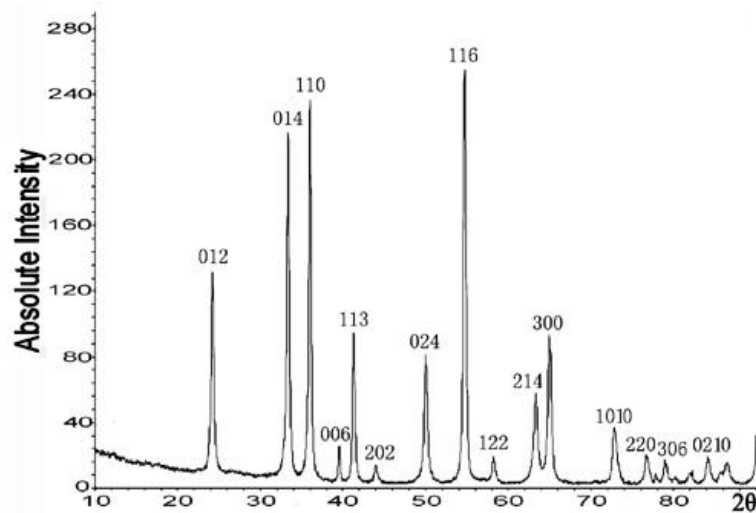


Figure 3-8. XRD pattern of porous Cr_2O_3 templated by SBA-15.

3.2.3 NiO

NiO has a good electrochemical capacitance and can be potentially applied in electrochemical devices.¹³²⁻¹³⁴ Porous NiO templated by SBA-15 was synthesised using the evaporation method by Tian et al.,¹²² and its electrochemical capacitance was studied by Wang et al.¹³² recently. The porous NiO templated by SBA-15 and KIT-6 were also synthesised successfully by using the solid-liquid method for this project, based on the knowledge that the melting point (56.7 °C) of the precursor of $\text{Ni}(\text{NO}_3)_2 \cdot 6\text{H}_2\text{O}$ is much lower than its decomposition temperature (>110 °C). At a temperature higher than 57 °C, the liquid $\text{Ni}(\text{NO}_3)_2 \cdot 6\text{H}_2\text{O}$ can migrate into the silica pores, and decompose inside the pores at a higher temperature (>110 °C).

Figure 3-9 (a) and (c) show the TEM images of porous NiO templated by SBA-15 and KIT-6, and the structure of porous NiO in Figure 3-9(a) and (c) are viewed down the [110] and [531] directions of SBA-15 like mesostructure, respectively. Some bulk particles can be also observed around the porous particles by TEM (Figure 3-9c). These porous NiO templated by SBA-15 and KIT-6 are both single crystals, according to SAED patterns (insets of Figure 3-9a,c) and HRTEM images (Figure 3-9b,d), which can be indexed to NiO structure (space group $Fm\bar{3}m$, $a = 0.4176$ nm).

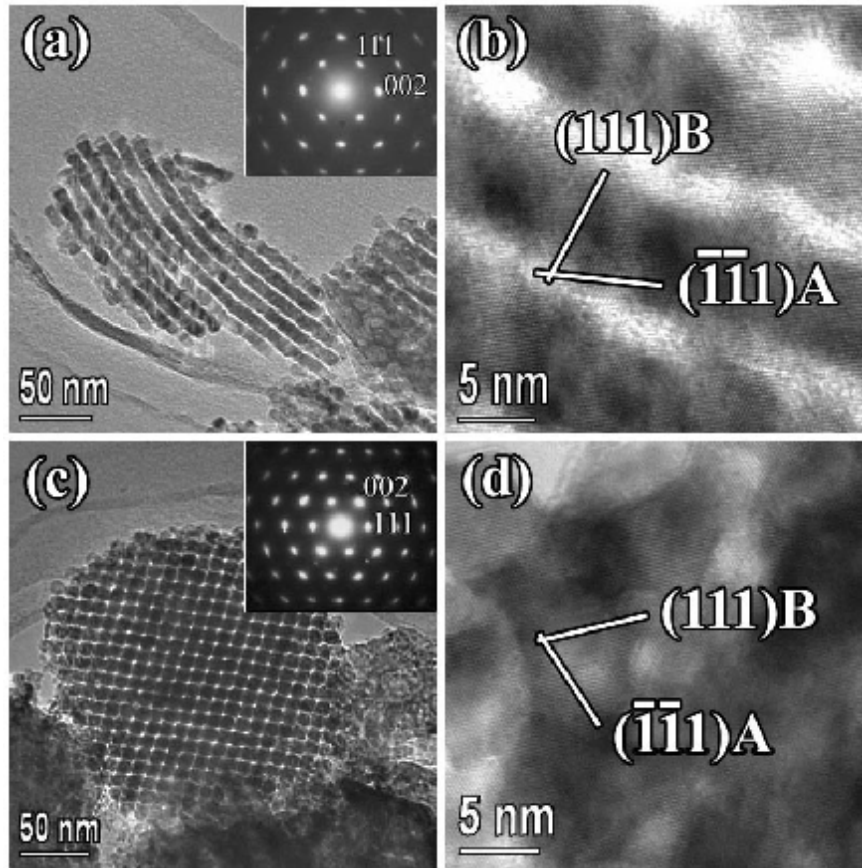


Figure 3-9. TEM and HRTEM images of porous NiO crystals templated by (a,b) SBA-15 and (c,d) KIT-6, respectively. The SAED patterns and HRTEM images are indexed to the NiO structure.

The EDX spectrum (Figure 3-10) shows three element peaks of Ni, O and Si. However, the Si element peak is so weak in comparison with Ni and O peaks, indicating that the silica template was almost removed.

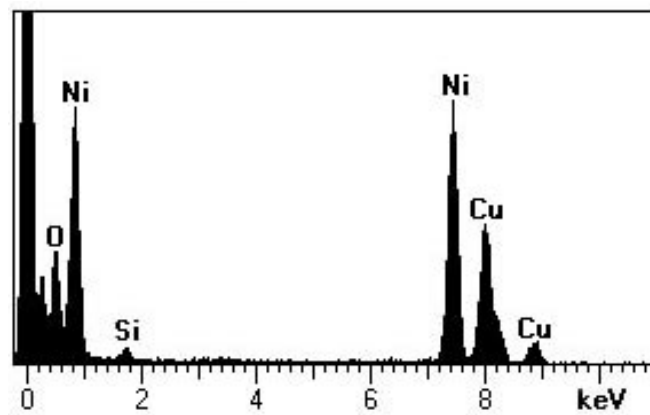


Figure 3-10. EDX graph of porous NiO templated by SBA-15

The characteristic peaks in the XRD pattern (Figure 3-11) are indexed to the NiO crystal, confirming the purity of NiO crystals.

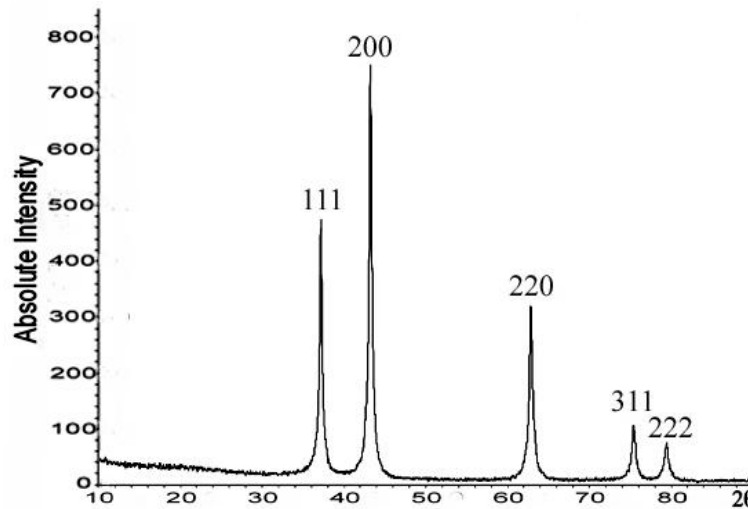


Figure 3-11. XRD pattern of porous NiO templated by SBA-15.

3.2.4 CeO₂

CeO₂ is a good catalyst for oxidation of acrylic acid and CO, and methanol decomposition.¹³⁵⁻¹³⁸ Porous CeO₂ templated by SBA-15 was also one of the porous metal oxides synthesised by Tian et al. using the evaporation method.¹²² KIT-6 templated CeO₂ was prepared using the same method by Shen et al.¹³⁵ and Rossinyol et al.¹³⁹ later. The monocrystalline porous CeO₂ specimens templated by SBA-15 and KIT-6 were also synthesised using the solid-liquid method in the present work because Ce(NO₃)₃·6H₂O crystal, whose melting point is 96 °C and decomposition temperature is 200 °C, is a suitable precursor in this method.

Figure 3-12 (a) and (c) shows the TEM images of SBA-15 and KIT-6 templated CeO₂ crystals, when viewed down the [110] and [531] zone axes of the mesostructures, respectively. Similar to porous NiO particles synthesised using the solid-liquid method, some non-porous particles were also observed by TEM. The yields of porous NiO and CeO₂ are not high according to the TEM observation. The monocrystalline properties of these porous CeO₂ particles (space group $Fm\bar{3}m$, $a = 0.5412$ nm) are confirmed by SAED patterns (insets of Figure 3-12a,c) and HRTEM images (Figure 3-12c,d).

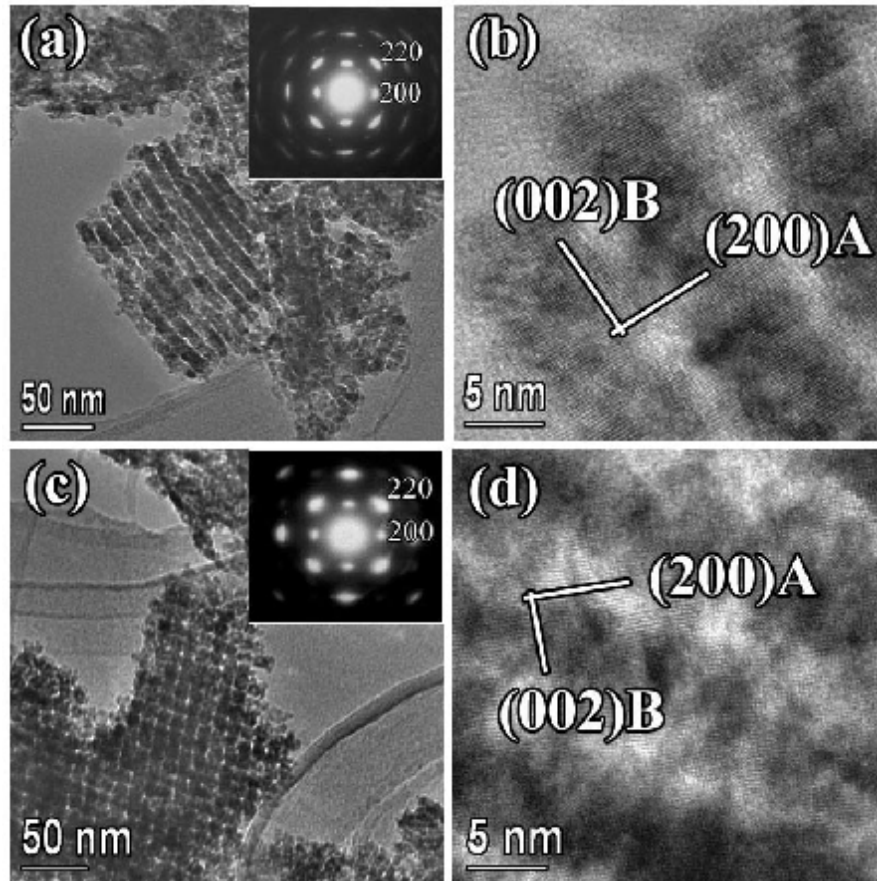


Figure 3-12. TEM and HRTEM images of porous CeO_2 crystals templated by (a,b) SBA-15 and (c,d) KIT-6, respectively. The SAED patterns and HRTEM images are indexed to the cubic CeO_2 structure.

Figure 3-13 shows the EDX spectrum of porous CeO_2 templated by SBA-15. Similar to porous NiO specimens, very little Si can be detected by EDX, indicating that the silica template was almost removed. Figure 3-14 is the XRD pattern of porous sample and the characteristic peaks are indexed to the CeO_2 crystal structure.

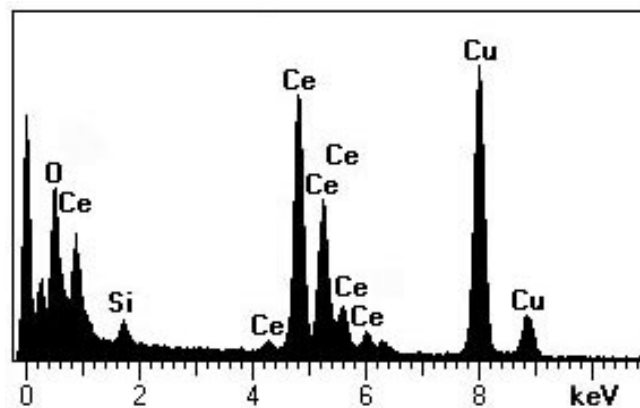


Figure 3-13. EDX graph of porous CeO_2 templated by SBA-15

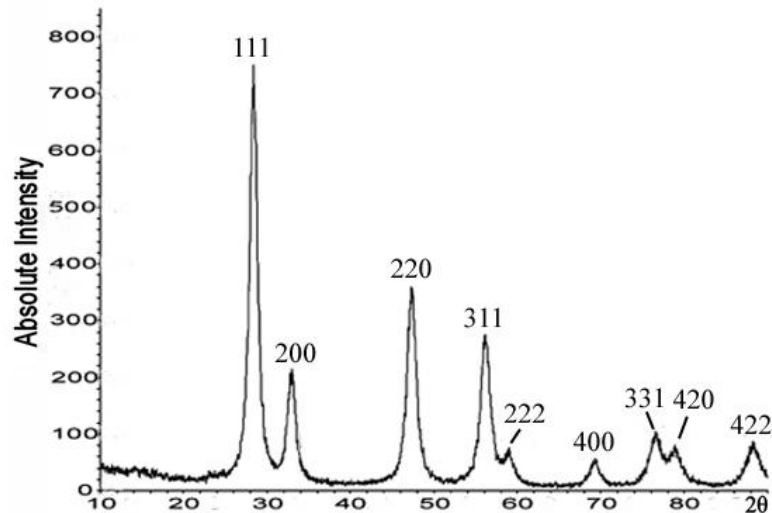


Figure 3-14. XRD pattern of porous CeO_2 templated by SBA-15.

3.2.5 In_2O_3

In_2O_3 is an important transparent conductive oxide, and has potential applications in solar cells, ultraviolet-visible (UV) lasers, detectors and gas sensors.¹⁴⁰⁻¹⁴³ Zhao's group first produced porous In_2O_3 using the one-step nanocasting method¹⁴⁴ and the evaporation method.¹²² Since hydrated $\text{In}(\text{NO}_3)_3$ melts at a low temperature (100 °C) before decomposition, porous In_2O_3 crystals can also be prepared using the solid-liquid method. Porous single crystals of In_2O_3 templated by SBA-15 and KIT-6 have been synthesised using this method and observed by TEM, respectively. The typical structures of replicas of SBA-15 and KIT-6 can be observed (Figure 3-15a,c). SAED patterns (insets of Figure 3-15a,c) and HRTEM images (Figure 3-15b,d) confirm the monocrystalline properties of cubic In_2O_3 crystals (space group $Ia\bar{3}$, $a = 1.0118$ nm).

Figure 3-16 and Figure 3-17 show EDX spectrum and XRD pattern of porous In_2O_3 templated by SBA-15, respectively. From the evidence, silica template was removed completely and no other materials were formed except In_2O_3 crystals. Although the observed XRD reflections of NiO , CeO_2 and In_2O_3 specimens are all quite broad, the yields of these porous particles are not high as indicated by the TEM observation. So the width of the characteristic peaks can not determine the crystallite size in these specimens.

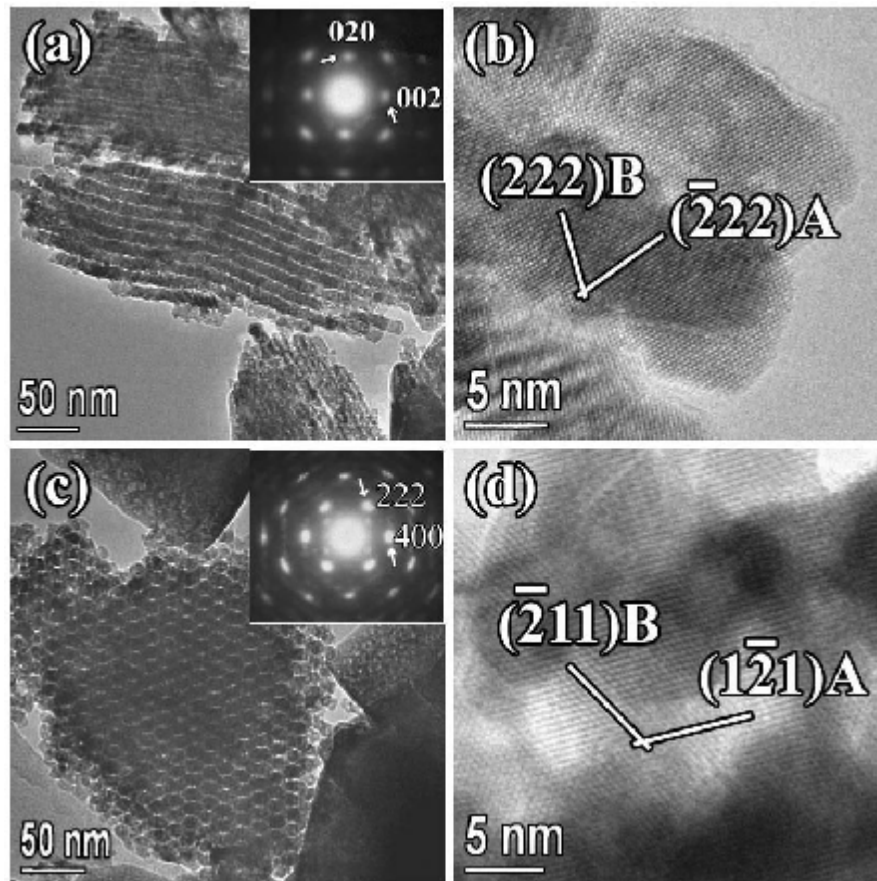


Figure 3-15. TEM and HRTEM images of porous In_2O_3 crystals templated by (a,b) SBA-15 and (c,d) KIT-6, respectively. The SAED patterns shown as the insets in (a) and (c), and HRTEM images in (b) and (d) are indexed to the cubic In_2O_3 structure.

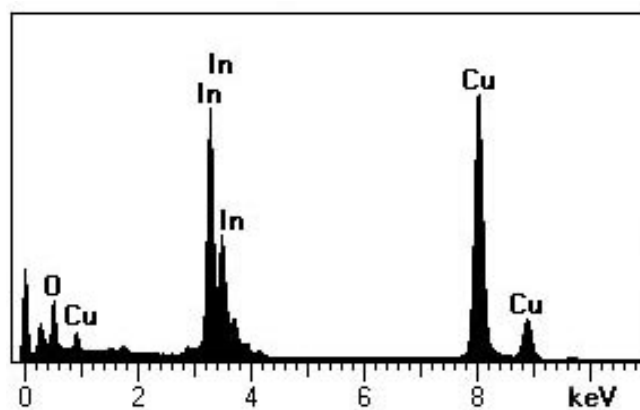


Figure 3-16. EDX graph of porous In_2O_3 templated by SBA-15

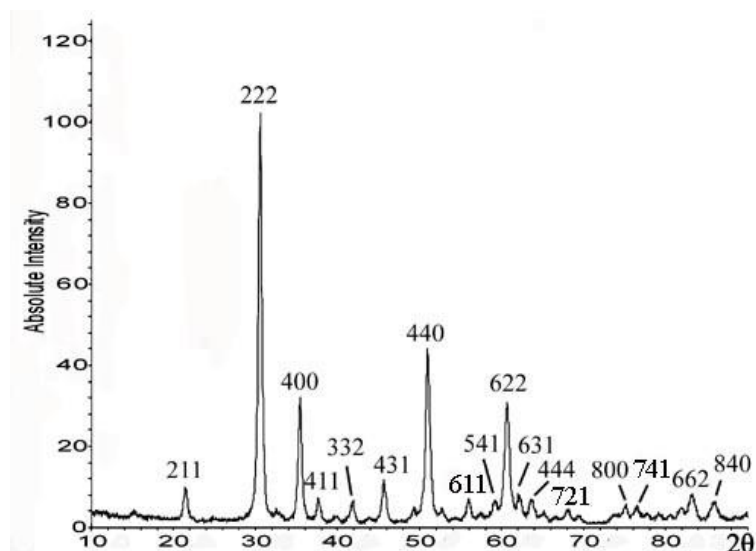


Figure 3-17. XRD pattern of porous In_2O_3 templated by SBA-15.

3.2.6 WO_3

WO_3 has a wide range of interesting catalytic, electrochromic and gas sensing properties.¹⁶⁰⁻¹⁶³ When SBA-15 was used as a template for producing porous crystals of WO_3 using the surface modification method by Zhu *et al.* in 2003.¹⁶⁴ Only WO_3 nanowires were observed from the product. The synthetic conditions were improved later and perfect 3D porous single-crystals of WO_3 were fabricated.¹⁶⁵ KIT-6 templated WO_3 was also prepared using the evaporation method by Rossinyol *et al.*¹³⁹

$\text{H}_3\text{PO}_4\text{W}_{12}\cdot x\text{H}_2\text{O}$ has a low melting point (107 °C) and decomposes completely to WO_3 at 600 °C. Therefore $\text{H}_3\text{PO}_4\text{W}_{12}\cdot x\text{H}_2\text{O}$ was used as the precursor in the solid-liquid method to synthesise SBA-15 and KIT-6 templated WO_3 . The typical structure of these porous particles was observed by TEM (Figure 3-18a,c), respectively. The common structure of WO_3 is tetragonal, space group $P4/nmm$, with $a = 0.5272$ nm $c = 0.3920$ nm, although the unit cell parameters are variable with different oxygen contents. Both SAED patterns (insets of Figure 3-18a,c) and HRTEM images (Figure 3-18b,d) confirm the monocrystalline properties of WO_3 (space group $P4/nmm$). However, the reproducibility of the synthesis of porous WO_3 using the solid-liquid method is not as good as other transition metal oxides.

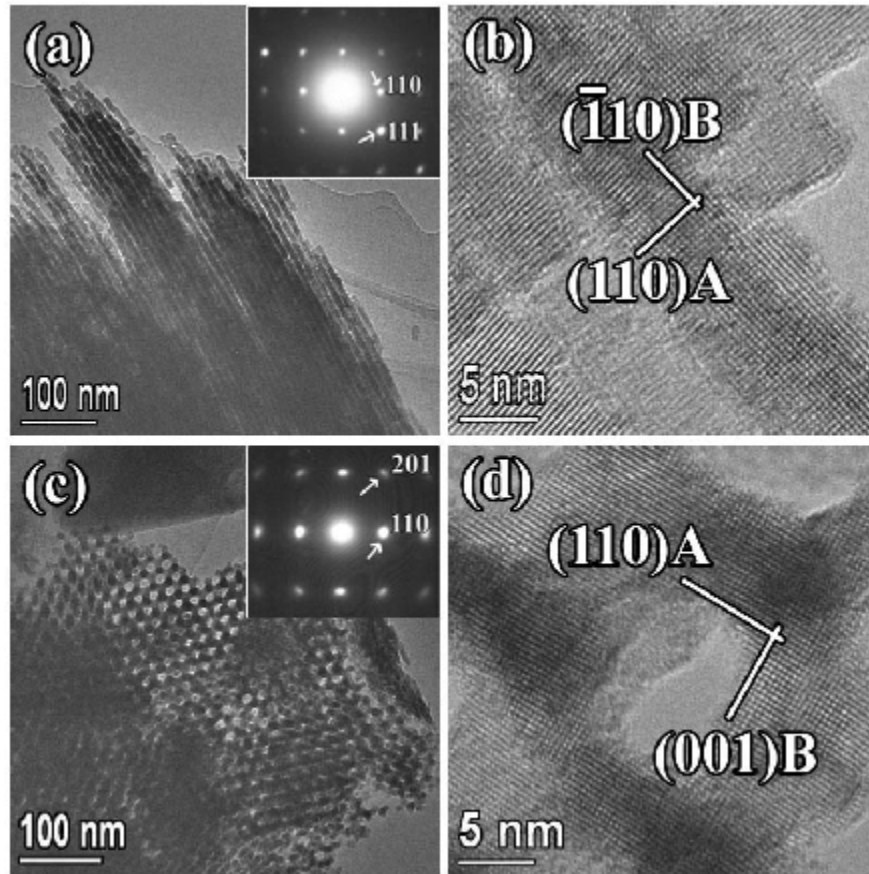


Figure 3-18. TEM and HRTEM images of porous WO_3 crystals templated by (a,b) SBA-15 and (c,d) KIT-6, respectively. The SAED patterns and HRTEM images are indexed to the tetragonal WO_3 structure.

The EDX spectrum (Figure 3-19) shows only W and O element peaks. However, the position of W ($M\alpha$, 1.774 keV) and Si ($K\alpha$, 1.739 keV) peaks in EDX graph is too close to be identified. So the complete removal of the silica template can not be proved using EDX.

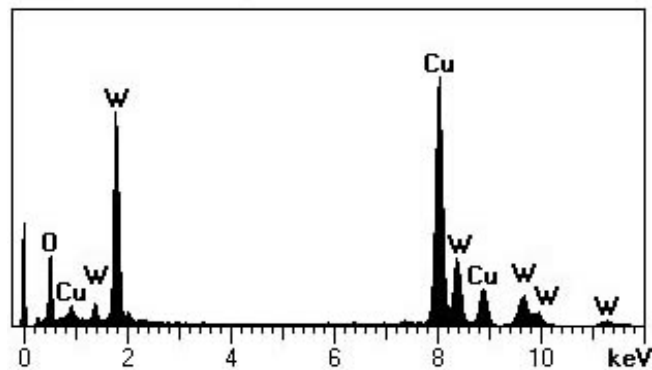


Figure 3-19. EDX graph of porous WO_3 templated by SBA-15

Figure 3-20 is the XRD pattern, which can be indexed to tetragonal WO_3 crystals (space group $P4/nmm$), and the wide amorphous silica peak is not detected, indicating that the silica template was almost removed.

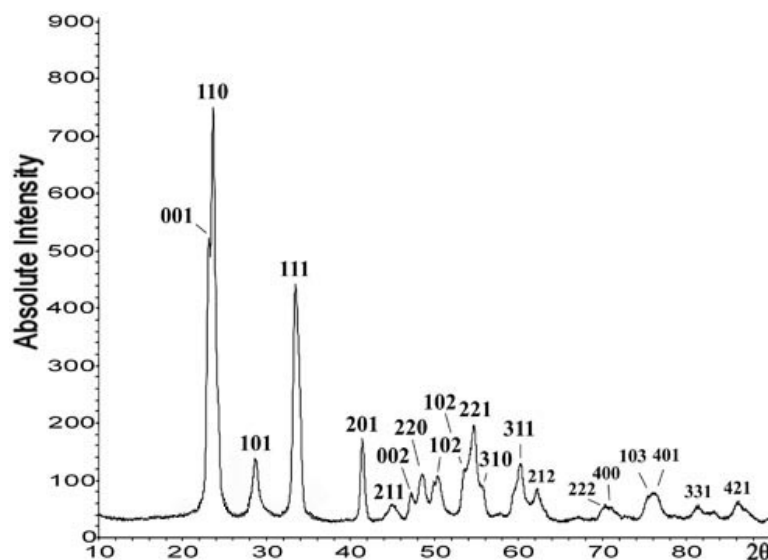


Figure 3-20. XRD pattern of porous WO_3 templated by SBA-15.

Consequently, according to the characterisation of specimens by using HRTEM, SAED, EDX and XRD, we can synthesise porous single crystals of Co_3O_4 , Cr_2O_3 , NiO , CeO_2 , In_2O_3 and WO_3 templated by SBA-15 and KIT-6 using a new simple approach so-called solid-liquid method, although the yields of some products are not high.

3.3 Comparison between the evaporation and solid-liquid methods

The assumption of the evaporation method is that the metal nitrate in ethanol is expected to migrate into the silica pores by a capillary action during the evaporation of ethanol. This is not completely proved by experiments, since nitrate may deposit on the outer surface of the template particles during the evaporation process and moves into the pores after it melts during the thermal treatment. The solid-liquid method was developed based on this consideration. Many metal nitrates have low melting points, which are higher than their decomposition temperatures. Therefore a solid metal nitrate is expected to migrate into the silica pores after melting when the temperature is increased above the melting point of the precursor. Then the liquid

precursor decomposes to generate the corresponding metal oxide inside the pores of silica when the temperature is increased above the decomposition temperature of the precursor. So if the aforementioned assumption of the evaporation method is correct, any nitrate solution can be used as the precursor and the migration process occurs during the evaporation process. However, in the solid-liquid method, the precursor must have a melting point lower than its decomposition temperature and the migration process occurred during calcination process. To elucidate more detailed processes of these two methods, some parallel experiments were designed as discussed below.

3.3.1 Porous Cr₂O₃ synthesised using the two methods

To investigate the mechanism of the formation and growth of metal oxide inside the mesopores of silica template, a set of parallel experiments for producing porous Cr₂O₃ using the evaporation and solid-liquid methods were carried out.¹⁹⁸ Cr(NO₃)₃·9H₂O and SBA-15 were selected as the precursor and template. These mixtures of Cr(NO₃)₃·9H₂O and SBA-15 were calcined at 70 °C, which is slightly higher than the melting point of Cr(NO₃)₃·9H₂O (66 °C), 110 °C, which is slightly higher than the decomposition temperature of Cr(NO₃)₃·9H₂O (100 °C) and 350 °C, a temperature close to the lowest temperature for crystal growth of Cr₂O₃ in SBA-15. Specimens prepared at different thermal stages were examined by XRD (Figure 3-21) and TEM (Figure 3-22).

Figure 3-21 shows the XRD patterns of Cr(NO₃)₃·9H₂O/SBA-15 mixture prepared by using the solid-liquid method. The XRD patterns of Cr(NO₃)₃·9H₂O/SBA-15 (not shown) prepared by using evaporation method is similar. The XRD pattern of the mixture before calcination in Figure 3-21(a) is indexed to the unit cell of Cr(NO₃)₃·9H₂O. When the Cr(NO₃)₃·9H₂O/SBA-15 was calcined at 70 °C and 110 °C for 5 h respectively, no characteristic peaks (Figure 3-21b,c) can be found in the XRD patterns, implying that the precursor decomposed into an amorphous phase or highly dispersed nanoparticles. When the mixture was calcined at 350 °C for 5 h, the characteristic peaks of the XRD pattern (Figure 3-21d) were indexed to the Cr₂O₃ structure (space group $R\bar{3}c$), indicating that the porous Cr₂O₃ was formed in SBA-15 at that thermal stage.

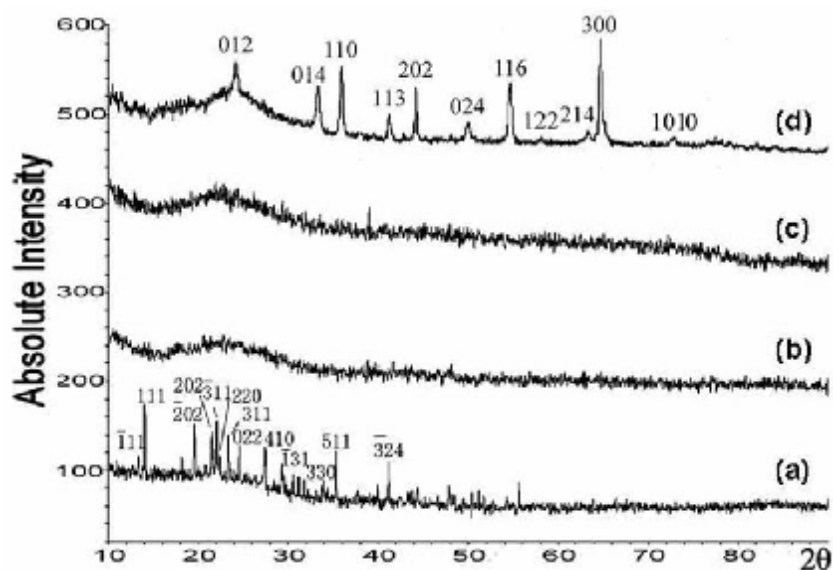


Figure 3-21. XRD patterns of $\text{Cr}(\text{NO}_3)_3 \cdot 9\text{H}_2\text{O}$ loaded SBA-15 specimens treated at different thermal stages: (a) before heating, (b) at $70\text{ }^\circ\text{C}$ for 5 h, (c) at $110\text{ }^\circ\text{C}$ for 5 h, and (d) at $350\text{ }^\circ\text{C}$ for 5 h, respectively. Pattern (a) is indexed to the structure of $\text{Cr}(\text{NO}_3)_3 \cdot 9\text{H}_2\text{O}$ and pattern (d) is indexed to the Cr_2O_3 structure.

Before calcination, two separated phases can be observed from the specimen prepared using the solid-liquid method, SBA-15 and $\text{Cr}(\text{NO}_3)_3 \cdot 9\text{H}_2\text{O}$ (Figure 3-22a). Some of the nitrate particles are indicated by the arrows. On the other hand, only SBA-15 particles can be identified without large nitrate crystallites on their surface in the specimen prepared using the evaporation method before calcination (Figure 3-22b). It is probably because $\text{Cr}(\text{NO}_3)_3 \cdot 9\text{H}_2\text{O}$ was dissolved in solvent (ethanol) and dispersed well on the outside surface of the SBA-15 particles, or moved into the pores completely.

Since the nitrate particles were very small and the compound, containing water, was beam sensitive, it was difficult to record HRTEM images from nitrate loaded specimens before the calcinations. The EDX spectrum (Figure 3-23) of nitrate loaded specimen without notable metal-containing particles as seen in Figure 3-22(b) prepared by the evaporation method also shows Cr peaks as well as O and Si peaks. After $\text{Cr}(\text{NO}_3)_3 \cdot 9\text{H}_2\text{O}/\text{SBA-15}$ was heated at $70\text{ }^\circ\text{C}$ for 5 h, only SBA-15-like particles could be observed from both samples prepared in these two methods (Figure 3-22c,d). Heating at $110\text{ }^\circ\text{C}$ for 5 h did not make any difference in the TEM appearance, and the EDX spectrums of these specimens still show the Cr, O and Si element peaks. After $\text{Cr}(\text{NO}_3)_3 \cdot 9\text{H}_2\text{O}/\text{SBA-15}$ prepared using both methods were

heated at 350 °C for 5 h, the oxides partially filled the pores of SBA-15, forming individual porous Cr_2O_3 particles, which were observed in the TEM images (Figure 3-22e). Some large particles were also observed around SBA-15, indicated by arrows in Figure 3-22(f). The final products after removing the template fabricated by the two methods are similar.

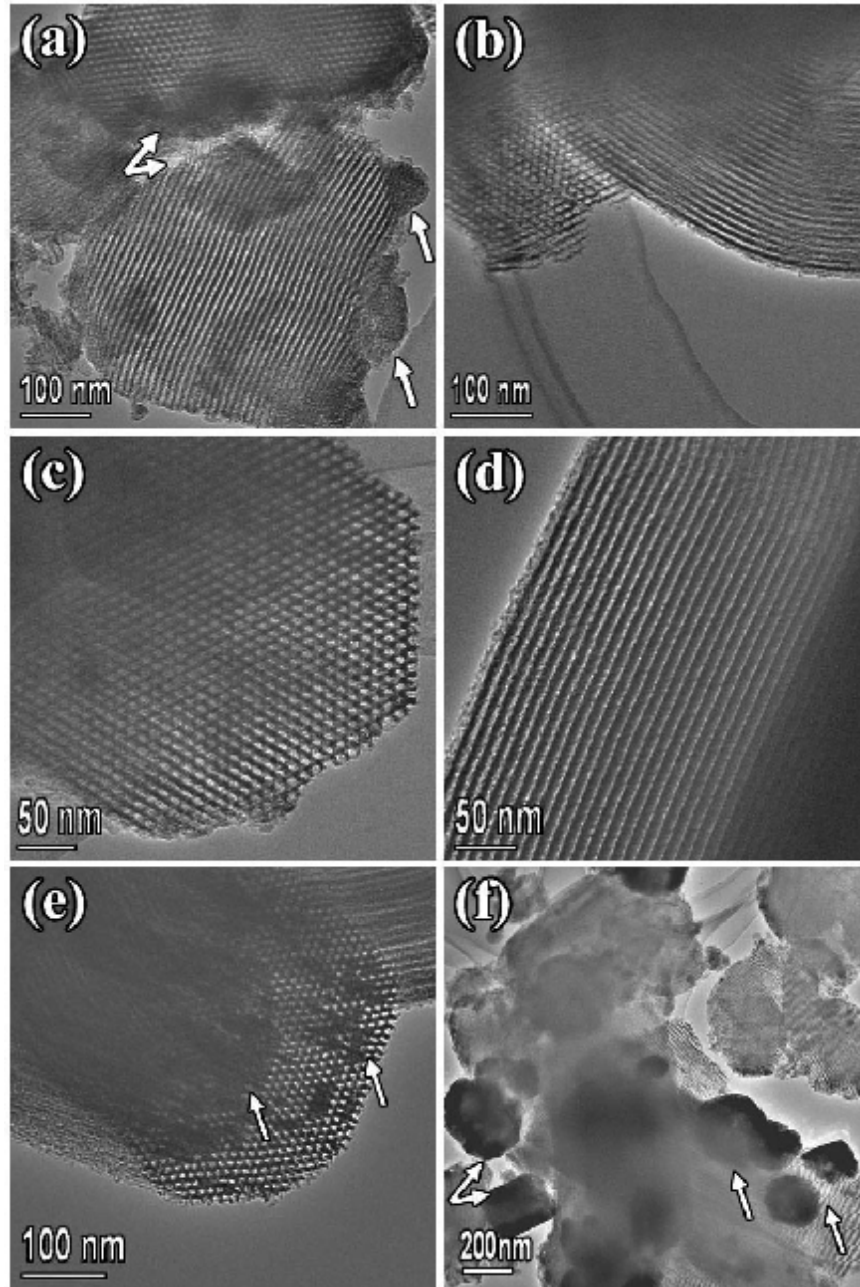


Figure 3-22. TEM images of decomposition process of $\text{Cr}(\text{NO}_3)_3 \cdot 9\text{H}_2\text{O}$ towards Cr_2O_3 within SBA-15 using the solid-liquid method (a, c, e) and the evaporation method (b, d, f). (a,b) $\text{Cr}(\text{NO}_3)_3 \cdot 9\text{H}_2\text{O}/\text{SBA-15}$ before calcination. Specimens after heating treatment at 70 °C for 5 h (c,d) and at 350 °C for 5 h (e,f).

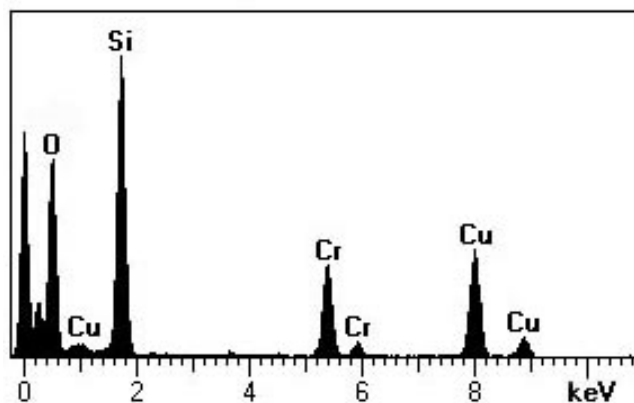


Figure 3-23. EDX graph of SBA-15 containing $\text{Cr}(\text{NO}_3)_3 \cdot 9\text{H}_2\text{O}$ crystals prepared using evaporation method.

Consequently the porous Cr_2O_3 can be synthesised using both the evaporation and solid-liquid methods, and the only difference between these two methods is that the precursor has a higher dispersion before calcination in the evaporation method. However, the nitrate migrating into the template pores has not been detected.

3.3.2 $\text{Pb}(\text{NO}_3)_2$ and $(\text{NH}_4)_2\text{Cr}_2\text{O}_7$ used as precursors

The limitation of the solid-liquid method is that the precursor must have melting point lower than its decomposition temperature. To further understand the difference between the solid-liquid and evaporation methods, $\text{Pb}(\text{NO}_3)_2$ and $(\text{NH}_4)_2\text{Cr}_2\text{O}_7$, which decomposes at about 210°C and 180°C without melting (Table 1), were selected as precursors for fabricating porous crystals of PbO and Cr_2O_3 in the SBA-15 template.¹⁹⁸

PbO

PbO crystals templated by SBA-15 was synthesised by using $\text{Pb}(\text{NO}_3)_2$ as the precursor. Both methods were used in the experiments. Figure 3-24(a) was the TEM image of PbO crystals synthesised using the solid-liquid method and only bulk particles can be observed. The PbO synthesised using evaporation method was also non-porous particles in TEM observation (Figure 3-24b).

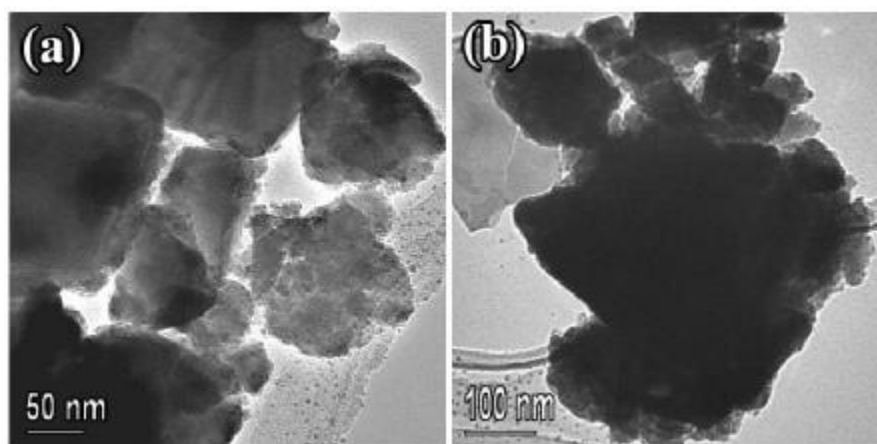


Figure 3-24. TEM image of PbO produced using $\text{Pb}(\text{NO}_3)_2$ as the precursor and SBA-15 as the template, prepared by using (a) the solid-liquid method and (b) the evaporation method.

$(\text{NH}_4)_2\text{Cr}_2\text{O}_7$

Crystalline porous Cr_2O_3 templated by SBA-15 and KIT-6 can be synthesised using $\text{Cr}(\text{NO}_3)_3 \cdot 9\text{H}_2\text{O}$ as the precursor in both the impregnation methods (Figure 3-22). TEM image (Figure 3-25a) shows the SBA-15 templated Cr_2O_3 crystals synthesised using $(\text{NH}_4)_2\text{Cr}_2\text{O}_7$ as the precursor, and only non-porous crystals were produced using either the evaporation method or the solid-liquid method. The large particles were confirmed as Cr_2O_3 crystals by using EDX and XRD (Figure 3-25b).

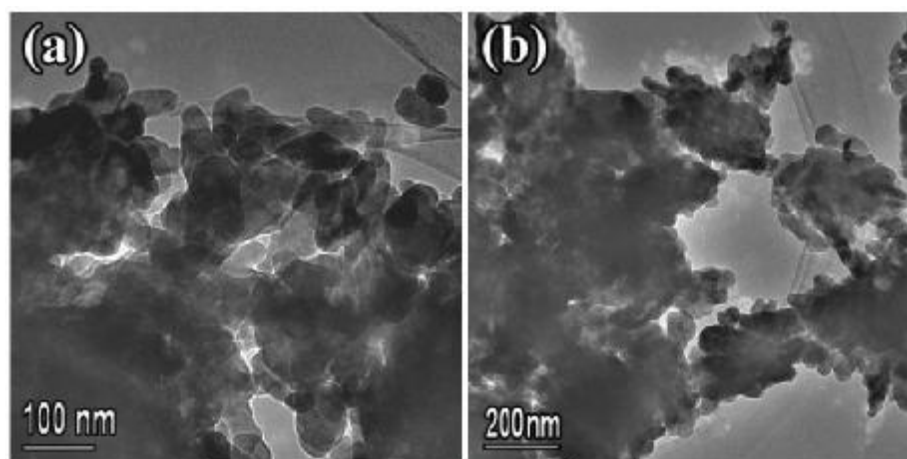


Figure 3-25. TEM image of Cr_2O_3 produced using $(\text{NH}_4)_2\text{Cr}_2\text{O}_7$ as the precursor and SBA-15 as the template, prepared by using (a) the solid-liquid method and (b) the evaporation method.

According to the previous report for the evaporation method, the precursor is dissolved in a solvent (ethanol) and can migrate into the silica pores when the solvent is evaporated. Both $\text{Pb}(\text{NO}_3)_2$ and $(\text{NH}_4)_2\text{Cr}_2\text{O}_7$ solutions are suitable precursors in the evaporation method, and are expected to migrate into the silica pores before calcination and decompose to generate porous metal oxides. However, only non-porous particles of PbO and Cr_2O_3 were formed after removing silica template, indicating that the precursors must decompose outside the silica pores. Consequently these precursors did not migrate into the silica pores during the evaporation process. The evaporation method only helps the precursor disperses well on the surface of silica. The precursors migrate into the silica pores when it melts and decompose in the thermal treatment.

Conclusion

We demonstrated a simple and solvent-free (therefore environmentally friendly) synthetic method for fabrication of porous single crystals of transition metal oxides. If a precursor has a low melting point, when it simply mixes with a silica template, it may melt before decomposition during thermal treatment and migrates into the template pores. Decomposition and crystal growth of oxides inside the mesopores will result in porous single crystals of oxides. In the present project, porous single-crystals of Co_3O_4 , Cr_2O_3 , NiO , CeO_2 , In_2O_3 and WO_3 templated by SBA-15 and KIT-6 have been synthesised successfully using the solid-liquid method. Additionally, $\text{Cr}(\text{NO}_3)_3 \cdot 9\text{H}_2\text{O}$ was selected as the precursor to synthesise porous Cr_2O_3 templated by SBA-15 using both the evaporation and solid-liquid methods. It has been found that the only difference between two methods is the dispersion of precursor before calcination. $\text{Pb}(\text{NO}_3)_2$ and $(\text{NH}_4)_2\text{Cr}_2\text{O}_7$ was also selected as precursors to synthesise porous oxides templated by SBA-15. However, only non-porous PbO and Cr_2O_3 particles were observed by TEM in both methods, indicating that the precursor can not migrate into the pores of silica during the evaporation of solvent. In both the evaporation and solid-liquid methods, a suitable precursor melts first before decomposition and then migrates into the pores of silica by capillary action. Therefore the selection of precursor is the key step for preparation of porous metal oxides.

4. Novel porous metal oxides templated by SBA-15 and KIT-6

In previous reports, many porous transition metal oxides of Co_3O_4 ,¹²²⁻¹²⁴ Cr_2O_3 ,^{120,121} NiO ,¹³² CeO_2 ,^{135,139} In_2O_3 ,¹⁴⁴ WO_3 ,^{164,165} Fe_2O_3 (Fe_3O_4),^{149,150} MnO_2 (Mn_2O_3 and Mn_3O_4)¹⁵⁶⁻¹⁵⁹ and V_2O_5 ¹⁶⁶ templated by SBA-15 and KIT-6 have been synthesised using various methods such as evaporation method. A new simple and solvent-free approach, the so-called solid-liquid method, has been designed to synthesise porous metal oxides. In the previous chapter, the porous single crystals of Co_3O_4 , Cr_2O_3 , NiO , CeO_2 , In_2O_3 and WO_3 templated by SBA-15 and KIT-6 were prepared by using the solid-liquid method.¹⁹⁸ The key point of the solid-liquid method is the selection of a suitable precursor whose melting point is lower than its decomposition temperature. This property is also required in the evaporation method as discussed in the previous chapter.

The metal nitrates listed in Table 4-1 were selected in the present project as metal-containing precursors to synthesise novel porous metal oxides which are not reported previously.

Table 4-1. Melting point (MP) and decomposition temperature (DT) of the nitrate precursors for porous transition metal oxides.

Precursor	MP(°C)	DT(°C)	Oxide
$\text{Ba}(\text{NO}_3)_2$	592	>592	BaO
$\text{Cd}(\text{NO}_3)_2 \cdot 4\text{H}_2\text{O}$	59.4	>360	CdO
$\text{Cu}(\text{NO}_3)_2 \cdot 3\text{H}_2\text{O}$	114.5	>170	CuO
$\text{Ga}(\text{NO}_3)_3 \cdot x\text{H}_2\text{O}$	110	200	Ga_2O_3
$\text{Gd}(\text{NO}_3)_3 \cdot 6\text{H}_2\text{O}$	91		Gd_2O_3
$\text{La}(\text{NO}_3)_3 \cdot 6\text{H}_2\text{O}$	40	>126	La_2O_3
$\text{Mg}(\text{NO}_3)_2 \cdot 6\text{H}_2\text{O}$	95	>129	MgO
$\text{Sr}(\text{NO}_3)_2$	570	645	SrO
$\text{Ti}(\text{NO}_3)_4$		240~270	TiO_2
$\text{Zn}(\text{NO}_3)_2 \cdot 6\text{H}_2\text{O}$	36.4	>131	ZnO
$\text{Zr}(\text{NO}_3)_4 \cdot 5\text{H}_2\text{O}$	100		ZrO_2

Mesoporous silica SBA-15 and KIT-6 were used as hard templates in the experiments. The products were characterised by using XRD, HRTEM, SAED, EDX, N_2 adsorption/desorption. The most successful synthesis is for porous TiO_2 . Therefore,

the chapter will focus on TiO₂. Syntheses and characterisations of other oxides are also briefly mentioned.

4.1 TiO₂

TiO₂ crystals occur in nature as the well-known brookite, anatase and rutile structures. Anatase TiO₂ has a strong photocatalytic activity and is used extensively as a photocatalyst, for example, for decomposition of methylene blue (MB) in an aqueous solution.²¹²⁻²¹⁴ Rutile TiO₂ is a thermodynamically stable phase and used as electrodes by addition of lithium and carbon,²¹⁵⁻²¹⁷ catalysts^{218,219} and Li storage materials.^{27,220} Both anatase and brookite usually convert to rutile when temperature is increased to above 900 °C. Therefore porous anatase or rutile TiO₂ is expected to exhibit great properties due to its large surface area and ordered pore networks. Up to date, mesoporous TiO₂ thin films²²¹ and particles¹¹³ as well as mesoporous TiO₂-silica composites²²² have been previously synthesised by soft templating (e.g. using P123). However, these porous TiO₂ materials are polycrystalline or silica containing TiO₂ nanoparticle domains. Herein is presented our successful synthesis of monocrystalline mesoporous rutile TiO₂ templated by SBA-15 and KIT-6, using freshly prepared titanium nitrate solution as a precursor.^{199,200} The porous anatase nanocrystal-silica composites were also fabricated using SBA-15 as a template.²⁰⁰ Some physico-chemical properties of these new porous products, e.g. proton conductivity, Li ion insertion and photoactivity, were also investigated to demonstrate their application potential.

4.1.1 TiO₂ templated by KIT-6

Porous TiO₂ can be fabricated by introducing a titanium precursor, Ti(NO₃)₄ solution, into the mesopores of KIT-6, allowing it to decompose and crystallize into TiO₂ in a thermal treatment. Calcination temperature was selected as 100 °C, 200 °C, 300 °C, 400 °C and 600 °C, respectively. The products were labelled TiO₂(KIT-6)-T, where T is the calcination temperature. Another experiment was also carried out to use a dilute HNO₃ solution instead of 68% HNO₃ solution, which can affect the crystal phase of TiO₂ specimens as well. The product synthesised at 200 °C was labelled TiO₂(d-HNO₃)-200.

TGA investigation of a titanium-loaded KIT-6 specimen was performed with an air flow rate of 35 ml/min and a heating rate of 5 °C/min, showing a single peak of weight loss, from ca. 36 to ~150 °C (Figure 4-1). In this region, water evaporation, decomposition of HNO₃, titanium nitrate, titanium oxide hydroxide are expected. The corresponding DTA curve shows one exothermic peak at 132 °C. There was no further weight loss when the temperature was increased from 150 °C up to 800 °C, implying a final crystalline product of pure TiO₂ and a possible low crystallisation temperature (< 150 °C) of TiO₂.

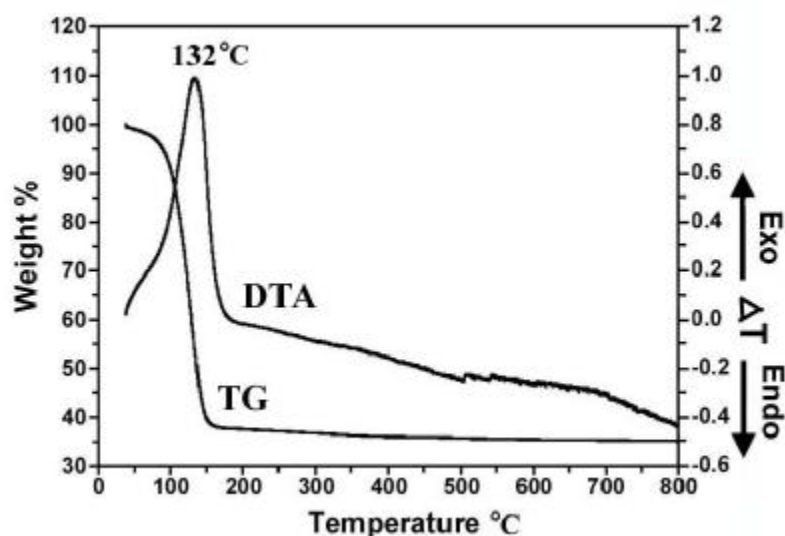


Figure 4-1. TG/DTA curves of titanium-loaded KIT-6 specimen.

The crystal phase and mesostructure of porous TiO₂ depended highly on the reaction temperature. The X-ray diffraction (XRD) patterns of mesoporous TiO₂(KIT-6)-T specimens for both small-angle and wide-angle regions are shown in Figure 4-2. The characteristic diffraction peaks of the mesostructure in Figure 4-2(a) can be observed at about 0.86°, indexed as the (211) reflection of the KIT-6 like mesostructure, which is cubic, space group $Ia\bar{3}d$. The unit cell parameters of all the observed mesostructure calculated from the (211) peaks are similar, ~25.1 nm, which is close to the value of 24.8 nm obtained from the TEM images (Figure 4-3).

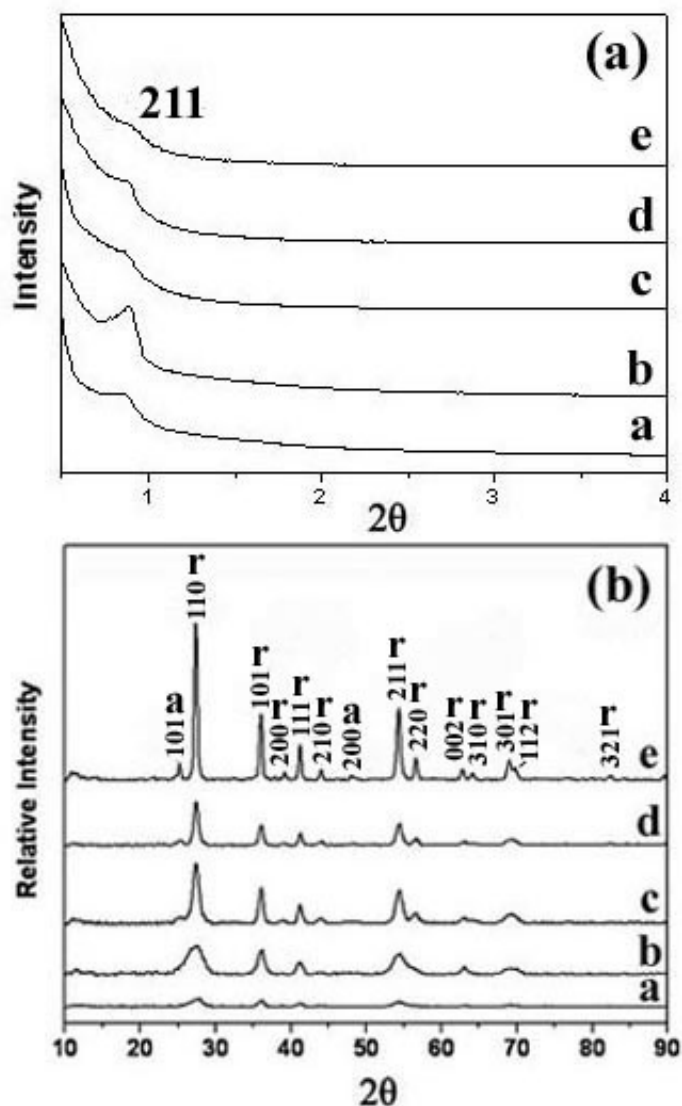


Figure 4-2. XRD patterns of porous TiO_2 crystals templated by KIT-6 in (a) small-angle and (b) wide-angle regions. The peaks in (b) are indexed onto the tetragonal rutile phase with $a = 0.4600$ nm, $c = 0.2965$ nm, marked by 'r' with two small peaks indexed to the tetragonal anatase phase with $a = 0.3785$ nm, $c = 0.9514$ nm, marked by 'a'. The specimens are labelled, **a**: $\text{TiO}_2(\text{KIT-6})$ -100, **b**: $\text{TiO}_2(\text{KIT-6})$ -200, **c**: $\text{TiO}_2(\text{KIT-6})$ -300, **d**: $\text{TiO}_2(\text{KIT-6})$ -400 and **e**: $\text{TiO}_2(\text{KIT-6})$ -600.

The large-angle XRD patterns (Figure 4-2b) indicate that rutile rather than anatase phase starts to appear at a low temperature (100°C). The intensities and sharpness of the diffraction peaks increase with the reaction temperature, and the rutile phase is the only phase ($< 200^\circ\text{C}$) or principle phase ($> 300^\circ\text{C}$) in all samples. The anatase TiO_2 phase was detected from the specimens prepared at high temperature. Two weak diffraction peaks of anatase, (101) and (200), are observed from the products prepared

at 300 °C and above (Figure 4-2c, d, e). The percentage of the anatase is low in all the samples (< 5%).

Bearing in mind that Shi et al. produced rutile TiO₂ powder by a hydrolysis method in a HNO₃ solution at low temperatures (80°C or lower), but pure anatase TiO₂ was obtained at a slightly higher temperature (e.g. 100 °C),²²³ the formation of rutile TiO₂ at a large temperature range from 100 to 600°C using KIT-6 as a template can probably attribute to a confinement effect of the mesopores. The presence of HNO₃ in the pores induced the crystallization of amorphous TiO₂ into rutile instead of anatase during thermal treatment. One of the most important structural differences in between rutile and anatase is that the former contains edge-sharing [TiO₆] octahedra but the latter forms by face-sharing [TiO₆] octahedra. Titanium exists in the form of a 6-fold coordinated hydrated ion [Ti(H₂O)₆]⁴⁺ rather than Ti⁴⁺ cation in a solution and finally the [TiO₆] octahedra are formed by olation and oxolation. The use of excess HNO₃ leads to a high degree protonation of the [TiO₆] octahedra, forming [(H₂O)₅Ti-(OH)]³⁺, whereas NO₃⁻ anions have a weaker affinity for titanium ions. These [(H₂O)₅Ti-(OH)]³⁺ ions share edges through olation, forming a linear chain polymer. This edge-sharing structural feature has a closer relation with rutile rather than anatase.²²³

The mesostructure of TiO₂(KIT-6)-T specimens were observed by TEM. Figure 4-3 shows some TEM images of the products prepared at different temperatures and HRTEM image of TiO₂(KIT-6)-600. Figure 4-3(a-c) show the porous TiO₂(KIT-6)-100, TiO₂(KIT-6)-200, TiO₂(KIT-6)-300 specimens with typical structure of replicas of KIT-6, viewed down {311}, {531} and {111} faces, respectively. Although TiO₂ crystals can not be filled completely in all pores of KIT-6 due to the loss of N and O in decomposition of Ti(NO₃)₄ to TiO₂, large porous particles can still be obtained by this method such as the large TiO₂(KIT-6)-300 particle of 650 nm in Figure 4-3(c).

Typical SAED pattern (the inset of Figure 4-3b) demonstrates that the particles of porous TiO₂ are monocrystalline, and can be indexed to the tetragonal TiO₂ rutile structure (space group *P42/mnm*). HRTEM image (Figure 4-3d) further confirms the single-crystal property. All the spherical nanocrystallites have the same orientation. It becomes possible only when any one of them is a part of a monocrystalline particle. These nanospheres are connected by small bridges which are not easy to be seen.

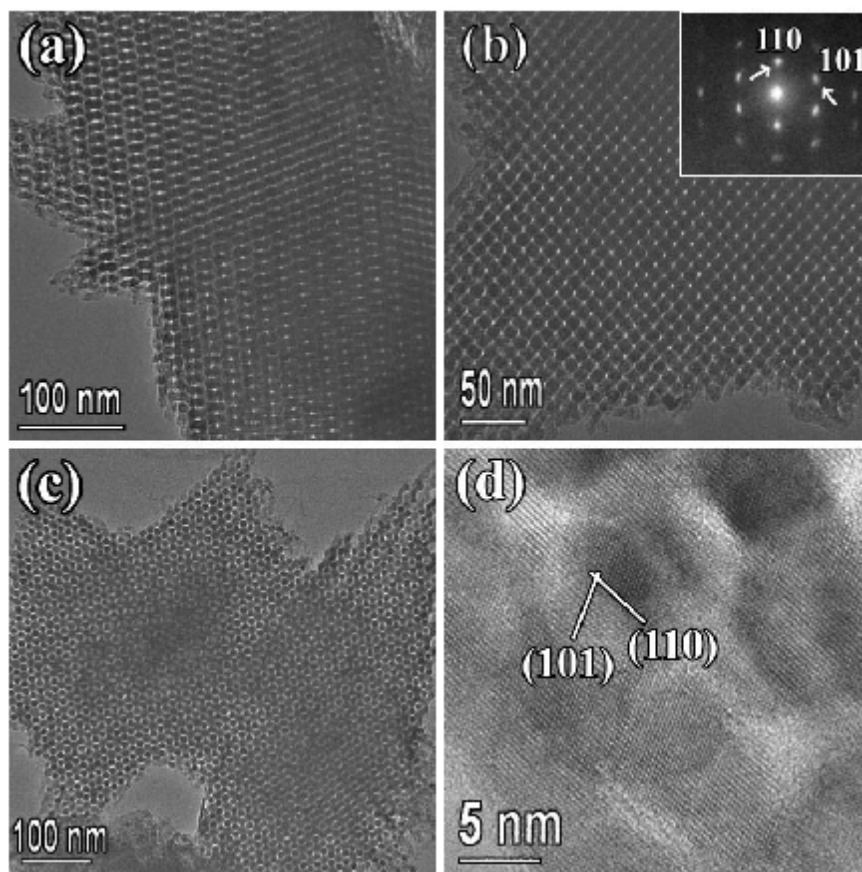


Figure 4-3. TEM images of mesoporous (a) $\text{TiO}_2(\text{KIT-6})-100$, (b) $\text{TiO}_2(\text{KIT-6})-200$ and (c) $\text{TiO}_2(\text{KIT-6})-300$ templated by KIT-6. The inset of (b) is a SAED pattern, indexed to the crystal structure of rutile TiO_2 . (d) HRTEM image of $\text{TiO}_2(\text{KIT-6})-600$, the d-spacings of the marked fringes are ca. 0.249 nm and 0.325 nm, corresponding to the (101) and (110) planes of rutile TiO_2 .

The chemical compositions of the products were examined by using EDX. A small amount of Si was observed in the products (Figure 4-4), an average atomic ratio of Si/Ti, $3.1 \pm 0.4\%$, from 22 randomly selected particles, indicating that the residual SiO_2 is possibly attributed to a formation of Si-O-Ti bonds on the surface of the TiO_2 crystals, which can not be removed completely by a dilute (0.2 M) NaOH solution. This amount of Si impurity is too small and does not introduce any notable changes in the rutile crystal structure. It is believed that the residual silicon normally does not affect the physico-chemical properties of the porous TiO_2 crystals. In proton conductivity, these surface Ti-O-Si functional groups may even enhance the conductivity.

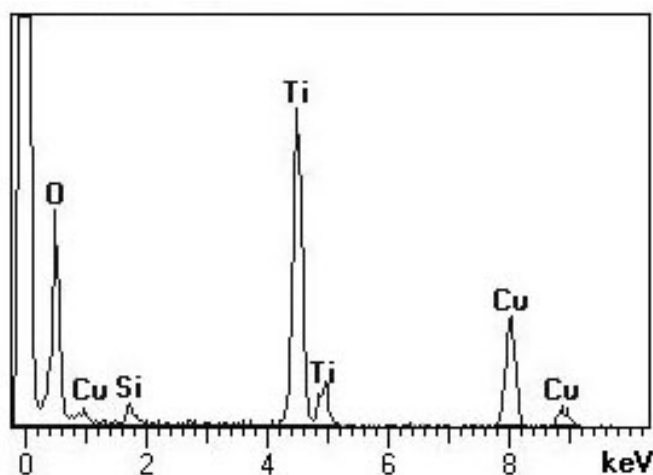


Figure 4-4. EDX graph of $\text{TiO}_2(\text{KIT-6})$ -200 specimen.

Porosities and pore sizes of the porous TiO_2 products templated by KIT-6 were also examined. N_2 adsorption/desorption isotherms of the $\text{TiO}_2(\text{KIT-6})$ -T specimens show a typical type IV curve with a hysteresis loop, indicating a mesopore feature as shown in Figure 4-5(a). Figure 4-5(b) shows the derived pore size distributions. The specific surface area, pore size and pore volume of the porous TiO_2 crystals are displayed in Table 4-2.

Generally speaking, a wide pore size distribution is expected from these porous crystals since the pore shapes, negative replicas of the wall of the silica templates, are complicated. However, it is still worth comparing the pore size distributions of the samples prepared at different temperatures. It is noted that the pore size distributions of the specimens prepared at low temperatures are narrower and the corresponding peak position increases from 4.9 nm in $\text{TiO}_2(\text{KIT-6})$ -100 to 7.2 nm in $\text{TiO}_2(\text{KIT-6})$ -600. This remarkable change is due to the density variation of the TiO_2 crystals, i.e. the crystals would ‘shrink’ at a high temperature, leaving relatively larger space. It is noted that some very large pores may exist in the samples prepared at high temperature, e.g. the broad peaks marked by 14.4 and 22.3 nm in Figure 4-5(b). These could be attributed to the space between nonporous TiO_2 nanoparticles, the percentage of these particles increases with the calcination temperature. The surface areas of mesoporous TiO_2 range from 44.9 to 130.2 m^2/g with the largest value observed from $\text{TiO}_2(\text{KIT-6})$ -200, also listed in Table 4-2.

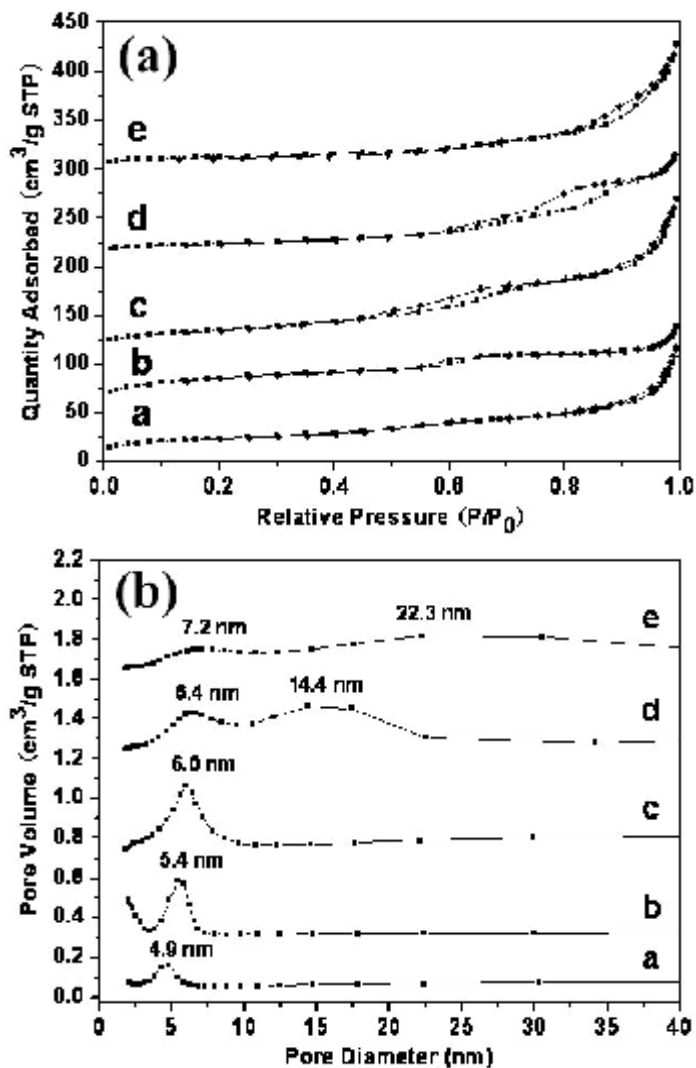


Figure 4-5. (a) Nitrogen adsorption/desorption isotherms measured at 77 K from porous crystals of TiO₂ templated by KIT-6. (b) Pore size distributions of the corresponding specimens with synthetic temperature **a** 100°C, **b** 200°C, **c** 300°C, **d** 400°C and **e** 600°C.

Table 4-2. Pore size (D), pore volume (V), surface area per unit weight (S_w) and per unit volume (S_v) of template KIT-6 and KIT-6 templated TiO₂ from BET measurements. T: calcinations temperature.

Sample	T (°C)	D (nm)	V (cm ³ /g)	S _w (m ² /g)	S _v (m ² /cm ³)
KIT-6	550	10.1	0.97	809.5	568.2
TiO ₂ -100	100	4.9	0.18	86.8	208.4
TiO ₂ -200	200	5.4	0.14	130.2	345.9
TiO ₂ -300	300	6.0	0.25	91.2	187.5
TiO ₂ -400	400	6.4	0.16	50.6	127.6
TiO ₂ -600	600	7.2	0.20	44.9	102.9

4.1.1.1 Proton conductivity

Figure 4-6(a) shows the change in conductivity of pressed pellets of porous $\text{TiO}_2(\text{KIT-6})\text{-200}$ and normal rutile powder on heating in air from room temperature to 100 °C. The values were obtained from a.c. impedance spectra at the low frequency intercept of the electrode processes (Figure 4-7) with the real axis and so is a combination of grain and intergrain contributions. It is reasonable to assume that this conductivity is related to adsorbed water in the intergrain regions. It was not reversible on cooling as the water lost on heating was not readily replaced on cooling and is likely to be protonic in nature. Important to note is that the conductivity of the mesoporous sample is much higher and much more resistant to cooling than the normal material, due mainly to the high internal surface area.

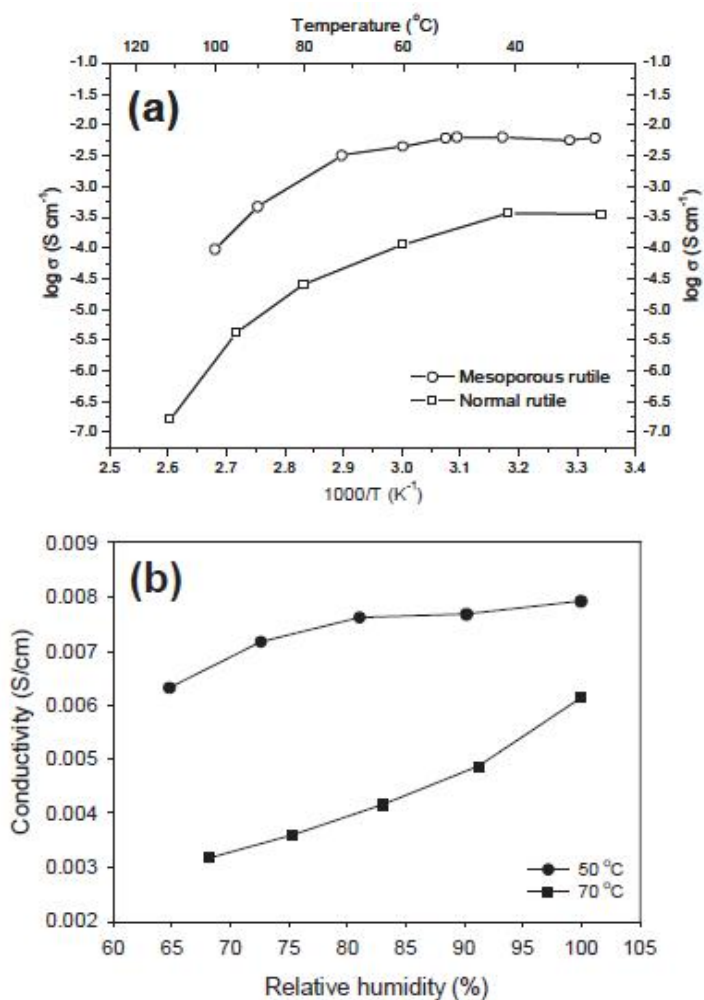


Figure 4-6. (a) Conductivity in air vs. temperature of porous rutile $\text{TiO}_2(\text{KIT-6})\text{-200}$ and normal rutile @3% RH and (b) conductivity of $\text{TiO}_2(\text{KIT-6})\text{-200}$ vs. relative humidity at 50 °C and 70 °C.

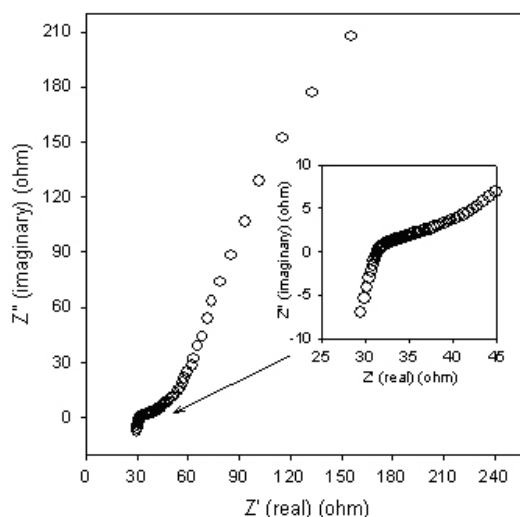


Figure 4-7. A.c impedance spectrum of $\text{TiO}_2(\text{KIT-6})\text{-200}$ at $50\text{ }^\circ\text{C}$ and 100% RH. The frequency is from 1 MHz to 10 mHz at 100 mV r.m.s.

The conductivity dependence upon relative humidity (RH) was also evaluated, equilibrating at each RH for 1 hour and is shown in Figure 4-6(b). Mesoporous TiO_2 presented a higher conductivity at $50\text{ }^\circ\text{C}$ than $70\text{ }^\circ\text{C}$ in the RH from 60% to 100%. The highest conductivity $8 \times 10^{-3}\text{ S}\cdot\text{cm}^{-1}$ was obtained at $50\text{ }^\circ\text{C}$ under 100% RH.

4.1.1.2 Li ion insertion capability

Electrodes made from $\text{TiO}_2(\text{KIT-6})\text{-200}$ were tested in both potentiostatic and galvanostatic mode. In the controlled potential scan, the electrode was cycled over a voltage window of 0.8 to 3.5 V_{Li} (Figure 4-8a). In the initial part of the cycle from open circuit voltage to 1.6 V, a small broad peak can be observed that can be ascribed to either initial partial reduction of Ti^{4+} or to impurities. A very typical reduction peak is observed at around 1.5 V as has previously been observed for two phase equilibria in reaction of lithium titanate spinels or ramsdellites. The second main peak that can be observed at 1.09 V_{Li} is at an unusually low potential for a titanate reduction, but would lead to significantly higher potential if utilised as a negative electrode in a lithium ion battery. A much broader peak is observed on the reverse scan at almost 2 V_{Li} which cycles reversibly with a broad peak at 1.8 V_{Li} . This change in form probably indicates disruption of the mesoporous titanate on Li insertion to 1 V.

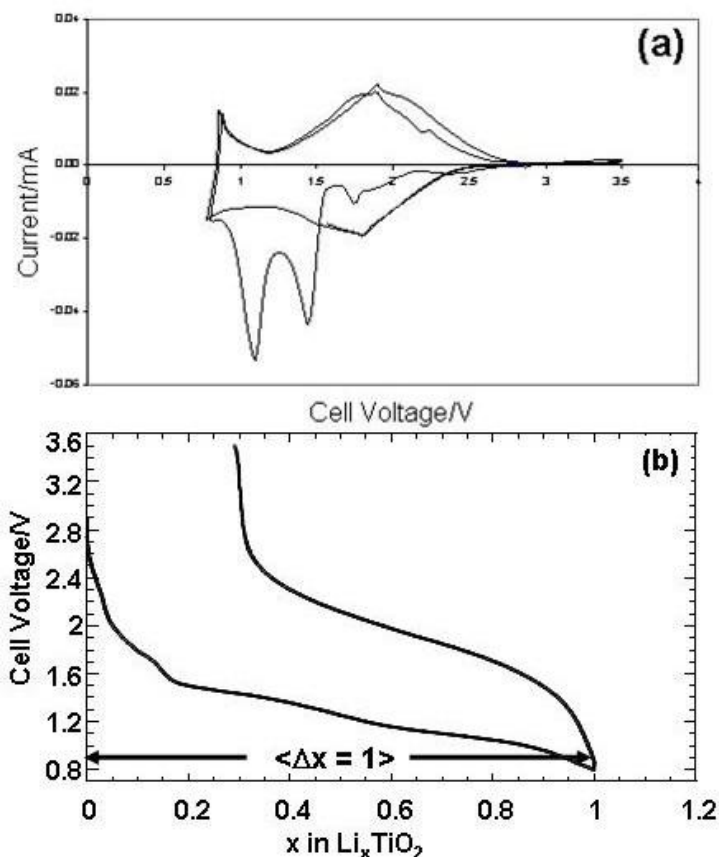


Figure 4-8. (a) Potentiostatic plot of TiO₂-200 in a voltage window of [0.8, 3.5V_{Li}] with a scan rate of ± 20 mV/hour. Total $x = 1$ inserted at 0.8V, (b) Galvanostatic plot of TiO₂ in a voltage window of [0.8, 3.5V_{Li}].

The capacity associated with the initial cycle indicated by the data obtained galvanostatically (Figure 4-8b) is 1 Li⁺ per TiO₂ unit for the first discharge sweep that corresponds to 335 mA h/g (the theoretical specific capacity of TiO₂ polymorphs of anatase, rutile, β -TiO₂ etc.). On the second sweep related to the first charge, 0.71 Li⁺ per TiO₂ was extracted leading to a nominal reversible capacity of 270 mA h/g. This good performance on first cycle is presumably due to the high surface area and high crystallinity of this mesoporous rutile TiO₂.

According to the literature,^{223,224} crystalline rutile TiO₂ can be formed from amorphous TiO₂ by thermal treatment in the presence of HNO₃ solution. To confirm this effect, different concentrations of HNO₃ was used in preparation of porous TiO₂. The TiO₂ products synthesised at 200 °C using dilute HNO₃ solution are labelled as TiO₂(d-HNO₃)-200. Compared with the XRD pattern of TiO₂(d-HNO₃)-200, only rutile phase was detected in TiO₂(KIT-6)-200 specimen (Figure 4-9a). However,

TiO₂(d-HNO₃)-200 specimen is a mixture of anatase and rutile TiO₂ (Figure 4-9b), indicating that the TiO₂ crystal phase depends highly on the amount of HNO₃ used. Porous anatase has not been observed by TEM.

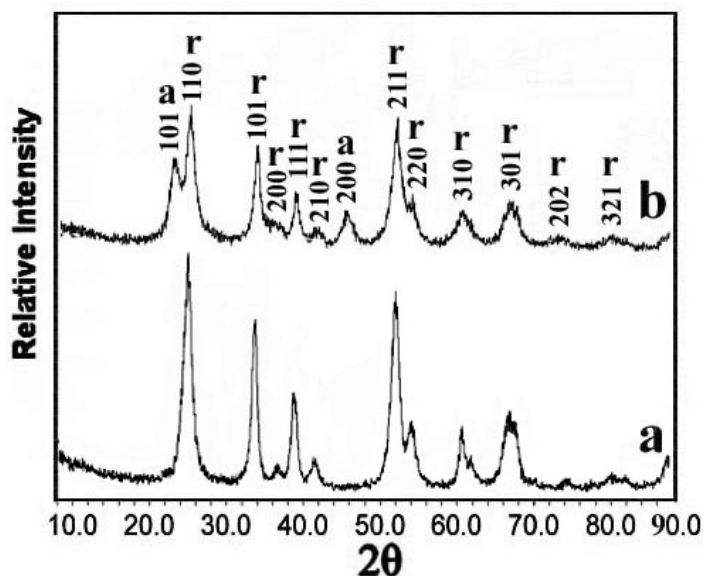


Figure 4-9. XRD patterns of porous TiO₂, (a) TiO₂(KIT-6)-200 and (b) TiO₂(d-HNO₃)-200.

4.1.2 TiO₂ templated by SBA-15

Ordered mesoporous monocrystalline rutile TiO₂ and porous anatase nanocrystals-silica composite were prepared using mesoporous silica SBA-15 as template, and freshly synthesised titanium nitrate and titanium chloride solutions as precursors. The crystal phase of TiO₂ products can be tuned by using different precursors such as titanium isopropoxide, Ti(NO₃)₄, TiCl₄ and Ti(SO₄)₂ solutions. The precursors of Ti(NO₃)₄, TiCl₄ and Ti(SO₄)₂ solutions were prepared by dissolving the hydrolysate of titanium isopropoxide (titanium hydroxide) in excess HNO₃, HCl and H₂SO₄ solutions, respectively. The products synthesised by using different precursors were labelled TiO₂(HNO₃)-T, TiO₂(HCl)-T, TiO₂(H₂SO₄)-T and TiO₂(TIP)-T, where T is the calcination temperature and TIP stands for titanium isopropoxide. Characterisations of these porous products were performed using XRD, HRTEM, SAED, EDX, N₂ adsorption/desorption. In addition, a high concentration solution of NaOH (2M) and long washing time were used in a contrast experiment to remove the SiO₂ template completely.

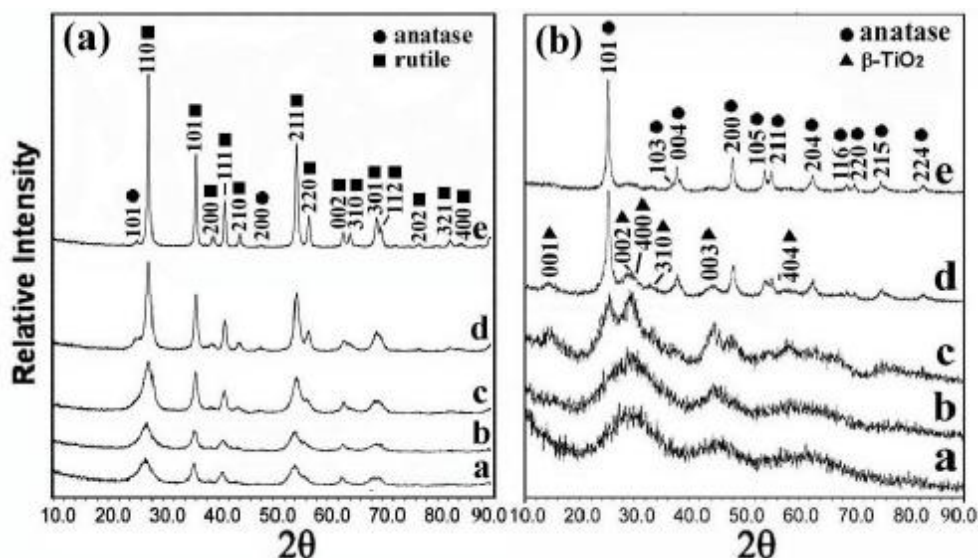


Figure 4-10. XRD patterns of porous (a) TiO₂(HNO₃)-T and (b) TiO₂(HCl)-T specimens. Reaction temperatures (T) are marked, **a**, 50; **b**, 100; **c**, 200; **d**, 300 and **e**, 600 °C.

The crystal phase and mesostructure of porous TiO₂ depend highly on the reaction temperature and the selection of precursors. Figure 4-10(a) shows XRD patterns of the specimens using titanium nitrate as precursor, designated TiO₂(HNO₃)-T, with thermal treatment at different temperatures, T, ranging from 50 °C to 600 °C. Corresponding XRD patterns for the specimens using titanium chloride as precursor are shown in Figure 4-10(b).

When titanium nitrate precursor was used, pure rutile TiO₂ started to form at a very low temperature, 50 °C, in Figure 4-10(a). The XRD peaks can be indexed to the tetragonal rutile TiO₂ structure (space group $P4_2/mnm$ with $a = 0.4600$ nm and $c = 0.2965$ nm). The intensities and sharpness of the diffraction peaks increase with the reaction temperature, and the anatase TiO₂ phase was detected from the specimens prepared at high temperature. Two weak diffraction peaks of anatase, (101) and (200), are observed from the products prepared at 300 °C and 600 °C, indicating a low percentage of the anatase phase in the mixed TiO₂ phase (< 5%). It is of interest to see that the rutile phase can exist at high temperature, which differs from the previous results reported by Shi et al.²²³ when a porous template was not present. They found that rutile TiO₂ powder could be only prepared by a hydrolysis method in a HNO₃ solution at low temperatures (80 °C or lower), and pure anatase TiO₂ was obtained at

a slightly higher temperature (e.g. 100 °C). In the present work, the limited space in the mesopores of silica might have a confinement effect on the TiO₂ phase formation. The presence of NO₃⁻ anions in the pores as opposed to Cl⁻, that induced the crystallization of amorphous TiO₂ into rutile instead of anatase during thermal treatment.^{223,224}

When titanium chloride was used as the precursor, some nanocrystallites were developed in amorphous TiO₂ at low temperature, as indicated by XRD in Figure 4-10(b). Two TiO₂ phases were identified from the specimen synthesised at 300 °C, namely tetragonal anatase TiO₂ (space group *I4₁/amd*, with *a* = 0.3785 nm and *c* = 0.9514 nm) and monoclinic *b*-TiO₂ (space group *C2/m*, with *a* = 1.2163 nm, *b* = 0.3735 nm and *c* = 0.6513 nm, $\beta = 107.3^\circ$). The crystallinity of the TiO₂(HCl)-T specimens increases with the reaction temperature. At high temperature the proportion of *b*-TiO₂ decreased significantly and only anatase TiO₂ was detected in TiO₂(HCl)-600 (Figure 4-10(b)-e), indicating that all the *b*-TiO₂ nanocrystallites transformed into anatase. When a template was not used, Shi et al. reported that anatase TiO₂ powder could be prepared in a HCl solution at low temperature (< 90 °C), but a mixture of rutile and anatase was obtained at 100 °C.²²³ Again, the confinement effect of SBA-15 mesopores seems to lead to the formation of metastable *b*-TiO₂ at low temperature, which transformed to anatase with a higher density at high temperature. The absence of rutile phase when non-nitrate precursor was used indicates that the nitrate ions play an important role in the formation of rutile.

TiO₂ crystals can be also synthesised by using a titanium isopropoxide (TIP) or Ti(SO₄)₂ solution as the precursor and SBA-15 as the template. XRD patterns (Figure. 4-11) of TiO₂(TIP)-600 and TiO₂(H₂SO₄)-600 indicate that they are both pure tetragonal anatase TiO₂. These results further imply an important role of NO₃⁻ anions in the formation of rutile TiO₂.

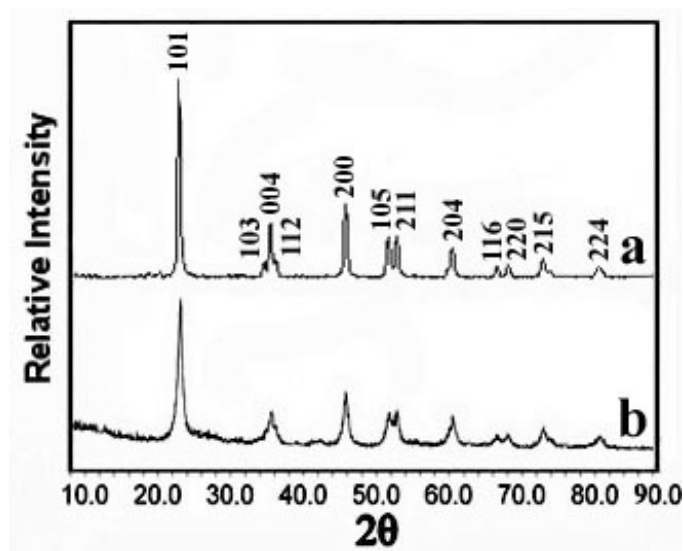


Figure 4-11. XRD patterns of **a**, TiO₂(TIP)-600 and **b**, TiO₂(H₂SO₄)-600 specimens, indexed into the tetragonal unit cell of anatase TiO₂ with $a = 0.3785$ nm and $c = 0.9514$ nm.

The chemical compositions of these porous products were examined by using EDX. A small amount of Si (an average atomic ratio of Si:Ti = 0.029(3)) was observed in all TiO₂(HNO₃)-T specimens (Figure 4-12a), indicating that residual SiO₂ was possibly connected with TiO₂ by a Ti-O-Si bond on the surface of rutile crystals, which could not be removed completely by a short time washing with a dilute (0.2 M) NaOH solution. When a high concentration solution of NaOH (2 M) was used for a long time washing (e.g. 6-18 h), no Si element was detected in EDX (Figure 4-12b). However, in the latter case, damage of the mesostructure of rutile products was observed from the TEM images (Figure 4-13). It is believed that a very low level of surface silicon would not affect the physico-chemical properties of the porous crystals.

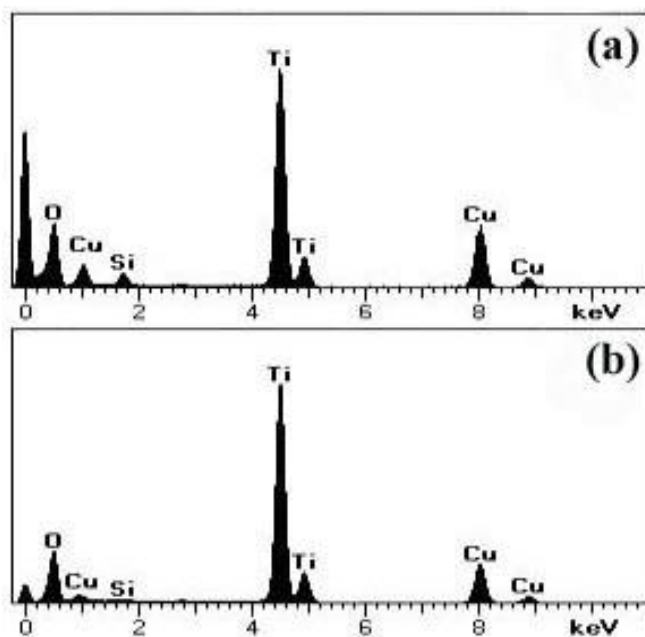


Figure 4-12. EDX spectra of TiO₂(SBA-15)-200 crystals washed with (a) a 0.2 M NaOH solution for 3 minutes and (b) a 2 M NaOH solution for over 6 h.

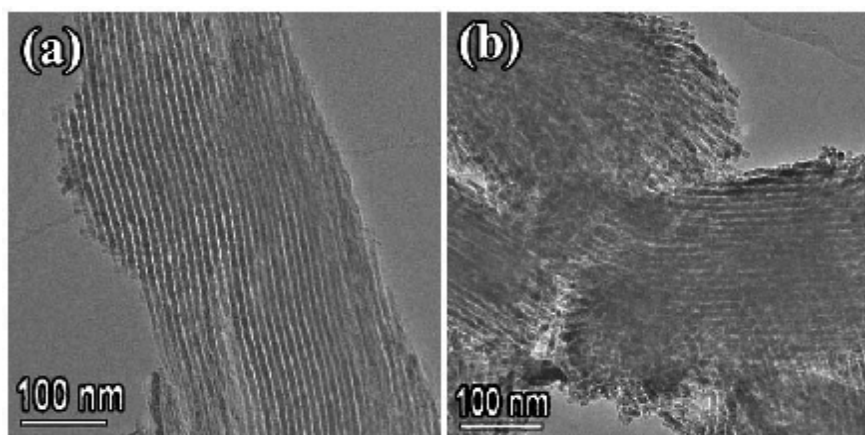


Figure 4-13. TEM images of TiO₂(SBA-15)-200 crystals washed with a 2 M NaOH solution for (a) 3 minutes and (b) for 18 h.

On the other hand, A large amount of Si was detected in all TiO₂(HCl)-T specimens (Figure 4-14a), e.g. an average atomic ratio of Si:Ti = 0.18(3) was obtained from more than 20 randomly selected particles of TiO₂(HCl)-600 that could not be removed completely by increasing the concentration of NaOH solution and washing time, indicating that the residual SiO₂ was possibly cross-linked with TiO₂ particles.²²⁵ It is interesting to see that Si peaks were absent in the EDX spectra

(Figure 4-14b,c) of $\text{TiO}_2(\text{TIP})$ -600 and $\text{TiO}_2(\text{H}_2\text{SO}_4)$ -600 prepared using titanium isopropoxide and $\text{Ti}(\text{SO}_4)_2$ solutions as the precursors respectively. The nature of interaction between silica and TiO_2 during the chemical processes in question is yet to be investigated.

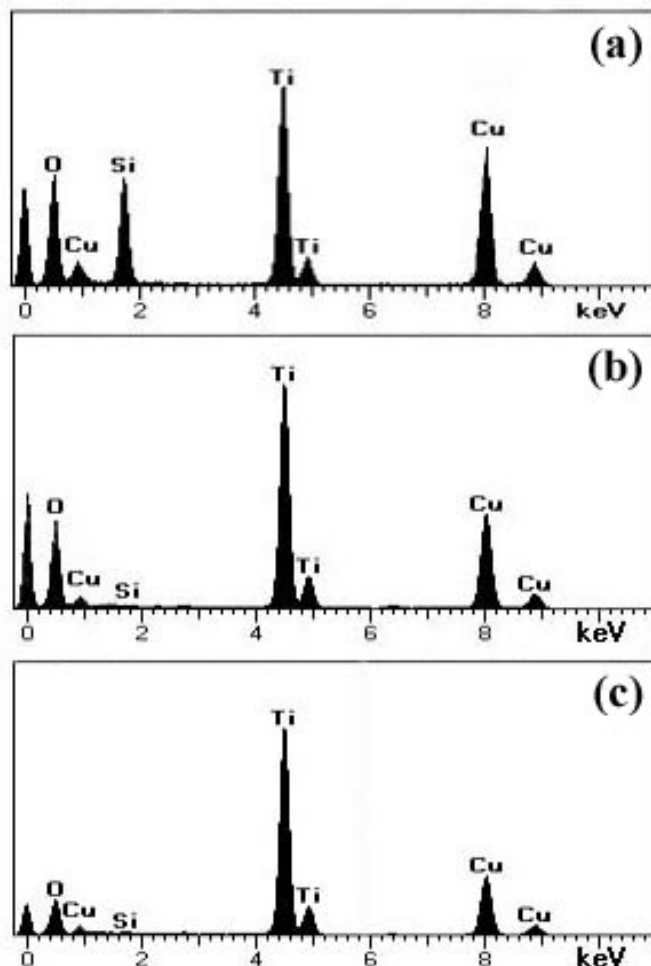


Figure 4-14. EDX spectra of (a) $\text{TiO}_2(\text{HCl})$ -600, (b) $\text{TiO}_2(\text{TIP})$ -600 and (c) $\text{TiO}_2(\text{H}_2\text{SO}_4)$ -600 porous crystals washed with a 0.2 M NaOH solution for 3 minutes.

Further structural characterisation of TiO_2 products with the rutile and anatase phases prepared using titanium nitrate and titanium chloride solutions was carried out by using low magnification TEM and HRTEM. Figure 4-15 shows some typical TEM and HRTEM images of the $\text{TiO}_2(\text{HNO}_3)$ -T and $\text{TiO}_2(\text{HCl})$ -T specimens which have both replicated structures of SBA-15. Figure 4-15(a) and (c) show two TEM images from $\text{TiO}_2(\text{HNO}_3)$ -T (T = 200 and 300 °C) viewed down the (a) [110] and (c) [001] axes of the negatively replicated mesostructure of SBA-15. These porous rutile TiO_2

particles have a hexagonal arrangement of nanorod arrays connected by small nanobridges.

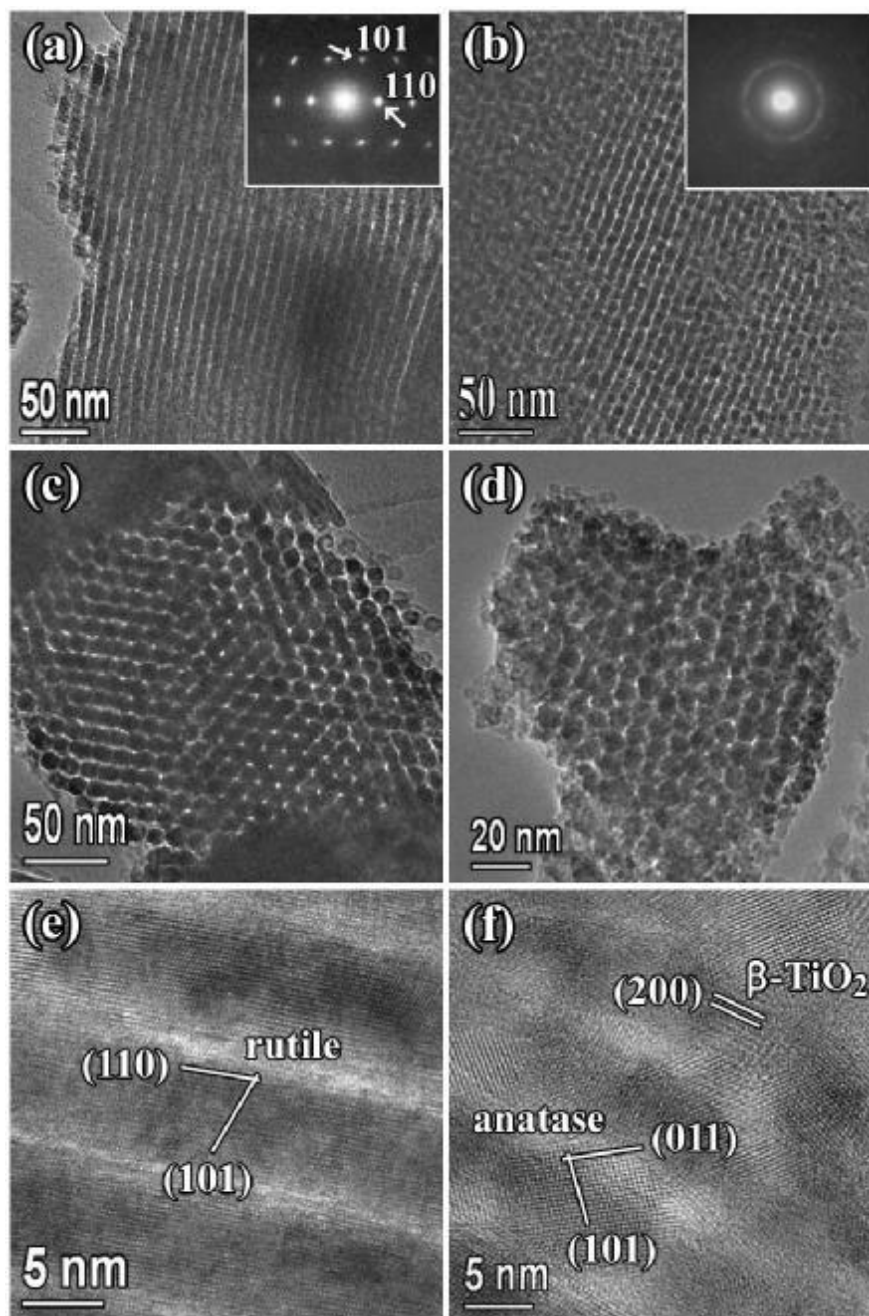


Figure 4-15. TEM images of mesoporous (a) $\text{TiO}_2(\text{HNO}_3)$ -200, (b) $\text{TiO}_2(\text{HCl})$ -200, (c) $\text{TiO}_2(\text{HNO}_3)$ -300 and (d) $\text{TiO}_2(\text{HCl})$ -300, and HRTEM images of (e) $\text{TiO}_2(\text{HNO}_3)$ -300 and (f) $\text{TiO}_2(\text{HCl})$ -300. The insets of (a), (b) are the corresponding SAED patterns from TiO_2 crystals. The principal d-spacings in (e) and (f) are indexed to different TiO_2 phases as indicated.

Some TiO₂ nanowires (Figure 4-16a) instead of 3D networks were obtained at low temperature (< 100 °C) when the amount of loading of titanium nitrate was reduced and the dry process at 35°C was skipped. The possible reason for the formation of nanowires is that the extension of crystal growth from the principal pores to the small bridging channels was not complete, similar to a previous synthesis of WO₃ nanowires also using SBA-15 as a template.¹⁶⁴

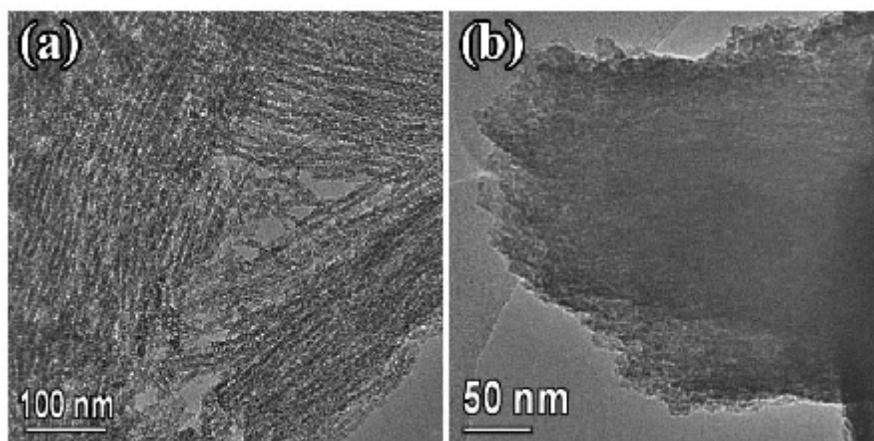


Figure 4-16. TEM images of (a) TiO₂(HNO₃)-100 nanowires and (b) TiO₂(HCl)-50 particles, respectively.

All the SAED patterns from TiO₂(HNO₃)-T specimens, covering many nanorods, show a monocrystalline property. For example, the SAED pattern shown as the inset of Figure 4-15(a) can be indexed to the tetragonal rutile structure with the view direction of $[1\bar{1}\bar{1}]$ of the rutile structure. HRTEM images (Figure 4-15e) also confirm that the mesoporous particles are monocrystalline rutile-type structure, i.e. the crystal orientations of all the nanorods as well as the inter-nanorod small bridges are exactly the same. The d-spacings of the marked fringes in Figure 4-15(e) are ca. 0.325 nm and 0.249 nm, corresponding to the (110) and (101) planes of rutile TiO₂. The d-spacings in (f) for an anatase crystallite are ca. 0.352 nm and 0.352 nm, corresponding to the (101) and (011) planes. The d-spacing on the right is about 0.579 nm, corresponding to the (200) plane of *b*-TiO₂. The particles can be regarded as single crystals with 3D regular mesopores.

However, the mesopore ordering of the porous anatase TiO₂-silica composite prepared from a titanium chloride solution (Figure 4-15b,d) was poor, although 3D connections between the nanorods are still formed. The diffraction pattern from the TiO₂(HCl)-T specimens, e.g. the inset of Figure 4-15(b), indicate a polycrystalline

state. The corresponding HRTEM images show nanocrystallites with random orientations, which can be identified as either anatase or β -TiO₂ (Figure 4-15f), in an agreement with the XRD results. Even so, the partially ordered mesopores in the particles are still visible. However, the composite synthesised at 50 °C, TiO₂(HCl)-50, was congregation of nanoparticles (Figure 4-16b) without mesopores, which can possibly be attributed to unsuccessful filling of the silica pores at low temperature.

The microstructures of TiO₂(TIP)-600 and TiO₂(H₂SO₄)-600 were also characterised by TEM (Figure 4-17a,b). Only some aggregates of spherical nanocrystallites were observed. These nanospheres, with almost uniform sizes, were obviously formed inside the mesoporous. However, these nanospheres did not develop into 3D connected porous crystals.

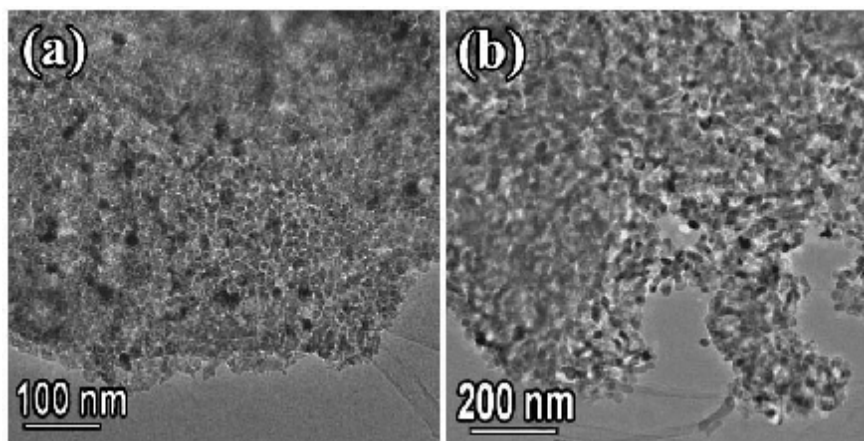


Figure 4-17. TEM images of (a) TiO₂(TIP)-600 and (b) TiO₂(H₂SO₄)-600 specimens.

The porosities and pore sizes of the porous crystals of TiO₂ templated by SBA-15 were examined by N₂ adsorption/desorption. The isotherms of both TiO₂(HNO₃)-T and TiO₂(HCl)-T specimens show typical type IV curves with a hysteresis loop, indicating a mesopore feature as shown in Figure 4-18(a) and (b). It is proven that high yields of porous rutile TiO₂ particles and anatase-silica composites can be achieved successfully in a wide range of temperature. Figure 4-18(c) and (d) show the corresponding pore size distributions of these two specimen series. Since the ideal pore geometry in the products is the same as the silica wall in SBA-15 as they have a negative replication relationship, the pore size distribution would not be as narrow as that in the template. On the other hand, it is noted that the pore size distributions of the porous TiO₂ prepared at low temperatures are relatively narrower. The corresponding peak position increases from 3.3 nm to 7.5 nm in the TiO₂(HNO₃)-T

specimens and from 2.9 nm to 6.0 nm in $\text{TiO}_2(\text{HCl})\text{-T}$ with the temperature increase. This remarkable change is due to the density variation of the TiO_2 crystals, and was also observed in other porous metal oxides. In other words, at high temperature, the formed crystals of TiO_2 are more dense and its volume shrinks, leaving a larger inter-nanorod space. The larger pores in $\text{TiO}_2(\text{HNO}_3)\text{-600}$ and $\text{TiO}_2(\text{HCl})\text{-600}$ specimens at positions of 21.1 nm and 23.6 nm could be attributed to the inter-particle spaces, which increases with the calcination temperature, leading to a yield reduction of mesoporous crystals.

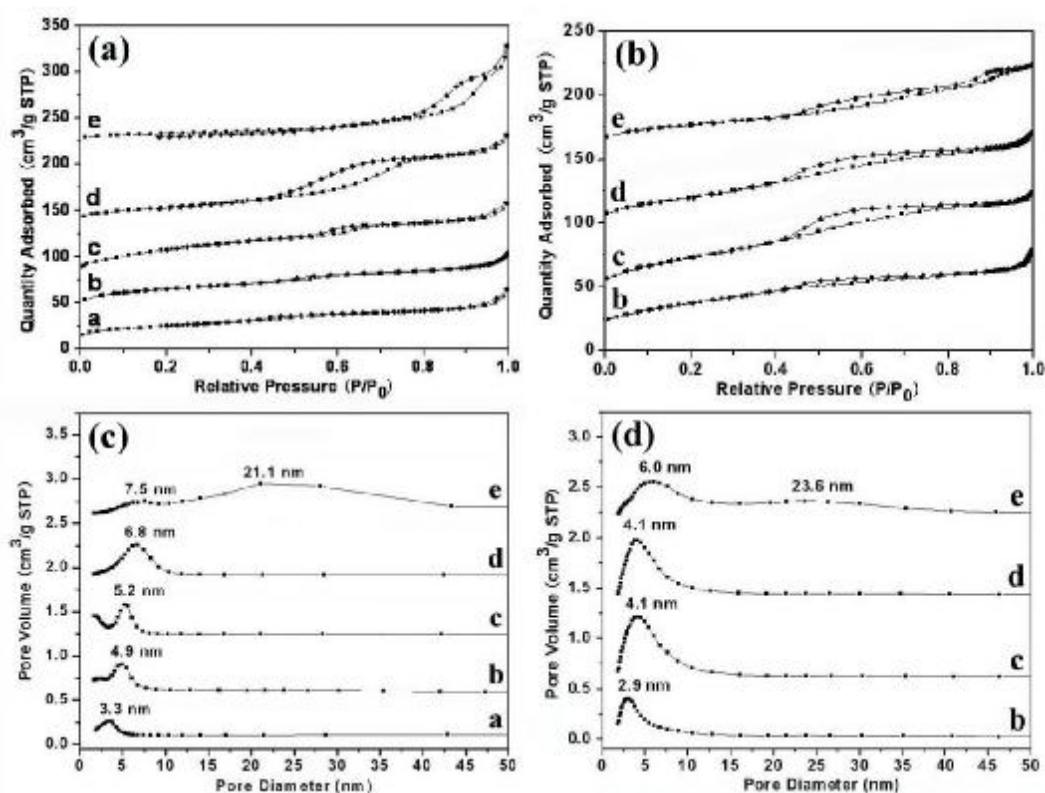


Figure 4-18. Nitrogen adsorption/desorption isotherms measured at 77 K from porous crystals of (a) $\text{TiO}_2(\text{HNO}_3)\text{-T}$ and (b) $\text{TiO}_2(\text{HCl})\text{-T}$ specimens, with synthetic temperature (T) of a, 50; b, 100; c, 200; d, 300 and e, 600°C. (c) and (d) The corresponding pore size distributions in $\text{TiO}_2(\text{HNO}_3)\text{-T}$ and $\text{TiO}_2(\text{HCl})\text{-T}$, respectively.

The specific surface area, pore size and pore volume of these porous TiO_2 crystals are displayed in Table 4-3. The value of surface area of SBA-15 (735.9 m²/g) can alter to 464.4 m²/g by using the value of pore volume (1.13 cm³/g) and density of silica (2.2 g/cm³). Likewise, the surface areas of $\text{TiO}_2(\text{HNO}_3)\text{-T}$ can also alter to

258.3, 326.1, 433.0, 217.4 and 78.4 m²/cm³ (the density of rutile TiO₂ is 4.23 g/cm³) as a function of synthetic temperature. The largest value of the surface area of TiO₂(HNO₃)-200 specimen (433.0 m²/cm³) is very close to the surface area of silica template (464.4 m²/cm³), indicating a high yield of mesoporous TiO₂ product. Since the TiO₂(HCl)-T samples contain two components, TiO₂ and SiO₂, with an undetermined ratio, it is difficult to calculate their surface areas in the unit of m²/cm³. It is noted that TiO₂(HCl)-T synthesised at 200 °C has also the largest surface area. A possible explanation is as follows.

Table 4-3. Data of Brunauer-Emmett-Teller (BET) measurements of SBA-15 and SBA-15 templated TiO₂ crystals with calcinations temperature (T), pore size (D), pore volume (V), surface area per unit weight (S_w) and surface area per unit volume (S_v).

Sample	T (°C)	D (nm)	V (cm ³ /g)	S _w (m ² /g)	S _v (m ² /cm ³)
SBA-15	550	10.2	1.13	735.9	464.4
TiO ₂ (HNO ₃)-50	50	3.3	0.09	84.3	258.3
TiO ₂ (HNO ₃)-100	100	4.9	0.10	109.7	326.1
TiO ₂ (HNO ₃)-200	200	5.2	0.14	163.0	433.0
TiO ₂ (HNO ₃)-300	300	6.8	0.15	84.4	217.4
TiO ₂ (HNO ₃)-600	600	7.6	0.14	29.5	78.4
TiO ₂ (HCl)-100	100	2.9	0.23	246.9	
TiO ₂ (HCl)-200	200	4.1	0.33	316.5	
TiO ₂ (HCl)-300	300	4.1	0.30	256.1	
TiO ₂ (HCl)-600	600	6.0	0.24	165.9	

At a low temperature (< 200 °C) TiO₂ does not fill in the pores of silica completely. Instead, many TiO₂ nanoparticles are present and aggregate into large clusters after removing the silica template, for example, the TiO₂(HCl)-50 specimen shown in Figure 4-16(b). The corresponding surface area is small. When the reaction temperature increases to around 200 °C, the pores of the template are almost fully filled by the precursor, which transforms to TiO₂ crystals gradually. The maximum surface area is achieved in the final porous crystalline product. At a higher temperature, a fast crystallisation process may results in pore blocking and the pores are only partially filled. Some non-porous TiO₂ crystals are developed outside of the templating pores. Consequently, the surface area of the product drops.

4.1.2.1 Li ion insertion capability

In the aforementioned discussion, the porous rutile TiO_2 templated by KIT-6¹⁹⁹ exhibited a high accommodation of Li^+ that upon the first discharge, 1 Li^+ per TiO_2 can be intercalated from the open circuit voltage (OCV) down to 0.8V that corresponds to a capacity of 335.4mAh/g, and 0.71 Li^+ per TiO_2 was extracted reversibly in the voltage window of 0.8-3.5V that corresponds to a reversible capacity of 237.2 mA h/g upon first charge. Herein the porous SBA-15 templated rutile TiO_2 -200 with larger surface area (163.0 m^2/g) than KIT-6 templated TiO_2 -200's (130.2 m^2/g) is expected to have a higher accommodation capacity of Li^+ .

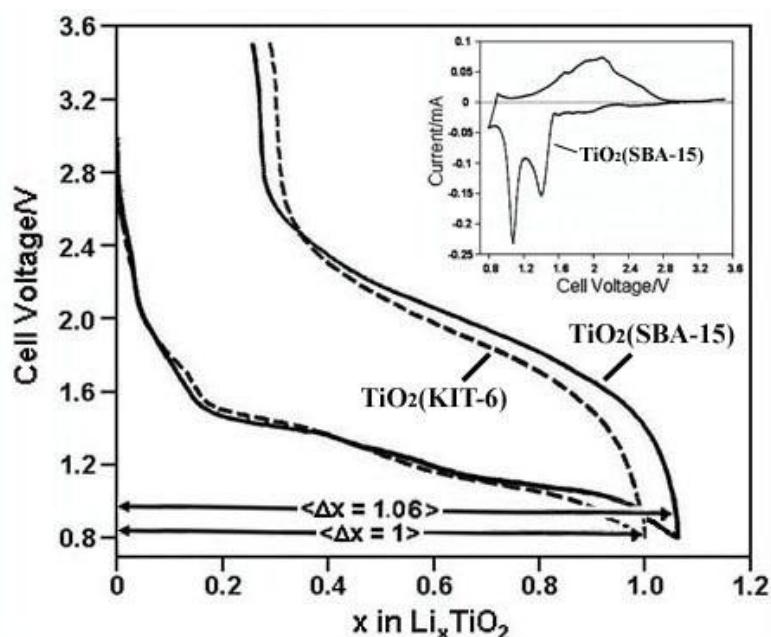


Figure 4-19. Galvanostatic plot of TiO_2 -200 templated by SBA-15 and KIT-6 in a voltage window of [0.8, 3.5V_{Li}]. The inset is the potentiostatic plot of TiO_2 -200 templated by SBA-15.

Electrodes made from dried $\text{TiO}_2(\text{HNO}_3)$ -200 specimen were tested in both potentiostatic and galvanostatic mode. In the controlled potential scan, the electrode was cycled over a voltage window of 0.8 to 3.5V_{Li} (the inset of Figure 4-19). From the potentiostatic curve, upon the first discharge two reduction peaks are observed around 1.4 and 1.08V based on titanium reduction from Ti^{4+} to Ti^{3+} indicating a two steps reactions. The mechanism involved in the reduction can be described as biphasic transformations and there are two that are related to each reduction peak observed in the potentiostatic curve. In between these two biphasic transformation a

narrow solid solution can be detected as the potential drop from 1.4V to 1.08V. The galvanostatic curve of $\text{TiO}_2(\text{HNO}_3)$ -200 specimen shown in Figure 4-19 indicates that 1.06 Li^+ per unit of TiO_2 can be stored from the OCV down to 0.8V upon the first discharge that corresponds to a capacity of 356.6 mA h/g. The behaviour exhibited upon the first charge corresponds to 0.81 Li^+ per TiO_2 extracted reversibly leading to a nominal reversible capacity of 270 mA h/g in the voltage window of 0.8 to 3.5V. The first discharge intercalate up to 1.06 Li^+ per unit of TiO_2 which is slightly in excess for a TiO_2 polymorph and it is believed to be structurally related. This better performance on first cycle confirms convincingly that the Li^+ insertion capability of TiO_2 electrode depends highly on its surface area. Further work is required to elucidate the mechanisms that occur upon the intercalation process of these materials and to obtain more structural information on the phase formed upon these transformations.

4.1.2.2 Photoactivity

The porous $\text{TiO}_2(\text{HCl})$ -T (T = 200, 300 and 600) specimens were also examined for their photocatalytic activities on the decomposition of methylene blue (MB) in an aqueous solution. The results from this experiment were shown graphically in Figure 4-20(a). It was found that these mesoporous TiO_2 composites have photoactivities and could bleach a 5×10^{-5} M MB almost completely in 3 h. Considering only the adsorption capacity alone, $\text{TiO}_2(\text{HCl})$ -200 is the best among the three samples, but the other two are not far behind. $\text{TiO}_2(\text{HCl})$ -200 could adsorb around 56 % of MB whereas $\text{TiO}_2(\text{HCl})$ -300 and $\text{TiO}_2(\text{HCl})$ -600 could adsorb 45 % and 42 %, respectively, which is consistent with their surface areas (Table 4-3). However, it was found that $\text{TiO}_2(\text{HCl})$ -600 is better than $\text{TiO}_2(\text{HCl})$ -200 and -300 specimens comparing only photoactivity. Because high concentrations of defects of amorphous cause rapid e^- - h^+ recombination, resulting in reduction of photoactivity,²²⁶ the photoactivity of $\text{TiO}_2(\text{HCl})$ -600, -300 and -200 was 53 %, 51 % and 41 %, respectively, corresponding to a higher crystallinity of anatase shown in Figure 4-10(b). Additionally the proportion of anatase in specimens might possibly have an effect on its photocatalytic activity. Comparison among the adsorb and photoactivity of $\text{TiO}_2(\text{HCl})$ -200, -300 and -600 specimens, $\text{TiO}_2(\text{HCl})$ -300 exhibits an interesting

photocatalytic performance because of reflecting a compromise between the degree of anatase crystallisation and the surface area of specimens.

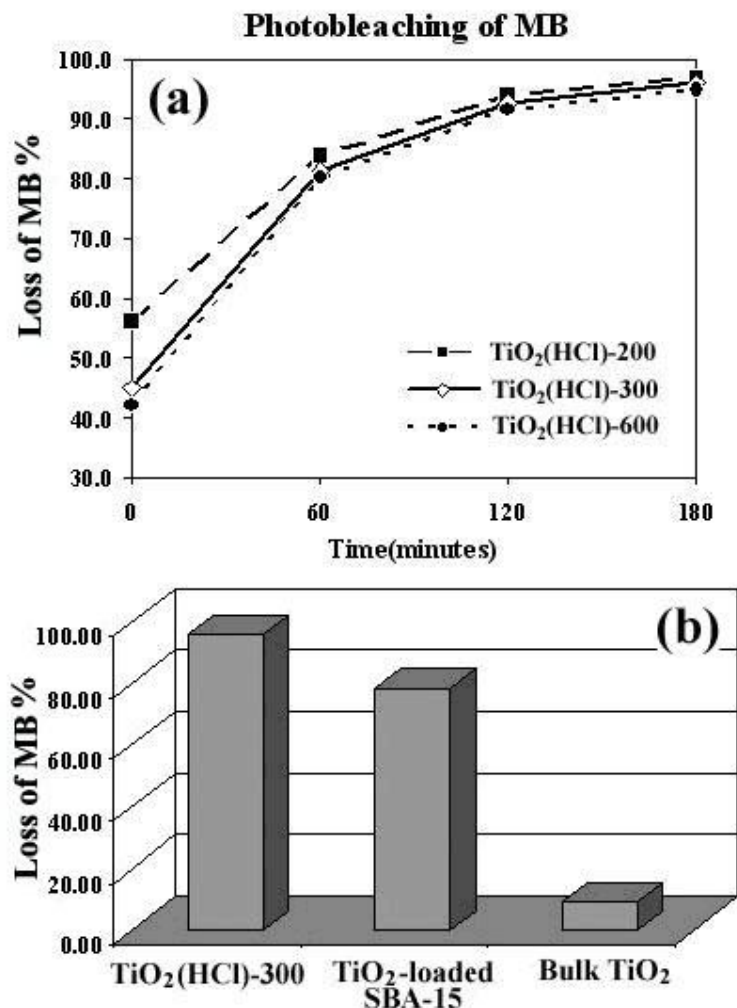


Figure 4-20. The photoactivity of (a) TiO₂(HCl)-T (T = 200, 300 and 600) specimens under different reaction time, and (b) removal of MB after 180 minutes for porous TiO₂-silica, TiO₂-loaded SBA-15 and bulk TiO₂ respectively.

To investigate the advantage of mesopore framework in photocatalytic process, three different kinds of TiO₂ synthesised at 300 °C, namely porous anatase nanocrystal-silica composites (TiO₂(HCl)-300), porous anatase TiO₂-loaded SBA-15 (using the same synthetic process but silica template was not removed by NaOH solution) and bulk anatase TiO₂ (using the same synthetic process but silica template was not used), have been compared under UVA after 3 hours reaction time and shown in Figure 4-20(b). It was found that bulk TiO₂ has the lowest photoactivity (9%) because of its low surface area. Mesoporous TiO₂(HCl)-300 has the highest

photoactivity (96%) and higher than mesoporous TiO₂-loaded SBA-15 (78%), probably because TiO₂(HCl)-300 has more active sites of TiO₂ particles due to almost complete removal of silica template. While some of active sites of TiO₂-loaded SBA-15 might be blocked because TiO₂ particles are embraced by silica walls, as a result, light and MB cannot penetrate inside the pores to reach all of TiO₂ active sites. Therefore TiO₂-loaded SBA-15 has lower photoactivity than TiO₂(HCl)-300.

4.2 MgO and CuO

MgO is used widely in lithium-ion batteries, dehydrogenation and methane oxidation.²²⁷⁻²²⁹ CuO is used in wet peroxide oxidation processes, oxidation of hydrogen and photocatalytic hydrogen production.²³⁰⁻²³² CdO is a catalyst for hydrogenation and ethanol decomposition,^{233,234} and BaO is a catalyst for NO_x storage and release.^{235,236} Therefore porous MgO, CuO and CdO with large surface area may exhibit some interesting properties. MgO-,^{80,237} CuO-,^{79,238,239} and CdO-loaded²⁴⁰ SBA-15 have been prepared as catalyst/support and molecule sieve recently. However, these porous metal oxides, after removal of SBA-15, have not been reported yet. Mg(NO₃)₂·6H₂O has a low melting point (95 °C) and higher decomposition temperature (129 °C). The melting points of Cu(NO₃)₂·3H₂O and Cd(NO₃)₂·4H₂O are 114.5 °C and 59.4 °C, which are lower than their decomposition temperature (170 °C and 360 °C), respectively. So the solid-liquid method can be applied to synthesise these porous metal oxides.

Figure 4-21 shows the TEM images of expected MgO particles before removing SBA-15 (a) and after removing SBA-15 (b). According to Figure 4-21(a), the expected MgO particles were possible embedded in the wall of SBA-15 rather than filled in the pores of the silica. After the silica template was removed by 2M NaOH solution, only non-porous particles were formed in Figure 4-21(b), and the Si element peak was still detected in EDX spectrum (Figure 4-22), implying the existing of Mg-Si-O structure in the particles. The average atomic ratio of Si/Mg in the product is 41 ± 0.9%. The XRD pattern (Figure 4-23) are indexed to the Mg(OH)₂ structure rather than MgO structure.

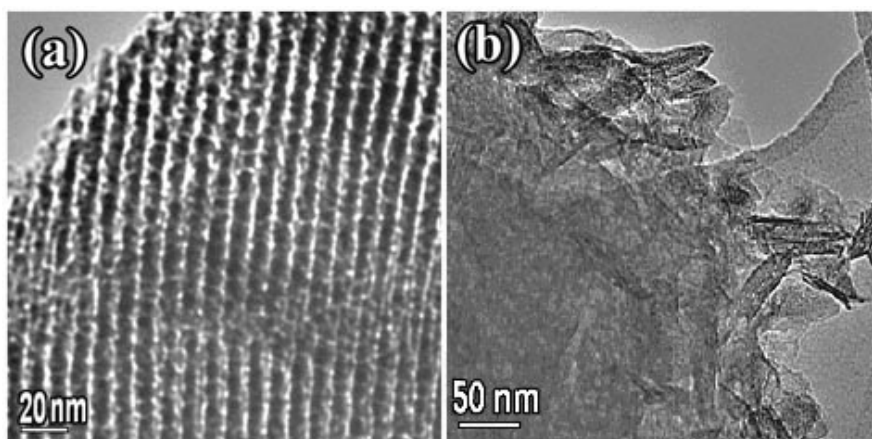


Figure 4-21. TEM images of (a) a particle of SBA-15 containing expected MgO particle and (b) the Mg-Si-O compound after removing the silica template.

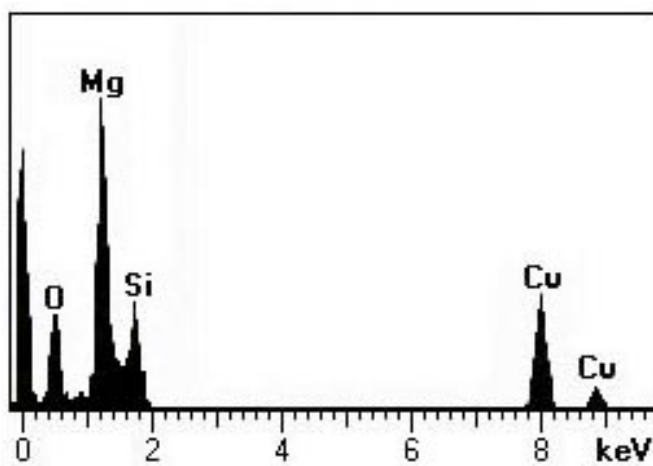


Figure 4-22. EDX graph of Mg-Si-O compound after removal of SBA-15.

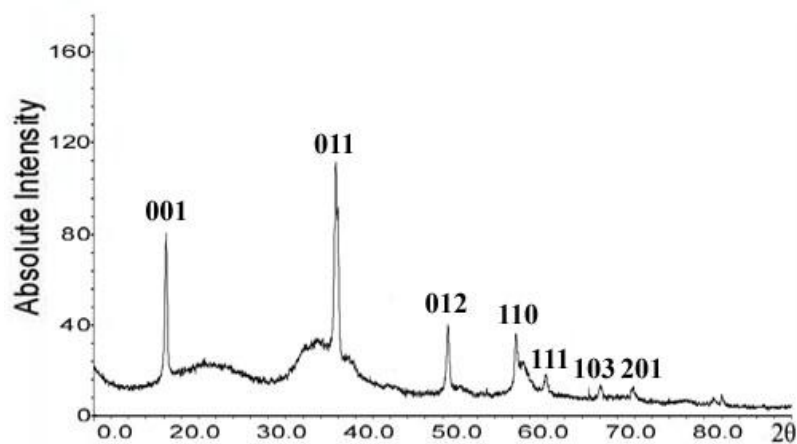


Figure 4-23. XRD pattern of Mg(OH)₂-silica particles after removing SBA-15.

Figure 4-24 shows the TEM image of CuO particles after SBA-15 was removed. Only nanoparticles and bulk material were observed by the TEM. No Si peak was detected in EDX spectrum (Figure 4-25), indicating no Si-O-Cu structure formation. The XRD pattern (Figure 4-26) confirms that the particles are pure CuO crystals. Therefore it denotes that CuO particles can be formed by decomposition of the precursor inside the pores of SBA-15. However, the porous structure of the particles was not observed, implying that the CuO was formed nanoparticles inside the silica pores or as bulk particles outside the silica pores. Recently a new instantaneous combustion method was designed by Ren et al. (personal communication) to generate porous CuO crystals instantaneously inside the pores of KIT-6. They reduced the concentration of NaOH solution to remove the silica template, to avoid destroying the porous structure of CuO particles because CuO is a weak amphoteric oxide.

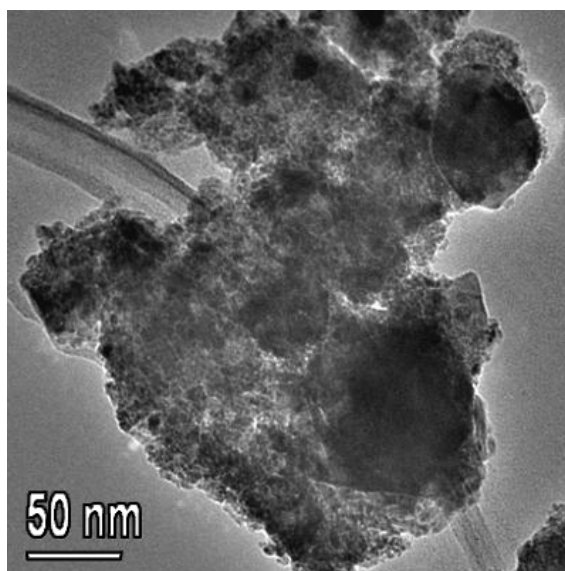


Figure 4-24. TEM image of CuO particles after removing SBA-15.

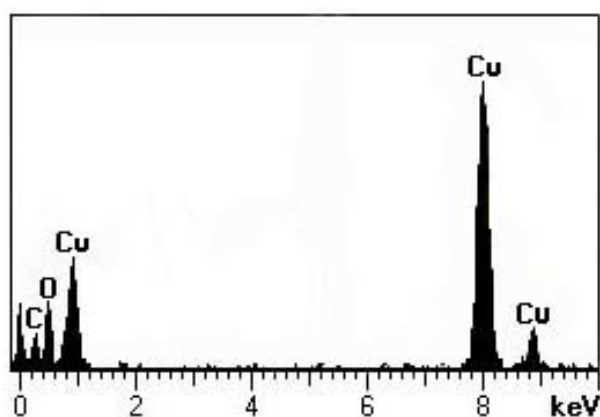


Figure 4-25. EDX graph of CuO after removing SBA-15.

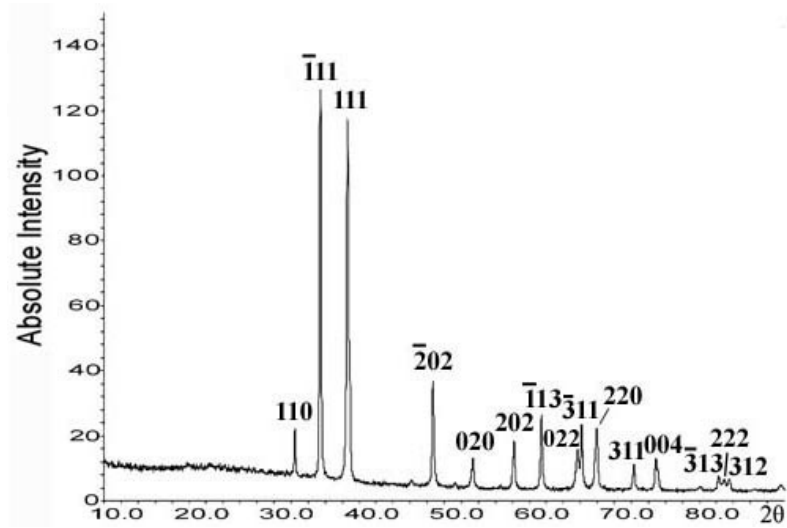


Figure 4-26. XRD pattern of non-porous particles after removing SBA-15, being indexed to the CuO structure.

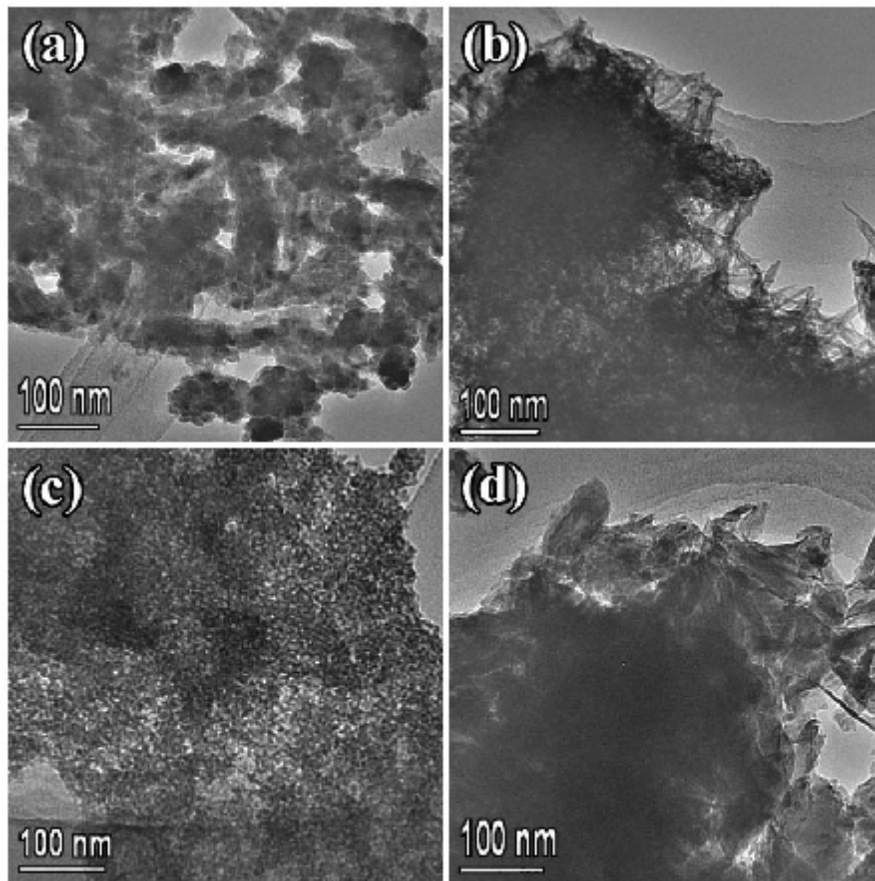


Figure 4-27. TEM images of (a) Ba-Si-O, (b) Cd-Si-O, (c) Gd-Si-O and (d) Sr-Si-O composites after removing SBA-15 template.

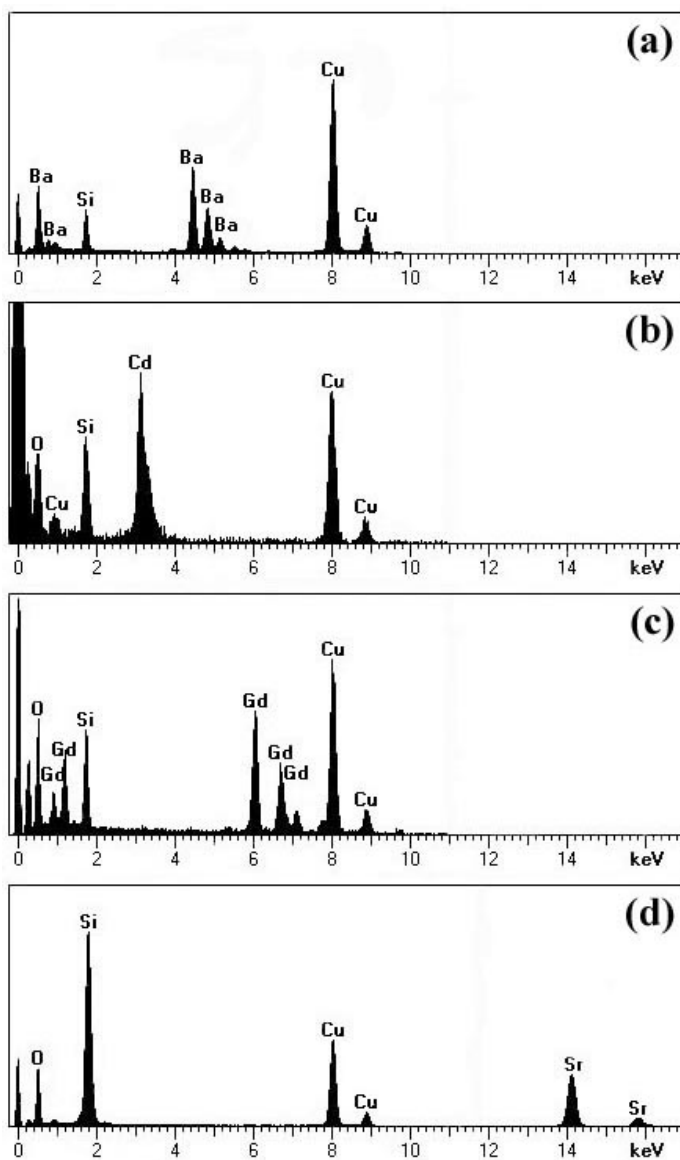


Figure 4-28. EDX spectra of (a) Ba-Si-O, (b) Cd-Si-O, (c) Gd-Si-O and (d) Sr-Si-O specimens.

In addition, BaO, CdO, Gd₂O₃ and SrO particles were expected to be prepared using the solid-liquid method due to their properties as precursors (Table 4-1). However, similar to Mg(OH)₂-silica composite, only non-porous particles with various morphologies were observed by TEM (Figure 4-27). Metal and oxygen elements as well as Si were detected by EDX (Figure 4-28) from the specimens after removing silica template. The average atomic ratio of Si/Metal (Ba, Cd, Gd and Sr) is $68.7 \pm 3.2\%$, $62.7 \pm 7.1\%$, $78.1 \pm 7.5\%$ and $84.3 \pm 5.4\%$, respectively. Each XRD pattern (e.g. Figure 4-29) was indexed to the complicated structure of a mixture

including metal oxide, metal hydroxide and metal silicate. Therefore these particles so-called metal-Si-O compounds were possible formed when the precursors reacted with silica walls during their decomposition inside the silica pores.

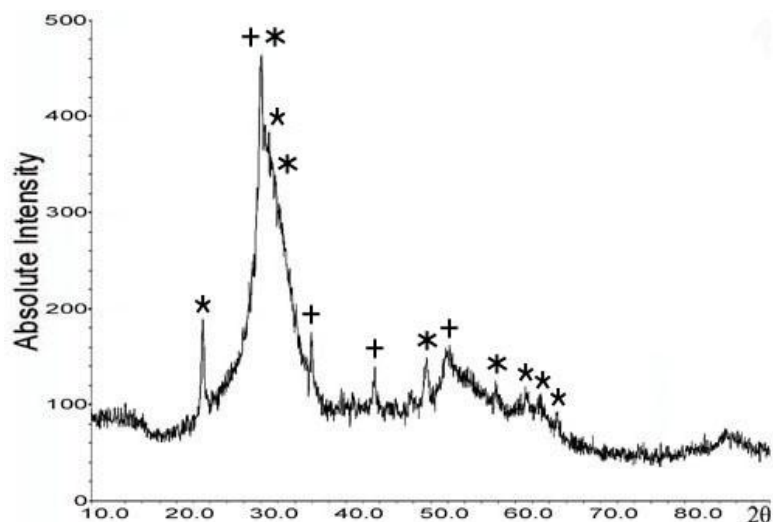


Figure 4-29. XRD pattern of Cd-O-Si specimen (\bullet CdO_2 , E $\text{Cd}(\text{OH})_2$ and O Cd_2SiO_4) after removing SBA-15.

4.3 Ga_2O_3 and ZnO

Ga_2O_3 is used as catalyst in dehydrogenation, methanol synthesis and oxidation of H_2 to H_2O_2 .²⁴¹⁻²⁴³ ZnO is used to detect the nitrosamine content in solution due to its photoluminescence⁷⁹ and produce hydrogen and methanol as the catalyst.^{244,245} So porous Ga_2O_3 and ZnO should exhibit better properties due to their large surface areas. $\text{Ga}(\text{NO}_3)_3 \cdot x\text{H}_2\text{O}$ and $\text{Zn}(\text{NO}_3)_2 \cdot 6\text{H}_2\text{O}$ melt at 110°C and 36.4°C before they decompose to the oxides at 200°C and 131°C , respectively. Therefore both porous Ga_2O_3 and ZnO particles can be prepared using the solid-liquid method.

Figure 4-30 shows a particle of SBA-15 with partial pores containing Ga_2O_3 particles (the Ga_2O_3 particles are indicated by arrows). However, the porous Ga_2O_3 and ZnO particles could not be obtained after SBA-15 was removed by using either HF or NaOH solution because both of them are amphoteric oxides and could dissolve in either acidic or basic solution. Therefore porous Ga_2O_3 and ZnO can not be obtained using silica as template until a new method is found to remove silica.

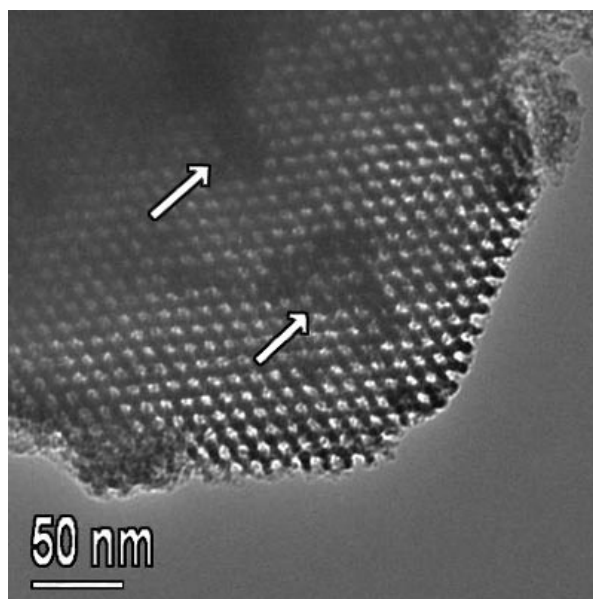


Figure 4-30. TEM image of SBA-15 particle containing some Ga_2O_3 crystals. The arrows indicate the Ga_2O_3 particles filling in the pores.

4.4 La_2O_3 and ZrO_2

La_2O_3 is used as catalyst in hydrogenation, dehydrogenation and CO oxidation.²⁴⁶⁻²⁴⁹ ZrO_2 has wide applications in catalyst, photocatalyst, sensor and electrode.²⁵⁰⁻²⁵³ $\text{La}(\text{NO}_3)_3 \cdot 6\text{H}_2\text{O}$ and $\text{Zr}(\text{NO}_3)_4 \cdot 5\text{H}_2\text{O}$ were selected as precursors and SBA-15 was selected as template for preparing porous La_2O_3 and ZrO_2 by using the solid-liquid method.

Figure 4-31 is TEM images of (a) porous La_2O_3 and (b) ZrO_2 particles with a typical structure of replica of SBA-15. However, both EDX spectra (Figure 4-32) of these porous particles show a Si element peak (the average atomic ratio of Si/La: $72.8 \pm 2.2\%$ and Si/Zr: $38.3 \pm 2.7\%$), which is similar to the anatase nanocrystal-silica composite (Figure 4-8, 4-9), implying these porous particles are La_2O_3 -silica and ZrO_2 -silica composites. For example, the mesostructure of ZrO_2 -silica particles was observed distinctly in the high magnification TEM image (Figure 4-33a). The porous composites are made of connected nanorod-like particles. The HRTEM image in Figure 4-33(b) further confirms the porous ZrO_2 nanocrystals connected by small bridges, and two ZrO_2 phases are observed. The XRD peaks (Figure 4-34) are also indexed to the monoclinic structure (space group $P21/c$, with $a = 0.5150$ nm, $b = 0.5212$ nm, $c = 0.5317$ nm and $\beta = 99.23^\circ$) and tetragonal structure (space group

$P42/nmc$, with $a = 0.3640$ nm and $c = 0.5270$ nm) of ZrO_2 , indicating that both monoclinic and tetragonal ZrO_2 crystals existed in the porous ZrO_2 -silica composites. Recently, a similar porous ZrO_2 -SR (porous ZrO_2 containing SiO_2) material was synthesised using $ZrOCl_2 \cdot 8H_2O$ as precursor by Liu et al.²⁵⁴ and characterised by XRD, TEM, EDX, SEM and nitrogen physisorption.

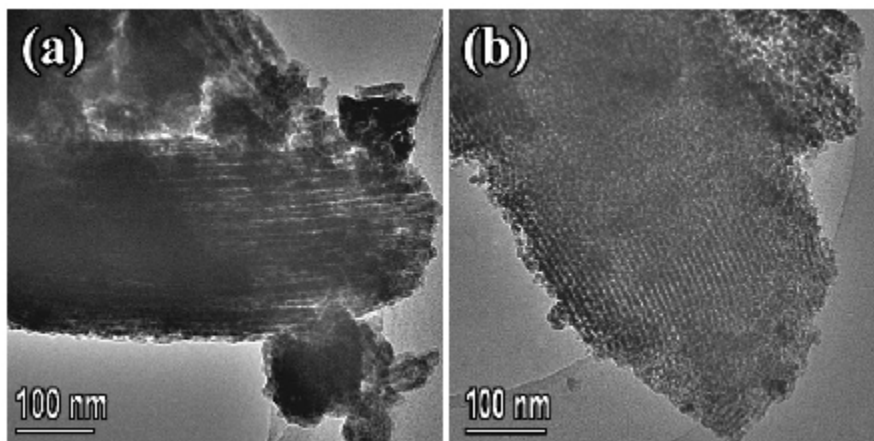


Figure 4-31. TEM images of porous La_2O_3 -silica (a) and ZrO_2 -silica particles (b) after removing SBA-15.

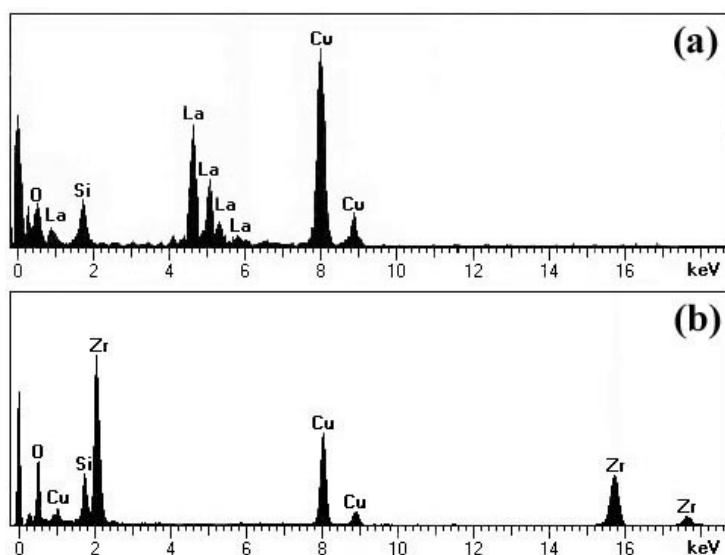


Figure 4-32. EDX graphs of (a) La_2O_3 -silica and (b) ZrO_2 -silica composites after removing SBA-15.

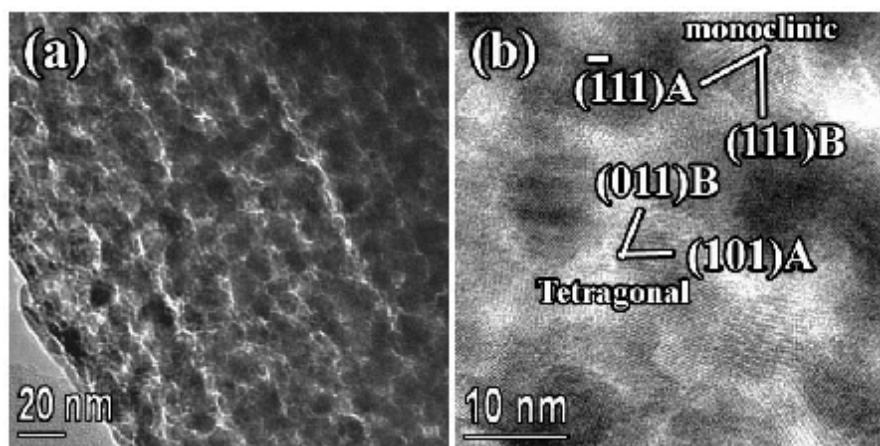


Figure 4-33. (a) TEM image of ZrO_2 -silica composite with high magnification and (b) HRTEM image of ZrO_2 -silica composite. The lattice fringes are indexed to the monoclinic and tetragonal phases of ZrO_2 .

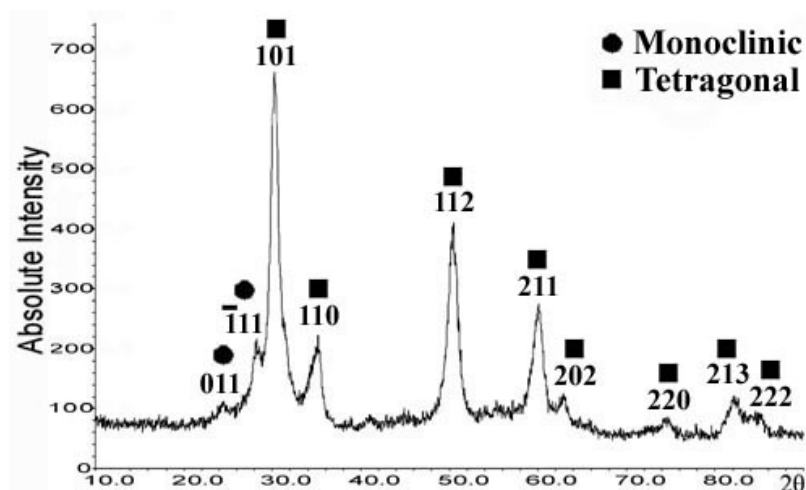


Figure 4-34. XRD pattern of porous ZrO_2 -silica composite after removing SBA-15.

Conclusion

Mesoporous TiO_2 crystals with various phases and large surface area can be synthesised by using SBA-15 and KIT-6 as hard templates. The structures can be tuned by altering the calcination temperature and the type of Ti-containing precursors. Porous pure rutile TiO_2 can be formed even at low temperature ($50\text{ }^\circ\text{C}$) by using a titanium nitrate solution as the precursor. A small amount of anatase appeared at high temperature ($> 300\text{ }^\circ\text{C}$) in the porous particles. Additionally the crystal phase of TiO_2 product also depends highly on the amount of HNO_3 used in preparation of $\text{Ti}(\text{NO}_3)_4$ solution. Because porous anatase has not been observed by TEM, the formed anatase

will reduce the yield of porous TiO₂ (rutile). On the contrary, a porous composite of polycrystalline anatase and β-TiO₂ with silica was produced by using a titanium chloride solution at low temperature (100 °C), which could transform to a porous anatase-silica composite at 600 °C. An interesting phenomenon in these porous particles is that both porous rutile TiO₂ and porous anatase/β-TiO₂ nanocrystals-silica synthesised at 200 °C have the largest surface areas in specimens possibly due to the crystallisation behaviour of TiO₂ inside the pores of silica at various calcination temperatures.

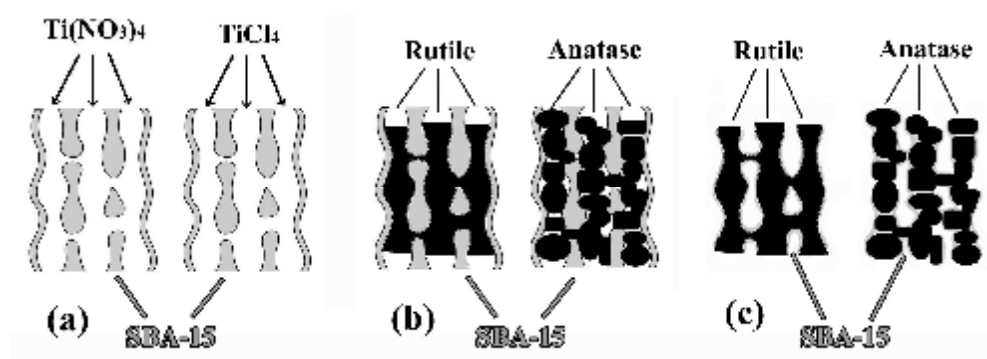


Figure 4-35. The scheme of porous rutile TiO₂ and anatase nanocrystal-silica composites synthesised using titanium nitrate and titanium chloride solutions as precursors, respectively. (a) Ti-containing precursors move into the pores of SBA-15 using evaporation method. (b) 3D rutile network and anatase nanoparticles formed in the pores of SBA-15. (c) Porous rutile TiO₂ and anatase nanocrystal-silica composite obtained after removing the SBA-15 template.

The possible synthetic mechanism of these two porous materials is shown as Figure 4-35. It is believed that the long Ti-O-Ti chains in titanium oxynitrate (Figure 4-36), which is the hydrolysate of titanium nitrate by partially losing HNO₃ during drying and thermal treatment, ensures a high loading of the precursor to form large TiO₂ crystals inside the SBA-15 pores instead of forming separated nanocrystallites or a layer of TiO₂ on the inner walls of silica.²⁵⁵ On the contrary, the hydrolysate of titanium chloride without long Ti-O-Ti chains lead to nanoparticle formation inside the silica pores. Anatase TiO₂ can also be prepared at 600 °C by using a titanium isopropoxide or Ti(SO₄)₂ solution as the precursor, whereas these products are all non-porous congregation of nanoparticles. No Ti-O-Si bonds connecting anatase products with SBA-15 template in TiO₂(TIP)-600 and TiO₂(H₂SO₄)-600 specimens,

confirmed by EDX spectra, would be the possible reason of unsuccessful maintenance of ordered mesostructure after removing silica template.

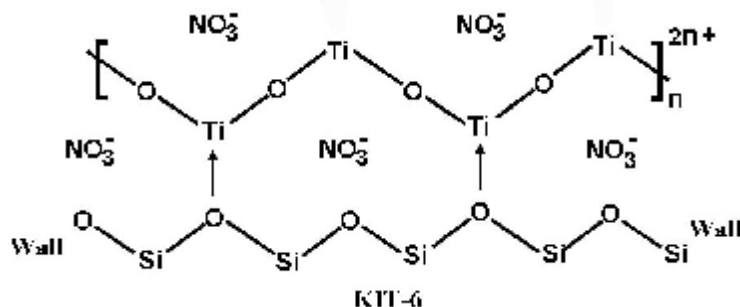


Figure 4-36. The structure of $\text{TiO}(\text{NO}_3)_2$ with long Ti-O-Ti chains.

The proton conductivity of mesoporous rutile TiO_2 templated by KIT-6 was found to be quite high ($8 \times 10^{-3} \text{ S} \cdot \text{cm}^{-1}$) at high relative humidity at temperatures of 50°C compared to normal rutile and such mesoporous materials might be useful as inorganic fillers in proton exchange membranes. Porous rutile TiO_2 templated by SBA-15 and KIT-6 has large surface area of $163.0 \text{ m}^2/\text{g}$ and $130.2 \text{ m}^2/\text{g}$ respectively, and can accommodate more Li^+ per TiO_2 unit than any other previously reported forms of TiO_2 . For example, up to 1.06 Li per TiO_2 in $\text{TiO}_2(\text{HNO}_3)$ -200 was detected for the first discharge that corresponds to a high capacity of 356.6 mA h/g . This good performance of porous rutile TiO_2 can be utilized as Li storage materials or electrodes. On the other hand, porous anatase-silica composites exhibit higher photocatalytic activities than TiO_2 -loaded mesoporous silica and can be applied as a good photocatalyst.

In addition, other porous metal oxides, such as MgO , CdO , ZnO , Ga_2O_3 , La_2O_3 and ZrO_2 , were not successfully synthesised using SBA-15 as template. Some non-porous particles of metal-O-Si compounds (e.g. $\text{Mg}(\text{OH})_2$ -silica) were formed after SBA-15 was removed. Ga_2O_3 - and ZnO -loaded SBA-15 can not be separated to obtain porous Ga_2O_3 and ZnO particles because both of them are amphoteric oxides and would be dissolved in either HF or NaOH solution. Although porous ZrO_2 - and La_2O_3 -silica composites were also synthesised successfully using SBA-15 as the template, pure porous ZrO_2 and La_2O_3 crystals can not be obtained after SBA-15 was removed. Further exploration of syntheses of these porous metal oxides were carried out later by using mesoporous carbons instead of mesoporous silicas as templates.

5. Porous metal oxides templated by FDU-12 and SBA-16

According to the chapter 3 and 4, porous metal oxides of Co_3O_4 , Cr_2O_3 , NiO , CeO_2 , In_2O_3 , WO_3 templated by SBA-15 and KIT-6 were synthesised successfully by using the solid-liquid method.¹⁹⁸ Additionally, the novel porous rutile TiO_2 and anatase nanocrystals-silica composite were also prepared using SBA-15 and KIT-6 as templates and exhibited interesting properties in proton conductivity, Li ion insertion and photoactivity.^{199,200} FDU-12 and SBA-16, as novel mesoporous silicas, have larger surface areas in comparison with SBA-15 and KIT-6 due to their nanospherical pore structure (Figure 5-1). Therefore, the metal oxides templated by FDU-12 and SBA-16 are expected to have larger surface areas and better properties than those templated by SBA-15 and KIT-6, as catalysts, electronic devices, semiconductors and gas sensors.¹⁰⁻¹²

Table 5-1. Melting point (MP) and decomposition temperature (DT) of the nitrate precursors for porous transition metal oxides.

Precursor	MP(°C)	DT(°C)	Oxide
$\text{Co}(\text{NO}_3)_2 \cdot 6\text{H}_2\text{O}$	55	>74	Cubic Co_3O_4
$\text{Ni}(\text{NO}_3)_2 \cdot 6\text{H}_2\text{O}$	56.7	>110	Cubic NiO
$\text{Ce}(\text{NO}_3)_3 \cdot 6\text{H}_2\text{O}$	96	200	Cubic CeO_2
$\text{In}(\text{NO}_3)_3 \cdot x\text{H}_2\text{O}$	100	>100	Cubic In_2O_3
$\text{Cr}(\text{NO}_3)_3 \cdot 9\text{H}_2\text{O}$	66	>100	Rhombohedral Cr_2O_3
$\text{Fe}(\text{NO}_3)_3 \cdot 9\text{H}_2\text{O}$	47	>100	Rhombohedral Fe_2O_3
$\text{Ti}(\text{NO}_3)_4$		240~270	tetragonal TiO_2
$\text{H}_3\text{PO}_4 \cdot \text{W}_{12} \cdot x\text{H}_2\text{O}$	107	>385	tetragonal WO_3
$\text{Mn}(\text{NO}_3)_2 \cdot 6\text{H}_2\text{O}$	26	>160	tetragonal MnO_2
		>530	cubic Mn_2O_3

In this project, porous single crystals of Co_3O_4 , NiO , CeO_2 and In_2O_3 templated by FDU-12 and SBA-16^{196,197} were synthesised by using the solid-liquid method and characterised by XRD, HRTEM, SAED, EDX and N_2 adsorption/desorption. Table 5-1 shows the melting point and decomposition temperature of these metal-containing precursors and the crystal systems of these metal oxides.

5.1 Mesoporous silicas of FDU-12 and SBA-16

Unlike SBA-15 and KIT-6, in which the basic building unit of pores is cylindrical, both FDU-12 and SBA-16 consist of spherical nano-cavities linked together by some very short nano-channels or windows.^{40,43,46} SBA-16 has a body-centred cubic structure (space group $Im\bar{3}m$) and FDU-12 is face-centred cubic (space group $Fm\bar{3}m$). Accordingly, each spherical nanocage is 8 coordinated by the neighbouring nanocages in SBA-16, but 12 coordinated in FDU-12. The large cavities in both phases were produced in the presence of triblock copolymer templates, $EO_{106}PO_{70}EO_{106}$ (Pluronic F127). The pore sizes of SBA-16 and FDU-12 are normally about 5.4 nm and 10-12.3 nm in diameter, respectively. It is even possible to increase the pore size up to 22.3 nm in FDU-12 with a hydrothermal treatment at 15 °C,⁴⁴ and the size of the entrances joining two adjacent cavities can be tuned in the range of 4-9 nm in diameter using different maturation temperatures in a range from 100 to 140 °C.

Figure 5-1(a) shows TEM image of FDU-12 with a face-centred cubic structure. Although this fcc phase dominates the structure, some stacking faults, i.e. an irregular intergrowth of the cubic close packed (ccp) phase (ABCABC stacking) and the hexagonal close packed (hcp) phase (ABAB stacking), were also observed, which is similar to the structural property observed in SBA-2.²⁵⁶ The body-centred cubic structure of SBA-16 was observed by TEM in Figure 5-1(b).

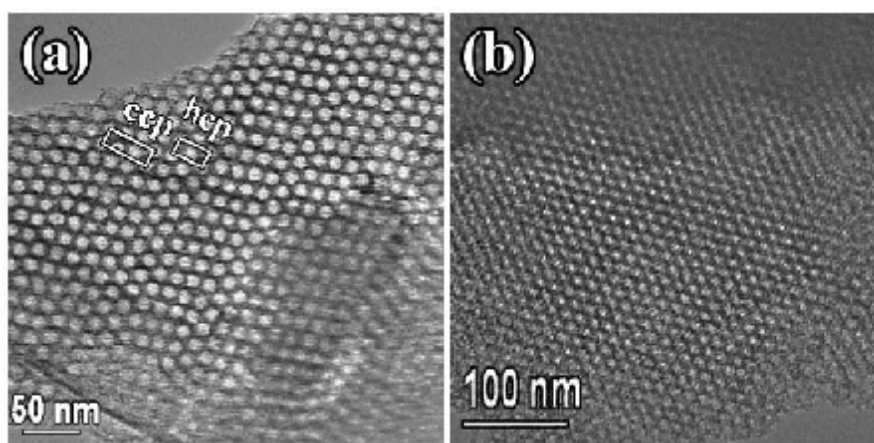


Figure 5-1. TEM images of (a) FDU-12 and (b) SBA-16, viewed down the [110] and [111] directions, respectively. The cubic close packed (ccp) phase and the hexagonal close packed (hcp) phase are indicated in image (a).

5.2 Cubic metal oxides

The cubic crystal has unit cell parameters of $a=b=c$ and $\alpha=\beta=\gamma=90^\circ$, and an isotropic property. Figure 5-2 shows primitive, body-centred and face-centred cubic symmetries. Some porous cubic metal oxides, such as Co_3O_4 , NiO , CeO_2 and In_2O_3 , have been synthesised by using SBA-15 and KIT-6 as templates in the previous work.^{122,124,198} Herein presents these porous cubic metal oxides synthesised by using FDU-12 and SBA-16 as templates, and their detailed structures were examined by XRD, HRTEM, SAED, EDX and N_2 adsorption/desorption.

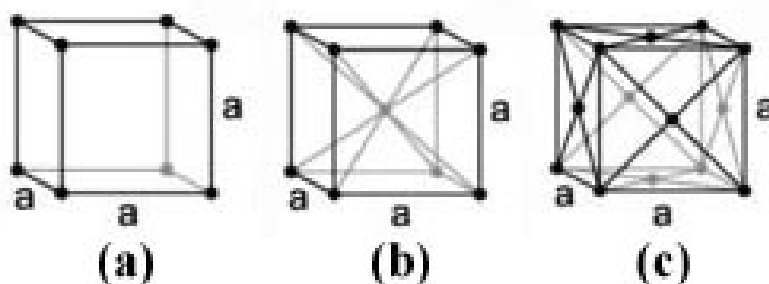


Figure 5-2. Schematic drawing of cubic (isometric) crystal; (a) primitive, (b) body-centered and (c) face-centered.

5.2.1 Co_3O_4

Co_3O_4 has a cubic structure with the unit cell parameter, $a = 0.8085$ nm, space group $Fd\bar{3}m$, and is an efficient catalyst to oxidize H_2 , CO , NO and methane.^{13,127-129} $\text{Co}(\text{NO}_3)_2 \cdot 6\text{H}_2\text{O}$, whose melting point (55°C) is lower than its decomposition temperature ($> 74^\circ\text{C}$), was selected as the precursor, and the solid liquid method was used to synthesise porous crystalline Co_3O_4 crystals templated by FDU-12 and SBA-16.^{196,197}

Figure 5-3(a) shows a TEM image of a FDU-12 particle whose spherical cavities have been partially filled with Co_3O_4 crystals (the dark areas in the image). The size of these particles is variable. For example, the particle in the centre of Figure 5-3(a) is about 150 nm in diameter, while at the top right corner, there is a much larger particle. The silica particles cannot be entirely filled by Co_3O_4 , because even it was fully filled at beginning by the precursor, $\text{Co}(\text{NO}_3)_2 \cdot 6\text{H}_2\text{O}$, the volume of the cobalt compound would be significantly reduced when it decomposed and formed Co_3O_4 . Figure 5-3(b) shows mesoporous Co_3O_4 crystals with spherical shape after the silica template was removed. The mesopore system in FDU-12 has been negatively replicated by the metal oxide.

The diameter of the main particle is about 600 nm and some small particles nearby are only about 100 nm in diameter.

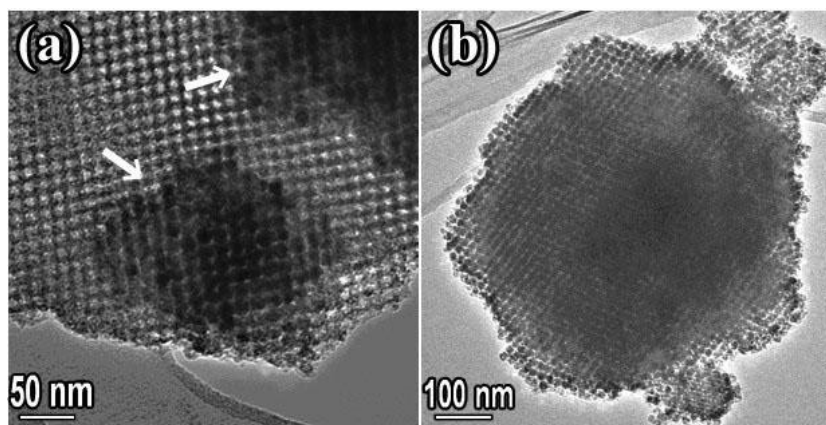


Figure 5-3. TEM image of (a) a particle of FDU-12 containing some cobalt oxide areas indicated by the arrows and (b) porous cobalt oxide crystals after removing the silica template.

The chemical composition of the specimen was examined by EDX. The EDX spectrum from cobalt oxide with the FDU-12 and SBA-16 template show the elements of cobalt, oxygen and silicon. After the template was dissolved, no silicon was present in the samples (the inset of Figure 5-4). The characterisation of the specimens was also performed by using XRD. Both XRD patterns (Figure 5-4) of the cobalt oxides templated by FDU-12 and SBA-16 indicate that the products are cubic Co_3O_4 crystals.

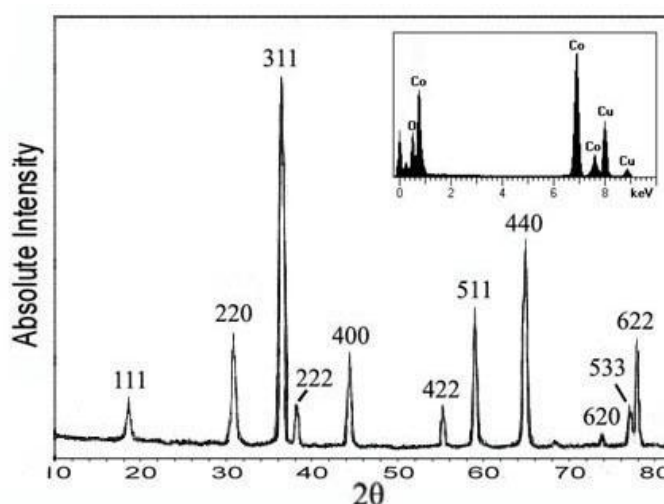


Figure 5-4. XRD pattern of porous Co_3O_4 particles after FDU-12 was removed (the inset is EDX spectrum of Co_3O_4 particles). The XRD pattern and EDX spectrum of Co_3O_4 templated by SBA-16 are similar with these.

TEM images with higher magnifications of the porous Co_3O_4 crystals templated by FDU-12 (Figure 5-5a) and SBA-16 (Figure 5-5c) indicates that the porous crystals are both made of nanoballs connected together by nanobridges. Such nanobridges could be observed at the edge of the particles as indicated by arrows in Figure 5-5(d). In the FDU-12 templated Co_3O_4 , the nanospheres are in a cubic close packed arrangement with stacking faults, namely irregular intergrowth of cubic close-packing (ccp) and hexagonal close packing (hcp), were often observed (Figure 5-5a). Such defects are also common in the FDU-12 template (Figure 5-1a). In the SBA-16 templated porous oxide, the nanospheres are in a body centred arrangement and such defects do not form (Figure 5-5c).

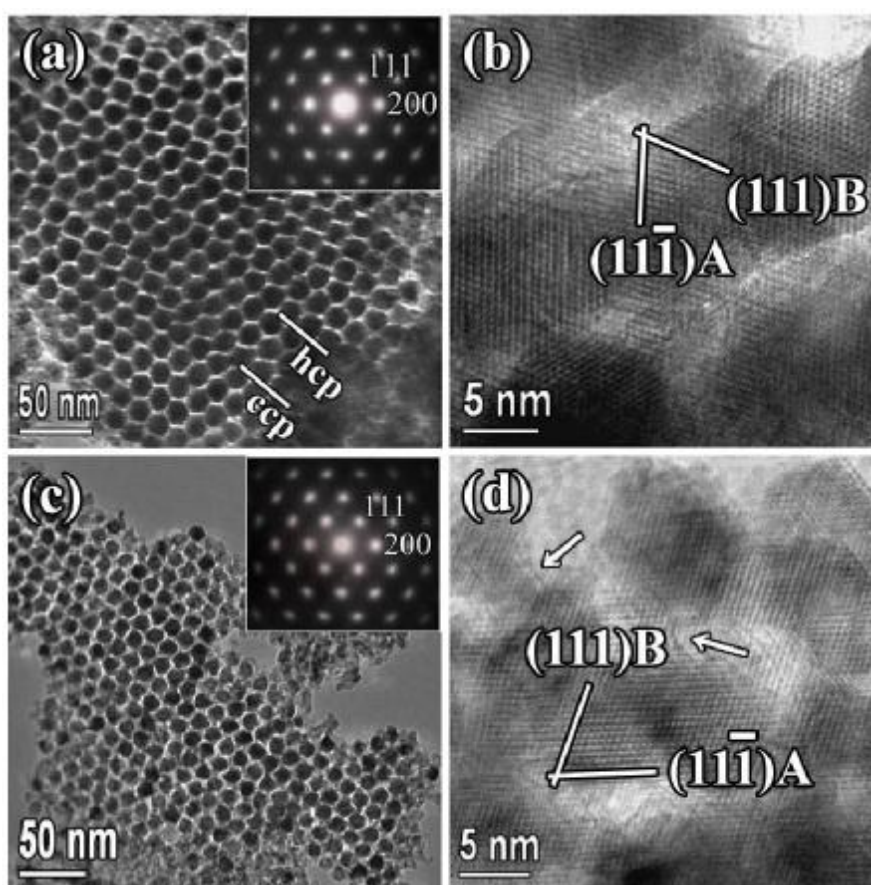


Figure 5-5. TEM images of porous Co_3O_4 templated by (a) FDU-12 and (c) SBA-16. In (a), irregular intergrowth of ccp and hcp stackings is indicated. The insets in (a) and (c) are SAED patterns from these two samples of crystalline Co_3O_4 . HRTEM images of Co_3O_4 templated by (b) FDU-12 and (d) SBA-16, respectively. The arrows in (d) point to bridges connecting two nanospheres.

SAED patterns from large areas show the single-crystal property and can be indexed to the cubic Co_3O_4 structure, space group $Fd\bar{3}m$ with $a = 0.8085$ nm, as shown in the insets in Figure 5-5(a) and (c). HRTEM images of the porous Co_3O_4 crystals further confirm the single-crystal property (Figure 5-5b,d). Since the crystal orientation of Co_3O_4 has no relation with the orientation of the mesopore network, it is difficult to find a viewing direction parallel to a principal orientation in both the Co_3O_4 crystal and the mesopore system, as demonstrated in the KIT-6 templated Cr_2O_3 .¹²¹ Consequently, when we found a good projection for the mesopore network, e.g. shown in Figure 5-5(a) and (c), we missed a principal crystal orientation of Co_3O_4 . Similarly, when we approached a principal orientation of the crystal as shown in Figure 5-5(b) and (d), the arrangement of the nanospheres could not be clearly revealed.

Theoretically, the surface areas of FDU-12 and SBA-16 are larger than those of SBA-15 and KIT-6, accordingly, therefore the FDU-12 and SBA-16 templated Co_3O_4 should have larger surface areas in comparison with the KIT-6 templated Co_3O_4 . Figure 5-6 shows the nitrogen adsorption/desorption isotherms of Co_3O_4 templated by FDU-12 and SBA-16, respectively. The isotherms of Co_3O_4 porous crystals are both type IV with a hysteresis loop, indicating the mesoporous property. The specific surface areas of Co_3O_4 crystals templated by FDU-12 and SBA-16 are 151 and 122.4 m^2/g , respectively, which are larger than the surface area of Co_3O_4 templated by KIT-6 (92 m^2/g).¹²⁴ For a comparison with the surface areas in FDU-12 (735.7 m^2/cm^3) and in SBA-16 (686 m^2/cm^3), the above values were altered to 450 m^2/cm^3 (FDU-12 templated, pore volume is 0.171 cm^3/g) and 298 m^2/cm^3 (SBA-16 templated, pore volume is 0.246 cm^3/g) when the densities of 2.2 g/cm^3 (SiO_2) and 6.07 g/cm^3 (Co_3O_4) were used. The diameters of the nanospheres in these two specimens are similar as seen in Figure 5-5. and the average pore size of the SBA-16 templated Co_3O_4 (6.6 nm) is slightly larger than that in the FDU-12 templated sample (6.1 nm). The large specific surface areas in the samples also indicate that the yields of the porous crystals are high.

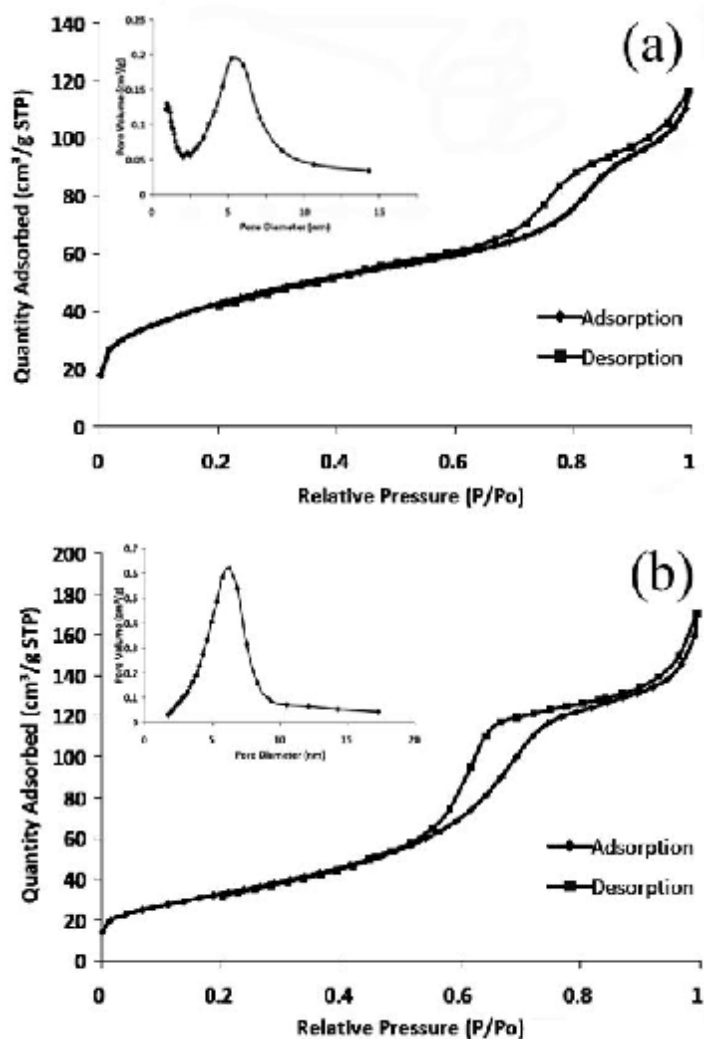


Figure 5-6. Nitrogen adsorption/desorption isotherms measured at 77 K from porous crystals of Co_3O_4 templated by (a) FDU-12 and (b) SBA-16. Insets: pore size distribution of the corresponding crystals.

5.2.2 NiO

NiO has a face-centered cubic structure with $a = 0.4176 \text{ nm}$, space group $Fm\bar{3}m$. This material has a good electrochemical capacitance and has a potential application in electrochemical devices.¹³²⁻¹³⁴ Therefore, the porous NiO with a large surface area is attractive and so was prepared by using the solid liquid method, as the precursor of $\text{Ni}(\text{NO}_3)_2 \cdot 6\text{H}_2\text{O}$ used in the experiment has a low melting point ($56.7 \text{ }^\circ\text{C}$) and a higher decomposition temperature ($>110 \text{ }^\circ\text{C}$).^{196,197}

The particles consisting of some nanospheres connected by nanobridges have a negative mesostructure of FDU-12 and SBA-16, which was observed by TEM in

Figure 5-7(a) and (c). Some disordered small particles (Figure 5-7a) and large bulk particles (Figure 5-7c) were also observed around the porous NiO particles, resulting in the low yields of porous products, say about 30 to 40 %, according to the TEM observation.

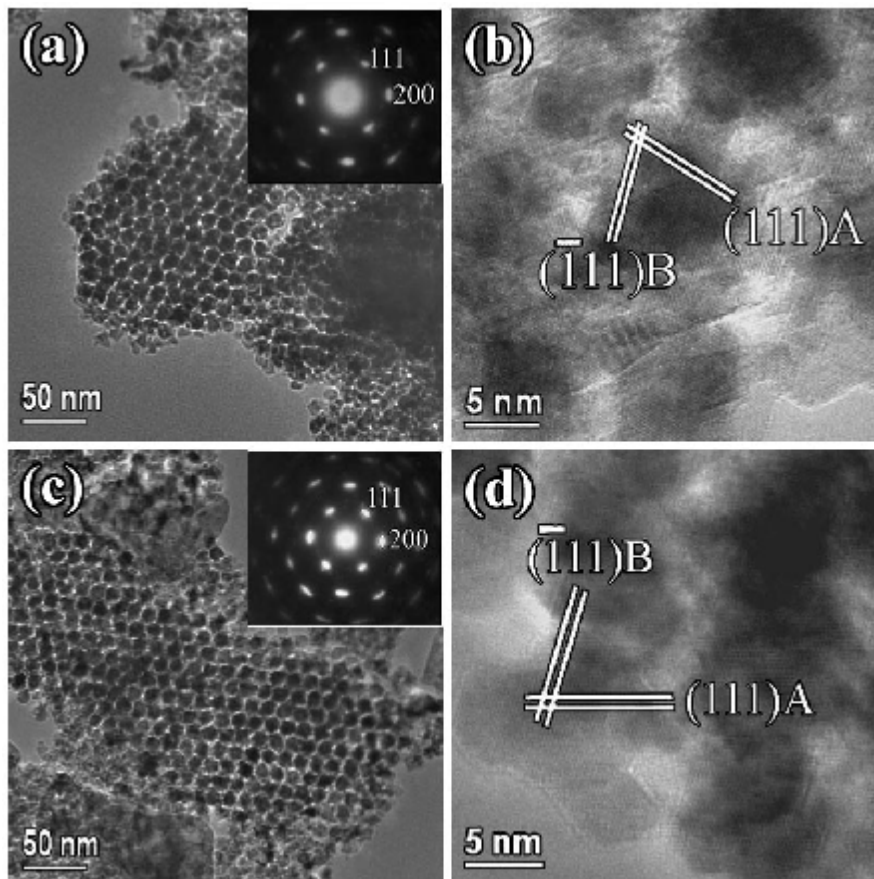


Figure 5-7. TEM images and HRTEM images of porous NiO templated by (a,b) FDU-12 and (c,d) SBA-16, respectively. The insets in (a) and (c) are SAED patterns, showing the monocrystalline NiO.

SAED patterns of FDU-12 and SBA-16 templated NiO particles (the insets of Figure 5-7a,c) indicate that both of them are single crystals, and are indexed to the cubic NiO structure, space group $Fm\bar{3}m$ with $a = 0.4176$ nm. HRTEM images (Figure 5-7b,d) further confirm the single-crystal property, although the crystal lattices in the images are not very distinct.

The EDX spectrum of porous NiO templated by FDU-12 (the inset of Figure 5-8) shows two strong element peaks of Ni and O, and a small amount of Si was detected, indicating the almost removal of silica template from the products. The XRD pattern (Figure 5-8) also confirms that these porous particles are NiO crystals.

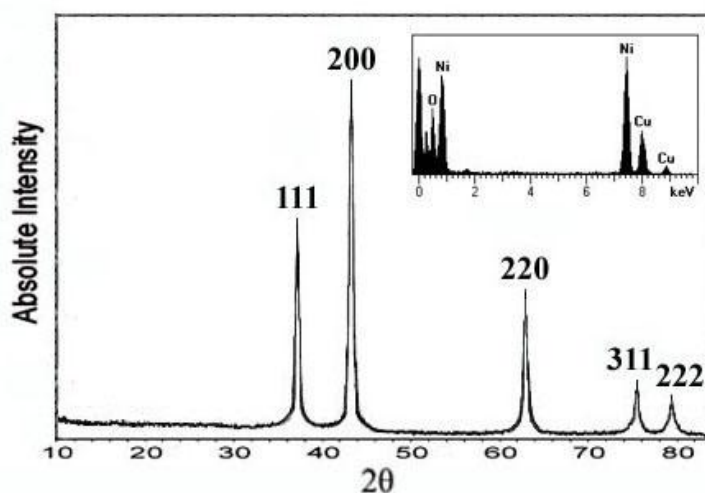


Figure 5-8. XRD pattern of porous NiO particles after FDU-12 was removed. The inset is EDX spectrum of NiO particles.

5.2.3 CeO₂

CeO₂ is a good catalyst for oxidation of acrylic acid and CO, and methanol decomposition.¹³⁵⁻¹³⁸ It has a cubic structure with the unit cell dimension, $a = 0.54124$ nm, space group $Fm\bar{3}m$. Porous monocrystalline CeO₂ templated by FDU-12 and SBA-16 were synthesised successfully using the solid-liquid method.^{196,197} In this method, Ce(NO₃)₃·6H₂O as the precursor has the melting point of 96 °C and the decomposition temperature of ~200 °C.

Figure 5-9 shows the TEM images and HRTEM images of CeO₂ templated by FDU-12 (Figure 5-9a,b) and SBA-16 (Figure 5-9c,d), respectively. The cubic arrangement of nanospheres connected by nanobridges could be observed in either TEM images or HRTEM images. The nanobridges indicated by the arrows are distinct in the HRTEM image of Figure 5-9(b). The yields of porous products are not high (~20%) according to the TEM observation, and some disordered small particles were formed simultaneously (Figure 5-9a). Nevertheless, formation of porous CeO₂ crystals in the cage-containing mesoporous silicas is certainly feasible. SAED patterns (the insets of Figure 5-9a,c) and HRTEM images (Figure 5-9b,d) confirm the single-crystal property and are indexed to cubic CeO₂ structure (space group $Fm\bar{3}m$, $a = 0.54124$ nm). The XRD pattern (Figure 5-10) also proves that the porous replicas of FDU-12 and SBA-16 are CeO₂ crystals, and only little silica were detected in the EDX spectrum (the inset of Figure 5-10) after removing the silica template.

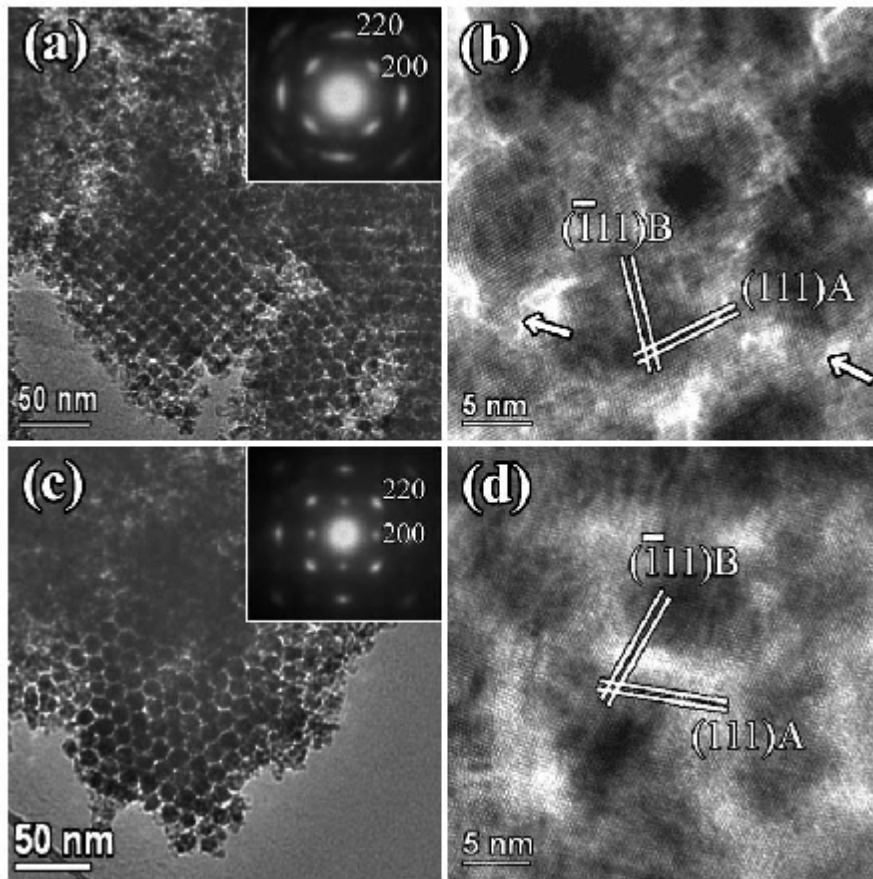


Figure 5-9. TEM images and HRTEM images of porous CeO_2 templated by (a,b) FDU-12 and (c,d) SBA-16, respectively. The insets in (a) and (c) are SAED patterns. The arrows in (b) point to the bridges connecting two nanospheres.

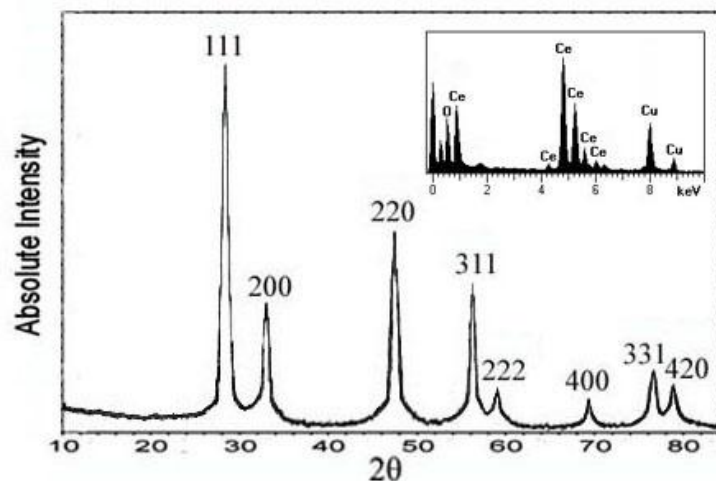


Figure 5-10. XRD pattern of porous CeO_2 particles after silica template was removed. The inset is EDX spectrum of CeO_2 particles.

5.2.4 In₂O₃

In₂O₃ which has a body-centred cubic structure with $a = 1.0118$ nm (space group $Ia\bar{3}$) is an important transparent conductive oxide, and has potential applications in solar cells, ultraviolet-visible (UV) lasers, detectors and gas sensors.¹⁴⁰⁻¹⁴³ Since the precursor of In(NO₃)₃· x H₂O melts at 100 °C before decomposition, porous In₂O₃ crystals templated by FDU-12 and SBA-16 can be made by using the solid-liquid method.^{196,197}

The typical structure of FDU-12 and SBA-16 templated In₂O₃ were observed by TEM in Figure 5-11(a-d). However, some bulk material could also be observed around the porous In₂O₃ crystals, and the yield of the products is still low (~20%). Figure 5-11(a) and (c) show a fcc structure, viewed down {110} face, and a bcc structure, viewed down {111} face, respectively. The arrangement of nanospheres is consistent with the structure of silica template FDU-12 (fcc) and SBA-16 (bcc).

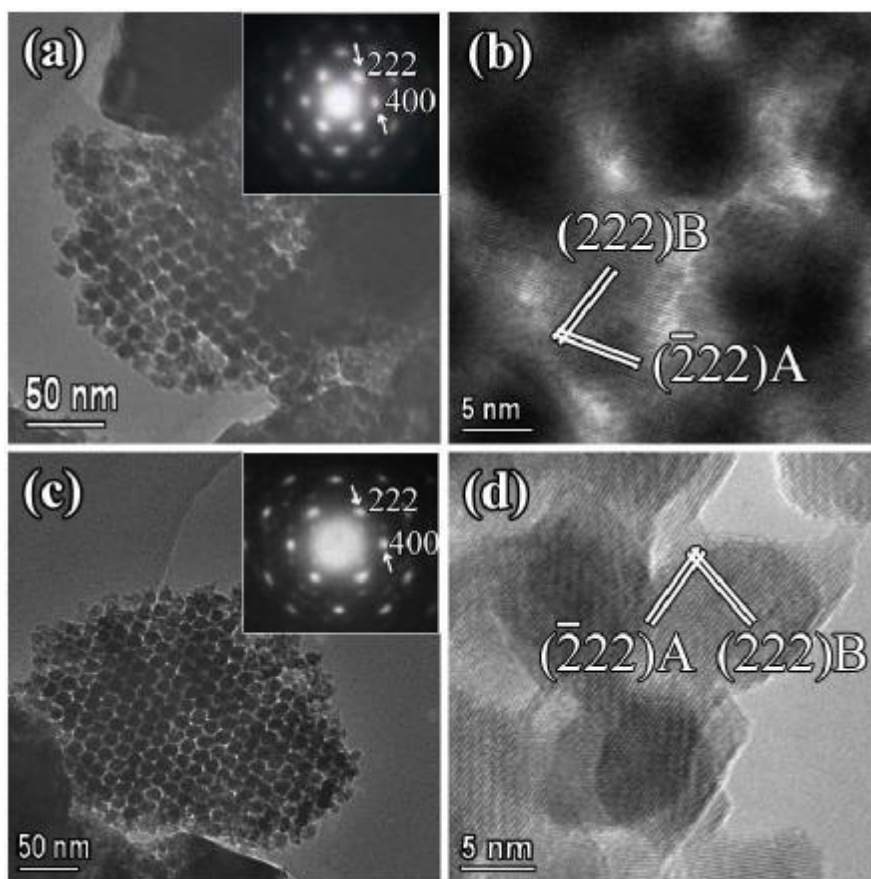


Figure 5-11. TEM images and HRTEM images of porous In₂O₃ templated by (a,b) FDU-12 and (c,d) SBA-16, respectively. The insets in (a) and (c) are SAED patterns.

The single-crystal property of the particles was confirmed by the SAED patterns, which were normally recorded from the whole particles covering many nanospheres. The insets of Figure 5-11(a) and (c) show the typical SAED patterns of cubic In_2O_3 structure from a large porous particle, when viewed down the $[0\bar{1}1]$ zone axis of the In_2O_3 structure. It is noticed that the (200) and (022) diffraction spots are not absent according to the symmetry of space group $Ia\bar{3}$, but they are too weak to be seen in the SAED patterns. The EDX spectrum (the inset of Figure 5-12) from FDU-12 and SBA-16 templated In_2O_3 particles show two elements of In and O after the silica template was removed. The In_2O_3 crystals were confirmed by XRD patterns (Figure 5-12), and the observed XRD reflections are quite broad, indicating a characteristic of nanoscale solid spheres in the specimens.

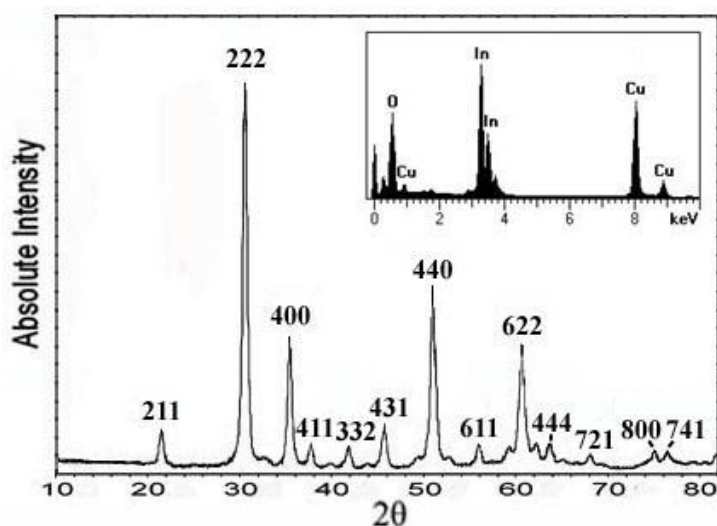


Figure 5-12. XRD pattern of porous In_2O_3 particles after silica template was removed. The inset is EDX spectrum of In_2O_3 particles.

5.3 Non-cubic metal oxides

The rhombohedral unit cell (Figure 5-13a) is relatively similar to the cubic unit cell, and can be seen as a cubic unit cell that has been stretched along a diagonal direction ($a=b=c$, and $\alpha, \beta, \gamma \neq 90^\circ$). The tetragonal unit cell (Figure 5-13b,c) is derived by stretching a cubic lattice along one of its lattice vectors, forming a rectangular lattice ($a=b \neq c$, and $\alpha=\beta=\gamma=90^\circ$). There are two tetragonal Bravais lattices: the simple tetragonal (from stretching the simple-cubic lattice) and the centered tetragonal (from stretching either the face-centered or the body-centered cubic lattice). Some porous

rhombohedral metal oxides such as Cr_2O_3 ^{120,121} and Fe_2O_3 ^{149,150} ($a=b\neq c$) and porous tetragonal metal oxides such as TiO_2 ^{199,200} and WO_3 ^{164,165} have been synthesised successfully by using SBA-15 and KIT-6 as templates. Therefore, these porous non-cubic metal oxides were expected to be also synthesised by using FDU-12 and SBA-16 as templates. Their structures were characterised by TEM.

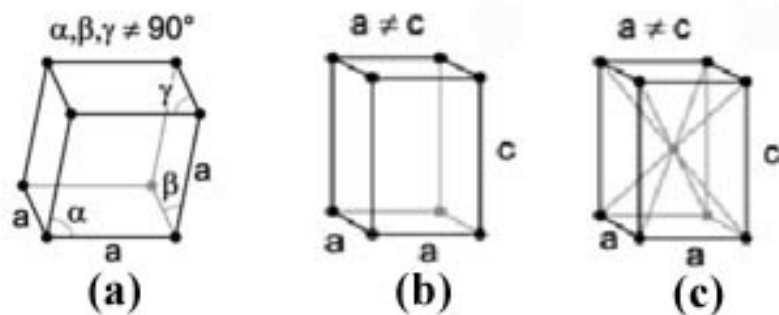


Figure 5-13. Schematic drawing of (a) rhombohedral (trigonal) unit cell, and tetragonal unit cells, (b) simple and (c) body-centered.

5.3.1 Cr_2O_3 and Fe_2O_3

Unlike the aforementioned cubic oxides, the structure of Cr_2O_3 and Fe_2O_3 is rhombohedral, space group $R\bar{3}c$, with the unit cell parameters $a = 0.4959$ nm, $c = 1.359$ nm, and $a = 0.5032$ nm, $c = 1.3733$ nm, respectively. Cr_2O_3 plays an important role in magnetics and catalysis such as polymerisation of caprolactam and dodecalactam, hydrogenation of aliphatic carboxylic acids and oxidative dehydrogenation of ethane with carbon dioxide.^{118,119} Fe_2O_3 is an important catalyst for hydroxylation of phenol, selective hydrogenation of acetic acid and methanol decomposition, and possibly a good material used in rechargeable lithium batteries.¹⁴⁵⁻¹⁴⁸ Therefore it is expected that porous Cr_2O_3 and Fe_2O_3 synthesised by using FDU-12 and SBA-16 as templates will have a large surface area and would present some interesting properties.

Fabrication of the porous crystals of Cr_2O_3 templated by SBA-15 and KIT-6 has been proven to be very successful, no matter which method was used for loading the Cr-containing precursors.^{120,121,124,198} However, crystal growth of Cr_2O_3 in FDU-12 and SBA-16 in the present work seems to be difficult, even when using the same synthetic conditions as reported. Figure 5-14(a) and (b) show a typical TEM image of the Cr_2O_3 product using FDU-12 and SBA-16 as templates. Although large particles

were formed consisting of nanocrystallites in a size comparable with the cage size in FDU-12, the ordering of these nanocrystallites is very poor with a large number of nanocrystallites missing. Most importantly, the morphologies of these nanocrystallites are not perfectly spherical in comparison with the porous cubic metal oxides as presented in Figure 5-5. The sizes of these nanocrystallites are also not uniform. The TEM image in Figure 5-14(b) shows the Cr_2O_3 synthesised using SBA-16 as a template. Its morphology seems more like porous particles containing some nanospheres. However its ordering is poor as well, similar to the morphology of Cr_2O_3 templated by FDU-12.

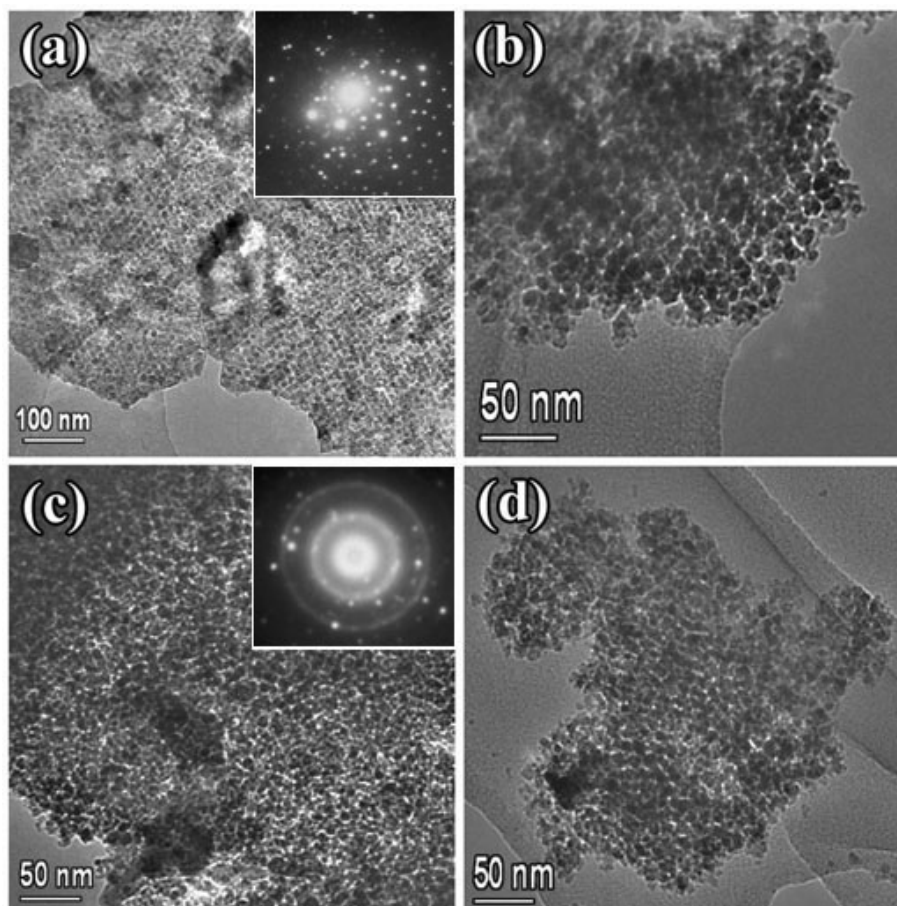


Figure 5-14. TEM images of Cr_2O_3 and Fe_2O_3 products using (a,c) FDU-12 and (b,d) SBA-16 as templates. The insets of (a) and (b) are SAED patterns of Cr_2O_3 and Fe_2O_3 templated by FDU-12, respectively.

Figure 5-14(c) and (d) shows the Fe_2O_3 products templated by FDU-12 and SBA-16, respectively. Compared with the morphologies of FDU-12 and SBA-16 templated by Cr_2O_3 observed in Figure 5-14(a) and (b), the FDU-12 and SBA-16

templated Fe_2O_3 have much poorer structure. The specimens appeared to be some congregations of nanocrystallites without any ordering. Bearing in mind that, under the same synthetic conditions, SBA-15 and KIT-6 templated porous crystals of Fe_2O_3 can be easily produced,^{149,150} the unsuccessful preparation of porous Cr_2O_3 and Fe_2O_3 using FDU-12 and SBA-16 as templates indicates that asymmetric rhombohedral crystals can not be fabricated well in the 3D cage-containing mesopores.

The inset of Figure 5-14(a) shows the SAED pattern of Cr_2O_3 templated by FDU-12, which includes regular dot array, indicating that the particle with poor mesostructure was made partially of single crystals. However, the XRD pattern of Fe_2O_3 templated by FDU-12 (the inset of Figure 5-14b) is an irregular set of dots and concentric rings, implying that the specimen is congregations of nanocrystallites.

5.3.2 TiO_2 and WO_3

Both rutile TiO_2 and WO_3 have a tetragonal structure with $a = 0.4600$ nm, $c = 0.2965$ nm (space group $P4_2/mnm$), and $a = 0.5272$ nm, $c = 0.3920$ nm (space group $P4/nmm$), respectively. Rutile is a thermodynamically stable phase of TiO_2 and is a popular choice as an electrode by addition of lithium and carbon,²¹⁵⁻²¹⁷ catalyst^{218,219} and Li storage material.^{27,220} WO_3 has a wide range of interesting catalytic, electrochromic and gas sensing properties.¹⁶⁰⁻¹⁶³ These porous rutile TiO_2 and WO_3 , which were proven to be prepared by using SBA-15 and KIT-6 as templates, were expected to be formed by using FDU-12 and SBA-16 as templates in this experiment.

Compared with the SBA-15 and KIT-6 templated rutile TiO_2 ,^{199,200} the mesostructures of TiO_2 particles templated by FDU-12 and SBA-16 were not perfect and the morphology of nanosphere unit was poor (Figure 5-15a,b). Similarly, differing from the porous WO_3 templated by SBA-15 and KIT-6,^{164,165} both FDU-12 and SBA-16 templated WO_3 particles have poor mesostructure in Figure 5-15(c) and (d). Although partial ordering can be found in a very small region (e.g. the right part of the particle shown in Figure 5-15d) and the morphologies of nanospheres are perfect, the particles are not highly ordered, as seen in Figure 5-15(c). Therefore it is proven again that high structural symmetry of a crystal has an important effect on the replication of porous metal oxides in cage-containing mesoporous silicas.

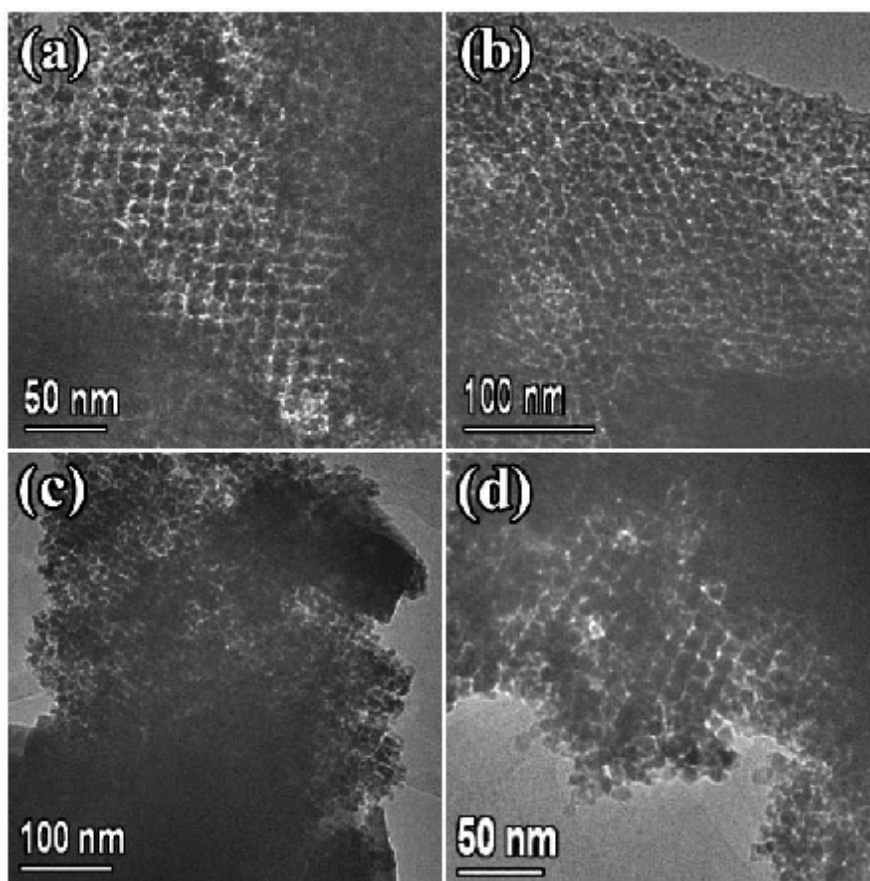


Figure 5-15. TEM images of TiO_2 and WO_3 products using (a,c) FDU-12 and (b,d) SBA-16 as templates, respectively.

5.4 Tetragonal MnO_2 and cubic Mn_2O_3

To further confirm this hypothesis, we carried out preparation of another transition metal oxide: manganese oxide. Formation of manganese oxides is not as simple as other oxides since they often exist in several forms with different Mn oxidation states. MnO_2 is of interest in Li/ MnO_2 batteries and has been widely used as magnetic materials, electrode materials and catalysts.¹⁵¹⁻¹⁵⁵ SBA-15 templated porous Mn_xO_y composed of MnO_2 , Mn_2O_3 and Mn_3O_4 was synthesised using the evaporation method firstly.¹²² Subsequently KIT-6 templated porous $\beta\text{-MnO}_2$ was produced¹⁵⁶⁻¹⁵⁸ and its electrochemical measurements of lithium-ion batteries exhibited high initial capacity, excellent high rate discharge performance, and supreme cycling reversibility. Recently, mesoporous crystalline Mn_2O_3 and Mn_3O_4 templated by KIT-6 was also reported by Feng et al..¹⁵⁹

The precursor used in the experiment is $\text{Mn}(\text{NO}_3)_2 \cdot 6\text{H}_2\text{O}$, which is a liquid at room temperature (melting point = $25.8\text{ }^\circ\text{C}$). Therefore, the evaporation method was applied to fill the template pores with the manganese nitrate. When the precursor loaded FDU-12 and SBA-16 specimens were heated up to $500\text{ }^\circ\text{C}$, manganese nitrate decomposed to form crystalline MnO_2 , which has a tetragonal structure with the unit cell parameters $a = 0.4396$ and $c = 0.2871$ nm, space group $P4_2/mnm$, as detected by XRD (Figure 5-16a) after removing the silica template. When the manganese nitrate loaded specimens were heated at $600\text{ }^\circ\text{C}$, the XRD pattern revealed a body-centred cubic Mn_2O_3 phase with the unit cell dimension $a = 0.9411$ nm, space group $Ia\bar{3}$ (Figure 5-16b).

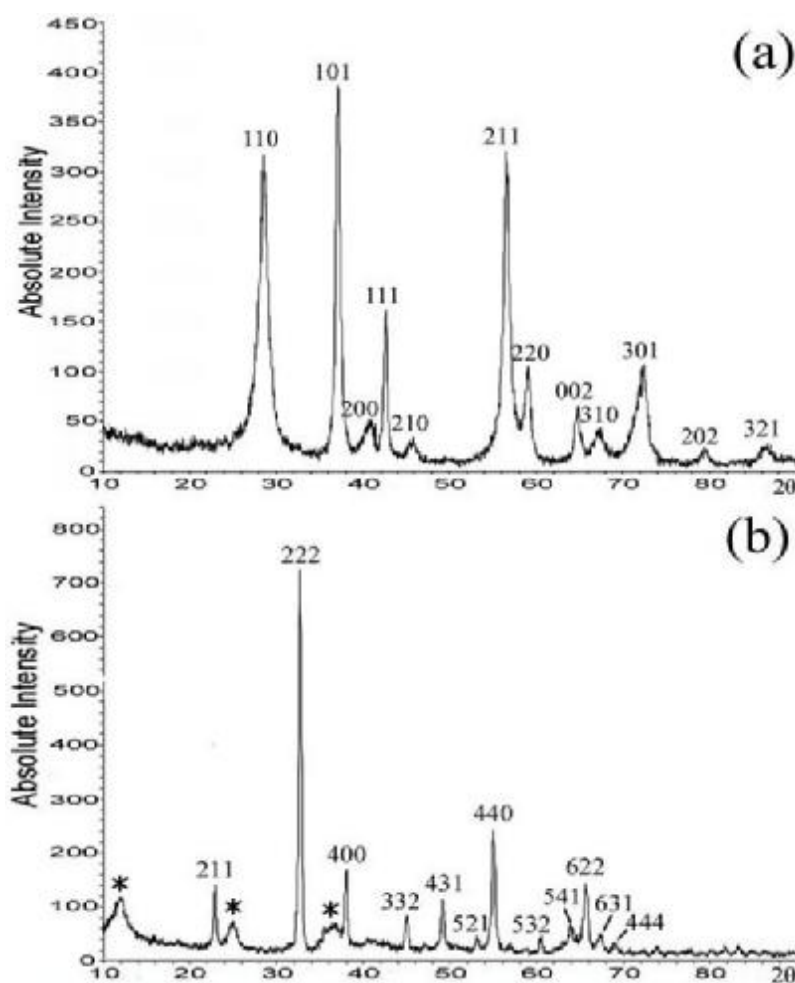


Figure 5-16. XRD patterns of FDU-12 templated mesoporous (a) tetragonal MnO_2 after a thermal treatment at $500\text{ }^\circ\text{C}$ and (b) cubic Mn_2O_3 ($\alpha\text{-MnO}_2$) after a thermal treatment at $600\text{ }^\circ\text{C}$. The silica templates had been removed.

The structure of MnO_2 products (Figure 5-17a) synthesised at 500 °C is very similar to the poor mesostructure of FDU-12 templated Cr_2O_3 particles, i.e. an aggregation of nanocrystallites with a poor spherical morphology (Figure 5-14a). Much better ordered porous particles were formed at 600 °C and observed by TEM in Figure 5-17(b). Figure 5-17(c,d) shows the similar results that MnO_2 products synthesised at 500 °C using SBA-16 as a template are an aggregation of nanospheres or nanoparticles with various size (Figure 5-17c) and Mn_2O_3 products synthesised at 600 °C were better ordered porous particles (Figure 5-17d) after the SBA-16 template was removed. Accordingly, the fact that the cage-containing pore systems in FDU-12 and SBA-16 can be replicated by cubic Mn_2O_3 , but not by tetragonal MnO_2 , gives us strong evidence that crystal symmetry affects the crystal growth in the confined nanocages.

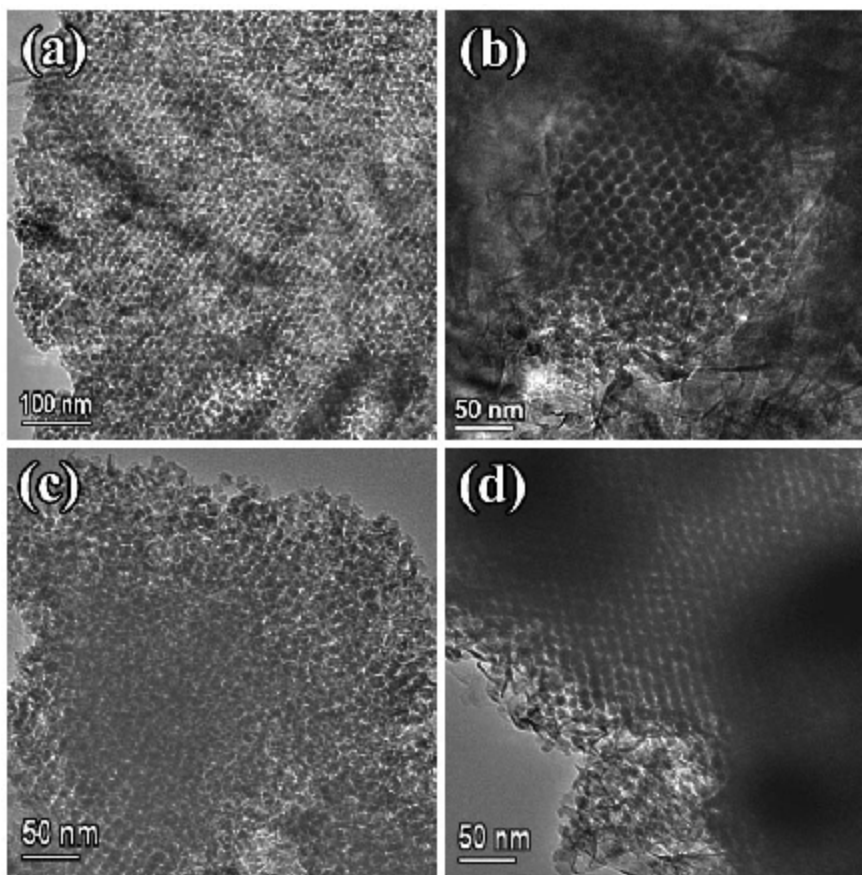


Figure 5-17. TEM images of FDU-12 and SBA-16 templated (a,c) tetragonal MnO_2 after a thermal treatment at 500 °C and (b,d) cubic Mn_2O_3 after a thermal treatment at 600 °C, respectively. The silica templates had been removed.

Conclusion

In chapter 3, we found that the most important step in the procedure of preparing porous transition metal oxides using hard templates was filling the template pores as much as possible with metal-containing precursor. It is believed that, benefited from the development of the surface functionalisation method, the evaporation method and the solid-liquid method, it is possible to introduce precursors in form of either a heteropolyacid or a nitrate, for most transition metal oxides. The inorganic precursors inside the nanochannels, such as those in SBA-15 and KIT-6, can decompose and grow into crystalline oxides. When focused on crystal growth of metal oxides inside the nanocages in FDU-12 and SBA-16, it was discovered that crystals of cubic oxides (e.g. Co_3O_4 and In_2O_3) can grow isotropically, filling the spherical cages completely and finally forming a network of connected nanospheres. However, non-cubic metal oxides (e.g. Cr_2O_3 and WO_3) cannot replicate the pore systems in FDU-12 and SBA-16 perfectly though the nitrate precursors can indeed fill the pores of the templates as implied by the formation of nanocrystallites (see Figure 5-17). These oxides even cannot replicate the spherical cages in the templates, as evidenced by the non-spherical nanocrystallites with variable sizes.

To fully understand the mechanism, further investigation is definitely required. With the evidence shown throughout this chapter, a crystal-template interaction model is proposed.

In early report of electron beam induced crystal growth of Ag nanowires from AgNO_3 loaded zeolites, the crystal growth of Ag could push and destroy the surrounding zeolite framework, creating a nanopore as a template for further crystal growth.²⁵⁷ The strong crystal-template interaction continued to exist until the nanopore extended to the particle surface, where the stress can be released. Similarly, in the process of crystal growth in silica templates, the three dimensional networks of the nanopores in SBA-15 and KIT-6 guarantee space available for a continuous crystal growth and reduces possible crystal-template interaction. When a cubic crystal grow to fill completely a spherical cage in FDU-12 or SBA-16, its interaction with the silica wall would increase. However, the interaction is even on the wall surface as shown in Figure 5-18(a). Possible induced distortion of the silica wall is small. On the other hand, when a non-cubic crystal develops in a cage, the crystal growth is anisotropical. The interaction between the crystal and the silica wall is not even on the whole surface of the cage, probably leading to a distortion of the silica framework

(Figure 5-18b). This distortion may affect further crystal growth extending from cage to cage through windows.

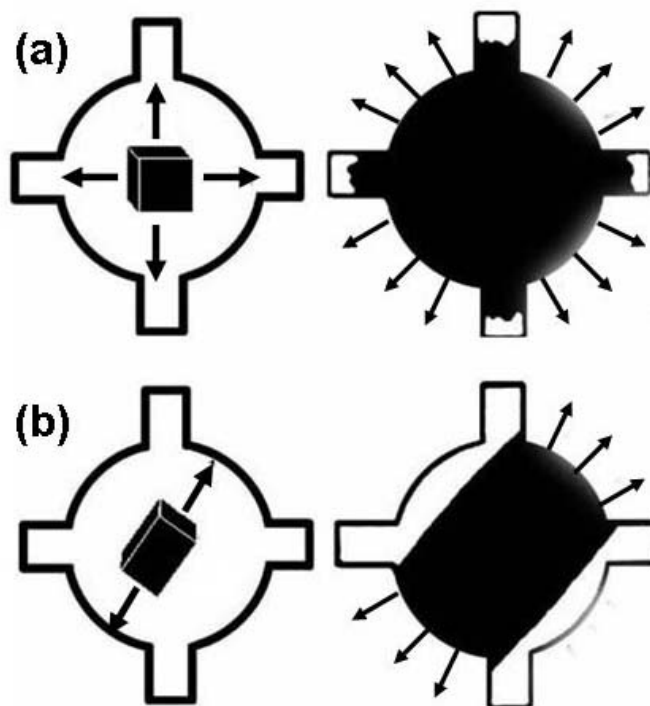


Figure 5-18. Schematic drawing of crystal growth of cubic (a) and non-cubic (b) metal oxides inside the spherical nanocages. The arrows show strength of the interaction between the crystals and the silica wall.

6. Metal oxides templated by mesoporous carbons

Porous crystalline materials, especially metal oxides, can be synthesised by using mesoporous silica such as SBA-15, KIT-6, FDU-12 and SBA-16 as hard templates. The general route for producing these porous single crystals of metal oxides includes the following steps: impregnating a metal-containing precursor into the silica pores, allowing the precursor to decompose inside the pores during a thermal treatment, controlling the crystal growth of the metal oxide at a higher temperature, and finally removing the silica template by using either a 10% HF aqueous solution at room temperature or a 2M NaOH solution at 80 °C. At present, porous crystalline Co_3O_4 , Cr_2O_3 , NiO, CeO_2 , In_2O_3 , WO_3 , Fe_2O_3 (Fe_3O_4), MnO_2 (Mn_2O_3 and Mn_3O_4), V_2O_5 and TiO_2 templated by SBA-15 and KIT-6, part of them templated by FDU-12 and SBA-16, have been synthesised by various methods such as the evaporation method and the solid-liquid method. However, some other porous metal oxides such as MgO, ZnO and ZrO_2 can not be synthesised using either method for the following reasons. (1) Their precursors can react with the silica template during the decomposition process (e.g. MgO) and non-porous metal-Si-O compounds may form after removing the silica template. (2) The metal oxides are amphoteric oxides (e.g. ZnO), and can be dissolved in HF solution as well as in hot NaOH solution during the removal process of the silica template.

Accordingly, mesoporous carbon has been selected as a hard template instead of mesoporous silica and has the following advantages in the synthesis of these porous metal oxides. (1) The metal precursor will not react with the carbon template during their decomposition process. (2) The carbon can be removed by thermal combustion at over 500 °C, and amphoteric oxide products can remain after removing the carbon template. Therefore, porous crystalline metal oxides which can not be templated by mesoporous silicas may be able to be prepared using mesoporous carbons as hard templates. Up to date, porous polycrystalline MgO,¹⁷¹⁻¹⁷² CuO¹⁷³ and ZnO¹⁷⁵⁻¹⁷⁷ specimens have been produced successfully using CMK-3,⁸⁸ a carbon replica of SBA-15, as a hard template. C-FDU-12 and C-SBA-16⁴³ are porous carbon replicas of FDU-12 and SBA-16, respectively, and have a much larger surface areas than CMK-3. FDU-14, FDU-15 and FDU-16⁹⁸ are novel ordered mesoporous carbon materials with hexagonal or cubic structures. We expect that porous MgO, CuO and

ZnO templated by C-FDU-12 and C-SBA-16 would have a much larger surface area and better properties than those templated by CMK-3, and these metal oxides templated by FDU-15 have similar porous structure with those templated by SBA-15.

6.1 Mesoporous carbon

The first ordered mesoporous carbon, CMK-1,⁸⁶ was synthesised via carbonising sucrose inside the pores of MCM-48 and obtained after removing the silica template in a HF solution. Subsequently, several porous carbons such as CMK-2⁸⁷ and CMK-3⁸⁸ with cubic or hexagonal structure were synthesised using SBA-1 and SBA-15 as templates, respectively. CMK-3, which has a negative structure of SBA-15, was widely used in the synthesis of porous metal oxides (e.g. MgO and ZnO)^{171-173,175-177} as a hard template. Mesoporous FDU-12 and SBA-16 consisting of nanospherical cavities have a larger surface area than SBA-15 or KIT-6. Therefore, mesoporous carbon C-FDU-12 and C-SBA-16 synthesised using FDU-12 and SBA-16 have much larger surface areas and their replicas (e.g. MgO and ZnO) should also have larger surface areas and better properties in comparison with those templated by CMK-3.

On the other hand, ordered mesoporous carbons with hexagonal or cubic structures can be synthesised through the self-assembly of phenol/formaldehyde resols and triblock copolymer templates.⁹⁸ Mesoporous carbon, FDU-14 with bicontinuous cubic (space group $Ia\bar{3}d$) structure, could be synthesised at a P123/phenol molar ratio higher than 0.04. FDU-15, with a 2-D hexagonal (space group $p6m$) structure, were prepared by using P123 as a template and a hydrocarbon (hexadecane or decane) as a swelling agent. FDU-16, synthesised using F127 as a template, has a body-centred cubic structure (space group $Im\bar{3}m$). Accordingly, their replicas such as ZnO templated by FDU-15 are expected to have negative structures, which are similar to these porous metal oxides templated by SBA-15.

6.1.1 C-FDU-12 and C-SBA-16

Mesoporous carbons C-FDU-12 and C-SBA-16 were synthesised using FDU-12 and SBA-16 as templates. Figure 6-1 shows TEM images of mesoporous carbons (a) C-FDU-12 and (b) C-SBA-16 after the silica templates were removed. The basic structure in both C-FDU-12 and C-SBA-15 are a three dimensional arrangement of solid nanospheres connected by some nanobridges. Some stacking faults in the

mesostructure of C-FDU-12 (Figure 6-1a), namely irregular intergrowth of cubic close-packing (ccp) and hexagonal close packing (hcp), were observed by TEM, which is similar to the structure of FDU-12 (Figure 5-1, chapter 5). In Figure 6-1(b), the nanobridges between nanospheres can be observed and indicated by a circle in the high magnification TEM image.

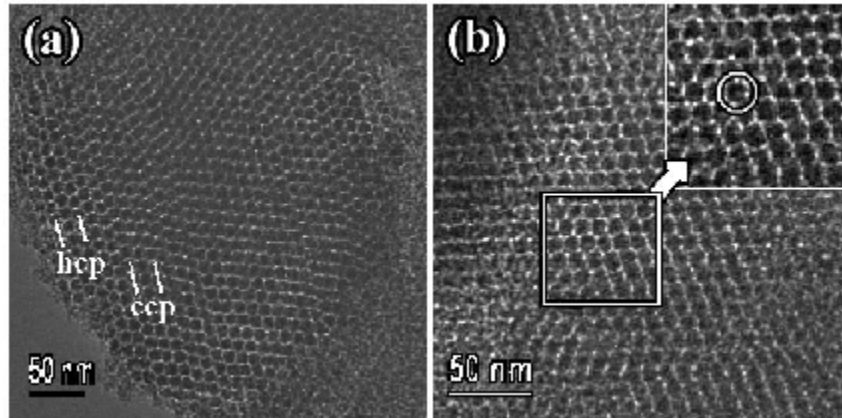


Figure 6-1. TEM images of mesoporous carbon (a) C-FDU-12 and (b) SBA-16 after removing silica template, respectively.

Figure 6-2 shows the nitrogen adsorption/desorption isotherms of C-FDU-12(a) and C-SBA-16 (b), respectively. The isotherms of these mesoporous materials are both type IV with a typical hysteresis loop, indicating the mesoporous property. The specific surface areas of C-FDU-12 and C-SBA-16 are 874.2 m²/g and 994.8 m²/g, and the average pore sizes are 3.6 nm and 3.7 nm, respectively. Although the BET areas are lower than the surface area of CMK-3 (1520 m²/g), possibly due to the lower yield, the surface area of C-FDU-12 and C-SBA-16 are still large.

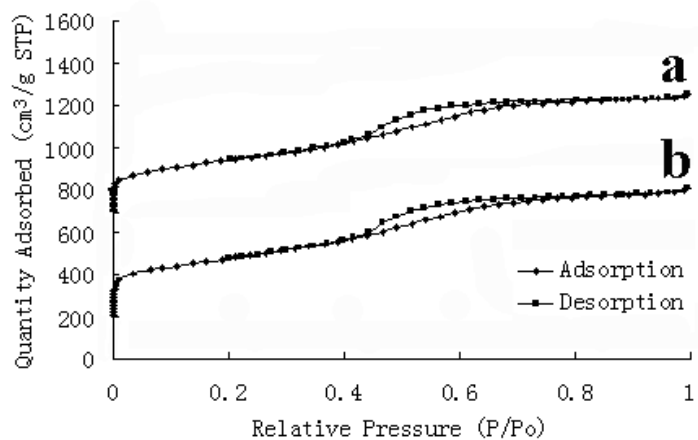


Figure 6-2. Nitrogen adsorption/desorption isotherms measured at 77 K from **a**, C-FDU-12 and **b**, C-SBA-16, respectively.

6.1.2 FDU-15

FDU-15 has a similar structure with SBA-15, which has a hexagonal arrangement of cylindrical pores connected by small nanochannels. The only difference between FDU-15 and SBA-15 is the chemical composition (one is made of carbon and another is silica). Figure 6-3 shows the typical structure of FDU-15, viewed down [110] and [001] zone axis, respectively, and no other mesophase was observed by TEM.

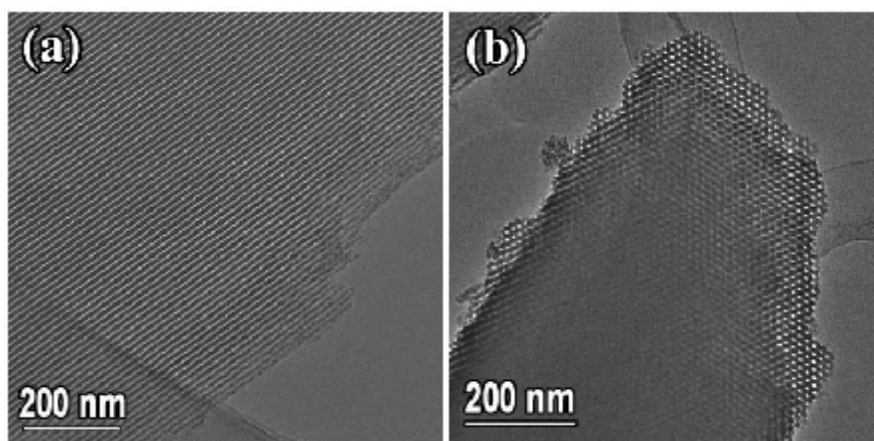


Figure 6-3. TEM images of mesoporous carbon FDU-15, viewed along the [110] (a) and [001] (b) directions, respectively.

6.2 MgO and CuO templated by C-FDU-12 and C-SBA-16

MgO particles were synthesised using $\text{Mg}(\text{NO}_3)_2 \cdot 6\text{H}_2\text{O}$ as the precursor and C-FDU-12 or C-SBA-16 as the hard template. Unlike the non-porous Mg-Si-O compounds synthesised using SBA-15 template, the products templated by C-FDU-12 or C-SBA-15 were pure crystalline MgO, which was confirmed by XRD patterns (Figure 6-4a). All peaks in the wide-angle region were indexed to the cubic MgO structure (space group $Fm\bar{3}m$, with $a = 0.4211$ nm) and no other materials were detected.

Figure 6-5(a) shows the TEM images of a C-FDU-12 particle containing some MgO crystals and Figure 6-5(b) shows MgO nanoparticles after C-FDU-12 was removed by thermal combustion. The porous framework of C-FDU-12 in Figure 6-5(a) was destroyed, possibly due to the growth of MgO inside the pores. The rigidity of amorphous carbon using sucrose as the carbon source was so fragile in comparison of crystalline MgO. Accordingly, when the MgO particles were formed and grew in the pores of C-FDU-12, the interaction forces on the wall surface increased and could not maintain the structure, due to the confined three dimensional

mesostructure of C-FDU-12, leading to the distortion of the carbon walls. So the MgO product after removing C-FDU-12 was the congregation of nanoparticles with various sizes as shown in Figure 6-5(b).

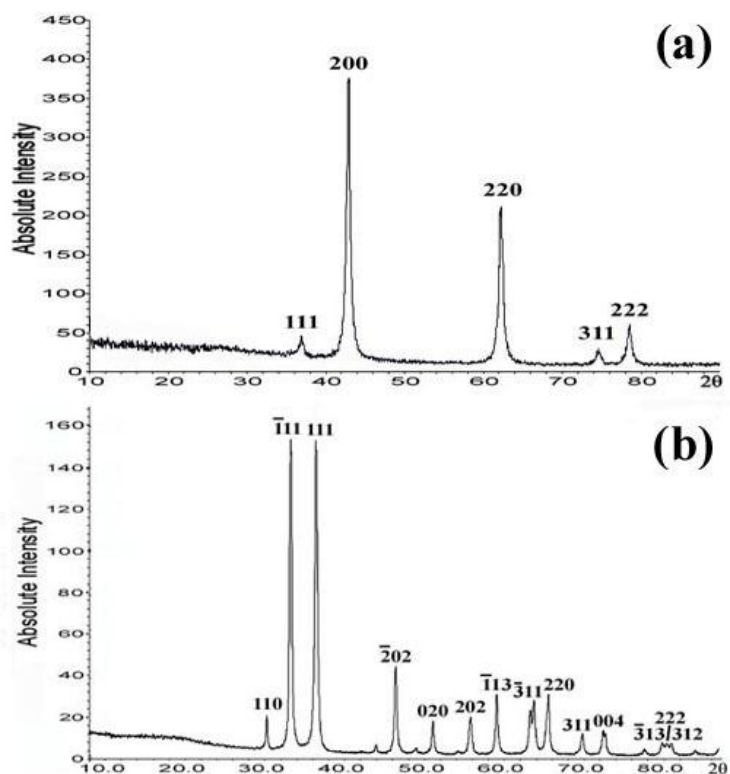


Figure 6-4. XRD patterns of (a) MgO and (b) CuO particles after removing carbon template, respectively.

CuO particles were also synthesised using the same method, with $\text{Cu}(\text{NO}_3)_2 \cdot 3\text{H}_2\text{O}$ as the precursor and C-FDU-12 or C-SBA-16 as the hard template. Figure 6-5(c) and (d) shows the TEM images of CuO-loaded C-FDU-12 template and CuO particles after removing C-FDU-12, respectively. Unlike the C-FDU-12 containing MgO particles, the porous structure of C-FDU-12 can remain in Figure 6-5(c). However, similar to the MgO particles templated by C-FDU-12, the CuO products after removing C-FDU-12 (Figure 6-5d) were still nanoparticles congregation. Based on the synthetic theory of instantaneous combustion used by Ren et al. (chapter 4) to synthesise porous CuO templated by KIT-6, although the $\text{Cu}(\text{NO}_3)_2 \cdot 3\text{H}_2\text{O}$ was impregnated in the pores of silica, the formed CuO particles moved outside the silica pores rather than remaining inside the pores during the slow calcination. Therefore they selected a thermal treatment to form porous CuO inside the silica pore instantaneously. Likewise the CuO formed inside the carbon pores might grow

outside the mesopores of carbon in this experiment, resulting in the remains of the intact mesostructure of carbon (Figure 6-5c). On the other hand, the CuO particles after removing the carbon framework (Figure 6-5d), which were seemingly not confined inside the carbon pores, were larger than the MgO particles (Figure 6-5b).

The peaks in the XRD pattern (Figure 6-4b) are indexed to monoclinic CuO structure (space group $C2/c$, with $a = 0.4680$ nm, $b = 0.3431$ nm, $c = 0.5136$ nm and $\beta = 99.26^\circ$), confirming that these particles are pure crystalline CuO crystals.

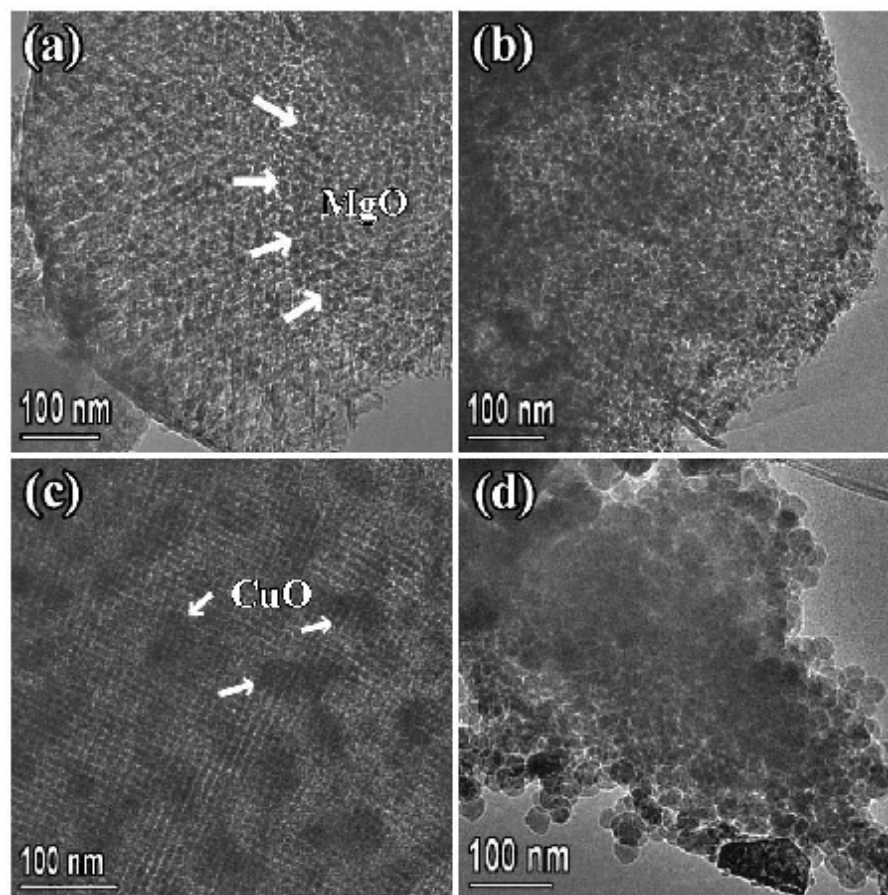


Figure 6-5. TEM images of (a) MgO, (c) CuO particles inside the pores of C-FDU-12 template, and (b) MgO, (d) CuO nanoparticles after carbon template was removed by thermal combustion.

MgO and CuO particles templated by C-SBA-16 were also synthesised and observed by TEM (Figure 6-6a,b). The results are similar. The MgO product is a congregation of small nanoparticles in comparison with relatively larger CuO particles. Additionally a local heat released by combustion of carbon template may destroy the connection between the units in the mesostructure of metal oxides, leading to individual nanoparticle formation as well as reunion. It is one of the

possible reasons that an aggregation of nanoparticles (e.g. MgO) and larger nanoparticles (e.g. CuO) were formed after carbon template was removed by combustion.

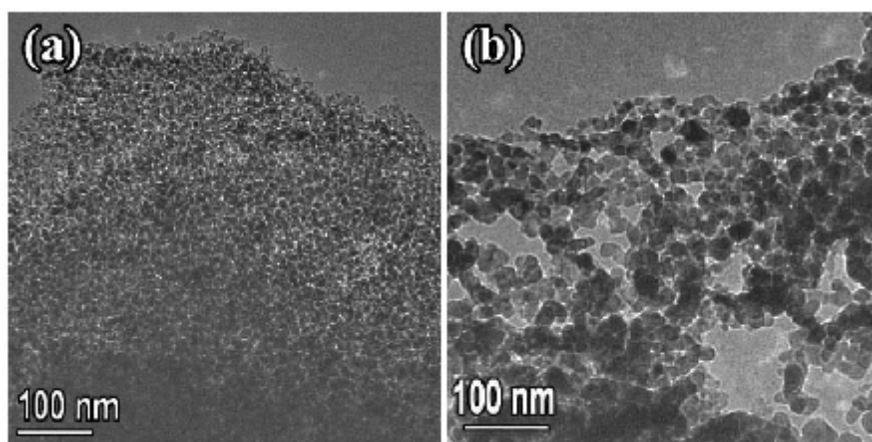


Figure 6-6. TEM images of (a) MgO and (b) CuO nanoparticles after C-SBA-16 was removed by thermal combustion, respectively.

6.3 MgO and ZnO templated by FDU-15

Since mesoporous carbon C-FDU-12 and C-SBA-16 have some possible disadvantages such as weak rigidity and 3D confined mesostructures, porous carbon FDU-15, consisting of a hexagonal arrangement of cylindrical pores, was selected as a hard template to synthesise porous MgO and ZnO particles in the experiment. Figure 6-7 shows the TEM images of (a) MgO and (b) ZnO particles after FDU-15 was removed by thermal combustion, and again, only congregation of nanoparticles can be found in both metal oxides.

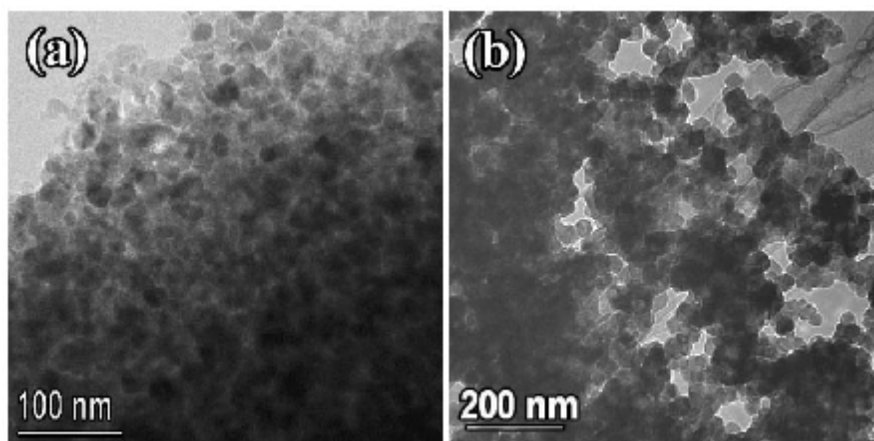


Figure 6-7. TEM image of (a) MgO and (b) ZnO particles after FDU-15 was removed by thermal combustion.

The ZnO property of the particles was confirmed by the XRD pattern in Figure 6-8, which can be indexed to the hexagonal ZnO structure (space group $P63mc$, with $a = 0.3253$ and $c = 0.5213$).

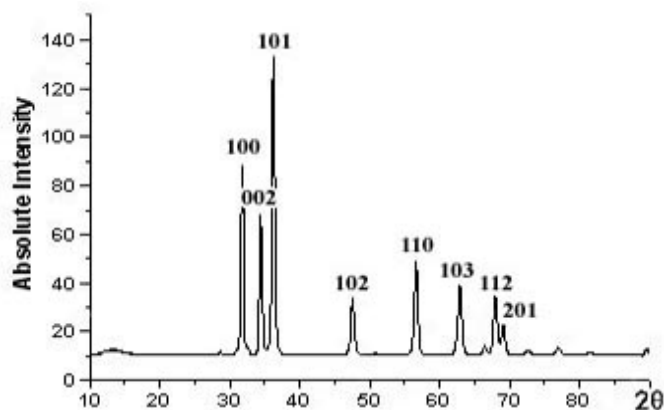


Figure 6-8. XRD pattern of ZnO particles after removing carbon template.

On the other hand, according to the literature,¹⁸⁰ the wettability of carbon has an important effect on the synthesis of porous metal oxides when porous carbon was used as a template. Accordingly, FDU-15 was pre-treated in 10 % H_2O_2 solution at 50 °C for 2 h to create a level of hydroxyl groups on the surface of the template, which can increase the wettability of carbon. Additionally, THF was selected as the solvent, instead of ethanol or water, due to its low solvent polarity and sufficient metal salt solubility, which increase the loading of the precursor inside the carbon pores since it can wet up the surface of porous carbon as well as dissolve the metal salt.¹⁸⁰ However, almost specimens were still aggregations of MgO nanoparticles, observed by TEM (Figure 6-9a), although few amount of nanorod-like particles can be observed by TEM (Figure 6-9b). Further exploration is needed in future.

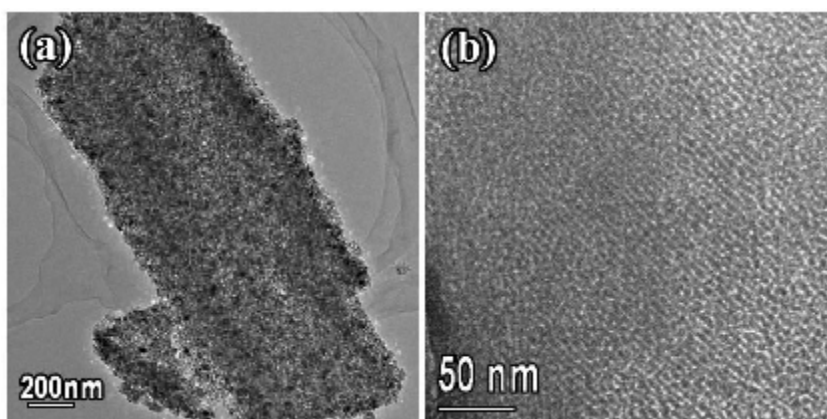


Figure 6-9. TEM images of MgO particles with (a) low magnification and (b) higher magnification, respectively.

Conclusion

The porous MgO, CuO and ZnO crystals, which were proven to be synthesised successfully using CMK-3 template,^{171-173,175-177} can not be synthesised using C-FDU-12, C-SBA-16 and FDU-15 templates. Unlike the Mg-Si-O compounds synthesised using silica template or inseparable amphoteric metal oxides/silica mixture, the products prepared using C-FDU-12, C-SBA-16 and FDU-15 template were pure crystalline metal oxides (e.g. MgO) and can be obtained after removing carbon template (e.g. ZnO). Similar to the synthetic process of metal oxides templated by silica, the important process in this experiment is the impregnation process of a metal-containing precursor into the carbon pores. Unfortunately the porous carbon surface is non-polar and has poor wettability to the polar solvent, such as water or ethanol. Although THF was used as the solvent and pre-treatment of porous carbon was made to increase the wettability of the carbon surface, porous metal oxides were still not formed. On the other hand, removal of carbon template by combustion will release a quantity of local heat, which may destroy the mesostructure of metal oxides, leading to large particles formation. A repeated experiment of preparation of porous MgO, CuO and ZnO using CMK-3 template was also carried out but only non-porous particles were observed by TEM.

According to literature,^{171-173,175-177} the impregnation process of metal-containing precursors into CMK-3 was usually repeated more than twice. On the assumption that the precursors could not migrate freely on the surface of carbon, the precursors decomposed to nanoparticles on the surface of carbon pores and could not grow into big crystals filling fully in the carbon pores after only one impregnation. Therefore, the impregnation process has to be repeated to fill the carbon pores completely with metal oxides, and it is also the reason that only polycrystalline porous metal oxides can be obtained. Consequently, an effective approach to increase the wettability of carbon and impel the precursors migrate freely on the carbon surface will be explored in future, and it is believed that single crystals of porous metal oxides can be generated by a single impregnation using mesoporous carbons as templates after increasing the wettability of the carbon.

7. Conclusions and future work

Highly ordered mesoporous materials, especially porous metal oxides, have a wide range of possible applications as nanoreactors, electronic devices, gas sensors and catalysts. A novel convenient method developed from evaporation method was used to prepare monocrystalline porous metal oxides, and novel porous metal oxides such as porous rutile TiO_2 were also synthesised successfully using SBA-15 and KIT-6 as templates. Novel mesoporous silicas such as FDU-12 and SBA-16 were also used as hard templates to prepare porous metal oxides with larger surface areas and novel morphologies. Additionally novel mesoporous carbons such as FDU-15 were selected as hard templates to produce porous metal oxides as well, although this part of synthesis was not quite successful.

7.1 Conclusion

Porous monocrystalline metal oxides such as Co_3O_4 and Cr_2O_3 can be synthesised by using mesoporous silicas (e.g. SBA-15 and KIT-6) as hard templates. The impregnation process in the accepted evaporation method is as follows: the metal-containing precursors was mixed with silica template in ethanol and then migrate into the pores of silica template by capillary action during the evaporation of solvent. A novel impregnation approach, the solid-liquid method, was developed from the evaporation method to synthesise monocrystalline porous metal oxides simply and effectively.

The solid-liquid method is very simple and solvent-free, which is attractive to industry. In detail, a precursor which has low melting point and high decomposition temperature was selected and ground with the silica template well in the mortar and pestle. The precursor then transformed to liquid and moved into the silica pores by capillary action. The porous metal oxides were formed and grew inside the pores of silica by the decomposition of precursor when the reaction temperature increased above its decomposition temperature and were collected after the silica template was removed using an HF or hot NaOH solution. Single crystals of porous Co_3O_4 , Cr_2O_3 , NiO, CeO_2 , In_2O_3 and WO_3 were proven to be synthesised successfully using the solid-liquid method and were characterised by XRD, TEM, SAED and EDX, etc. In addition, $\text{Pb}(\text{NO}_3)_2$ and $(\text{NH}_4)_2\text{Cr}_2\text{O}_7$ which decomposed directly without melting

were selected as the metal-containing precursors to synthesise porous PbO and Cr₂O₃. However, only large bulk particles were obtained instead of porous metal oxides using either the solid-liquid method or evaporation method, indicating that the precursors can not migrate into the pores of silica by the evaporation of ethanol alone, as commonly thought. The precursors were not impregnated into the silica pores without melting and decomposed to form bulk particles outside the silica pores. Therefore the precursor selected with lower melting point than its decomposition temperature is the key point to synthesise mesoporous metal oxides.

FDU-12 and SBA-16 consist of nanospherical cavities linked by some small nanochannels. SBA-16 has a body-centred cubic structure and FDU-12 has a face-centred cubic structure. Theoretically, porous metal oxides templated by FDU-12 and SBA-16 should have larger surface areas than those templated by SBA-15 and KIT-6. Porous single crystals of cubic metal oxides, Co₃O₄, NiO, CeO₂ and In₂O₃, have been synthesised successfully using the solid-liquid method, and the surface areas of FDU-12 and SBA-16 templated Co₃O₄ are 151 and 122.4 m²/g respectively, larger than the surface area (92 m²/g) of KIT-6 templated Co₃O₄. However, porous non-cubic metal oxides (e.g. rhombohedral Cr₂O₃, Fe₂O₃ and tetragonal TiO₂, WO₃) which can be prepared using SBA-15 and KIT-6 templates did not form a perfect mesostructure. Additionally, using the same precursor and templates, tetragonal MnO₂ lead to a poor mesostructure whereas cubic Mn₂O₃ lead to a perfect mesostructure, confirming this phenomenon again. A possible mechanism is brought forward that the nanopores in SBA-15 and KIT-6 is cylindrical and guarantee space available for a continuous crystal growth, reducing possible crystal-template interaction. However, when the crystals grow to fill completely a spherical cage in FDU-12 or SBA-16, its interaction with the silica wall would increase. When a non-cubic crystal develops in a cage, the crystal growth is anisotropical and leads to the distortion of silica walls due to the unbalanced interaction force. Consequently, non-cubic metal oxides with perfect mesostructure are difficult to be prepared using FDU-12 and SBA-16 as templates. On the other hand, the growth of cubic metal oxides is isotropical, which will not result in the distortion of the silica wall.

Novel porous metal oxides, rutile TiO₂ templated by SBA-15 and KIT-6, were synthesised successfully by using freshly synthesised Ti(NO₃)₄ solution as the precursor and characterised by XRD, TEM, SAED, EDX and BET techniques. These porous rutile TiO₂ exhibited high proton conductivity of $8 \times 10^{-3} \text{ S} \cdot \text{cm}^{-1}$ at high relative

humidity at temperatures of 50 °C, and Li ion insertion capability (e.g. 1-1.06 Li⁺ per TiO₂ unit can be accommodated at the first discharge). Furthermore, porous anatase/ β -TiO₂ nanocrystals-silica composites were also synthesised using TiCl₄ solution instead of Ti(NO₃)₄ as the precursor, and only anatase-silica composites were formed at 600 °C. However, other novel porous metal oxides such as MgO and ZnO could not be prepared using porous silicas as templates. The potential disadvantages of silica selected as a template are as follows: some precursors can react with silica template during their decomposition and non-porous metal-Si-O compounds (e.g. Mg-Si-O compounds) or porous metal oxides nanoparticles-silica composites (e.g. ZrO₂-silica) were formed after the silica template was removed. In another case, the formed amphoteric metal oxide/silica mixture can not be separated using either an HF or hot NaOH solution, leading to unavailable porous metal oxides (e.g. ZnO/silica). Therefore mesoporous carbon was selected as a hard template instead of mesoporous silica to synthesise these porous metal oxides later.

Mesoporous carbon was synthesised by decomposition of either sucrose inside the pores of mesoporous silica (e.g. C-FDU-12 and C-SBA-16) or phenol/formaldehyde on the surface of triblock copolymer (e.g. FDU-15) under N₂ protection. Although some porous polycrystalline metal oxides of MgO, CuO and ZnO were proven to be synthesised using CMK-3 as a template by another group, it appeared difficult to synthesise porous metal oxide (e.g. MgO and ZnO) using C-FDU-12/C-SBA-16 or FDU-15 as a template. The possible reason is that carbon has poor wettability and the precursor or solvent can not migrate into the carbon pores smoothly, leading to the formation of bulk materials outside carbon pores or nanoparticles inside the carbon pores. Consequently, an effective approach to increase the wettability of carbon such as modifying the carbon surface with hydroxyl group will be explored. Additionally the localised heating caused by thermal combustion of carbon would lead to the collapse of mesostructure and will also be explored in future work.

From the current work, the mechanism for the synthesis of mesoporous metal oxides is established, based on the conclusion from the successful and unsuccessful preparation of porous metal oxides. The precursors whose melting points are lower than their decomposition temperature must be selected. They should not react with silica during decomposition process when mesoporous silica was used as template. Otherwise an alternative template of mesoporous carbon can be used to replace

mesoporous silica. However, the synthetic conditions are rigorous due to the poor wettability of carbon. Additionally the mesostructure of template have an important effect on the growth of metal oxides crystals, which is relative to the crystal system of metal oxides.

7.2 Future work

The synthesis of novel porous metal oxides (e.g ZrO_2), the use of novel mesoporous templates and the development of novel synthetic methods are the main areas concentrated on in this section. In detail, mesoporous carbon FDU-14, FDU-15 and FDU-16, which have a mesostructure like SBA-15, KIT-6 and SBA-16, can be selected as the hard templates to synthesise porous metal oxides. The key point in this experiment is the high wettability of the carbon template. The porous carbon surface can be modified by treatment in HNO_3 or H_2O_2 solution to increase the quantity of hydroxyl groups and therefore its wettability. On the other hand, some novel metal oxides such as ZrO_2 which can not be prepared using silica template will also be investigated to be synthesised using carbon template. Once the novel porous metal oxides are synthesised, their properties will be examined such as the catalytic activity, solid state electrochemical properties and energy storage. Additionally, the CVD (Chemical vapor deposition) technique will be applied to synthesise porous materials and nanowires in future.

Novel porous monocrystalline rutile TiO_2 templated by SBA-15 and KIT-6 will be used as framework to synthesise porous Li_4TiO_{12} or be doped with lanthanide such as Co and Y. The former is a good cathode material and the latter has better optical properties than pure TiO_2 .

References

- 1 U. Schubert and N. Hüsing, 'Synthesis of Inorganic Materials', Wiley-VCH, Weinheim, 2000.
- 2 J. Rouquerol, D. Avnir, C. W. Fairbridge, D. H. Everett, J. M. Haynes, N. Pernicone, J. D. F. Ramsay, K. S. W. Sing and K. K. Unger, *Pure Appl. Chem.*, 1994, **66**, 1739.
- 3 M. Takahashi and M. Fujii, *Kona*, 2002, **20**, 84.
- 4 M. E. Davis, C. Saldarriaga, C. Montes, J. Garces and C. Crowder, *Nature*, 1988, **331**, 698.
- 5 C. C. Freyhardt, M. Tsapatsis, R. F. Lobo, K. J. Balkus and M. E. Davis, *Nature*, 1996, **381**, 295.
- 6 P. Wagner, M. Yoshikawa, M. Lovallo, K. Tsuji, M. Taspatsis and M. E. Davis, *Chem. Commun.*, 1997, 2179.
- 7 A. V. Ramaswamy, *Bull. Catal. Soc. India*, 2003, **2**, 140.
- 8 S. M. Csicsery, *Pure Appl. Chem.*, 1986, **58**, 841.
- 9 G. Tasi, I. Pálincó, Á. Molnár and I. Hannus, *J. Mol. Struct.: Theochem*, 2003, **666-667**, 69.
- 10 T. Sano and Y. Oumi, *Catal. Surv. Asia*, 2004, **8**, 295.
- 11 A. N. Phillip and R. O. John, *J. Electrochem. Soc.*, 2003, **150**, A1313.
- 12 T. Hyodo, Y. Shimizu and M. Egashira, *Electrochemistry*, 2003, **71**, 387.
- 13 D. Mehandjiev and E. Nikolovazhecheva, *J. Catal.*, 1980, **65**, 475.
- 14 R. Ryoo, J. M. Kim, C. H. Ko, and C. H. Shin, *J. Phys. Chem.*, 1996, **100**, 17718.
- 15 J. M. Kim, S. Jun and R. Ryoo, *J. Phys. Chem. B*, 1999, **103**, 6200.
- 16 S. A. Bagshaw, E. Prouzet and T. J. Pinnavaia, *Science*, 1995, **269**, 1242.
- 17 E. Prouzet and T. J. Pinnavaia, *Angew. Chem. Int. Ed. Engl.*, 1997, **36**, 516.
- 18 K. M. McGrath, D. M. Dabbs, N. Yao, I. A. Aksay and S. M. Gruner, *Science*, 1997, **277**, 552.
- 19 D. Y. Zhao, C. Nie, Y. M. Zhou, S. J. Xia, L. M. Huang and Q. Z. Li, *Catal. Today*, 2001, **68**, 11.
- 20 J. C. Jansen, Z. P. Shan, L. Marchese, W. Z. Zhou, N. van der Puil, T. Maschmeyer, *Chem. Commun.*, 2001, **8**, 713.

- 21 J. Wang, J. C. Groen, W. B. Yue, W. Z. Zhou and M. -O. Coppens, *Chem. Commun.*, 2007, 4653.
- 22 J. Wang, J. C. Groen, W. B. Yue, W. Z. Zhou and M. -O. Coppens, *J. Mater. Chem.*, 2008, **18**, 468.
- 23 J. Wang, W. B. Yue, W. Z. Zhou and M. -O. Coppens, *Microp. and Mesop. Mater.*, 2009, **120**, 19.
- 24 N. Nishiyama, S. Tanaka, Y. Egashira, Y. Oku and K. Ueyama, *Chem. Mater.*, 2002, **14**, 4229.
- 25 N. Nishiyama, S. Tanaka, Y. Egashira, Y. Oku and K. Ueyama, *Chem. Mater.*, 2003, **15**, 1006.
- 26 T. Maruo, S. Tanaka, H. W. Hillhouse, N. Nishiyama, Y. Egashira and K. Ueyama, *Thin Solid Films*, 2008, **516**, 4771.
- 27 D. H. Wang, D. Choi, Z. G. Yang, V. V. Viswanathan, Z. M. Nie, C. M. Wang, Y. J. Song, J. -G. Zhang and J. Liu, *Chem. Mater.*, 2008, **20**, 3435.
- 28 L. Xu, Y. Q. Feng, L. S. Da and Z. G. Shi, *Chinese J. Anal. Chem.*, 2004, 32, 374.
- 29 C. T. Kresge, M. E. Leonowicz, W. J. Roth, J. C. Vartuli and J. S. Beck, *Nature*, 1992, **359**, 710.
- 30 J. S. Beck, J. C. Vartuli, W. J. Roth, M. E. Leonowicz, C. T. Kresge, K. D. Schmitt, C. T. -W. Chu, D. H. Olson, E. W. Sheppard, S. B. McCullen, J. B. Higgins and J. L. Schlenker, *J. Am. Chem. Soc.*, 1992, **114**, 10834.
- 31 A. Monnier, F. Schüth, Q. Huo, D. Kumar, D. Margolese, R. S. Maxwell, G. D. Stucky, M. Krishnamurty, P. Petroff, A. Firouzi, M. Janicke and B. F. Chmelka, *Science*, 1993, **261**, 1299.
- 32 S. Ajaikumar and A. Pandurangan, *J. Mol. Catal. A: Chem.*, 2008, **290**, 35.
- 33 L. Huang, Q. L. Huang, H. N. Xiao and M. Eic, *Microp. Mesop. Mater.*, 2008, **114**, 121.
- 34 M. Vallet-Regi, A. Rámila, R. P. del Real and J. Pérez-Pariente, *Chem. Mater.*, 2001, **13**, 308.
- 35 W. Zeng, X. F. Qian, J. Yin and Z. K. Zhu, *Mater. Chem. Phys.*, 2006, **97**, 437.
- 36 X. S. Zhao, G. Q. Lu and X. Hu, *Colloid. Surface. A*, 2001, **179**, 261.
- 37 T. Yanagisawa, T. Shimizu, K. Kuroda and C. Kato, *Bull. Chem. Soc. Jpn.*, 1990, **63**, 988.
- 38 S. Inagaki, Y. Fukushima and K. Kuroda, *J. Chem. Soc. Chem. Commun.*, 1993, 680.

- 39 D. Y. Zhao, J. L. Feng, Q. S. Huo, N. Melosh, G. H. Fredrickson, B. F. Chmelka and G. D. Stucky, *Science*, 1998, **279**, 548.
- 40 D. Y. Zhao, Q. S. Huo, J. L. Feng, B. F. Chmelka and G. D. Stucky, *J. Am. Chem. Soc.*, 1998, **120**, 6024.
- 41 F. Kleitz, S. H. Choi and R. Ryoo, *Chem. Commun.*, 2003, 2136.
- 42 O. Terasaki, T. Ohsuna, Z. Liu, Y. Sakamoto and A. E. Garcia-Bennett, *Stud. Surf. Sci. Catal.*, 2004, **148**, 261.
- 43 J. Fan, C. Z. Yu, F. Gao, J. Lei, B. Z. Tian, L. M. Wang, Q. Luo, B. Tu, W. Z. Zhou and D. Y. Zhao, *Angew. Chem. Int. Ed.*, 2003, **42**, 3146.
- 44 J. Fan, C. Z. Yu, J. Lei, Q. Zhang, T. C. Li, B. Tu, W. Z. Zhou and D. Y. Zhao, *J. Am. Chem. Soc.*, 2005, **127**, 10794.
- 45 P. I. Ravikovitch and A. V. Neimark, *Langmuir*, 2002, **18**, 9830.
- 46 Y. Sakamoto, M. Kaneda, O. Terasaki, D. Y. Zhao, J. M. Kim, G. Stucky, H. J. Shin and R. Ryoo, *Nature*, 2000, **408**, 449.
- 47 T. Yu, H. Zhang, X. W. Yan, Z. X. Chen, X. D. Zou, P. Oleynikov and D. Y. Zhao, *J. Phys. Chem. B*, 2006, **110**, 21467.
- 48 S. L. Burkett, S. D. Sims and S. Mann, *Chem. Commun.*, 1996, 1367.
- 49 D. J. Macquarrie, *Chem. Commun.*, 1996, 1961.
- 50 R. P. Hodgkins, A. E. Garcia-Bennett and P. A. Wright, *Microp. Mesop. Mater.*, 2005, **79**, 241.
- 51 H. H. P. Yiu, P. A. Wright and N. P. Botting, *J. Mol. Catal. B Enzym.*, 2001, **15**, 81.
- 52 M. Fujiwara, K. Kuraoka, T. Yazawa, Q. Xu, M. Tanaka and Y. Souma, *Chem. Commun.*, 2000, 1523.
- 53 W. D. Bossaert, D. E. de Vos, W. M. van Rhijn, J. Bullen, P. J. Grobet and P. A. Jacobs, *J. Catal.*, 1999, **182**, 156.
- 54 D. Brunel, F. Fajula, J. B. Nagy, B. Deroide, M. J. Verhoef, L. Veum, J. A. Peters and H. van Bekkum, *Appl. Catal. A: Gen.*, 2001, **213**, 73.
- 55 H. Kosslick, G. Lischke, B. Parlitz, W. Storek and R. Fricke, *Appl. Catal. A: Gen.*, 1999, 184, 49.
- 56 A. -N. Ko, C. -C. Hung, C. -W. Chen and K. -H. Ouyang, *Catal. Lett.*, 2001, **71**, 219.
- 57 Z. H. Luan, C. Cheng, W. Z. Zhou and J. Klinowski, *J. Phys. Chem.*, 1995, **99**, 1018.

- 58 P. T. Tanev, M. Chibwe and T. J. Pinnavaia, *Nature*, 1994, **368**, 321.
- 59 A. Corma, M. T. Navarro and J. P. Pariente, *J. Chem. Soc. Chem. Commun.*, 1994, 147.
- 60 N. C. King, C. Dickinson, W. Z. Zhou and D. W. Bruce, *J. Chem. Soc. Dalton Trans.*, 2005, 1027.
- 61 J. Bowers, M. J. Danks, D. W. Bruce and R. K. Heenan, *Langmuir*, 2003, **19**, 292.
- 62 T. Maschmeyer, F. Rey, G. Sankar and J. M. Thomas, *Nature*, 1995, **378**, 159.
- 63 R. D. Oldroyd, J. M. Thomas, T. Maschmeyer, P. A. Macfaul, D. W. Snelgrove, K. U. Ingold and D. D. M. Wayner, *Angew. Chem. Int. Ed.*, 1996, **35**, 2787.
- 64 H. Chen, W. -L. Dai, J. -F. Deng and K. N. Fan, *Catal. Lett.*, 2002, **81**, 131.
- 65 G. M. Lü, R. Zhao, G. Qian, Y. X. Qi, X. L. Wang and J. S. Suo, *Catal. Lett.*, 2004, **97**, 115.
- 66 A. Sakthivel, S. E. Dapurkar and P. Selvam, *Catal. Lett.*, 2001, **77**, 155.
- 67 M. L. Peña, A. Dejoz, V. Fornés, F. Rey, M. I. Vázquez and J. M. L. Nieto, *Appl. Catal. A: Gen.*, 2001, **209**, 155.
- 68 K. Mukhopadhyay, B. R. Sarkar and R. V. Chaudhari, *J. Am. Chem. Soc.*, 2002, **124**, 9692.
- 69 S. E. Dapurkar, S. K. Badamali and P. Selvam, *Catal. Today*, 2001, **68**, 63.
- 70 W. Chang, J. Shin, M. Kim and B. J. Ahn, *J. Ind. Eng. Chem.*, 2001, **7**, 62.
- 71 K. -H. Jung, K. -H. Chung, J. -H. Kim and G. Seo, *React. Kinet. Catal. Lett.*, 2000, **69**, 55.
- 72 Y. H. Yue, Y. Sun and Z. Gao, *Catal. Lett.*, 1997, **47**, 167.
- 73 L. P. Wang, A. G. Kong, B. Chen, H. M. Ding, Y. K. Shan and M. Y. He, *J. Mol. Catal. A: Chem.*, 2005, **230**, 143.
- 74 M. L. Zhang, S. F. Ji, L. H. Hu, F. X. Yin, C. Y. Li and H. Liu, *Chin. J. Catal.*, 2006, **27**, 777.
- 75 F. X. Li, F. Yu, Y. L. Li, R. F. Li and K. C. Xie, *Microp. Mesop. Mater.*, 2007, **101**, 250.
- 76 F. Ying, J. H. Li, C. J. Huang, W. Z. Weng and H. L. Wan, *Catal. Lett.*, 2007, **115**, 137.
- 77 Y. M. Wang, Z. Y. Wu and J. H. Zhu, *J. Solid State Chem.*, 2004, **177**, 3815.
- 78 Y. M. Wang, Z. Y. Wu, L. Y. Shi and J. H. Zhu, *Adv. Mater.*, 2005, **17**, 323.
- 79 Q. Jiang, Z. Y. Wu, Y. M. Wang, Y. Cao, C. F. Zhou and J. H. Zhu, *J. Mater. Chem.*, 2006, **16**, 1536.

- 80 Y. M. Wang, Z. Y. Wu, Y. L. Wei and J. H. Zhu, *Microp. Mesop. Mater.*, 2005, **84**, 127.
- 81 S. S. Fan, M. G. Chapline, N. R. Franklin, T. W. Tomblor, A. M. Cassell and H. J. Dai, *Science*, 1999, **283**, 512.
- 82 T. Rueckes, K. Kim, E. Joselevich, G. Y. Tseng, C. -L. Cheung, C. M. Lieber, *Science*, 2000, **289**, 94.
- 83 J. M. Planeix, N. Coustel, B. Coq, V. Brotons, P. S. Kumbhar, R. Dutartre, P. Geneste, P. Bernier and P. M. Ajayan, *J. Am. Chem. Soc.*, 1994, **116**, 7935.
- 84 A. C. Dillon, K. M. Jones, T. A. Bekkedahl, C. H. Kiang, D. S. Bethune and M. J. Heben, *Nature*, 1997, **386**, 377.
- 85 B. J. Hinds, N. Chopra, T. Rantell, R. Andrews, V. Gavalas and L. G. Bachas, *Science*, 2004, **303**, 62.
- 86 R. Ryoo, S. H. Joo and S. Jun, *J. Phys. Chem. B*, 1999, **103**, 7743.
- 87 R. Ryoo, S. H. Joo, M. Kruk and M. Jaroniec, *Adv. Mater.*, 2001, **13**, 677.
- 88 S. Jun, S. H. Joo, R. Ryoo, M. Kruk, M. Jaroniec, Z. Liu, T. Ohsuna and O. Terasaki, *J. Am. Chem. Soc.*, 2000, **122**, 10712.
- 89 S. H. Joo, S. J. Choi, I. Oh, J. Kwak, Z. Liu, O. Terasaki and R. Ryoo, *Nature*, 2001, **412**, 169.
- 90 J. Ruokolainen, R. Mäkinen, M. Torkkeli, T. Mäkelä, R. Serimaa, G. ten Brinke and O. Ikkala, *Science*, 1998, **280**, 557.
- 91 H. Kosonen, J. Ruokolainen, P. Nyholm and O. Ikkala, *Macromolecules*, 2001, **34**, 3046.
- 92 H. Kosonen, S. Valkama, A. Nykänen, M. Toivanen, G. ten Brinke, J. Ruokolainen and O. Ikkala, *Adv. Mater.*, 2006, **18**, 201.
- 93 C. D. Liang, K. L. Hong, G. A. Guiochon, J. W. Mays and S. Dai, *Angew. Chem. Int. Ed.*, 2004, **43**, 5785.
- 94 C. D. Liang and S. Dai, *J. Am. Chem. Soc.*, 2006, **128**, 5316.
- 95 S. Tanaka, N. Nishiyama, Y. Egashira and K. Ueyama, *Chem. Commun.*, 2005, 2125.
- 96 F. Q. Zhang, Y. Meng, D. Gu, Y. Yan, C. Z. Yu, B. Tu and D. Y. Zhao, *J. Am. Chem. Soc.*, 2005, **127**, 13508.
- 97 Y. Meng, D. Gu, F. Q. Zhang, Y. F. Shi, H. F. Yang, Z. Li, C. Z. Yu, B. Tu and D. Y. Zhao, *Angew. Chem. Int. Ed.*, 2005, **44**, 7053.

- 98 F. Q. Zhang, Y. Meng, D. Gu, Y. Yan, Z. X. Chen, B. Tu and D. Y. Zhao, *Chem. Mater.*, 2006, **18**, 5279.
- 99 Y. Huang, H. Q. Cai, T. Yu, F. Q. Zhang, F. Zhang, Y. Meng, D. Gu, Y. Wan, X. L. Sun, B. Tu and D. Y. Zhao, *Angew. Chem. Int. Ed.*, 2007, **46**, 1089.
- 100 Y. H. Deng, T. Yu, Y. Wan, Y. F. Shi, Y. Meng, D. Gu, L. J. Zhang, Y. Huang, C. Liu, X. J. Wu and D. Y. Zhao, *J. Am. Chem. Soc.*, 2007, **129**, 1690.
- 101 Y. H. Deng, C. Liu, D. Gu, T. Yu, B. Tu and D. Y. Zhao, *J. Mater. Chem.*, 2008, **18**, 91.
- 102 A. Fernández, G. Lassaletta, V. M. Jiménez, A. Justo, A. R. González-Elipe, J. -M. Herrmann, H. Tahiri and Y. Ait-Ichou, *Appl. Catal. B: Environ.*, 1995, **7**, 49.
- 103 G. S. Attard, J. C. Glyde and C. G. Goltner, *Nature*, 1995, **378**, 366.
- 104 G. S. Attard, C. G. Goltner, J. M. Corker, S. Henke and R. H. Templer, *Angew. Chem. Int. Ed.*, 1997, **36**, 1315.
- 105 G. S. Attard, P. N. Bartlett, N. R. B. Coleman, J. M. Elliott, J. R. Owen and J. H. Wang, *Science*, 1997, **278**, 838.
- 106 U. Ciesla, D. G. Demuth, R. Leon, P. M. Petroff, G. D. Stucky, K. K. Unger and F. Schuth, *J. Chem. Soc. Chem. Commun.*, 1994, 1387.
- 107 Q. S. Huo, D. I. Margolese, U. Ciesla, D. G. Demuth, P. Y. Feng, T. E. Gier, P. Sieger, A. Firouzi, B. F. Chmelka, F. Schuth and G. D. Stucky, *Chem. Mater.*, 1994, **6**, 1176.
- 108 D. M. Antonelli and J. Y. Ying, *Angew. Chem. Int. Ed.*, 1995, **34**, 2014.
- 109 U. Ciesla, S. Schacht, G. D. Stucky, K. K. Unger and F. Schuth, *Angew. Chem. Int. Ed.*, 1996, **35**, 541.
- 110 P. D. Yang, D. Y. Zhao, D. I. Margolese, B. F. Chmelka and G. D. Stucky, *Nature*, 1998, **396**, 152.
- 111 P. D. Yang, D. Y. Zhao, D. I. Margolese, B. F. Chmelka and G. D. Stucky, *Chem. Mater.*, 1999, **11**, 2813.
- 112 B. Z. Tian, X. Y. Liu, B. Tu, C. Z. Yu, J. Fan, L. M. Wang, S. H. Xie, G. D. Stucky and D. Y. Zhao, *Nat. Mater.*, 2003, **2**, 159.
- 113 B. Z. Tian, H. F. Yang, X. Y. Liu, S. H. Xie, C. Z. Yu, J. Fan, B. Tu and D. Y. Zhao, *Chem. Commun.*, 2002, 1824.
- 114 P. V. Braun, P. Osenar, V. Tohver, S. B. Kennedy and S. I. Stupp, *J. Am. Chem. Soc.*, 1999, **121**, 7302.
- 115 Y. -J. Han, J. M. Kim and G. D. Stucky, *Chem. Mater.*, 2000, **12**, 2068.

- 116 H. J. Shin, R. Ryoo, Z. Liu and O. Terasaki, *J. Am. Chem. Soc.*, 2001, **123**, 1246.
- 117 Z. Liu, O. Terasaki, T. Ohsuna, K. Hiraga, H. J. Shin and R. Ryoo, *Chemphyschem*, 2001, **2**, 229.
- 118 T. Yokoyama and N. Fujita, *Appl. Catal. A: Gen.*, 2004, **276**, 179.
- 119 S. B. Wang, K. Murata, T. Hayakawa, S. Hamakawa and K. Suzuki, *Catal. Lett.*, 1999, **63**, 59.
- 120 K. K. Zhu, B. Yue, W. Z. Zhou and H. Y. He, *Chem. Commun.*, 2003, 98.
- 121 K. Jiao, B. Zhang, B. Yue, Y. Ren, S. X. Liu, S. R. Yan, C. Dickinson, W. Z. Zhou and H. Y. He, *Chem. Commun.*, 2005, 5618.
- 122 B. Z. Tian, X. Y. Liu, H. F. Yang, S. H. Xie, C. Z. Yu, B. Tu and D. Y. Zhao, *Adv. Mater.*, 2003, **15**, 1370.
- 123 B. Z. Tian, X. Y. Liu, L. A. Solovyov, Z. Liu, H. F. Yang, Z. D. Zhang, S. H. Xie, F. Q. Zhang, B. Tu, C. Z. Yu, O. Terasaki, and D. Y. Zhao, *J. Am. Chem. Soc.*, 2004, **126**, 865.
- 124 C. Dickinson, W. Z. Zhou, R. P. Hodgkins, Y. F. Shi, D. Y. Zhao and H. Y. He, *Chem. Mater.*, 2006, **18**, 3088.
- 125 C. Dickinson, A. Harrison, J. A. Anderson and W. Z. Zhou, *Stud. Surf. Sci. Catal.*, 2006, **165**, 335.
- 126 L. Dupont, S. Laruelle, S. Grugeon, C. Dickinson, W. Z. Zhou and J. -M. Tarascon, *J. Power Sources*, 2008, **175**, 502.
- 127 S. J. Miao and Y. Q. Deng, *Appl. Catal. B: Environ.*, 2001, **31**, L1.
- 128 R. D. Waters, J. J. Weimer and J. E. Smith, *Catal. Lett.*, 1995, **30**, 181.
- 129 R. -J. Wu, C. -H. Hu, C. -T. Yeh and P. -G. Su, *Sensor. Actuator. B: Chem.*, 2003, **96**, 596.
- 130 Y. Q. Wang, C. -M. Yang, W. Schmidt, B. Spliethoff, E. Bill and F. Schüth, *Adv. Mater.*, 2005, **17**, 53.
- 131 F. Jiao, K. M. Shaju and P. G. Bruce, *Angew. Chem. Int. Ed.*, 2005, **44**, 6550.
- 132 Y. G. Wang and Y. Y. Xia, *Electrochim. Acta.*, 2006, **51**, 3223.
- 133 R. Palombari and F. Pierri, *J. Electroanal. Chem.*, 1997, **433**, 213.
- 134 K. K. Purushothaman and G. Muralidharan, *J. Sol-Gel Sci. Technol.*, 2008, **46**, 190.
- 135 W. H. Shen, X. P. Dong, Y. F. Zhu, H. R. Chen and J. L. Shi, *Microp. Mesop. Mater.*, 2005, **85**, 157.

- 136 A. M. T. Silva, R. R. N. Marques and R. M. Quinta-Ferreira, *Appl. Catal. B: Environ.*, 2004, **47**, 269.
- 137 M. Lundberg, B. Skarman and L. R. Wallenberg, *Microp. Mesop. Mater.*, 2004, **69**, 187.
- 138 M. P. Kapoor, Y. Ichihashi, T. Nakamori and Y. Matsumura, *J. Mol. Catal. A: Chem.*, 2004, **213**, 251.
- 139 E. Rossinyol, J. Arbiol, F. Peiró, A. Cornet, J. R. Morante, B. Z. Tian, B. Tu and D. Y. Zhao, *Sensor. Actuator. B: Chem.*, 2005, **109**, 57.
- 140 J. C. Manificier and L. Szepessy, *Appl. Phys. Lett.*, 1977, **31**, 459.
- 141 J. Kleperis, M. Kundzinš, G. Vitinš, V. Eglitis, G. Vaivars and A. Lūsis, *Sensor. Actuator. B: Chem.*, 1995, **28**, 135.
- 142 A. Gurlo, M. Ivanovskaya, N. Bârsan, M. Schweizer-Berberich, U. Weimar, W. Göpel and A. Diéguez, *Sensor. Actuator. B: Chem.*, 1997, **44**, 327.
- 143 B. L. Zhu, C. S. Xie, D. W. Zeng, A. H. Wang, W. L. Song and X. Z. Zhao, *J. Mater. Sci.*, 2005, **40**, 5783.
- 144 H. F. Yang, Q. H. Shi, B. Z. Tian, Q. Y. Lu, F. Gao, S. H. Xie, J. Fan, C. Z. Yu, B. Tu and D. Y. Zhao, *J. Am. Chem. Soc.*, 2003, **125**, 4724.
- 145 F. Jiao, B. Yue, K. K. Zhu, D. Y. Zhao and H. Y. He, *Chem. Lett.*, 2003, **32**, 770.
- 146 D. Larcher, C. Masquelier, D. Bonnin, Y. Chabre, V. Masson, J. -B. Leriche and J. -M. Tarascon, *J. Electrochem. Soc.*, 2003, **150**, A133.
- 147 J. Sarradin, M. Ribes, A. Guessous and K. Elkacemi, *Solid State Ionics*, 1998, **112**, 35.
- 148 T. Tsoncheva, J. Rosenholm, C. V. Teixeira, M. Dimitrov, M. Linden and C. Minchev, *Microp. Mesop. Mater.*, 2006, **89**, 209.
- 149 F. Jiao, A. Harrison, J. -C. Jumas, A. V. Chadwick, W. Kockelmann and P. G. Bruce, *J. Am. Chem. Soc.*, 2006, **128**, 5468.
- 150 F. Jiao, J. -C. Jumas, M. Womes, A. V. Chadwick, A. Harrison and P. G. Bruce, *J. Am. Chem. Soc.*, 2006, **128**, 12905.
- 151 M. M. Thackeray, M. H. Rossouw, A. de Dekock and A. P. de la Harpe, *J. Power Sources*, 1993, **43**, 289.
- 152 Y. Shao-Horn, S. A. Hackney, C. S. Johnson and M. M. Thackeray, *J. Electrochem. Soc.*, 1998, **145**, 582.
- 153 J. B. Yang, X. D. Zhou, W. J. James, S. K. Malik and C. S. Wang, *Appl. Phys. Lett.*, 2004, **85**, 3160.

- 154 G. L. Wang, B. Tang, L. H. Zhuo, J. C. Ge and M. Xue, *Eur. J. Inorg. Chem.*, 2006, 2313.
- 155 A. R. Armstrong and P. G. Bruce, *Nature*, 1996, **381**, 499.
- 156 Q. Zhou, X. Li, Y. G. Li, B. Z. Tian, D. Y. Zhao and Z. Y. Jiang, *Chin. J. Chem.*, 2006, **24**, 835.
- 157 J. Y. Luo, J. J. Zhang and Y. Y. Xia, *Chem. Mater.*, 2006, **18**, 5618.
- 158 F. Jiao and P. G. Bruce, *Adv. Mater.*, 2007, **19**, 657.
- 159 F. Jiao, A. Harrison, A. H. Hill and P. G. Bruce, *Adv. Mater.*, 2007, **19**, 4063.
- 160 E. B. Franke, C. L. Trimble, J. S. Hale, M. Schubert and J. A. Woollam, *J. Appl. Phys.*, 2000, **88**, 5777.
- 161 J. Khalack and P. V. Ashrit, *Appl. Phys. Lett.*, 2006, **89**, 211112.
- 162 Y. D. Wang, Z. X. Chen, Y. F. Li, Z. L. Zhou and X. H. Wu, *Solid State Electron.*, 2001, **45**, 639.
- 163 R. H. Jin, H. X. Li and J. F. Deng, *J. Catal.*, 2001, **203**, 75.
- 164 K. K. Zhu, H. Y. He, S. H. Xie, X. Zhang, W. Z. Zhou, S. L. Jin and B. Yue, *Chem. Phys. Lett.*, 2003, **377**, 317.
- 165 B. Yue, H. L. Tang, Z. P. Kong, K. K. Zhu, C. Dickinson, W. Z. Zhou and H. Y. He, *Chem. Phys. Lett.*, 2005, **407**, 83.
- 166 K. K. Zhu, B. Yue, S. H. Xie, S. Y. Zhang, B. Zhang, S. L. Jin, H. Y. He, *Chin. J. Chem.*, 2004, **22**, 33.
- 167 K. Lee, Y. -H. Kim, S. B. Han, H. Kang, S. Park, W. S. Seo, J. T. Park, B. Kim and S. Chang, *J. Am. Chem. Soc.*, 2003, **125**, 6844.
- 168 A. H. Lu, W. Schmidt, A. Taguchi, B. Spliethoff, B. Tesche and F. Schüth, *Angew. Chem. Int. Ed.*, 2002, **41**, 3489.
- 169 M. Kang, S. H. Yi, H. I. Lee, J. E. Yie and J. M. Kim, *Chem. Commun.*, 2002, 1944.
- 170 Q. Liu, A. Q. Wang, X. D. Wang and T. Zhang, *Chem. Mater.*, 2006, **18**, 5153.
- 171 J. Roggenbuck and M. Tiemann, *J. Am. Chem. Soc.*, 2005, **127**, 1096;
- 172 J. Roggenbuck, G. Koch and M. Tiemann, *Chem. Mater.*, 2006, **18**, 4151.
- 173 X. Y. Lai, X. T. Li, W. C. Geng, J. C. Tu, J. X. Li and S. L. Qiu, *Angew. Chem. Int. Ed.*, 2007, **119**, 752.
- 174 S. -I. Fujita, Y. Kanamori, A. M. Satriyo and N. Takezawa, *Catal. Today*, 1998, **45**, 241.
- 175 S. Polarz, A. V. Orlov, F. Schüth and A. H. Lu, *Chem. Eur. J.*, 2007, **13**, 592.

- 176 T. Waitz, M. Tiemann, P. J. Klar, J. Sann, J. Stehr and B. K. Meyer, *Appl. Phys. Lett.*, 2007, **90**, 123108.
- 177 T. Wagner, T. Waitz, J. Roggenbuck, M. Fröba, C.-D. Kohl and M. Tiemann, *Thin Solid Films*, 2007, **515**, 8360.
- 178 J. Roggenbuck, H. Schäfer, T. Tsoncheva, C. Minchev, J. Hanss and M. Tiemann, *Microp. Mesop. Mater.*, 2007, **101**, 335.
- 179 S. C. Laha and R. Ryoo, *Chem. Commun.*, 2003, 2138.
- 180 J. Roggenbuck, T. Waitz and M. Tiemann, *Microp. Mesop. Mater.*, 2008, **113**, 575.
- 181 F. Keller, M. S. Hunter and D. L. Robinson, *J. Electrochem. Soc.*, 1953, **100**, 411.
- 182 H. Masuda and K. Fukuda, *Science*, 1995, **268**, 1466.
- 183 O. Jessensky, F. Müller and U. Gösele, *Appl. Phys. Lett.*, 1998, **72**, 1173.
- 184 G. K. Singh, A. A. Golovin and I. S. Aranson, *Phys. Rev. B*, 2006, **73**, 205422.
- 185 O. K. Varghese, D. Gong, M. Paulose, K. G. Ong, E. C. Dickey and C. A. Grimes, *Adv. Mater.*, 2003, **15**, 624.
- 186 A. Fujishima and K. Honda, *Nature*, 1972, **238**, 37.
- 187 G. K. Mor, K. Shankar, M. Paulose, O. K. Varghese, C. A. Grimes, *Nano Lett.*, 2006, **6**, 215.
- 188 J. M. Macak, H. Tsuchiya, L. Taveira, S. Aldabergerova and P. Schmuki, *Angew. Chem. Int. Ed.*, 2005, **44**, 7463.
- 189 Z. X. Su and W. Z. Zhou, *Adv. Mater.*, 2008, **20**, 3663.
- 190 H. -C. Shin, J. Dong and M. L. Liu, *Adv. Mater.*, 2004, **16**, 237.
- 191 G. B. Stefanovich, A. L. Pergament, A. A. Velichko and L. A. Stefanovich, *J. Phys.: Condens. Matter*, 2004, **16**, 4013.
- 192 I. Sieber, H. Hildebrand, A. Friedrich and P. Schmuki, *Electrochem. Commun.*, 2005, **7**, 97.
- 193 I. Sieber, B. Kannan, P. Schmuki, *Electrochem. Solid-State Lett.*, 2005, **8**, J10.
- 194 H. Tsuchiya and P. Schmuki, *Electrochem. Commun.*, 2005, **7**, 49.
- 195 H. Tsuchiya, J. M. Macak, I. Sieber and P. Schmuki, *small*, 2005, **1**, 722.
- 196 W. B. Yue, A. H. Hill, A. Harrison and W. Z. Zhou, *Chem. Commun.*, 2007, 2518.
- 197 W. B. Yue and W. Z. Zhou, *J. Mater. Chem.*, 2007, **17**, 4947.
- 198 W. B. Yue and W. Z. Zhou, *Chem. Mater.*, 2007, **19**, 2359.

- 199 W. B. Yue, X. X. Xu, J. T. S. Irvine, P. S. Attidekou, C. Liu, H. Y. He, D. Y. Zhao and W. Z. Zhou, **DOI**: 10.1021/cm900197p.
- 200 W. B. Yue, C. Randorn, P. S. Attidekou, J. T. S. Irvine and W. Z. Zhou, submitted for publication.
- 201 X. H. Liu, J. Yang, L. Wang, X. J. Yang, L. D. Lu and X. Wang, *Mater. Sci. Eng. A*, 2000, **289**, 241.
- 202 C. M. Wang, H. Wu and S. L. Chung, *J. Porous Mater.*, 2006, **13**, 307.
- 203 J. Z. Chen, ‘*Modern Crystal Chemistry-Theories and Techique*’, High Education Press, Beijing, 2001.
- 204 P. B. Hirsch, A. Howie, R. B. Nicholson, D. W. Pashley and M. J. Whelan, ‘*Electron Microscopy of Thin Crystals*’, Krieger Publishing Company, New York, 1977.
- 205 J. C. H. Spence, ‘*High-Resolution Electron Microscopy*’, Oxford University Press, New York, 2003.
- 206 R. Jenkins and R. L. Snyder, ‘*Introduction to X-ray Powder Diffraction*’, Wiley-Interscience, New York, 1996.
- 207 A. L. Patterson, *Phys. Rev.*, 1939, **56**, 978.
- 208 I. Langmuir, *J. Am. Chem. Soc.*, 1916, **38**, 2221.
- 209 E. P. Barrett, L. G. Joyner and P. P. Halenda, *J. Am. Chem. Soc.*, 1951, **73**, 373.
- 210 L. E. A. Godfrey, *Text. Res. J.*, 1970, **40**, 116.
- 211 P. A. Connor, F. Belliard, M. Behm, L. G. Tovar and J. T. S. Irvine, *Ionics*, 2002, **8**, 172.
- 212 C. Randorn, J. T. S. Irvine and P. Robertson, *Int. J. Photoenergy*, 2008, doi:10.1155/2008/426872.
- 213 A. Houas, H. Lachheb, M. Ksibi, E. Elaloui, C. Guillard and J. -M. Herrmann, *Appl. Catal. B: Environ.*, 2001, **31**, 145.
- 214 X. L. Yan, T. Ohno, K. Nishijima, R. Abe, B. Ohtani, *Chem. Phys. Lett.*, 2006, **429**, 606.
- 215 K. Zaghib, M. Simoneau, M. Armand and M. Gauthier, *J. Power Sources*, 1999, **81**, 300.
- 216 E. M. Sorensen, S. J. Barry, H. K. Jung, J. R. Rondinelli, J. T. Vaughey and K. R. Poeppelmeier, *Chem. Mater.*, 2006, **18**, 482.
- 217 J. Kim and J. Cho, *Electrochem. Solid-State Lett.*, 2007, **10**, A81.

- 218 T. Ohno, D. Haga, K. Fujihara, K. Kaizaki and M. Matsumura, *J. Phys. Chem. B*, 1997, **101**, 6415.
- 219 H. Iida and A. Igarashi, *Appl. Catal. A: Gen.*, 2006, **298**, 152.
- 220 C. H. Jiang, I. Honma, T. Kudo and H. S. Zhou, *Electrochem. Solid-State Lett.*, 2007, **10**, A127.
- 221 D. Grosso, G. J. D. A. A. Soler-Illia, F. Babonneau, C. Sanchez, P. A. Albouy, A. Brunet-Bruneau and A. R. Balkenende, *Adv. Mater.*, 2001, **13**, 1085.
- 222 W. Y. Dong, Y. J. Sun, C. W. Lee, W. M. Hua, X. C. Lu, Y. F. Shi, S. C. Zhang, J. M. Chen and D. Y. Zhao, *J. Am. Chem. Soc.*, 2007, **129**, 13894.
- 223 L. J. Shi, R. Yang and M. Li, *Chin. J. Inorg. Chem.*, 2006, **22**, 1196.
- 224 C. C. Wang and J. Y. Ying, *Chem. Mater.*, 1999, **11**, 3113.
- 225 Z. Y. Wang, F. X. Zhang, Y. L. Yang, B. Xue, J. Cui and N. J. Guan, *Chem. Mater.*, 2007, **19**, 3286.
- 226 B. Ohtani, Y. Ogawa and S. -I. Nishimoto, *J. Phys. Chem. B*, 1997, **101**, 3746.
- 227 Z. X. Wang, C. A. Wu, L. J. Liu, F. Wu, L. Q. Chen and X. J. Huang, *J. Electrochem. Soc.*, 2002, **149**, A466.
- 228 J. X. Li, W. -L. Dai and K. N. Fan, *J. Phys. Chem. C*, 2008, **112**, 17657.
- 229 S. Seimanides and M. Stoukides, *J. Electrochem. Soc.*, 1986, **133**, 1535.
- 230 J. A. Melero, G. Calleja, F. Martínez, R. Molina, *Catal. Commun.*, 2006, **7**, 478.
- 231 E. -K. Lee, K. -D. Jung, O. -S. Joo and Y. -G. Shul, *React. Kinet. Catal. Lett.*, 2006, **87**, 115.
- 232 K. -S. Focsaneanu and J. C. Scaiano, *Photochem. Photobiol. Sci.*, 2005, **4**, 817.
- 233 T. Okuhara and K. -I. Tanaka, *J. Catal.*, 1980, **61**, 135.
- 234 K. M. A. El-Salaam and E. A. Hassan, *Surf. Technol.*, 1982, **16**, 121.
- 235 A. Amberntsson, H. Persson, P. Engstrom and B. Kasemo, *Appl. Catal. B: Environ.*, 2001, **31**, 27.
- 236 K. S. Kabin, R. L. Muncrief and M. P. Harold, *Catal. Today*, 2004, **96**, 79.
- 237 Y. L. Wei, Y. M. Wang, J. H. Zhu and Z. Y. Wu, *Adv. Mater.*, 2003, **15**, 1943.
- 238 C. H. Tu, A. Q. Wang, M. Y. Zheng, X. D. Wang and T. Zhang, *Appl. Catal. A: Gen.*, 2006, **297**, 40.
- 239 Y. Xu, Q. Jiang, Y. Cao, Y. L. Wei, Z. Y. Yun, J. H. Xu, Y. Wang, C. F. Zhou, L. Y. Shi and J. H. Zhu, *Adv. Funct. Mater.*, 2004, **14**, 1113.
- 240 H. F. Yang, Q. Y. Lu, F. Gao, Q. H. Shi, Y. Yan, F. Q. Zhang, S. H. Xie, B. Tu and D. Z. Zhao, *Adv. Funct. Mater.*, 2005, **15**, 1377.

- 241 B. J. Xu, T. Li, B. Zheng, W. M. Hua, Y. H. Yue and Z. Gao, *Catal. Lett.*, 2007, **119**, 283.
- 242 T. Fujitani, M. Saito, Y. Kanai, T. Watanabe, J. Nakamura and T. Uchijima, *Appl. Catal. A: Gen.*, 1995, **125**, L199.
- 243 C. Samanta and V. R. Choudhary, *Appl. Catal. A: Gen.*, 2007, **326**, 28.
- 244 Y. Yang, J. X. Ma and F. Wu, *Int. J. Hydrogen Energy*, 2006, **31**, 877.
- 245 J. W. Andreasen, F. B. Rasmussen, S. Helveg, A. Molenbroek, K. Stahl, M. M. Nielsend and R. Feidenhans'l, *J. Appl. Cryst.*, 2006, **39**, 209.
- 246 T. Arai, K. Maruya, K. Domen and T. Onishi, *Bull. Chem. Soc. Jpn.*, 1989, **62**, 349.
- 247 L. Zhao, J. X. Chen and J. Y. Zhang, *J. Mol. Catal. A-Chem.*, 2006, **246**, 140.
- 248 Y. Tanaka, H. Hattori and K. Tanabe, *Bull. Chem. Soc. Jpn.*, 1978, **51**, 3641.
- 249 J. C. Fierro-Gonzalez, V. A. Bhirud and B. C. Gates, *Chem. Commun.*, 2005, 5275.
- 250 T. Yamaguchi, *Catal. Today*, 1994, **20**, 199.
- 251 A. S. Carrillo, T. Tagawa and S. Goto, *Mater. Res. Bull.*, 2001, **26**, 1017.
- 252 E. Hafele, K. Kaltenmaier and U. Schonauer, *Sensor. Actuat. B-Chem.*, 1991, **4**, 525.
- 253 L. Vianin and C. Comninellis, *Electrochim. Acta*, 1998, **43**, 1109.
- 254 B. Liu and R. T. Baker, *J. Mater. Chem.*, 2008, **18**, 5200.
- 255 L. Vradman, M. V. Landau, D. Kantorovich, Y. Kolytyn, A. Gedanken, *Microp. Mesop. Mater.*, 2005, **79**, 307.
- 256 W. Z. Zhou, H. M. A. Hunter, P. A. Wright, Q. Ge and J. M. Thomas, *J. Phys. Chem. B*, 1998, **102**, 6933.
- 257 M. J. Edmondson, W. Z. Zhou, S. A. Seiber, I. P. Jones, I. Gameson, P. A. Anderson and P. P. Edwards, *Adv. Mater.*, 2001, **13**, 1608.

Publications

- 1 **W. B. Yue**, A. H. Hill, A. Harrison and W. Z. Zhou, 'Mesoporous single-crystal Co_3O_4 templated by cage-containing mesoporous silica', *Chem. Commun.*, **2007**, 2518.
- 2 **W. B. Yue** and W. Z. Zhou, 'Synthesis of porous single crystals of metal oxides via a solid-liquid route', *Chem. Mater.*, **2007**, 19, 2359.
- 3 **W. B. Yue** and W. Z. Zhou, 'Porous crystals of cubic metal oxides templated by cage-containing mesoporous silica', *J. Mater. Chem.*, **2007**, 17, 4947.
- 4 **W. B. Yue** and W. Z. Zhou, 'Mesoporous metal oxides templated by FDU-12 using a new convenient method', *Stud. Surf. Sci. Catal.*, **2007**, 170, 1755. (conference papers)
- 5 J. Wang, J. C. Groen, **W. B. Yue**, W. Z. Zhou and M. -O. Coppens, 'Single-template synthesis of zeolite ZSM-5 composites with tunable mesoporosity', *Chem. Commun.*, **2007**, 4653.
- 6 J. Wang, J. C. Groen, **W. B. Yue**, W. Z. Zhou and M. -O. Coppens, 'Facile synthesis of ZSM-5 composites with hierarchical porosity', *J. Mater. Chem.*, **2008**, 18, 468.
- 7 **W. B. Yue** and W. Z. Zhou, 'Crystalline mesoporous metal oxide', *Prog. Natural Sci.*, **2008**, 18, 1329. (review article)
- 8 J. F. Geng, W. Z. Zhou, P. Skelton, **W. B. Yue**, I. A. Kinloch, A. H. Windle and B. F. G. Johnson, 'Crystal structure and growth mechanism of unusually long fullerene (C_{60}) nanowires', *J. Am. Chem. Soc.*, **2008**, 130, 2527.
- 9 J. F. Yao, D. Li, X. Y. Zhang, C. -H. Kong, **W. B. Yue**, W. Z. Zhou, H. T. Wang, 'Cubes of zeolite A with an amorphous core', *Angew. Chem. Int. Ed.*, **2008**, 47, 1.

- 10 J. Wang, **W. B. Yue**, W. Z. Zhou and M. -O. Coppens, 'TUD-C: A tunable, hierarchically structured mesoporous zeolite composite', *Microp. Mesop. Mater.*, **2009**, 120, 19.
- 11 **W. B. Yue**, X. X. Xu, J. T. S. Irvine, P. S. Attidekou, C. Liu, H. Y. He, D. Y. Zhao and W. Z. Zhou, 'Mesoporous Monocrystalline TiO₂ and Its Solid State Electrochemical Properties', DOI: 10.1021/cm900197p.
- 12 **W. B. Yue**, C. Random, P. S. Attidekou, J. T. S. Irvine and W. Z. Zhou, 'Syntheses, Li Insertion and Photoactivity of Mesoporous Crystalline TiO₂', *submitted for publication*.
- 13 A. H. Hill, A. Harrison, C. Ritter, Calum Dickinson, **W. B. Yue** and W. Z. Zhou, 'Neutron powder diffraction and magnetic studies of mesoporous Co₃O₄', *submitted for publication*.